Mémoire

Auteur : Hennuy, Thomas
Promoteur(s) : Houbrechts, Geoffrey; 28780
Faculté : Faculté des Sciences
Diplôme : Master en sciences géographiques, orientation global change, à finalité approfondie
Année académique : 2024-2025
URI/URL : http://hdl.handle.net/2268.2/23889

Faculty of Sciences
Department of Geography

University of Liege

OSL dating and sedimentary and morphological analysis of the gold panning mounds along two streams in the Ardennes (Rougerie and Schinderbach, Belgium)

Master thesis presented by: **Thomas HENNUY**

for obtaining the title of

Master in geography, Global Change, research focus in geomorphology and environmental risks

Academic year: **2024-2025**
Date of defense: **September 2025**

President of jury: Pr. **Xavier FETTWEIS**
Promoters: Pr. **Geoffrey HOUBRECHTS**
Pr. **Dimitri VANDENBERGHE**
Reading jury: Pr. **Xavier FETTWEIS**
Pr. **Serge SCHMITZ**

Faculté des sciences
Département de géographie
Université de Liège

Datation OSL et analyse sédimentaire et morphologique des tertres d'orpaillage de deux ruisseaux ardennais (Rougerie et Schinderbach, Belgique)

Mémoire présenté par : **Thomas HENNUY**

pour l'obtention du titre de

Master en sciences géographiques, orientation Global Change, à finalité approfondie en géomorphologie et risques environnementaux

Année académique :	**2024-2025**
Date de défense :	**Septembre 2025**
Président de jury :	Pr. **Xavier FETTWEIS**
Promoteurs :	Pr. **Geoffrey HOUBRECHTS**
	Pr. **Dimitri VANDENBERGHE**
Jury de lecture :	Pr. **Xavier FETTWEIS**
	Pr. **Serge SCHMITZ**

Acknowledgement

I would like to thank everyone who, directly or indirectly, contributed to the success of my internship and supported me during the writing of this thesis.

First and foremost, I wish to express my deepest gratitude to my promoter, Geoffrey Houbrechts, and my co-promoter, Dimitri Vandenberghe, for their commitment, availability, and insightful advice, which greatly contributed to the successful completion of this work.

I am also sincerely grateful to Bruno Van Eerdenbrugh and Christelle Draily for their assistance, expertise, and enthusiasm during the different field campaigns.

My thanks also go to Nasrin and Jef from Ghent University for their warm welcome, their guidance and advice during the preparation of the samples in the laboratory, as well as for the many hours spent together conducting the measurements.

More generally, I would like to thank the entire team of *Laboratoire d'Hydrographie et de Géomorphologie Fluviatile* (LHGF) for their support in data processing and laboratory analyses.

These five years of study would undoubtedly have been much more challenging without the presence and mutual support of my fellow geography students, to whom I am truly grateful.

Finally, this thesis would not have been possible without the unwavering support of my family and my girlfriend throughout my academic journey, as well as the interest they have shown in this work.

Résumé

En Ardenne belge, l'orpaillage alluvial antique a profondément remodelé les rivières et les fonds de vallée. Les morphologies qui en résultent demeurent encore visibles aujourd'hui et influencent toujours l'évolution des cours d'eau. Pourtant, elles ont fait l'objet de peu de recherches scientifiques et sont de plus en plus menacées de destruction par les pratiques agricoles et forestières.

Ce travail vise à combler cette lacune en évaluant le potentiel de la luminescence stimulée optiquement (OSL) appliquée au quartz pour la datation des tertres d'orpaillage et en analysant les méthodes d'exploitation ainsi que les dépôts associés. Deux sites ont été étudiés : le ruisseau de la Rougerie et le Schinderbach-A. Le protocole SAR (single-aliquot regenerative dose) a été appliqué en supposant que les grains de quartz avaient été suffisamment exposés à la lumière du jour lors des opérations de lavage. Des datations radiocarbone ont également été réalisées sur des charbons issus des deux sites. Des approches complémentaires ont inclus des levés topographiques, des carottages en travers de la vallée, l'étude de coupes stratigraphiques, ainsi que l'élaboration d'une typologie des morphologies d'orpaillage, sur base d'observations de terrain et d'analyses LiDAR.

L'application inédite de l'OSL aux résidus d'orpaillage s'est révélée prometteuse : bien que le blanchiment incomplet des grains ait limité la précision des âges finaux, les distributions des doses équivalentes montrent une prédominance de valeurs jeunes, cohérentes avec la période d'exploitation. Les datations radiocarbone apportent des ancrages chronologiques solides, datant la Rougerie de la période romaine (230–380 cal. AD) et le Schinderbach-A de la période celtique ou gallo-romaine (196–41 cal. BC). Les analyses géomorphologiques ont permis d'affiner le modèle conceptuel d'évolution de vallée pour la Rougerie et d'en proposer un nouveau pour le Schinderbach-A. Les résidus d'orpaillage ont également été caractérisés et comparés à ceux issus de la ruée vers l'or américaine du XIXe siècle.

Ces résultats constituent le premier cadre chronologique fiable pour les tertres d'orpaillage du massif de Stavelot. Ils apportent de nouvelles perspectives sur l'histoire de l'exploitation aurifère en Ardenne et démontrent le potentiel de l'OSL pour des applications aux résidus d'orpaillage à l'échelle mondiale.

Abstract

In the Belgian Ardennes, ancient alluvial gold mining profoundly reshaped rivers and valley bottoms. The resulting morphologies remain visible today, still influencing the evolution of rivers. Yet, they have received little scientific attention and are increasingly threatened with destruction by agriculture and forestry.

This study addresses this gap by evaluating the potential of quartz-based optically stimulated luminescence (OSL) dating for gold-panning mounds and by analysing exploitation methods and related deposits. Two sites were investigated: the Rougerie stream and the Schinderbach-A. The single-aliquot regenerative dose (SAR) protocol was applied under the assumption that quartz grains were sufficiently bleached during washing operations. Radiocarbon dating was also performed on charcoal samples from both sites. Complementary approaches included topographic surveys, coring across valley transects, stratigraphic logging, and the development of a typology of mining-related morphologies based on fieldwork and LiDAR-based mapping

The unprecedented application of OSL to gold-mining mounds proved promising: although incomplete resetting limited the accuracy of final ages, equivalent dose distributions revealed a predominance of young values consistent with mining activity. Radiocarbon ages provided firm chronological anchors, dating the Rougerie to the Roman period (230–380 cal. AD) and the Schinderbach-A to the Celtic or Gallo-Roman period (196–41 cal. BC). Geomorphological analyses further led to a revised conceptual model of valley evolution for the Rougerie and a new model for the Schinderbach-A. Tailings deposits were also characterised and presented similarities with those produced during the 19th-century American gold rush.

These findings establish the first reliable chronological framework for gold-panning mounds in the Stavelot Massif. They also provide new insights into the history of ancient mining in the Ardennes and demonstrate the potential of OSL for broader applications to gold mining tailings worldwide.

Table of content

List of abbreviations

σ: standard deviation

^{14}C: Carbon 14

D_e: equivalent dose, radiation energy absorbed since resetting of the OSL signal

DEM: digital elevation model

DTM: digital terrain model

D_r: dose rate

GIS: geographic information system

Gy: Gray, unit of the absorbed radiation, 1 Gy = 1 $J.kg^{-1}$

IR: infrared, wavelength 0.7 – 1 mm

IRSL: infrared stimulated luminescence

ka: kilo-annum, 1 ka = 1000 years

LiDAR: light detection and ranging

OSL: optically stimulated luminescence

RSD: relative standard deviation

RTK: real time kinematic

SI: the international system of units

TL: thermoluminescence

INTRODUCTION

Today, few rivers in the world have escaped modification by human activity. Over the past millennia, humans have exerted considerable pressure on fluvial systems through both direct and indirect actions. Most rivers have been diverted, straightened, channelised, dredged, or dammed. Hillslopes have also been reshaped through clearing and agriculture to meet human needs. These changes often reflect specific periods in human history and the characteristic land-use practices of each era. They have also frequently altered sedimentary dynamics, and consequently fluvial environments.

Mineral extraction is among the main anthropogenic pressures on rivers. In the Ardennes, gold was intensively exploited in the past: huge amounts of alluvium were removed and processed for gold, profoundly altering valley bottom topography. Many rivers still show the scars of this activity, the most visible being gold-panning mounds. According to a LiDAR-based inventory by Baudoux (2018), 3,235 mounds are distributed across 150 sites in the valley bottoms of 31 rivers and streams in the Ardennes. These mounds consist of gold-washing tailings, mainly gravel, sand, and sterile silty alluvium that once covered auriferous deposits. In addition to mounds, numerous other features reflect ancient mining, such as paleochannels, excavations, and mining fronts. They are however understudied and this immaterial heritage, informing on human mining and associated environmental impact, is under serious threat of destruction by agriculture and forestry.

These remains of past gold mining are found across five distinct geological regions: the southern edge of the Stavelot Massif, the Serpont Massif, along the Herbeumont Fault, within the metamorphosed zone east of the Givonne Massif, and locally along the Rocroi Massif near the Croix-Scaille. Impacted rivers are generally located in headwater basins, where gold is less dispersed and sufficiently concentrated in valley bottom deposits to make extraction profitable (Baudoux, 2018).

Several studies have attempted to date the periods of gold mining in the Ardennes. The first to propose a relative chronology supported by proofs was Q. Esser (1880), who suggested a Gallo-Roman origin based on the presence of small horseshoes, which he attributed to a breed present in the region at that time. This hypothesis was taken up and refined by J. Bastin (1911), who rejected the Roman attribution on the grounds that no Roman texts mention these mining features. He argued instead for a Celtic origin, an interpretation adopted by most subsequent authors, despite his own acknowledgement that the absence of evidence was a weak argument. In the late 1970s and early 1980s, Dumont (1976, 1979, 1980) obtained radiocarbon dates from samples taken at the base of gold-panning mounds in the Stavelot and Serpont Massifs. His results supported Bastin's hypothesis (2σ[1] probability): one date fell between 75 cal. BC and 35 cal. AD, the other between 360 cal. BC and 280 cal. BC. These findings have since been widely cited as the basis for attributing Ardennes gold mining to the Celts (Grailet, 1998; Detaille & Van Eerdenbrugh, 2014; Baudoux, 2018).

More recently, Van Ruymbeke (2021) and Draily (2022) have questioned these Celtic attributions. Bastin's reasoning, based on the absence of Roman documentation, has been criticised, and the small horseshoes could equally date from the Roman or medieval periods. Furthermore, when recalibrated using the current calibration curve (IntCal20), Dumont's first

[1] σ: standard deviation

date now falls (2σ) between 54 cal. BC and 211 cal. AD, largely within the Roman period. The second date still falls within the Celtic Second Iron Age (400–204 cal. BC, 2σ). However, it has been discredited by another date from above the Celtic layer which is significantly older but was not published by the author (Draily, 2022).

For the Stavelot Massif specifically, the only reliable dates currently available come from an underground gold mine at the Trou des Massotais (Plateau des Tailles), which indicate Roman exploitation from the late 3rd to early 5th centuries AD (Cauuet, 2005; Draily et al., 2022). Because these dates come from a gold mine, there is still no reliable dating of alluvial gold mining in the Stavelot Massif. The first objective of this study is therefore to address this significant gap in the understanding of gold mining in the Ardennes.

More precisely, the aim is to explore the potential, i.e. possibilities and limitations, of quartz-based optically stimulated luminescence (OSL) dating for application to gold-panning mounds. Two study sites were selected based on predefined criteria following a field prospection phase:

- Rougerie stream (Vielsalm, Province of Luxembourg): an affluent of the Salm bordered by numerous mounds, previously studied by Baudoux (2018), who analysed several sections, collected samples, and proposed a conceptual model of valley exploitation. This site was selected to build upon and refine Baudoux's findings.
- Schinderbach-A stream (Amel, Province of Liège): an unnamed tributary of the Schinderbach, part of the Amel basin. The site features numerous mounds of varying shapes and sizes, as well as clearly marked paleochannels. The mining morphologies are exceptionally well preserved, which is why the site was selected.

To meet the first objective, OSL dating was applied to sediments from the mounds and to sandy infill from a paleochannel. The method uses the property of quartz grains to act as natural dosimeter, in order to determine the time elapsed since their last exposure to sunlight. Exposure to light or heat resets the luminescence signal, which then rebuilds over time once the grains are buried. This signal is measured in the laboratory to establish the age of the deposits. The working hypothesis is that quartz grains were exposed to sunlight, and thus reset, during washing operations in sluice-type structures. Once deposited in the mounds, they were shielded from light, allowing the luminescence signal to accumulate. As of today, this method has never been applied to gold-panning tailings, except Deprez *et al.* (2018) in a different context. If successful, it would open the way for numerous applications related to alluvial gold mining and would represent a breakthrough in contextualising and understanding gold exploitation in the Ardennes. To validate the OSL ages, two radiocarbon dates were also obtained and are presented in this work.

The second objective is to understand the methods of gold exploitation, including an inventory of mining-related morphologies, the study of exploited valley bottom deposits, and their formation.

The approach to achieve this objective combines sediment coring, stratigraphic section recording, and morphological analysis. A total of 43 sediment cores were taken from 14 coring sites (five along the Rougerie and nine along the Schinderbach). In the laboratory, the cores were first described in terms of colour, texture, and coarse-element content, then analysed for grain size distribution and characteristic particle size in texturally uniform layers. Stratigraphic sections were recorded from vertical exposures along the streams, providing direct observations of *in-situ* sedimentary sequences. The analysis of mining morphologies helped identify

recurring patterns in mining features, revealing past exploitation strategies such as river diversion, trench excavation, and the creation of water storage basins.

In this study, the term gold panning refers specifically to the washing of alluvium to recover gold, while (alluvial) gold mining refers more broadly to the entire range of extraction activities, including panning, alluvium removal, river diversion, and any other associated operations.

Chapter I :
GOLD MINING

Summary of chapter I: This chapter reviews state-of-the-art knowledge on gold mining in Belgium and, to a lesser extent, in Europe. Following a "top-down" approach, the first section briefly assesses the history and impacts of ancient gold mining in Western Europe. The second section consists of the history of the early discoveries in Belgium, more precisely in the northeastern Ardennes, and the various attempts to establish a chronology. Finally, the gold mining structures and techniques are explained, as well as the localisation of the remains in Belgium. The last section examines the impact of 19th-century gold mining on streams worldwide.

1. History of gold exploitation in Europe

During antiquity, gold was extensively exploited by different civilisations from the Bronze Age to the Roman period. Multiple regions across Europe are known to contain gold, either hosted in vein deposits or in alluvial deposits of rivers. The most exploited and studied region is the Iberian Peninsula (Domergue, 1990) but, as explained by Cauuet (2005), many more metalliferous regions exist in Europe that had not been sufficiently studied by the time of Cauuet's publication. The main auriferous regions are, as illustrated in Figure I.1, (1) the Iberian peninsula; (2) the Pyrenees; (3) Limousin-Auvergne; (4) the Armorican massif; (5) Dolaucothi; (6) the Western Italian Alps; (7) Transylvania; (8) the Belgian Ardennes.

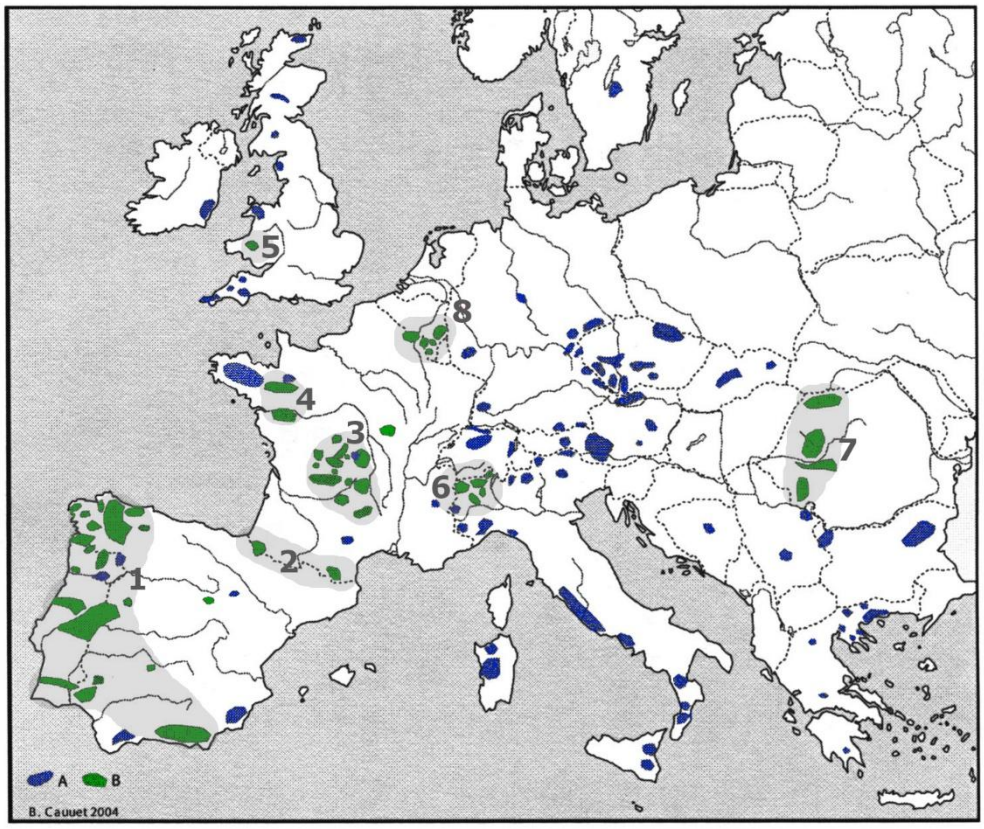

Figure I.1: Vein and alluvial gold deposits in Europe: (A) Exploitation of unknown age, (B) Exploitation attributed to the Iron Age and/or the Roman period (Cauuet, 2005; modified)

The Iberia, i.e. the actual Spain and Portugal (Figure I.1, region 1), had a significant importance in ore mining activities and economy. The scale of the mining operations was considerable,

leading to huge impacts on the landscape (Domergue, 1990; Domergue & Hérail, 1999; Fernández-Lozano *et al.*, 2019). Various metals (silver, lead, copper, iron, mercury) were already exploited during the Iron Age, but gold exploitation mainly occurred during the Roman period, with a peak during the 1st and 2nd centuries AD (Silva-Sánchez & Armada, 2023). The northwest of the Iberian Peninsula was impacted most, especially by the technique of the *ruina montium*. The principle of this technique is that cavities are dug in the mountains and then filled with water that would lead to a sudden increase in pressure, resulting in the fragmentation of rock walls (Ghezzi y Alvarez, 2022). This resulted in a ruiniform landscape (Figure I.2). Recently, multiple studies used new technologies, such as airborne LiDAR or UAV-based photogrammetry, to assess the methods and impacts of gold exploitation (Fernández-Lozano *et al.*, 2015, 2019; Fernández-Lozano & Sanz-Ablanedo, 2021).

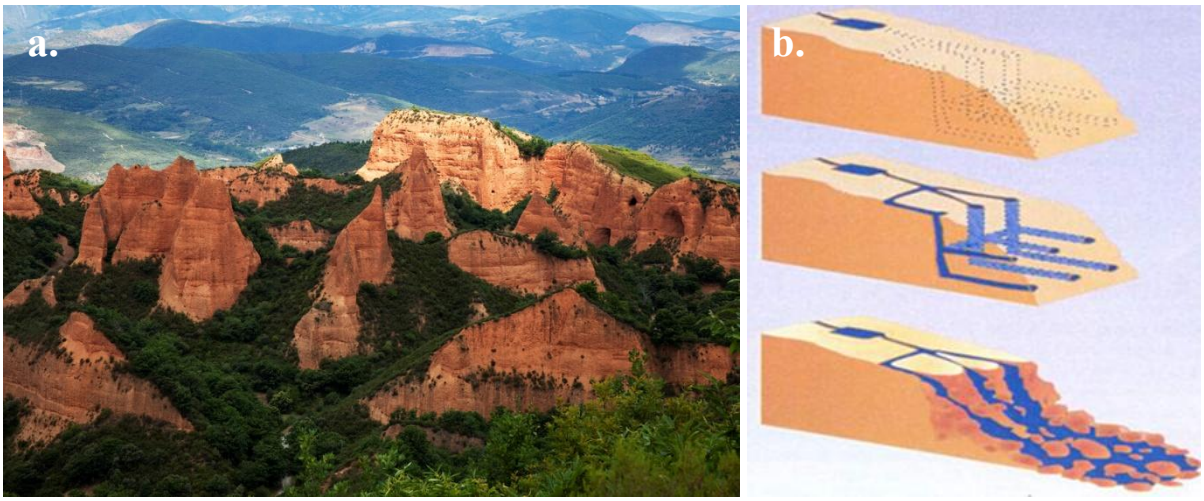

Figure I.2: (a) Las Médulas ruiniform landscape (UNESCO, 2025); (b) Ruina montium mining technique (Universidad de Granada, nd)

In France, the most studied area covers the Limousin and Auvergne (Figure I.1, region 3). This zone, located in the northwest of the Massif Central, was exploited during the La Tène period (~450-25 BC) principally by two Gallic civilisations: the Lemovices in the Limousin (Cauuet, 1991, 2004), and the Arvernes in Auvergne (Cauuet, 2005; Trément, 2016, 2023a, 2023b). The scale of the excavations is, in this case, less extensive than in the Iberian Peninsula, but is still non negligible. The remains of gold activities consist notably of open-pit mines, bordered by mounds and pits. Pits are generally 5 m to 20-30 m wide, 10 m up to more than 100 m long, and 2 m to 10-15 m deep, while mounds can reach 5 m high and their dimensions vary depending on the pits (Cauuet, 1991). In the same way as in Iberia, recent studies used technologies, such as LiDAR, to evaluate the characteristics of gold exploitation (Trément, 2016, 2023a, 2023b).

Other areas in France and Iberia are also linked to ancient gold exploitation, this is the case of the Pyrenees (Figure I.1, region 2) and of the Armorican massif (Figure I.1, region 4), where gold appears both in veins and in alluvial deposits (Chauris, 1989; Cauuet, 2005). Gold mining activities in the Pyrenees occurred during the Roman period, most notably between the 1st century and 4th century AD. The remnants of this period are small mines with galleries, and rounded pits of dimensions close to those found in Limousin-Auvergne, with mounds directly linked to the pits (Cauuet & Tãmas, 2017). Gold in the Armorican massif was mainly exploited in the early Gallo-Roman period (1st century BC to 1st century AD) (Dalmont, 2013). The remains share similarities with those from the Limousin-Auvergne sector, with open-pit mines

and trenches of various sizes (Dalmont, 2013). According to Le Carlier (2023), alluvial gold has probably been intensively exploited, but no archaeological evidence has yet been found.

In northern Italy (Figure I.1, region 6), mines in the western Alps were exploited mostly during the Iron Age, before being abandoned in the 1st century BC because of the higher profitability of the Iberian mines (Agostinetti *et al.*, 1995). The principal evidence of this activity is some mines and the gold panning mounds. The latter result from the sieving and the washing of gold-bearing sediments, in the same way as in Belgium (see further). Other remains are ancient canals and mining fronts. (Agostinetti *et al.*, 1995; Vaudagna, 2012).

Research in Wales about ancient gold exploitation focuses on the Dolaucothi area, the only ancient gold mine in the United Kingdom (Cauuet, 2005). Mining activities occurred from the 1st century AD to the 4th century AD, and reached their peak between 75 and 125 AD (Burnham & Burnham, 2004). The remains of the exploitation are open-pit and closed mines, associated with a network of channels and basins, and pits with mounds of various sizes (Ancel *et al.*, 2000).

Globally, gold mining activities in Europe started during the Iron Age, and the peak of gold extraction was reached during the Roman period, mainly due to the high productivity of the Iberian Peninsula. The remains share similarities across the various areas, with mines associated with pits and mounds, even if their scale varies hugely depending on the scale of the mining activities.

2. History of discoveries in Belgium

2.1. The early discoveries and hypotheses

The first author to mention the presence of gold in the Ardennes is Gilles-Jean de Moors in 1754. He is a courtier of Charles of Lorraine, governor in the Austrian Netherlands. De Moors was sent by Charles of Lorraine to research ore and fossils in the Ardennes, which he describes as ‘mountains’. In one of his travel reports, the author notes that “A small fraction of these mountains, that I covered and that join those from France, from which we extracted for several years so many resources such as gold, silver, copper, lead, iron, sulfur, etc., give the same example as in France”. De Moors also adds that “they were, however, neglected for centuries, even if we see the huge work that Romans did”. It should still be noted that a lot of his reports are fantasist or incorrect. Still, gold was effectively mentioned, and several mines cited have been afterwards confirmed to be exploited (Detaille, 2012).

The idea of possible gold exploitation does not spread across the population, which considers mounds as a part of the landscape and does not give them much attention (Grailet, 1998). In 1841, a hypothesis emitted by Father Bormann suggests that the mounds could be remains of Celtic or Gallo-Roman defense infrastructures against invasions (De Rauw, 1912; Gillet, 1970). A local historian, Anton Hecking, proposes in 1875 the idea that piles could be ancient tombs, also called *tumuli* (Gillet, 1970; Grailet, 1998).

A year later, in 1876, a head miner named Julius Jung emits the hypothesis that the hillocks are associated with gold exploitation. According to him, these are the remains of an ancient, large-scale washing of streams aimed at exploiting a vein deposit (De Rauw, 1912; Grailet, 1998). Jung defends this hypothesis against the renowned geologist Von Dechen, who compares the formations to the *tumuli* observed in Poland, despite the absence of supporting evidence (Bastin,

1911). To verify his theory, Jung decides to pan the mounds and a few samples are enough to see gold flakes at the bottom of the pan, confirming his interpretation (Grailet, 1998).

Jung's hypothesis is afterwards more widely spread by Q. Esser in a monthly journal published in 1880, *Kreisblatt für den Kreis Malmedy* (De Rauw, 1912). Esser asserts that the piles lie on a humus layer, identical to the one of the riverbanks, and that they are made up of the same material as the riverbed, i.e. sand and gravel. He also adds that the gold panning mounds date back to the Celtic or Roman period. His assessment is based on the discovery of a very small horseshoe (10 x 10 cm) belonging to an old species of horse, the 'Przewalski', that lived in the Ardennes during the Gallo-Roman period (Bastin, 1911).

The idea of an auriferous origin of the mounds is supported by a major discovery in 1895, the first finding of gold in alluvial deposits. The finding is made in terrain located in the former Prussian Ardennes (Dewalque, 1896). Dewalque (1896) notes that gold is not found in the rock layers but rather in alluvium and accumulates in valley bottoms in the form of small mounds. According to the author, gold deposits spread from Saint-Vith northwestwards to Recht and northwards to the Amel region, near Born, Deidenberg, Montenau, Ondenval, and Faymonville. G. Dewalque (1896) adds that the alluvium is still sufficiently rich for a new exploitation. This eventually led to the attribution of gold mining concessions (Figure I.3), Jung even got 218 ha of land in the Amel region (Dewalque, 1897). However, the gold mining activities prove to be unprofitable and cease quite rapidly by the beginning of the 20th century.

Starting from 1908, different Belgian geologists, such as M. Lohest and H. De Rauw, decide to conduct research with the aim of verifying the presence of gold in the Ardennes. And, if it is effectively present, their second objective is to determine the source of gold and the potential profitability of its exploitation. It was not until 1920 that its presence in the upper Amel basin was recognised by the scientific community in Belgium (De Rauw, 1920).

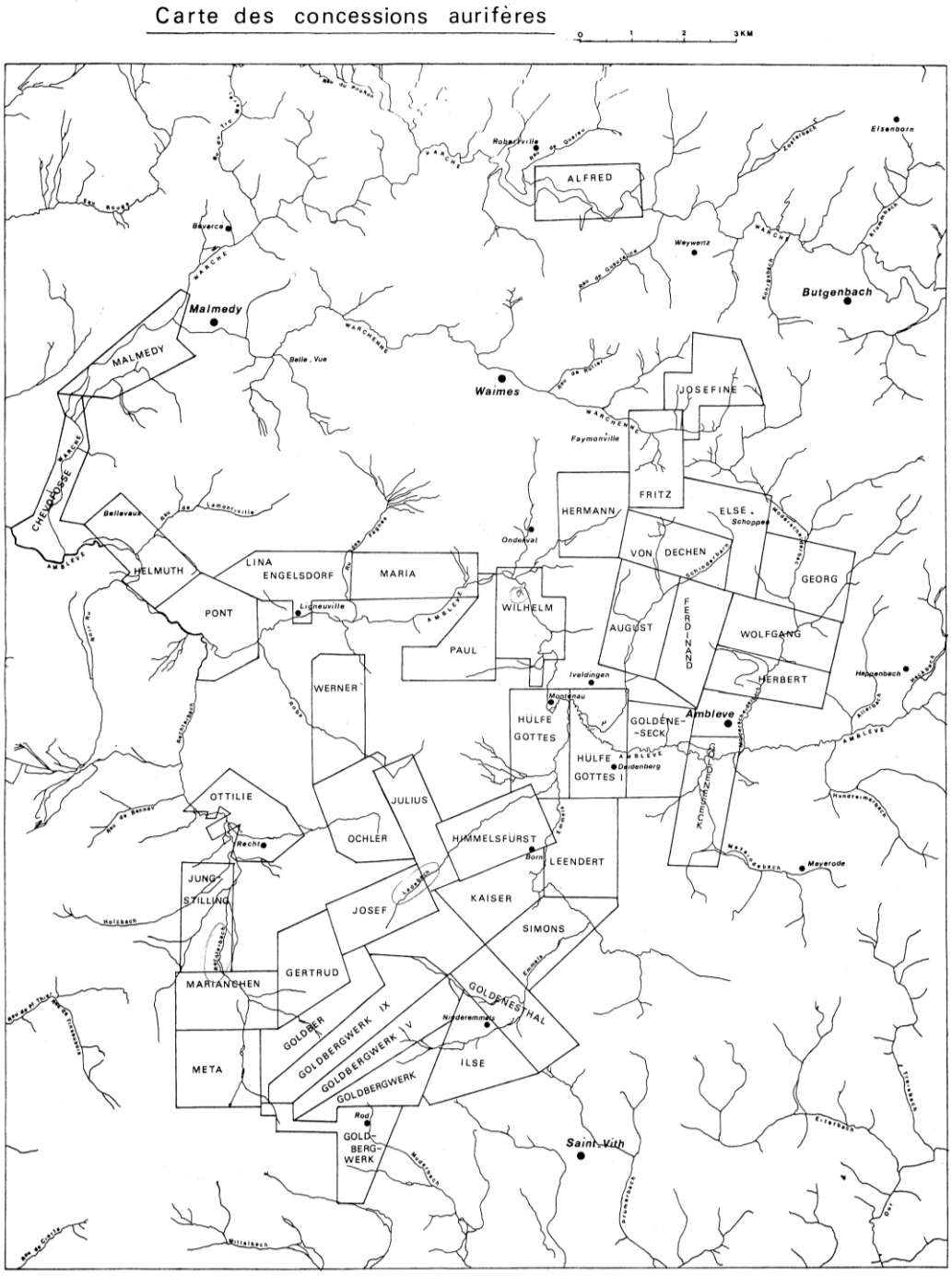

Figure I.3: Map of the gold mining concessions at the beginning of the 20th century (Godfroid, 1980).

In the 1970s and 1980s, the study of gold mining in the Ardennes regains importance. J.-C. Gillet (1970, 1976) is the first to try to reconstruct the history of both ancient and modern (19th century) exploitations. He also makes the first detailed description of the morphology and localisation of the gold panning mounds. J.-M. Dumont (1976, 1979, 1980), in an attempt to date more precisely the ancient gold mining, shares the first radiocarbon dating results along the Stavelot and Serpont massifs. Since then, these dates have been questioned and invalidated (see below). In 1980, J. Godfroid (1980) publishes a major work, in which he inventories and proposes initial interpretations of all the gold panning mounds located in the upper Amel basin. This study is remarkable by the quantity of data recorded and by the precision of observations. The author records the number of mounds per sector that he identifies and evaluates the

dimensions (average and maximum) of the structures observed. Notwithstanding, a number of morphologies have not been inventoried (Figure I.4). This in no way discredits Godfroid's impressive work, given the conditions in which the observations were made (unpruned pine trees, wetland). He himself recognises this difficulty and expresses clearly in his study that he used vegetation differences to distinguish excavations and mounds. However, the development of new technologies, such as LiDAR imagery and GIS[2], and the evolution of field observation conditions raise the need to update Godfroid's observations and interpretations (Figure I.4). This is done in the present work for the Schinderbach, and more precisely for Schinderbach-A.

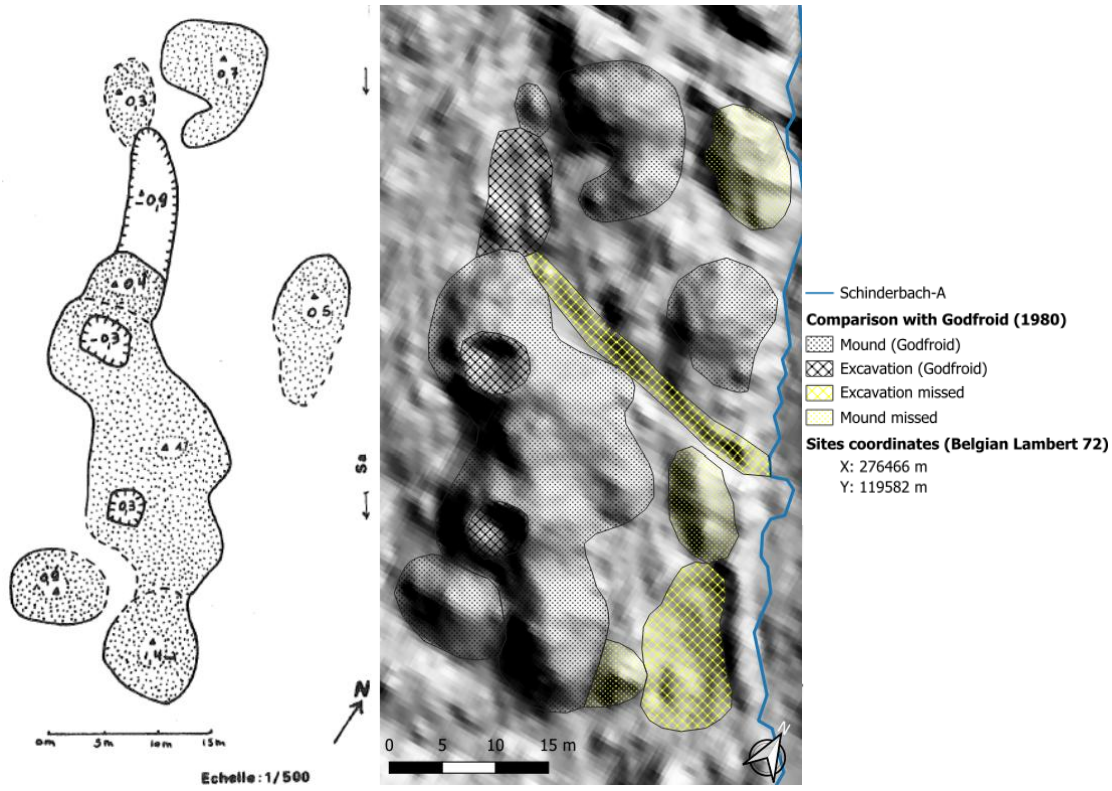

Figure I.4: Comparison between morphologies identified along Schinderbach-A by Godfroid (1980) and by LiDAR observation (present work).

Similarly, B. Wavreille (1987) produced a detailed inventory of the gold panning mounds in the Serpont massif. This work, which is just as remarkable as that of Godfroid (1980), lists the dimensions of each mound found in the field and on aerial images. Wavreille (1987) consciously acknowledges that his work is an introduction to the study of gold mining remains in the Serpont massif, since only the mounds are inventoried and no other features, such as channels, excavations and retention basins. Furthermore, although only a few interpretations are proposed, this does not diminish the significance of the work accomplished. However, a more in-depth update would be appropriate for this auriferous region.

In 1986, E. Hanssen, W. Viaene and F. Gullentops analyse the stratigraphy and mineralogy of the auriferous alluvium of the southeastern edge of the Stavelot massif (Hanssen *et al.*, 1986). Based on core sampling in four sites (*Ru de Poteau*, a tributary of the *Emmels* stream, *Ladebach*, *Warchenne* and *Goldbach* near Faymonville), their study reveals a generalised stratigraphic sequence: at the base is the bedrock, composed mainly of schist. It is covered by silty alluvium consisting of rounded gravel in a silty matrix. This layer corresponds to a first gold-bearing

[2] LiDAR: Light Detection And Ranging; GIS: Geographic Information System

level with low gold concentrations, between 12 and 95 mg/t. Above this layer is silty colluvium, which differs from the previous layer in that the gravel is not rounded. It does not contain gold. Higher up, in the cores from the central axis of the valley, is an accumulation of fluvial gravel. The gravels are rounded, well washed and poorly sorted and, according to the authors, originate from Holocene reworking. This layer is auriferous, with the highest gold concentrations from 154 mg/t to 1 g/t occasionally, at its base. Finally, these deposits are covered by a layer of sterile silt resulting from erosion due to agricultural practices (Hanssen *et al.*, 1986).

2.2. Temporal attributions and dating attempts

In 1880, Q. Esser is the first to suggest that gold panning activities occurred during the Gallo-Roman period, based on the presence in the mounds of small horseshoes that are characteristic for Przewalski horse (see Chapter I2.1).

The presence of small horseshoes in the mounds is also confirmed by Father J. Bastin in 1911. In addition, Bastin (1911) underlines that the horseshoes were found in the superficial part of the soil. According to him, however, the auriferous exploitation should be attributed to the Celts. His reasoning is based on the absence of mention of gold in Roman texts. If Romans had exploited gold in the Ardennes during their period, they would have referred to it in their writings. It is, still according to Bastin, especially true given that iron exploitation is mentioned in literature until late in the Middle Ages. Furthermore, Diodorus of Sicily (90-30 BC) speaks of the gold of the Celts and their mining methods that use washings in the rivers. However, J. Bastin recognises that there is no absolute certainty because he based his argumentation on the absence of documentation (Bastin, 1911; Draily, 2022).

In the years and decades that followed, most authors reiterated Bastin's hypothesis regarding the Celtic origin of gold mining. However, his initial caution, based solely on the absence of Roman documentation, was gradually overlooked. As a result, what was originally presented as a tentative hypothesis progressively came to be treated as an established fact in the literature. (Dumont, 1976; Draily, 2022).

In the late 1970s, J.-M. Dumont critics the existing literature on the fact that the Celtic attribution of the mounds rely on the sole reasoning of Bastin (Dumont, 1976). That is why he carries out two surveys in peatlands located in the *Anciennes Troufferies* reserve in the Serpont massif. Out of eight radiocarbon dates, one sampled at the top of the peat, right below the base of a mound, gives an age between 75 BC and 35 AD. Dumont (1979) considers this date as the formation of the mound, leading to the stoppage of the peat growth. Since then, this age has been commonly used as a basis for the attribution of gold mining in the Ardennes to the Celtic civilisation (Grailet, 1998; Dejonghe, 2000; Detaille & Van Eerdenbrugh, 2014; Bruni & Hatert, 2017; Baudoux, 2018). However, the calibrated date according to current calibration curves gives an age between 54 cal. BC and 211 cal. AD, i.e. during the Roman period (Draily, 2022).

The following year, in 1980, Dumont points out that one date is not sufficient to affirm the Celtic origin of the gold panning mounds. Therefore, he proceeds to four surveys in piles located on the *Plateau des Tailles*, near the *Baraque Fraiture* (Stavelot massif), and obtained radiocarbon age of (2σ) 360 cal. BC - 280 cal. BC, i.e. the Celtic period. The dated sample was taken, once again, at the top of a peat layer (Dumont, 1980). The current calibration gives an age between 400 cal. BC and 204 cal. BC, still corresponding to the Celtic period (second Iron Age) (Draily, 2022).

In 2018, A. Baudoux applies radiocarbon dating to two samples. The first dating is undertaken on a piece of charcoal sampled in a stratigraphic section of a sedimentation basin. The idea is that this basin could have been used by the gold panners. The result of the radiocarbon dating gives an age of (2σ) 1494-1656 cal. AD, which Baudoux considers rather as a result of land clearing for coal production from the late Middle Ages (Baudoux, 2018). The second dating comes from a hazelnut taken at the base of a peat accumulation. The peat is located in a peatland that grew between the mounds and the slope of the valley. Baudoux's hypothesis is that peat started accumulating after gold exploitation, its base would thus correspond to the end of the site exploitation. However, the dating gives an age of the 5th millennium BC, which discredits the hypothesis (Baudoux, 2018; Draily, 2022).

As a result of more than a century of discoveries and hypotheses, it was commonly accepted that gold panning activities in the Ardennes occurred during the Celtic period (e.g. Detaille & Van Eerdenbrugh, 2014; Bruni & Hatert, 2017; Baudoux, 2018). However, Van Ruymbeke (2021) and Draily (2022) questioned these assumptions, reiterating and raising new significant issues linked to the hypotheses of Esser and Bastin, as well as the dates of Dumont.

First, the absence of documentation from the Romans about gold exploitation is not sufficient to corroborate their non-implication. As Van Ruymbeke (2021) explains, Roman literature does not mention any lead or zinc exploitation in Belgium as well. Still, it is proven that this exploitation effectively occurred during their time. Secondly, the presence of small horseshoes in the mounds has been verified, even if they have been lost since their findings. Van Ruymbeke (2021) and Draily (2022) both recognise that Celts shod the horses and hence that this hypothesis is relevant. However, the authors argue that the small horseshoes can also correspond to the Roman or the medieval period.

The date from the *Anciennes Troufferies*, when recalibrated using the current calibration curve (IntCal20), falls within the Roman rather than the Celtic period. While Van Ruymbeke (2021) and Draily (2022) do not reject its validity, they emphasize that it cannot be linked to Celtic occupation. The result is thus reliable, but Dumont's interpretation is questioned, as it appears to have been driven by his determination to support his hypothesis.

Recently, the dates obtained by Dumont on the *Plateau des Tailles* have been discredited by Draily (2022; Figure I.5). Following E. Gilot's retirement, he publishes in 1997 all of the dating that he proceeded with during his career at the radiocarbon laboratory in Leuven. Despite his statement, Dumont (1979) collected four radiocarbon samples beneath the mound rather than one. Furthermore, the sample presented in his work was taken, according to Gilot's laboratory notes, '70 cm under the gold panning pile' and gives an age of 400-204 cal. BC (2270 ±43 BP). However, another sample that Dumont took '60 cm under the gold panning pile', i.e. 10 cm higher than the previous, gives an age of 1396-1056 cal. BC (3000 ±43 BP; Draily, 2022). Thus, the date proposed by Dumont should be considered invalid because of an older age lying over a younger age. A final issue encountered with Dumont's Celtic date is that he describes a peat layer 8-9 cm thick, but the layer would be a minimum of 40 cm thick. Indeed, the four samples are located 60 cm, 70 cm, 90 cm, and 100 cm under the gold panning pile, and they are all situated in the same peat layer. Furthermore, Dumont does not specify the reference point used for depth measurements. He writes 'under the gold panning pile', but does not explain whether is referring to the top or the base of the mound.

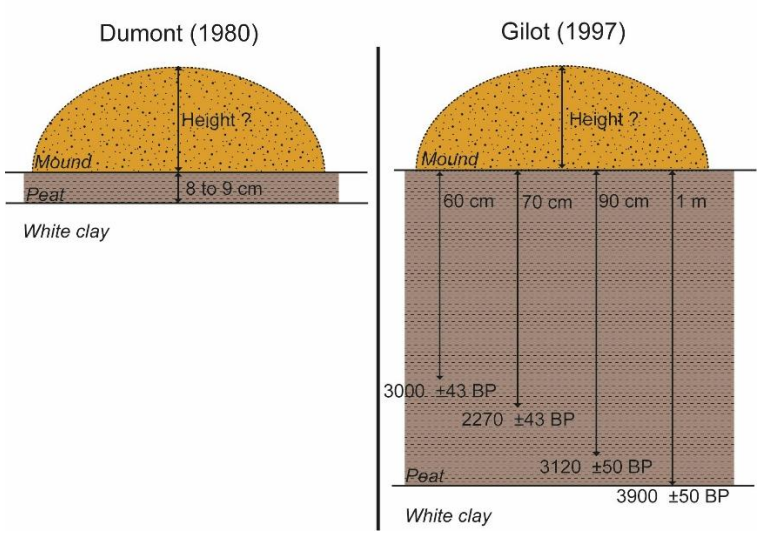

Figure I.5: Schematic representation of the stratigraphic sequence and ^{14}C samplings from the Plateau des Tailles described by Dumont (1980). Reference point considered as the base of the mound (modified after Draily, 2022).

As a result, the only relevant dates concerning gold exploitation along the Stavelot massif come from a gold mine found in 2000 (Figure I.6). The mine is located in the hamlet *Trou des Massotais*, on the *Plateau des Tailles* (Vielsalm). Most of the time, it is submerged by the water table, but during intense droughts, such as in 1921 and in 1976, an entry to a gallery is visible (Detaille & Van Eerdenbrugh, 2014). Thanks to the emptying and the exploration of the mine in 2000, a 10 m deep gallery was brought to light. Wooden supports, an arkose millstone and a wooden shovel were also discovered. A beech wedging board was radiocarbon dated by B. Cauuet (2005) between 249 and 440 cal. AD, i.e. the late Roman Empire. The wooden shovel radiocarbon dated by Draily *et al.* (2022) at 260-434 cal. AD agrees perfectly with that of the wedging board. These two dates include a major event in Roman history. In the early 4th century AD, Roman emperor Constantine I the Great (reign: 306-337 AD) introduced the *solidus*, a gold coin that became the basis of the Roman coinage system. It replaced the silver denarius and stabilised the coinage system thanks to its fixed weight (~4.4 g of gold). Due to that, gold regained importance in the Roman civilisation, which could explain gold mining (re)exploitation in the Ardennes (Grierson, 1999).

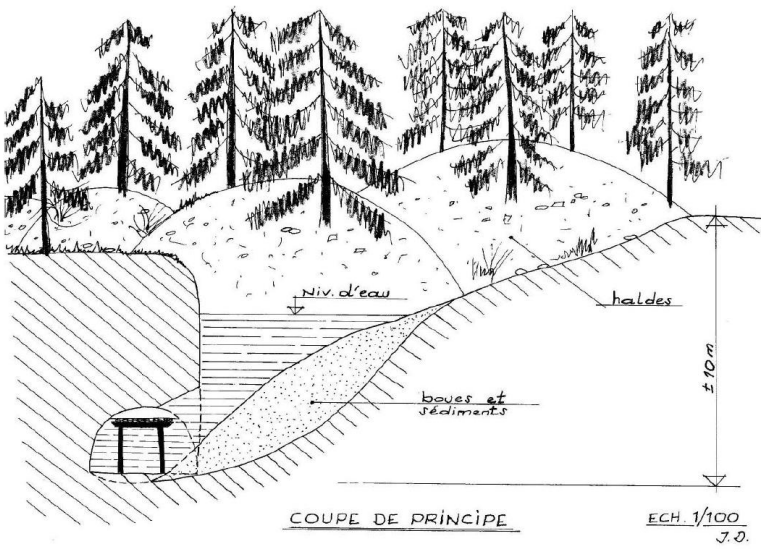

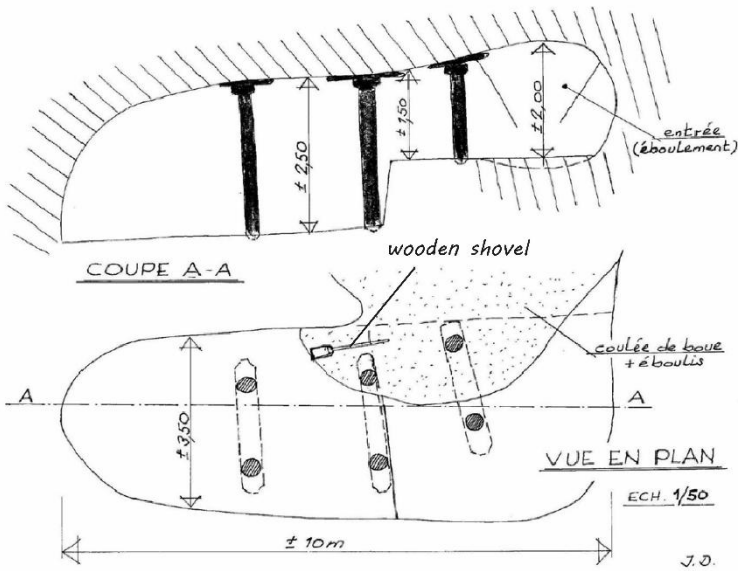

Figure I.6: Cross-section (both above) and plan view (below) of the Massotais gold mine (Detaille & Van Eerdenbrugh, 2014).

3. Gold mining remains – Identification and localisation

3.1. Structures of gold mining

Gold mining remains (Figure I.7) are grouped into three main categories, suggested by Godfroid (1980): mounds, excavations, and channels

Mounds are made up of tailings resulting from gold exploitation and extraction. They are primarily composed of gravel, pebbles, and coarse sand, though varying amounts of silt and clay may also be present. These structures are located on both sides of the valley bottom, sometimes a few dozen metres from the river, and can be isolated from each other or coalescent (De Rauw, 1920; Godfroid, 1980; Baudoux, 2018). The dimension of the piles is highly variable. Their height generally doesn't exceed 5 m, but some of the mounds can exceptionally reach 10 m. The width of these structures is a maximum of 15 m wide, according to Bastin (1911) and De Rauw (1912). However, Baudoux (2018), with the use of LiDAR technology, notices that their diameter can reach up to 53 m. These particularly wide piles mainly concern perturbed sites that have spread out. Some of the mounds have been, in the past, re-exploited by locals for concrete fabrication. Indeed, they represent an interesting source of gravel for concrete because they are free and easy to exploit, often close by the villages, and quite abundant (Godfroid, 1980).

Figure I.7: Types of gold mining structures: (a) Mound along the Rougerie, (b) Paleochannel along the Rechterbach, (c) Excavation pit along the Schinderbach.

Excavations are depressions of various sizes and morphologies. Godfroid (1980) distinguishes two types, depending on their origin: deep and shallow excavations. Deep excavations are linked to gold extraction and can reach up to 2 m deep, whereas shallow excavations are linked to gravel exploitation. The limit between the two types is 0.3 m deep. According to Godfroid (1980), the auriferous material is covered by a sterile layer, and it is therefore necessary to dig below 0.3 m deep in order to find gold. Most of the shallow excavations correspond to gravel extraction from the tailing piles, as explained above. Both kinds of excavations are characterised either by lateral trenches or by the presence of a tailing ridge around the pit. Ridges resulting from gravel extraction are usually more uniform. According to Godfroid (1980), differences between 'recent' and 'ancient' gold exploitation, i.e. late 19th to early 20th century versus Antiquity, can be observed. Recent gold mining is characterised by excavations with clear edges and angles, whereas ancient gold mining excavations show less distinct edges and present a circular to elliptical morphology.

Finally, channels are defined as excavations exhibiting a length-to-width ratio of at least five. They are generally larger than normal excavations and had several uses. They could have the same utility as the excavations, i.e. extraction pits for auriferous deposits, but also could be used to divert rivers in order to drain valley bottoms and to facilitate gold panning operations.

Another possibility is the use of channels to provide sufficient water supply to the washing of sediments from other excavation pits (Godfroid, 1980; Draily, 2022).

3.2. Gold prospection techniques

The two principal and complementary techniques used to exploit alluvial gold deposits are ‘panning’ and ‘sluicing’. Both are known as gravity concentration techniques, which are a way of concentrating gold using the density difference between gold and sterile material. Indeed, with a density of 19.3 g/cm³, gold is significantly denser than most of the common minerals, such as quartz with a density of 2.65 g/cm³ (Boericke, 1936; Veiga *et al.*, 2006; Blaber, 2009).

Both prospection techniques need a preliminary step, which consists of clearing gold of mud. This step is probably the most important, because gold is often trapped in a clay-silt matrix, and if it is not cleared, gold can be removed during the process. The clearing operation is executed under a thin trickle of water. There should be enough water to carry suspended clay and silt particles away, but too much water would mean that gold can also be carried out of the prospection tool (Godfroid, 1980).

Panning represents the most ancient form of gold prospection. The traditional equipment is the ‘batea’ or the ‘American pan’, the latter being a more recent tool developed during the 19th-century American gold rush. The form and material composing the batea have changed over time, from a simple wooden container to a flared, inverted cone made of metal. The principle of the method relies on the circular (batea) or back-and-forth (American pan) shaking of sediments, causing heavy minerals to settle at the bottom of the pan. The overlying fraction, consisting of lighter and less dense particles, is then removed. This operation is repeated until a dense mineral concentrate is obtained in the bottom of the pan. The last step consists in applying a small rotational movement in order to isolate gold from other heavy minerals (Boericke, 1936; Veiga *et al.*, 2006).

A sluice box is a long, inclined, and flat-bottomed trough with riffles on the bottom. It is positioned in a way that a trickle of water flows and carries away the sediment. Gold and heavy minerals, as they are denser, are trapped in the riffles and are therefore separated from lighter minerals. Trapped sediments are afterward panned in a batea to recover gold. The efficiency of this technique depends on various parameters, such as inclination, water flow or riffle design. When installed correctly, sluicing allows for a considerable increase in the quantity of material washed. Sluice boxes measure from one to several dozen metres (Boericke, 1936; Veiga *et al.*, 2006). This technique was, for instance, employed by De Rauw (1920) and is thought to have been used in the past in the Ardennes (Detaille & Van Eerdenbrugh, 2014).

Sometimes, sieves are also used before panning or sluicing to remove the bigger elements. Mesh sizes are commonly of the order of one to several centimetres. The biggest gold nugget found in Belgium in recent years measures 12 x 8 x 4.5 mm, as far as is known (Detaille & Van Eerdenbrugh, 2014).

Figure I.8: Gold prospection tools: (a) batea, (b) American pan (©IRL supplies), (c) sluice box (©Western Mining History). Coarser cobbles are removed from the sluice box and piled up alongside.

3.3. Localisation of the remains

The origin of gold deposits in Belgium remains incompletely understood. The question has been investigated by many authors, yet the majority of proposed hypotheses have ultimately been either rejected or nuanced. As it is rather the work of a geologist instead of a geographer, the different theories are not described in this document. A non-exhaustive list of literature on the topic comprises De Rauw (1912, 1920), Gillet (1970), Hanssen & Viaene (1979), Hanssen *et al.* (1986), Grailet (1998), Detaille & Van Eerdenbrugh (2014), Bruni & Hatert (2017).

Still, it is generally accepted that there is a direct link between gold deposits, on one hand, and metamorphism and faulting, on the other hand. In fact, gold is principally found along the Cambro-Ordovician massifs (Figure I.9): the southern edge of the Stavelot massif, the Serpont massif, and punctually along the Givonne and Rocroi massifs. Gold is also present near the cities of Neufchâteau (Suxy) and Bastogne. These regions correspond to metamorphic areas that are strongly faulted; the main faults are the Herbeumont, Opont, and Vencimont faults (Detaille & Van Eerdenbrugh, 2014; Bruni & Hatert, 2017).

In total, 3235 gold panning mounds have been reported in the Ardennes by Baudoux (2018), using LiDAR technology and in combination with earlier finds (Gillet, 1970; Godfroid, 1980; Detaille & Van Eerdenbrugh, 2014). This number is probably underestimated compared to ancient times because, according to Gillet (1970), almost 90 %[3] of all the mounds have been destroyed. The main reasons for their disappearance are soil levelling for agriculture, forest exploitation and clearing, or even gravel extraction for construction. Most of the mounds are located in the upper Amel sector (1857 piles). The areas most affected by gold exploitation are mainly headwater streams, where gold is not too widely dispersed and thus its concentration is still high enough to be profitable. Moreover, small rivers have a low flow, facilitating excavation operations, such as diversion and channelling, but it is sufficiently high for gold panning operations. This is confirmed by Baudoux (2018), as more than 75 % of the mounds are located along rivers whose watershed covers less than 10 km².

[3] Note that different authors consider this value as an overestimation.

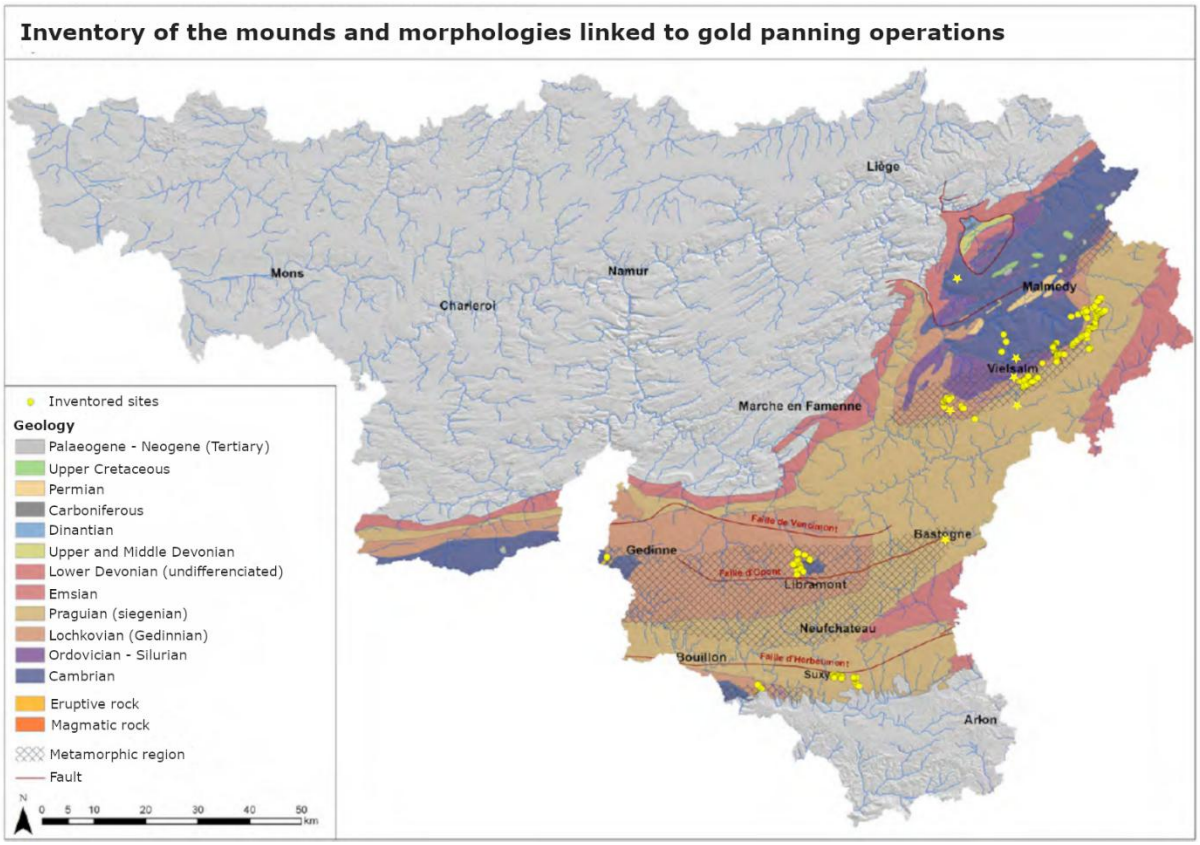

Figure I.9: Localisation of the gold panning mounds and morphologies in Wallonia (modified from Baudoux, 2018).

In the Ardennes, gold concentrations in the rivers are generally low compared to other European auriferous regions, as they rarely exceed 0.2 g/t (Hanssen *et al.*, 1986). Notwithstanding, higher concentrations can be encountered in certain favourable contexts. Indeed, concentrations of the order of 2 g/t can be observed (Van Eerdenbrugh, pers. comm.). The favourable conditions to find higher gold concentrations are a silty-clay layer located close to large boulders at the base of the alluvial gravel layer, in contact with bedrock. As it is denser than most of the material, gold is trapped and migrates gradually over time to concentrate in these deeper levels. These are probably the layers that were exploited in the past.

4. Impacts of gold mining on streams

Ore mining represents one of the main anthropogenic disturbances on rivers. It is characterized by the mobilisation of huge amounts of soil and sediments, and by the perturbation of the surrounding environment. Additionally, water is most of the time essential to the development of extracting activities, leading to changes in stream and floodplain morphology and dynamics (Graf, 1979; Hilmes & Wohl, 1995).

Alluvial gold mining techniques have evolved through time and space. Still, as mentioned above, the principle remains the same: as heavy gold particles settle deep into riverbed gravels, mining operations include excavating the riverbed down to bedrock to find gold (Boericke, 1936; Harding & Boothroyd, 2004). Gold panning activities hugely rely on a continual supply of water. The early uses of water included the sieving, washings and sluicing of gold-bearing sediments. Later, water was used to assist excavation, a process called *hydro-mining*. Both uses require the manipulation of flow conditions. The watercourse is diverted to expose and dry the riverbed, making it easier to extract and pan the sediments. Water is also stored in retention

basins and sediment-settling ponds, perturbing the natural flow of the river. Other than direct modification of watercourse, mining activities generate large amounts of suspended sediment levels, as finer particles such as silt and clay are carried out by the river. Increased turbidity causes a considerable decrease in light penetration, altering underwater visibility and therefore fish feeding capacity. Suspended sediment deposition reduces algal productivity and cements interstitial habitats, contributing to a decline in fish populations and in aquatic habitat quality. On the other side, coarser particles such as sand and pebbles are deposited as tailings, which form ridges and mounds along riverbanks, in the alluvial plain. As the river evolves, these can create artificial ponds and alter the development of riparian vegetation, leading to mineral weathering and erosion, with cascading effects such as pH alteration, higher suspended sediment loads, and degradation of aquatic habitats (Graf, 1979; Pentz & Kostaschuk, 1999; Harding & Boothroyd, 2004; Davies *et al.*, 2019).

A great number of studies worldwide have evaluated the impacts of gold mining activities on channels and streams. The impacts observed are very similar between them, even in distant regions or with different research methodologies. Some illustrative examples are depicted in the following.

Lapierre *et al.* (1983) evaluated the effects of gold placer mining on interior Alaskan stream ecosystems. They studied during two consecutive summers various parameters (i.e. water discharge, turbidity, conductivity, heavy metals). By comparing two streams, one with and one without gold mines, their study revealed that an increase in suspended sediments resulted in deposition downstream, leading to the cementation of the riverbed. This, in turn, caused the surface flow to be hydraulically isolated from the groundwater flow. They also observed the significant embeddedness of the mined stream.

In the Yukon (Canada), Pentz & Kostaschuk (1999) analysed the impacts on suspended sediments in relation to sensitive fish habitats. Their study revealed the significant effects of erosion of deposits from previously mined areas on ecosystems. Notably, the breach of a settling pond resulted first in a release of water with low suspended sediment concentrations, and as the water level in the pond lowered, greater amounts of sediment were released to the stream. They concluded that abandoned exploitations impact the suspended sediments episodically, mostly during spring snowmelt floods and summer rainstorms.

Nelson & Church (2012) examined the geomorphic impact along the Fraser River (British Columbia, Canada). By analysing excavated sediments and their transport potential in the river, the authors estimated huge amounts of sediments to be excavated, therefore lowering ground and water surfaces, and steepening riverbanks. They also observed the downstream progression of a sediment wave consequent to the washing operations releasing sediments. Their observations were supported by grain-size analyses of the tailings: 14% ± 7% small cobbles, 32% ± 9% gravel, 41% ± 4% granules and sand, and 13% ± 4% silt and clay. Lower fractions of silt and clay are explained by the fact that sufficiently fine sediments are carried as suspended load and washed out directly by the river in the sluice boxes. Ferguson *et al.* (2015) confirmed the succession of the lowering of riverbed surface followed by an aggradation linked with a sediment pulse. They noticed this through modelling and simulation of the river response to an increase in sediment supply. They validated their simulations against detailed gravel budgets from 1952–1999, obtaining results consistent with observed data.

Davies *et al.* (2019), by studying mining modification of river systems in Australia, underlined that LiDAR is a powerful technique to study the effects of mining on river systems. It allowed the authors to depict the wide range of morphological features related to gold mining, such as settling ponds, tailings, mining dams, or diverting channels. Their analyses revealed a change of fluvial system from an anabranching network to a straightened and deeply incised channel developed in a wider trench. LiDAR imagery also allowed them to estimate the quantity of sediments mobilised through mining operations.

Channel response to alluvial gold mining can be summarised as a succession of erosion-aggradation, resulting from the evolution of gold-panning operations. The channel initially undergoes an incision phase, during which the riverbed is excavated following the diversion of the main course and the creation of secondary channels. This process entrenches the valley centre, producing a narrow, flat-floored valley bottom.. However, it is rapidly partially, or sometimes completely, compensated by a subsequent aggradation phase. Mining operations generate high quantities of sediments. Furthermore, these activities are often linked with land use changes, such as deforestation and agricultural practices. Deforestation is a very common feature of gold mining, because of the demand for lumber for sluice boxes, housing, and fuel. Slope denudation generates an increase in erosion and therefore in sediments transported to the river. Aggradation and an increase in sediment supply can provoke a change of fluvial style of the river, from a unique channel to a braided or anabranching river. After the stoppage of mining operations, an incision phase begins. Sediment supply linked to washing operations decreases and causes channel incision. Incision is sometimes important because the riverbed is mostly constituted of finer particles previously released instead of a gravel bed like most auriferous rivers. This phase can last up to several centuries before reaching a new equilibrium between erosion and deposition, often different from the pre-mining equilibrium. Over time, the river is recharged in gravel and sand thanks to overflowing floods that erode tailings and reintegrate coarser particles in the fluvial system (Graf, 1979; James, 1991). Gold mining in Belgium seems to follow this general evolution (Baudoux, 2018). More details about gold mined river evolution are available in **Erreur ! Source du renvoi introuvable.**.

Chapter II :
STUDY SITES

Summary of chapter II: This chapter presents the site selection methodology, from the pre-selection criteria to the final study sites retained. The contexts of the two selected streams are then described: situation, stream characteristic, geology, and archaeological features nearby.

1. Site selection methodology

Site selection is a fundamental step in scientific research. The choice of the study sites directly influences data relevance, analyses and results. This section aims to presents the selection criteria and the approach used to determine the study sites.

1.1. Selection procedure

The preliminary step is the delimitation of the studied area in its broad sense. In other terms, it is necessary to determine which auriferous region is to be analysed. In this case, the studied area is the southeastern edge of the Cambrian Stavelot massif. As illustrated on Figure II.1, the region stretches from the *Plateau des Tailles* on the west to Bütgenbach on the northeast, passing by Recht (Saint-Vith). This area is covered by 2419 mounds spread over 20 rivers but, as explained above, this number is an underestimation of the original number of mounds, as many have been wrecked since then. Nevertheless, it still represents over 800,000 m³ of reworked sediments (Baudoux, 2018).

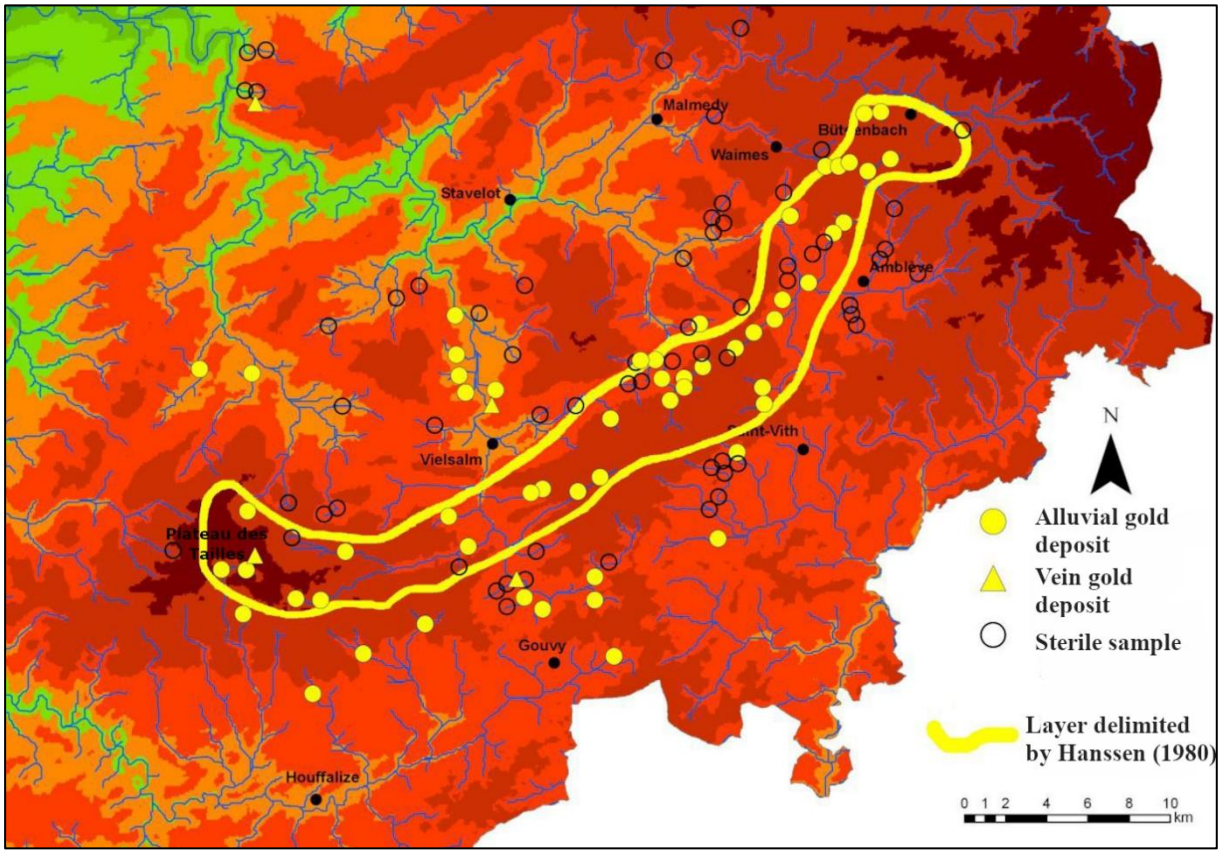

Figure II.1: Gold presence along the Stavelot massif (Detaille & Van Eerdenbrugh, 2014).

Based on the works of Godfroid (1980), Detaile & Van Eerdenbrugh (2014) and Baudoux (2018), the exploited rivers of the Stavelot massif are inspected through the digital elevation model (DEM; SPW, 2025a). A list of criteria is then used to make a pre-selection of interesting rivers and sites. The criteria are the following:

- Presence of visible mounds: an obvious requirement to study the mounds and their characteristics is their visible presence. Because they are of variable sizes and forms, only the sites with clearly defined mounds are retained.
- Catchment area: rivers/sites with small catchment area (< 10 km²) are preferred. Smaller rivers are less impacted by tributary streams. Therefore, factors explaining valley bottom morphologies are less weakened.
- Accessibility: it is an important requirement. As the study of the site involves multiple field visits and measurements, it should be situated within a reasonable distance of a road accessible by motorized vehicles. A certain amount of equipment, including a motorised coring drill, is required for the measurements and cannot be transported over long distances by hand. Also, equipment needs to be transported on both river banks; an accessible site as well as a small catchment area (see above) make it easier to move on both sides of the river.
- Urbanisation: a non-negligible criterion is the low urbanisation around the site, to avoid perturbation or reworking of the mounds due to factors not natural nor linked to gold exploitation. As the Stavelot massif is mostly rural, this condition should be fulfilled most of the time.
- Other criteria: other criteria of lesser importance are also considered. This is the case of presence of mining front and/or paleochannels. As explained in section Chapter I3.1, channels are structures attesting to gold exploitation. This is also the case of mining fronts, they correspond to the limit until which sediments were extracted. The presence of one, or both, of these structures adds interest to the study site.

The analysis based on these criteria allows to select different sites of interest, which, for instance, comprise the Rougerie stream, the Rechterbach stream, two tributaries of the Schinderbach stream or even different sites along the Amel river near Montenau.

Following the initial pre-selection, field prospections were conducted to identify suitable study sites. Observations from LiDAR were validated through several days of on-site investigations, which focused on the morphologies and structures related to gold exploitation, as well as site accessibility. Fieldwork took place during the first two weeks of July 2024, partly in the company of Geoffrey Houbrechts and Bruno Van Eerdenbrugh, who contributed their expertise. Stratigraphic sections were sought along watercourses and mounds to obtain detailed sedimentary sequences. Finally, the texture of the mounds was assessed by excavating a pit of approximately 50 cm depth using a shovel. The aim was to identify sandy deposits, as OSL dating of alluvial sediments has proven to be more reliable for medium- to coarse-grained sands than for silts or very fine sands (Vandenberghe *et al*., 2007). Field prospections for OSL sampling sites were carried out with G. Houbrechts and B. Van Eerdenbrugh, as well as OSL specialists Dimitri Vandenberghe and Johan De Grave, and archaeologist Christelle Draily.

1.2. Study sites selection

Following the procedure explained above, two sites were selected for exploratory OSL dating and sedimentary and morphological analysis of the gold panning mounds. The choice was

oriented toward the Rougerie stream and a tributary of the Schinderbach. The latter having no denomination, it will be called Schinderbach-A for the rest of this work for the sake of clarity.

The Rougerie was selected for the variety of the structures still present along its course. The river is flowing within a large trench, bordered by an alignment of mounds on both sides. The mounds are of great dimensions, with a mean diameter of approximately 30 m (Baudoux, 2018). They are also well conserved. Several paleochannels are also present, as well as a distinctive mining front on the left bank. Moreover, two stratigraphic sections have been identified, one seeming to have been little affected by gold exploitation. The site is easily accessible by car, a forested road passing a little bit more than a hundred metres to the south. The absence of urbanisation upstream (protected forest) and the small catchment area (6.65 km² at confluence) are definitely major advantages. Finally, the detailed knowledge of the site by B. Van Eerdenbrugh cannot be neglected. The sites were also selected because of the previous work of Baudoux (2018), allowing us to pursue and complete his analyses.

The second site, Schinderbach-A, was selected because it verifies all the criteria. Large-sized mounds are visible, even if the mean diameter for the whole stream is relatively low, ~19 m (Baudoux, 2018). Paleochannels are also visible. The structures are well-conserved, the site is located in a state-owned forest, the valley bottom has been widely exploited. The site is accessible through a forested road situated less than a hundred metres to the north. Catchment area is extremely small (0.74 km²), that means explanatory factors are site-specific and are not attenuated by tributaries. Sediments composing the mounds have a coarse sandy texture and seem to have been well washed, an essential requirement for OSL dating.

2. Rougerie stream near Bêche (Vielsalm)

The Rougerie stream (Figure II.2), sometimes called ‘the stream of Bêche’ in reference to the village along its course, is a right bank tributary of the Salm river, in the Amel watershed. It is located near Vielsalm, in the Luxembourg province. Its source is situated near the hamlet ‘*So Bêchefa*’ at an approximate elevation of 530 m above sea level. The confluence is in Salmchâteau, at an altitude of 375 m. The Rougerie is a single channel meandering river flowing westward. Upstream from Bêche, the valley is open and quite large compared to the river dimension and the slopes are gentle. However, between Bêche and Salmchâteau, the valley is getting narrower and the slopes are increasing (V-shaped valley), with the river being more incised. This narrowing is due to a knickpoint, linked to the tectonic uplift of the Ardennes massif. This uplift generated a wave of regressive erosion that can be seen in most of the Ardennes rivers (Beckers, 2010).

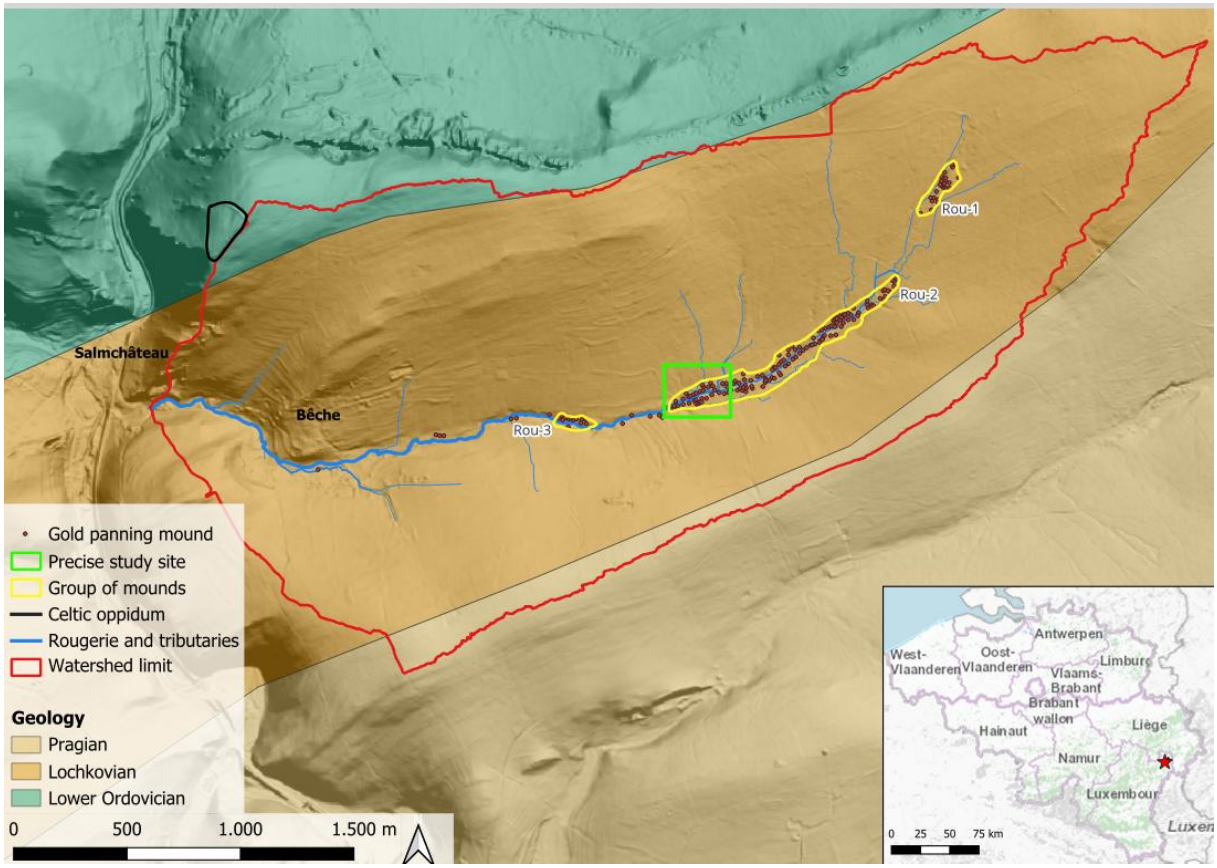

Figure II.2: Context of the Rougerie study site. Geology based on Vandenven (1990). Inspired by Baudoux (2018).

The Rougerie is approximately 5.4 km long and its catchment area[4] is 6.65 km². The average slope of the river is 2.86 %, but there is a strong difference between the section upstream from Bêche (2.48 %) and the section downstream, with the knickpoint (4.24 %). The group of mounds *Rou-2* is situated in the lowest slope sector (2.08 %) of the stream. At the confluence with Salm river, the bankfull discharge of the Rougerie is of the order of 0.85 m³/s, using the empirical formula for the Ardennes rivers in Petit *et al.* (2005b, 2008):

$$Q_b = 0.1346 * A^{0.974}$$

with Q_b the bankfull discharge (m³/s) and A the catchment area (km²). The specific stream power can also be calculated using the formula (Petit *et al.*, 2005a):

$$\omega = \frac{\rho g Q S}{w}$$

with ρ the fluid density (kg/m³), g the acceleration due to gravity (m/s²), Q the water discharge (m³/s), S the slope of the energy line (m/m) and w the width between the banks at the level of overflow. The longitudinal slope of the bed, or the alluvial plain, on long sections of rivers is considered a good approximation of the slope of the energy line to determine S. Generally, the bankfull discharge is used for Q to allow comparisons between rivers (Petit *et al.*, 2005a). Therefore, the specific stream power of the Rougerie at the confluence is estimated to 33 W/m².

[4] Catchment area measured 200 m upstream of the confluence to avoid perturbation of watershed determination due to urbanisation.

Such specific stream power classifies the river in the category between 'river uncapable of auto-adjusting' and 'active meanders' (Brookes, 1988 and Ferguson, 1991 *in* Petit *et al.*, 2008).

Figure II.3: Rougerie stream (pictures: J.-M. Marion (left), C. Draily (right)).

Regarding the geology of the study site (Figure II.2), the Rougerie is flowing in Lochkovian rocks of the Waimes formation (Lower Devonian). They are composed of puddingstones and coarse sandstones, sometimes with micas incursions, with thin layers of shale. On top of the northern crest, rocks date from the Lower Ordovician, more precisely from the 'Salm group', a geologic unit that can be included in the Tremadocian stage. The lithology of this group is characterised by metamorphic shales, quartzites and arkose. The contact between the Lochkovien and the Lower Ordovician corresponds to the southern edge of the Stavelot massif, which extends from the *Plateau des Tailles* (SO) to Düren (NE) in Germany. On the other side of the valley lies Pragian rocks dating from the Amel formation (Lower Devonian). They consist of quartzitic sandstones and shales (Vandenven, 1990; Bouezmarni & Debbaut, 2013).

A Celtic oppidum is also present on the northern crest (Figure II.2). A charcoal found in the rampart was dated to (1σ) 470 – 440 cal. BC, during La Tène period (Cahen-Delhaye, 1977 *in* Baudoux, 2018). Gillet (1970) uses its proximity to the gold mining site to affirm the Celtic origin of the mounds. Even if this possibility should not be ruled out, proximity does not mean that there is a relationship between the fortification and gold panning activities.

3. Schinderbach-A stream near Eibertingen (Amel)

The second study site (Figure II.4) is a stream that has no official name. Both Godfroid (1980) and Baudoux (2018) named it *Schinderbach-A*, this name is thus also used in this paper. The Schinderbach-A is a right bank tributary of the 'real' Schinderbach. It belongs to the upper Amel basin. It is flowing along the hamlet *'Rohrbusch'*, between the villages of Eibertingen and Ondenval in the German-speaking region of Belgium. The stream rises at an altitude of 491 m and flows into the Schinderbach at an altitude of 457 m. The Schinderbach-A is flowing southward. The river is a single channel meandering stream channelised and straightened over 300 m in its central section. The upstream part is dominated by natural small gullies. Except the extreme upstream part, the entire watershed is covered by a timber forest, where spruce trees were planted during the 20th century. This explains the difficult conditions in which Godfroid (1980) identified gold panning morphologies. This also the reason why the conditions were more favourable during the present study, as the trees have grown sufficiently to make the morphologies visible (Figure II.6).

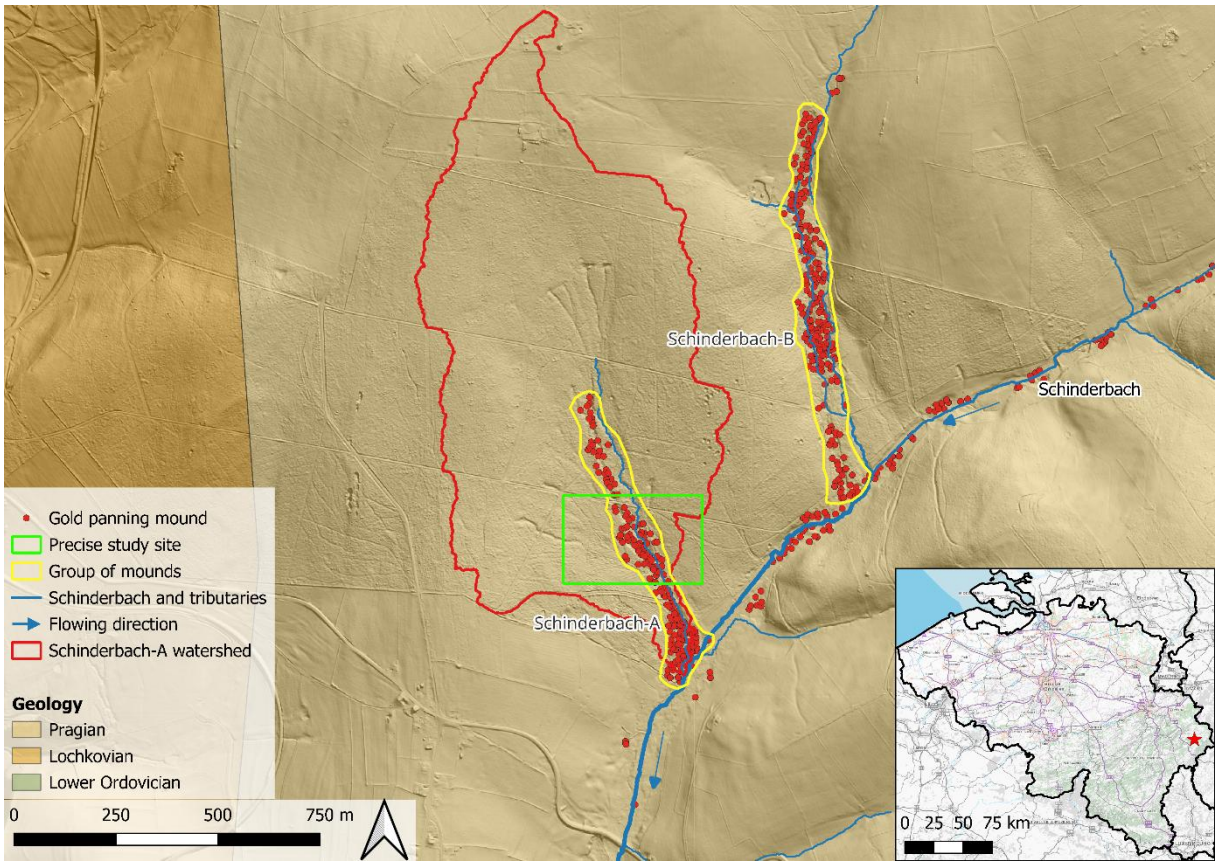

Figure II.4: Context of the Schinderbach-A study site. Geology based on Vandenven (1990).

The stream is 0.99 km long, with a catchment area of 0.74 km². The slope is 3.42 % on average and is relatively uniform along the watercourse, with a slight decrease downstream (Figure II.5). In the same way as for the Rougerie stream, the empirical formula for the Ardennes rivers $Q_b = 0.1346 * A^{0.974}$, developed by Petit *et al.* (2005b, 2008), can be used to estimate the bankfull discharge at the confluence. It gives a bankfull discharge of the order of 0.1 m³/s. Similarly, applying the formula $\omega = \frac{\rho g Q S}{w}$ (Petit *et al.*, 2005a) gives a specific stream power of 25.8 W/m², corresponding to river uncapable of auto-adjusting (Brookes, 1988 *in* Petit *et al.*, 2008).

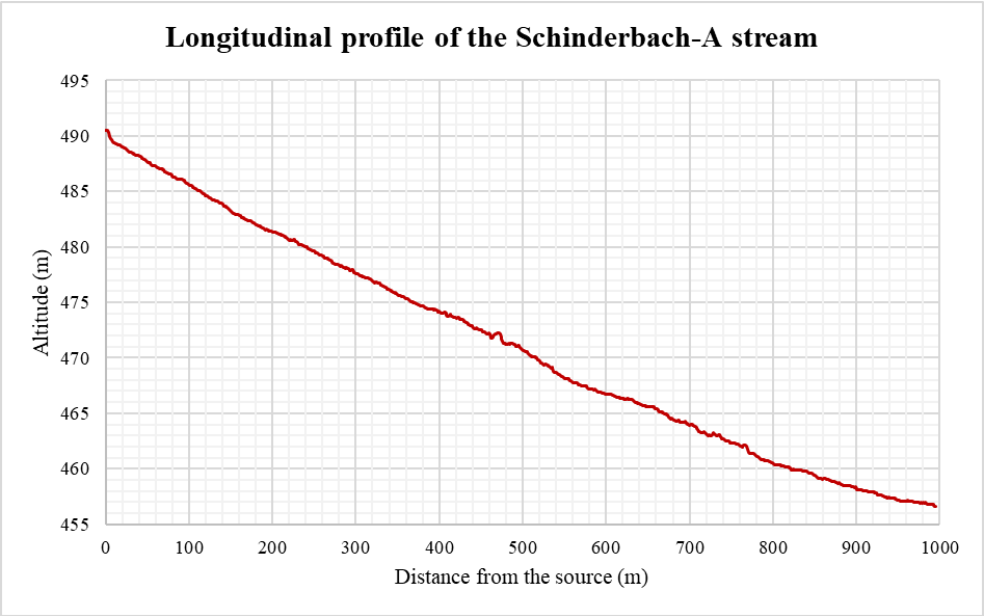

Figure II.5: Longitudinal profile of the Schinderbach-A stream.

Initially, another river was selected during the site selection process, located to the north of the Schinderbach-A (Figure II.4Figure II.7). As it does not have any denomination, it is called *Schinderbach-B*, in reference to the work of Godfroid (1980) and Baudoux (2018). The stream presents approximately the same criteria as Schinderbach-A: structures are well-conserved, with large-sized mounds and paleochannels, a widely exploited valley bottom and a sandy texture of the mounds. The study site is accessible via the same forested road as Schinderbach-A, except that the potential transversal profile is 250 m from the road, making it more difficult to transport equipment. Regarding its characteristics, Schinderbach-B is similar to Schinderbach-A. Its watershed covers an area of 1.52 km² and it is 1.99 km long. From an altitude of 536 m at the source to an altitude of 467 m at the confluence, the average slope is 3.46 %. The reason for the preference of Schinderbach-A is the easier accessibility of site and the presence along the Schinderbach-B of a certain number of excavations seemingly dating back to the 19th-century gold exploitations. Therefore, Schinderbach-A has been preferred. Still, some analyses are conducted on both streams for the sake of comparing two similar and proximal sites. Figure II.6 is a view of Schinderbach-B, from one of the highest mounds present along the stream, it is very similar to the view of Schinderbach-A.

Figure II.6: Field view of Schinderbach-B, with grown spruce trees.

Both streams are included in the 'real' Schinderbach watershed (Figure II.7). The latter river is a right bank tributary of the upper Amel river. It is 6.78 km and its catchment area is 8.14 km². In term of size, it is closer to the Rougerie than are the Schinderbach-A and -B. The source is at an elevation of 523 m above sea level and its confluence is located near the village of Montenau at an elevation of 424 m. The average slope is 1.47 %. Following Petit *et al.* (2005b; 2008), the bankfull discharge at the confluence with the Amel river can be estimated at 1.04 m³/s. Like the Rougerie, the Schinderbach is a single channel meandering river. However, a vast majority of the gold panning morphologies have been destroyed or levelled, mostly due to agricultural practices. To this day, the floodplain topography of the Schinderbach is still perturbed, with undulations and odd morphologies, and the structures cannot be identified precisely, except in some specific areas.

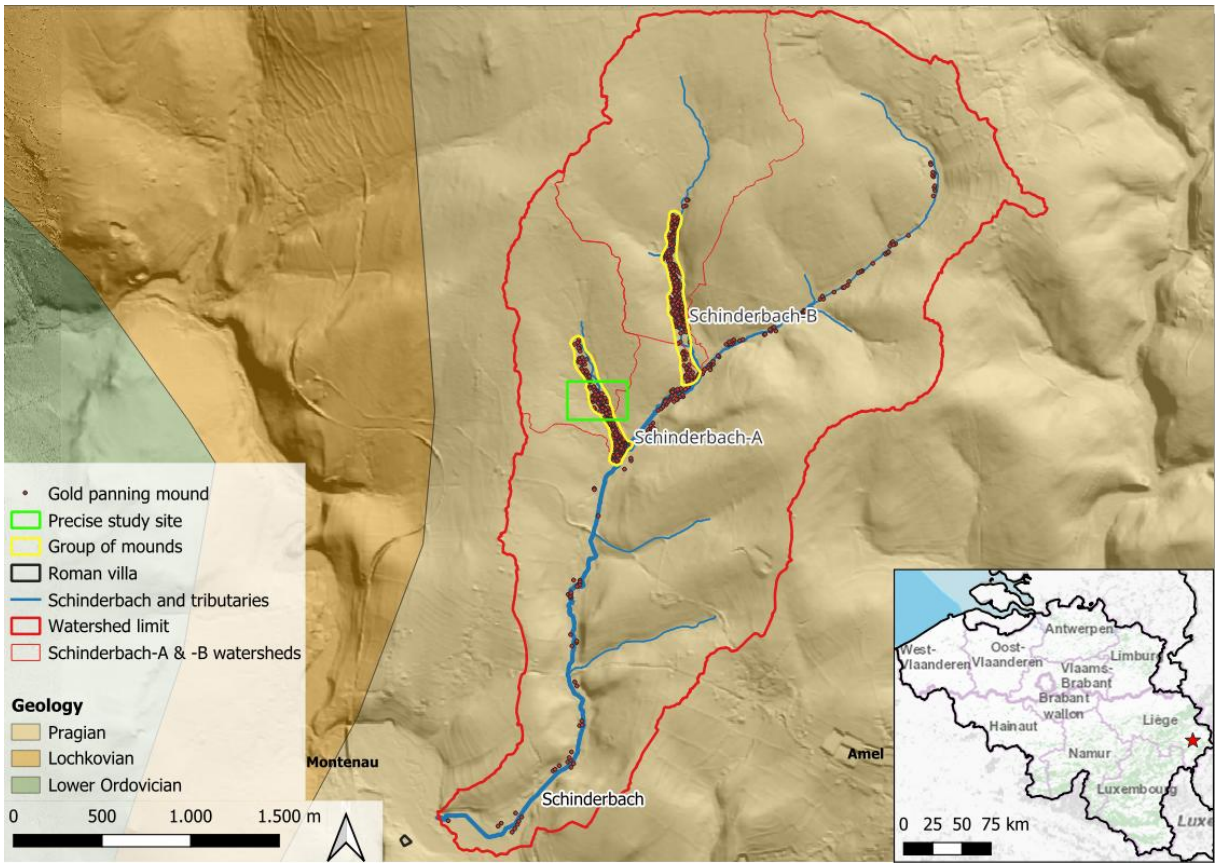

Figure II.7: Context of the Schinderbach study site. Geology based on Vandenven (1990).

Regarding geology (Figure II.7), the Schinderbach watershed lies on Pragian rocks of the Amel formation (Lower Devonian). It is characterised by an alternation of shales and shists with quartzitic shales and layers of quartzite or sandstone. The layout of the geological structures is the same as for the Rougerie, with the difference that the directions are rotated 90° counterclockwise. The rocks observed are, from east to west, Pragian rocks of the Amel formation, followed by Lochkovian rocks of the Waimes formation (Lower Devonian), and finally Tremadocian rocks of the Salm group (Lower Ordovician) corresponding to the eastern edge of the Stavelot massif (Vandenven, 1990; Cesar *et al.*, 2017).

It worth noting that a Roman villa is located near the confluence of the Schinderbach with the Amel river (Figure II.7, right next to the north arrow). It is commonly called *the Roman villa of Montenau*. Even if no absolute dating has ever been made, the villa is definitely Roman, because of discoveries of white walls with yellow and red bands, and typical Roman paintings

(Hecking, 1862 *in* Seiler, 2015). Seiler (2015) suggested it to date from between the 1st and 3rd century AD: Roman prosperity reached isolated peripheric regions of the Eifel and the Ardennes by the end of the 1st century AD or mid-2nd century AD at the latest, while the violentl destruction of the villa could be linked to German incursions during the 3rd century AD. The Roman villa of Montenau, due to its above-average size (75 m long, 22-30 m wide), was probably not a purely subsistence-based villa but rather a fairly wealthy establishment exporting its products. It remains unknown what kind of product was exported (Seiler, 2015). Some authors (*Kreisblatt für den Kreis Malmedy*, 1895 *in* Draily, 2022; Draily, 2022) use the wealth of the villa and its location at the centre of the gold mined upper Amel basin as evidence for gold mining in this region during the Roman period. As also highlighted earlier, caution is required because proximity does not necessarily mean relationship. Gillet (1970), on the other hand, asserted that the villa must be more recent than the gold panning mounds, as some of these mounds were destroyed during its construction. This assertion remains to be substantiated, however (Gillet, pers. comm., 2022 *in* Draily, 2022).

Chapter III : OPTICALLY STIMULATED LUMINESCENCE DATING

Summary of chapter III: This chapter briefly explains the fundamentals of optically stimulated luminescence (OSL) dating of quartz. The analytical facilities and methods used for sampling, sample preparation, and laboratory measurements are then summarised. Finally, the OSL dates obtained are presented and compared with those from radiocarbon (^{14}C) dating, and the difficulties encountered evaluated.

1. General principles of luminescence dating

Luminescence dating is a chronological method based on the emission of light, luminescence, by commonly occurring minerals such as quartz and K-rich feldspar (e.g. Duller, 2008; Cordier, 2010, Bateman, 2019, Murray *et al.*¸2021). Therefore, luminescence dating can be applied to a wide range of materials. The method can for instance be applied to fired archaeological materials (e.g. pottery, bricks,…), in which case the event dated corresponds to the last heating of the object. Another application of luminescence dating is to unheated sediments, which is also one of the topics of this study. In this case, the event dated is the last exposure to sunlight before the burial of the sediment. *Figure III.1* shows the principle of luminescence dating of sediments. As explained by Vandenberghe (2004):

> Minerals are continuously exposed to a low-level of natural radioactivity, through which they can acquire a latent luminescence signal. During erosion, transport and deposition, the minerals are exposed to sunlight and all the previously accumulated luminescence is removed (a process also known as 'bleaching'). Once shielded from the sunlight, the signal starts to build up again, until the moment of measurement in the laboratory. The age that is being determined is consequently the time that has elapsed between these two zeroing events. The luminescence is measured in the laboratory by exposing the mineral grains to light (optically stimulated luminescence, OSL) or heat (thermoluminescence, TL).

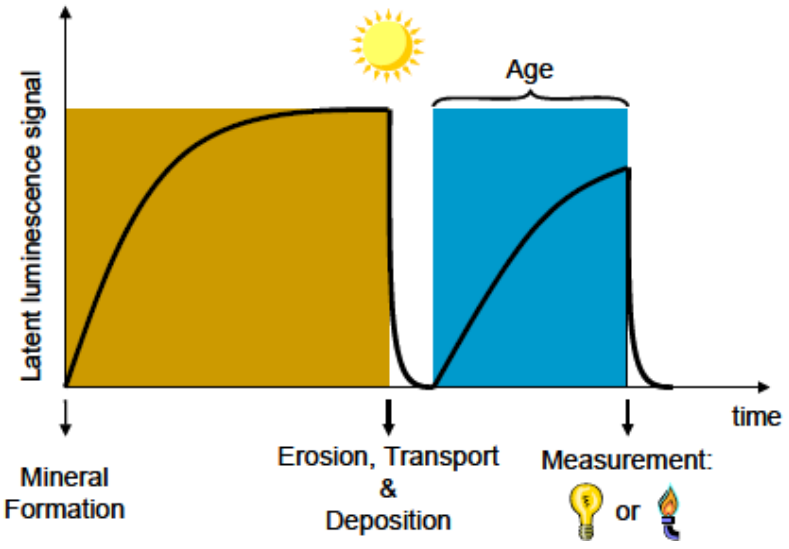

Figure III.1: Schematic representation of the principle of luminescence dating of sediments (Vandenberghe, 2004).

Luminescence dating was developed and first applied in the 1960s, mostly on pottery and other types of heated archaeological materials (Aitken *et al.*, 1964, 1968; Zimmerman, 1967). Since then, huge progress has been made in understanding the phenomena as well as in measurement technology and methodology, developing the method to unheated sediments. This has led to a significant increase in number of luminescence dating studies over the past few decades, and the method is now commonly applied in a wide range of Late Quaternary studies (Cordier, 2010; Bateman, 2019; Murray *et al.*, 2021). It typically covers an age range from a few years to several hundreds of thousands years (*Figure III.2*; Murray *et al.*, 2021; Mahan *et al.*, 2023). As such, luminescence dating can be considered as an alternative and complementary dating method to ^{14}C-dating (see e.g. Murray & Olley, 2002; Moayed, 2023; Moayed *et al.*, 2023). Although the latter is probably still the most widely used Quaternary radiometric method, especially in archaeology, luminescence has the advantages of being less material specific, being applicable over a significantly wider age range, and of more directly dating particular events of interest (e.g. when exactly was a ceramic find manufactured, or a sediment deposited). The younger age limit of luminescence dating spreads from months, or even weeks, to several years and is dictated by signal sensitivity and potentially adverse thermal effects. The older age limit extends up to 500 ka or more, depending on luminescence characteristics (saturation), incomplete resetting, and dose rate (Rhodes, 2011).

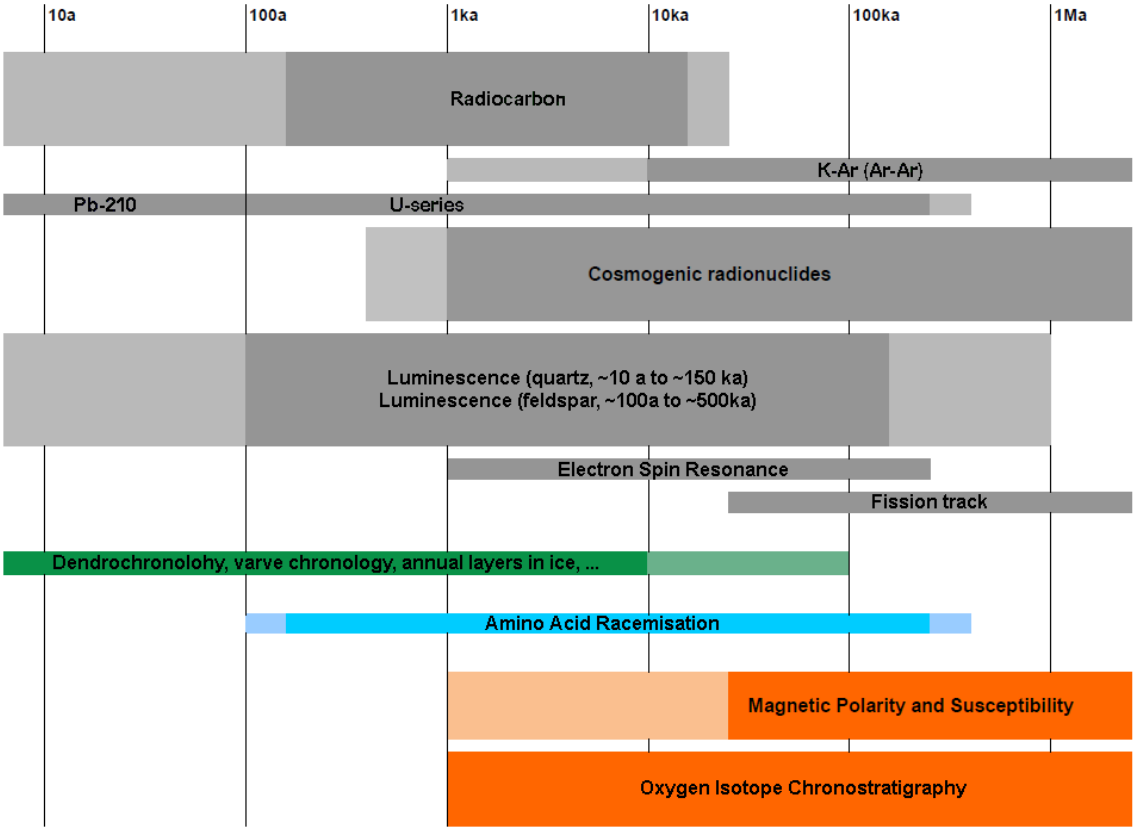

Figure III.2 : Age range of Quaternary dating methods (modified after Aitken, 1998 and Moayed, 2023). Limits depend on circumstances, e.g. state of sample preservation. Lighter shades indicate where methods approach their operational limits. Bar width is a marker of its relative importance, based on applied published studies. Grey bars: radiometric/radiation damage; Green bar: counting methods; Blue bar: relative method; Orange bar: correlative dating.

Luminescence dating is based on the time-dependent accumulation of radiation damage in minerals. This damage results from the exposure of the minerals to naturally occurring

radioactivity (mainly *α, β,* and *γ*-radiation from ^{40}K and the ^{238}U and ^{235}U & ^{232}Th decay series, as well as cosmic radiation). The damage in the minerals increases the longer they are exposed to this continuous flux of ionising radiation. The intensity of the radiation damage is thus a measure for the total amount of energy absorbed by the material over a certain period of time. In luminescence dating, the intensity of the damage is detected as a small amount of light, i.e. the luminescence signal. The phenomenon can be explained in terms of, for example, the energy level diagram (*Figure III.3*; Aitken, 1985; Duller, 2008). In this model, electrons are linked with bands that represent discrete ranges of energy. Two bands characterize the crystalline structure: the 'valence band', which is the lowest energy band, and the 'conduction band', which is the highest energy band. Between the two bands lies a gap called the 'forbidden zone'. This zone is electron-free in an ideal crystal. However, in natural crystals, defects are present that give rise to energy levels in the forbidden zone. These act as traps for electrons resulting from exposure of the crystal to ionizing radiations. Electron traps can be categorised in many kinds, but two types are usually distinguished: shallow traps and deep traps. Electrons situated in shallow traps don't remain trapped durably, i.e. for the whole duration of the period that is to be dated. This means that these traps are 'unstable'. The other way around, deeper traps are considered as more stable and are linked with higher energy levels. This means that electrons trapped in these defects have a higher thermal lifetime. For luminescence dating, we are only interested in traps that are deep enough, and are thus sufficiently thermally stable to not significantly leak electrons during the sample's age span (Aitken, 1998; Vandenberghe, 2004; Walker, 2005). Upon exposure to heat or light, electrons can be released again from these traps, which can result in the emission of luminescence. Once the crystal is no longer exposed to heat or light, electrons can accumulate again in the traps.

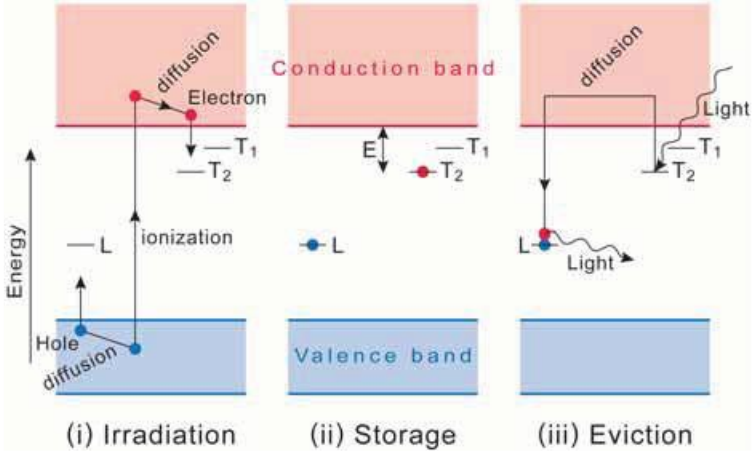

Figure III.3 : Energy level diagram representing the luminescence process (Duller, 2008; modified from Aitken, 1985). Red dot: electron; blue dot: hole.

The process of energy transfer, storage and release can be summarised as follows (*Figure III.3*): (i) exposure of the crystal to radiation (ionization) leads to the transfer of electrons from the valence band to the conduction band, leaving 'holes' in the valence band; (ii) some of the electrons can be trapped in defects (T_1, T_2) and the electron residence time, i.e. its stability, in the traps depends on the depth of the latter below the conduction band (E) (the deeper the more stable); (iii) exposure to heat or light releases the electrons, which recombine with holes stored at luminescence centres (L), and results in the emission of light, i.e. the luminescence signal (Aitken, 1985, 1998; Duller, 2008, 2015).

Apart from incomplete resetting of grains, two main factors limit the applicability of luminescence dating. The first one is that the total number of traps which can store electrons is limited. This means that the traps are gradually filled over time and, at one point, can reach saturation. The second limitation concerns the spontaneous leakage of electrons from the traps. This phenomenon is called 'anomalous fading' and will be explained in Chapter III2.

Further details on luminescence dating can be found in e.g. Aitken (1985, 1998), Wintle (2008, 2014) and Bateman (2019).

2. OSL dating and the use of quartz

Luminescence dating can be divided in two categories, depending on whether the electrons trapped within the mineral are released by exposure to heat, resulting in thermoluminescence (TL) or light, resulting in optically stimulated luminescence (OSL).

Luminescence dating was originally developed using thermoluminescence signals (Aitken *et al.*, 1964, 1968; Zimmerman, 1967). The term refers to the light emitted by a mineral, other than incandescence or black body radiation, when heated. The principle of the method is that the sample is heated at a constant rate, typically between 1°C/s and 5 °C/s, from ambient temperature to temperatures between 450 °C and 700 °C, depending on the mineral (Preusser *et al.*, 2008). The resulting signal is graphically plotted as a function of the measurement temperature, also referred to as glow curve. This curve commonly shows a series of peaks at different temperatures, representing recombination of electrons from deeper (and hence thermally more stable) traps with increasing peak temperature. Until the mid-1980s, TL was the only method used in luminescence dating. Thereafter, optically stimulated luminescence techniques were gradually developed and, from the mid-1990s onwards, relatively rapidly became the preferred method for dating unheated sediments. At present, TL signals are most commonly used for authenticity testing (Stoneham, 1991; Preusser *et al.*, 2008; Wintle, 2008).

Optically stimulated luminescence (OSL) dating of sediments was first introduced by Huntley *et al.* (1985). The principle of the method is approximately the same as TL dating, with the huge difference that the electrons are stimulated by visible light (Huntley *et al.*, 1985), or even infrared (IR) (Hütt *et al.*, 1988). The term OSL has often been used as an 'umbrella' term that refers to stimulation by light from any wavelength, including IR. The more specific terms, depending on the wavelengths used for stimulation, are InfraRed Stimulated Luminescence (IRSL), Blue-plus-Green Stimulated Luminescence (BGSL), Green Light Stimulated Luminescence (GLSL or GSL), and Blue Light Stimulated Luminescence (BLSL or BSL) (Aitken, 1998). However, most of the literature nowadays employs the term OSL to encompass stimulation by visible light (blue and/or green), and IRSL for stimulation by infrared light (Preusser *et al.*, 2008; Mahan *et al.*, 2022). This designation will therefore be considered in this work.

In any case, the principle of OSL (and of IRSL) dating remains the same. Electrons are stimulated by exposing the sample to visible light thanks to a laser beam, a filtered halogen lamp, or high-power light emitting diodes (LEDs). LED stimulation is currently used in the majority of luminescence laboratories, as LED are much cheaper than lasers and more reliable than halogen lamps (Bøtter-Jensen, 1997). One of the main reasons for preferring OSL over TL signals for dating unheated sediments, is the rate of resetting by exposure to light. Indeed, the bleaching of the OSL signal is much faster and more complete compared to the TL signal

(Duller, 2008; Preusser *et al.*, 2008). As shown in *Figure III.4*, an exposure of grains to light during a range of 10 to 100 seconds is sufficient to reduce the quartz OSL signal by 99.9 % compared to its initial level while, after the same duration, over 85 % of the TL signal remains. *Figure III.4* also highlights the important distinction between the duration of charging of the luminescence signal (10^1-10^5 years) and charge removal during bleaching and OSL measurements (10^0-10^2 seconds) (Rhodes, 2011). It should be noted that, in nature, the bleaching process is often more complex, because of the non-uniformity of the environment, i.e. different grain sizes, grain compositions, and strengths of incident daylight, but also because of transport and depositional modes (Duller, 2008).

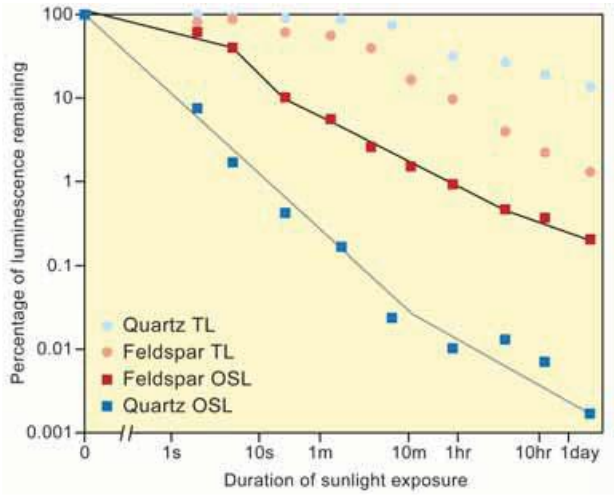

Figure III.4: Reduction of TL and OSL signals from quartz and feldspar by exposure to light (Duller, 2008; modified after Godfrey-Smith et al., 1988).

The two most widely used minerals in luminescence dating are quartz and K-rich feldspar. They both act as dosimeters, recording the amount of radiation to which sediments have been exposed. When optically stimulated, the signal from quartz shows a rapid decrease with time, which corresponds to the eviction of discrete electron traps, thus producing an emission of light that decreases as the traps are emptied. On the other hand, feldspar OSL signal decreases more slowly than that from quartz, because a continuum of traps generates a more complex decay form. Quartz and (K-rich) feldspar have their own advantages and disadvantages for dating. The use of one mineral over another depends principally on their availability within the sample and the age of sediments (Rhodes, 2011).

Usually, feldspar would be preferred with older sediments, as it saturates at higher doses than quartz (Aitken, 1998; Vandenberghe, 2004; Buylaert *et al.*, 2012). Feldspar usually also emits more uniform and brighter luminescence signals (Duller, 2015). On the other hand, it is well-known that feldspar signals are not stable owing to anomalous fading, which leads to age underestimation (Aitken, 1985, 1998; Buylaert *et al.*, 2012). While several approaches have been suggested to overcome this (Lamothe & Auclair, 1999; Huntley & Lamothe, 2001; Auclair *et al.*, 2003, Buylaert *et al*, 2012), the accuracy of measurements of the dose accumulated in K-feldspar remains contentious (Buylaert *et al.*, 2018), while the slower reduction of the signal upon exposure to daylight may limit or even prevent its general application to Holocene deposits (Buylaert et al., 2012) .

In the frame of this exploratory study, quartz has been selected as the mineral of choice. Indeed, quartz is more ubiquitous than feldspar in the study region (the Ardennes), and gold has been

often associated with quartz inclusions (Hanssen & Viaene, 1979; Lefevre & Hatert, 2003; Bruni & Hatert, 2017). In addition, gold exploitation activities in the Ardennes are linked to human presence and metallurgy, implying an expected age for the remaining gold panning tailings younger than ~ 2.5 - 3 ka (Destatte, 2013). Given this age frame and the anthropogenic depositional context, incomplete resetting is of prime concern. These considerations, associated with the fact that sediment must have been exposed to sunlight during the exploitation process, provided the incentive for investigating the potential of quartz-based OSL dating for application to gold tailing deposits. To our knowledge, and apart from the single OSL date presented by Deprez *et al.* (2018), this potential has not yet been explored. Similar research is currently being conducted in France (Trément, pers. comm.).

3. Age equation, equivalent dose and dose rate determination

3.1. Age equation

A luminescence age is obtained from three parameters that must be experimentally determined: the natural luminescence signal, the luminescence sensitivity of the dosimeter to radiation, and the dose rate. The *equivalent dose* (D_e) combines the first two components and can be defined as the total amount of energy accumulated over the whole burial duration. It is obtained by comparing the natural luminescence signal with an artificially induced signal. The absorbed radiation is expressed, in the SI[5], in Gray (Gy; 1 Gy = 1 $J.kg^{-1}$). On the other hand, the *dose rate* (D_r) is the amount of energy absorbed by the dosimeter per unit of time. It is expressed in Gray per year ($Gy.year^{-1}$) (Duller, 2008). The dose rate can be obtained either by directly measuring the radiation emitted by radioisotopes naturally occurring in the surrounding, or by determining their concentration through a chemical analysis (Vandenberghe, 2004; Duller, 2008). Therefore, the age equation giving the duration of burial is defined as (Aitken, 1998):

$$Age\ (years) = \frac{Equivalent\ dose\ (Gy)}{Dose\ rate\ (Gy.year^{-1})}$$

3.2. Equivalent dose determination

Several laboratory techniques exist to determine the equivalent dose (D_e) and can be grouped in two categories: additive dose and regenerative dose methods (Aitken, 1985; Duller, 2008, 2015). Both concern the measurement of, and the comparison between, signals that are acquired in nature, and that are induced in the laboratory.

Additive dose methods (*Figure III.5*a) consist of measuring the intensity of the luminescence signal acquired during burial, and of signals induced by adding known radiation doses on top of that. The growth of the luminescence signal with added laboratory dose is then mathematically modelled, resulting in a *dose response* or *growth curve*. Extrapolation of this curve to the dose axis then yields the equivalent dose. The drawback of this approach is that the equivalent dose derived from the extrapolation heavily depends on the choice of the mathematical function that is used to describe the dose response.

In regenerative dose methods (*Figure III.5*b), the intensity of the natural luminescence signal is measured, as in the additive approach. Here, however, this signal is compared to those induced by different laboratory doses administered after complete removal of the natural signal. In this

[5] SI = the International System of Units

case, the equivalent dose is thus determined by interpolation of natural signal on the dose-response curve. The advantage of this approach is that the equivalent dose is less dependent on the choice of the mathematical function that is used to describe the dose response (because it is derived through interpolation). The drawback, however, is that the sensitivity for acquiring a luminescence signal may have significantly changed after artificial resetting. As such, there is an inaccurate relation between natural and induced signals, and hence also the equivalent dose derived from their comparison.

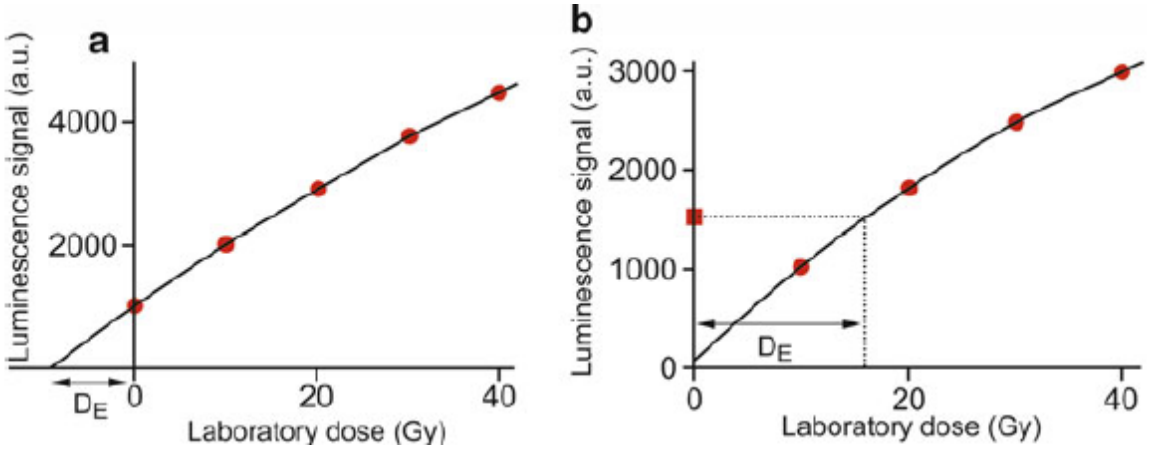

Figure III.5: Equivalent dose (D_e)determination using: (a) additive dose method, (b) regenerative dose method (Duller, 2015). Red dot: luminescence measurement after artificial irradiation; Red square: luminescence signal from natural irradiation.

The original luminescence measurement protocols required the preparation and measurement of a large number of different subsamples, called 'aliquots', to arrive at one single equivalent dose estimate for a particular sample. The methods are called multiple aliquot methods, with the acronyms MAAD and MAR, referring to the added dose and regenerative approaches, respectively. Because of the advantages and disadvantages of each of them, both were commonly used in parallel.

The first to propose a protocol using a single aliquot was Duller (1991). The principle of this method is that all of the measurements needed to obtain D_e are performed on one single subsample or aliquot. This approach offers a multitude of (interconnected) advantages. Firstly, as there is need for normalization between aliquots and individual D_e's can be obtained more precisely. Secondly, as only a single-aliquot is needed, less sample is required; the scale of single-aliquot can be even reduced to a single sand-sized grain of e.g. quartz. Finally, as it allows obtaining different estimates of D_e in a single sample, the scatter in these estimates can be explicitly examined (e.g. to assess completeness of resetting) together with the influence of the various measuring parameters and variability in intrinsic luminescence behaviour (Vandenberghe, 2004). On the other hand, several challenges with single-aliquots methods arose at the time, e.g. luminescence sensitivity variation with repeated measurements on the same aliquot. Since then, a substantial amount of methodological research has been undertaken that culminated in the approach formalised by Murray & Wintle (2000, 2003). This approach is called the *single-aliquot regenerative-dose* (SAR) protocol and is briefly outlined below. The SAR-protocol has been shown to be applicable to many samples, and is currently the most widely adopted method for estimating burial doses (Wintle & Adamiec, 2017).

3.3. The SAR protocol

While the general principle of the single-aliquot regenerative-dose (SAR) protocol (Murray & Wintle; 2000) appears quite straightforward nowadays, it is the result of years of intensive research, as summarised by e.g. Wintle and Murray (2006) and Murray et al. (2021). This procedure is particularly advantageous as it is a single aliquot procedure, i.e. all measurements to obtain one D_e estimate are performed on one aliquot, and because the D_e can be derived through interpolation, as it is a regenerative approach (see higher). A SAR procedure basically consists of a succession of measurement cycles outlined in Figure III.6 (Duller, 2008).

In the first half of each cycle, either the natural OSL signal (L_N; first cycle) is measured, or the OSL responses to various laboratory regenerative doses ($L_{i;\ i\ =\ 1,\ 2,\ldots}$). Each of these measurements resets the signal to zero, and is preceded by some thermal pretreatment, for quartz usually at some fixed temperature in between 160 °C and 300 °C for 10 s. This *preheat* aims at removing electrons from shallow, thermally unstable traps, so that all measured OSL signals relates to charge in the main OSL-dosimetric trap used for dating. The various regenerated OSL responses ($L_{i;\ i\ =\ 1,\ 2,\ldots}$) can be used to characterize the growth of the signal with dose. It is well known however that the luminescence properties, and more specifically the *sensitivity* or amount of luminescence emitted per unit of dose, may change upon repeated pre-treatment and measurement of an aliquot. If not taken into account, a plot of L_i versus regenerative dose would result in inaccurate estimates of D_e.

The second half of each cycle in the SAR protocol is specifically intended to accommodate upon this issue. Here, the OSL response to a fixed dose (*test dose*) is measured. These signals (T_N *and* $T_{i;\ x\ =1,\ 2,\ldots}$) represent measurements of sensitivity and thus allow monitoring and correcting for any changes in sensitivity that may have occurred through the SAR measurement procedure. A sensitivity corrected growth curve can then be obtained by plotting L_i/T_i versus regenerative dose, from which the D_e is then derived through interpolation of the sensitivity corrected natural OSL signal L_N/T_N (*Figure III.7*)

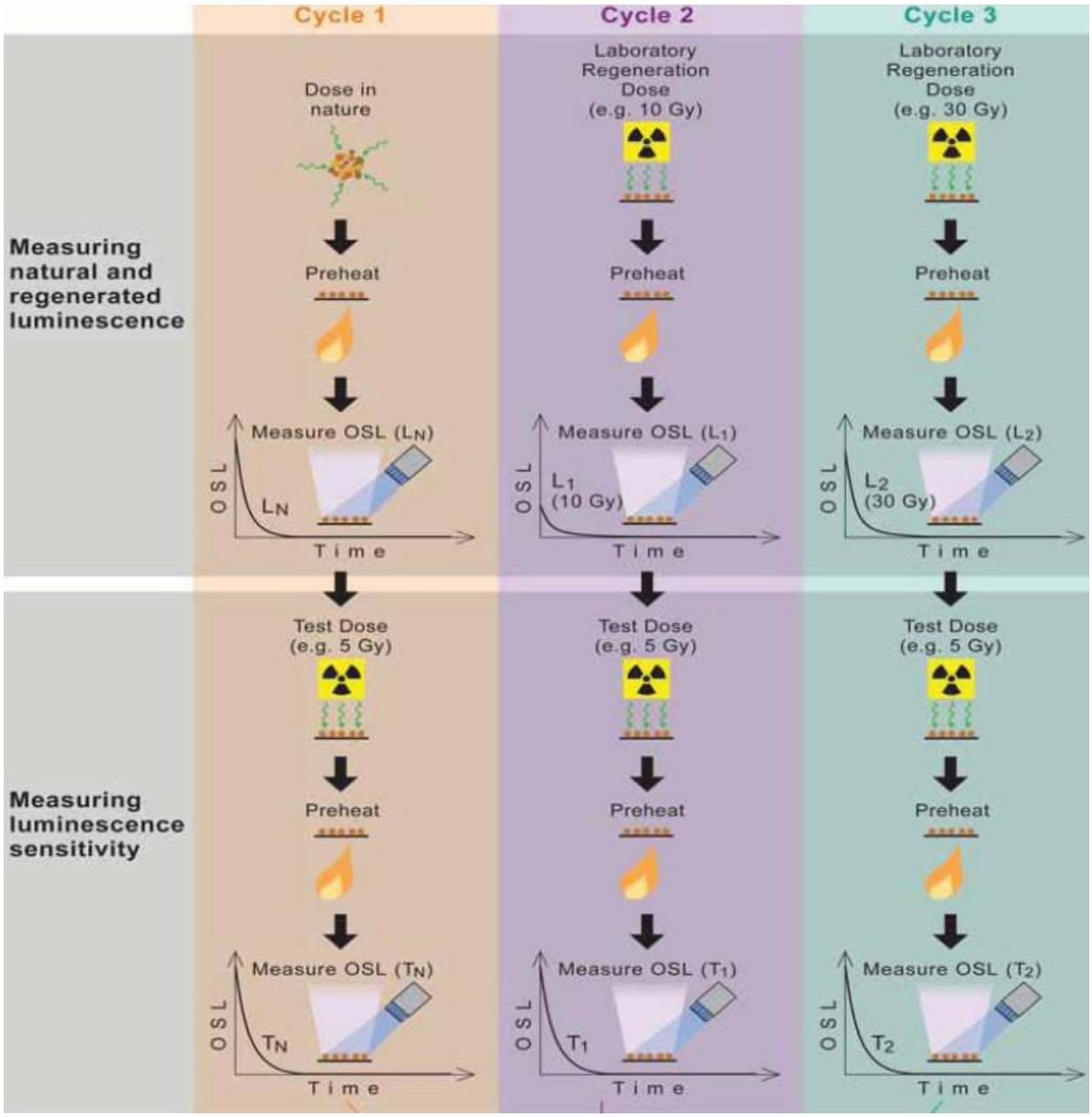

Figure III.6 : Single-aliquot regenerative-dose (SAR) method applied to quartz (Duller, 2008).

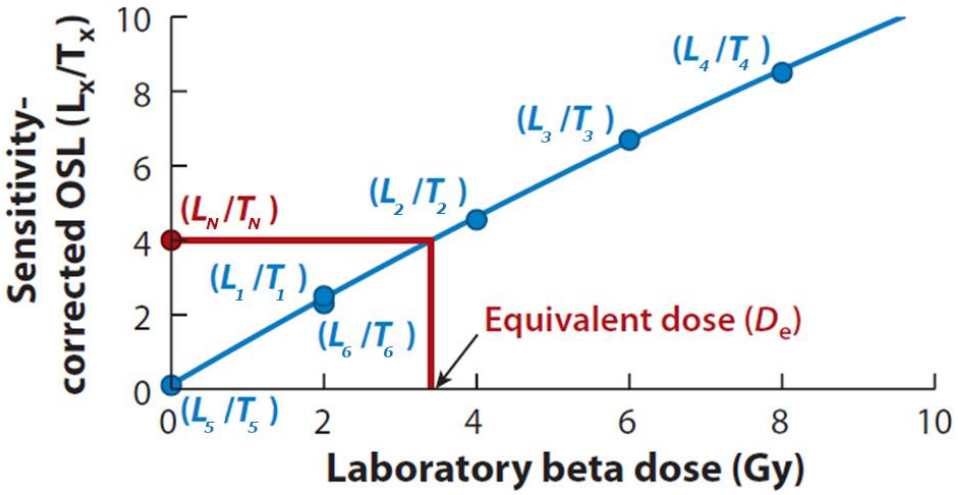

Figure III.7: Single-aliquot regenerative-dose (SAR) response curve comprising six steps (Rhodes, 2011). Red dot: natural OSL; blue dots: regenerative-dose OSL. Recycling ratio applied with L_1/T_1 and L_6/T_6.

To test the applicability of a given SAR protocol on a particular sample, a number of procedural tests have been suggested (e.g. Murray and Wintle, 2000; 2003; Wintle and Murray, 2006). Some of these can be built into any individual SAR measurement sequence (such as measurements of recycling ratio, OSL-IR depletion and recuperation), while others require separate suites of analyses (e.g. investigations into the dependence of measured dose on particular measurement parameters such as preheat and size of the test dose, and dose recovery). These are briefly outlined below.

At the end of the suite of measurements needed to characterize the dose response, it has become quite common to include a repeat measurement of the response to a regenerative dose that was administered earlier (Figure III.7). The ratio between the two sensitivity-corrected luminescence signals is called the *recycling ratio*, and allows testing the accuracy of the sensitivity correction. Ideally, this ratio should be close or equal to unity, Murray & Wintle (2000) originally suggested values in between 0.9 and 1.1 as a possible range of acceptancy. Several subsequent studies (see e.g. Murray et al., 2021), however, observed no correlation between recycling ratio and measured dose, suggesting that it may not always be possible to identify a suitable threshold to reject individual aliquots from a particular dataset. The same holds for the OSL-IR depletion ratio and recuperation.

A second check is the *OSL-IR depletion ratio* (Duller, 2003) It is comparable to the recycling ratio, but differs in that a stimulation with IR is now performed immediately before the measurement of the response to repeated regenerative dose. The test exploits the fact that feldspar is sensitive to stimulation with IR, but quartz is not, and thus allows assessing the purity of a single aliquot of quartz. This is important as feldspar is also sensitive to stimulation with visible light and may thus contribute to the observed quartz OSL signal, which is undesirable. If the OSL-IR depletion ratio is close to unity, it is unlikely that the quartz OSL signal is significantly contaminated with feldspar OSL.

A third procedural test commonly built into a routine SAR sequence, is a measurement of the sensitivity-corrected response to a zero regenerative dose. The resulting value is called *recuperation* (usually expressed as percentage of the corrected natural signal) and is used to assess the importance of charge carryover from one SAR cycle to the next. Murray and Wintle (2000) suggested that it should be small (< 5%). An additional stimulation at elevated temperatures (for quartz typically with blue diodes at 280°C) can be inserted at the end of each SAR cycle to minimize it (Murray and Wintle, 2003). It remains to be established, however, to what extent seemingly significant recuperation affects the accuracy of dose estimation.

Apart from the aforementioned built-in checks, it is not uncommon examine the dependence of measured dose on specific SAR measurement parameters, mainly (but not exclusively) to evaluate the importance of undesirable charge transfer processes. Such tests involve e.g. measurements of D_e following different preheats, cut heats or test dose sizes, and looking for the range over which the D_e is independent (i.e. the *plateau*). Another test specifically aims at evaluating the importance of thermal transfer, which is the transfer of charge by heating from light-insensitive (or less light sensitive) but thermally stable traps, into light-sensitive traps. If significant, it leads to an overestimation of the equivalent dose (D_e) and hence the age. The phenomenon is usually considered to be of greater concern for younger samples, especially from depositional environments where daylight exposure may have been limited. The significance of thermal transfer is most commonly investigated using a set of aliquots from

which the naturally acquired signal is first bleached, and the apparent dose is subsequently measured as one would do in any of the aforementioned (but mainly preheat) plateau tests. Low preheats usually result in negligible measured doses (Wintle & Murray, 1998, 2006).

While all the procedural tests summarised in the above are informative to some extent, the *dose recovery* test is currently considered as the most powerful and complete test to assess the performance and applicability of a given SAR protocol to a given sample. For unheated sediments, this test basically consists of resetting the OSL signal in an aliquot by exposing it to light (thereby mimicking bleaching conditions prior to final deposition and burial), giving it a known laboratory dose, and then measuring this dose using the same SAR protocol as one would use for measuring the natural dose. The ratio between the measured dose and the known given laboratory dose is the *dose recovery ratio*. This ratio should be close to unity. The most important aspect of this test is that, apart from the optical resetting, the laboratory dose is administered prior to any thermal pretreatment. As such, it allows an evaluation of the extent to which the first sensitivity measurement ($T_{"N"}$) matches that of the sample when it was given the laboratory dose (resulting in $L_{"N"}$). A dose recovery test thus allows detecting a very initial change in sensitivity. It differs from the recycling ratio in that the latter monitors the accuracy of the correction for sensitivity changes that occurred throughout the remainder of the SAR sequence. It should be noted that, while a dose recovery test is an essential procedural test, it cannot be applied to exactly the same aliquots as used for D_e determination. It provides a means to test, on average, the performance of a given SAR protocol on a particular sample ('average sample descriptor'; Murray et al., 2021) but cannot establish whether natural doses (i.e. D_e's in practice) are measured with the same degree of accuracy or inaccuracy. The most complete and comprehensive procedural tests of OSL dating therefore remain comparisons with reliable independent age information.

3.4. Dose rate

The dose rate is the average rate at which the minerals to be dated absorb the energy from the surrounding naturally radioactive environment. In luminescence dating, we are mainly concerned with the dose rate provided by the decay of uranium (U), thorium (Th), potassium (K), and, to a significantly lesser extent, rubidium (Rb). Cosmic rays contribute as well. The latter contribution is usually small, depends on the burial depth, altitude and latitude, and is usually calculated from literature sources (e.g. Prescott & Hutton, 1994). In most cases, radioisotopes are the main contributors to the total dose rate. The three types of radiation emitted (alpha, beta and gamma radiation) have very different properties. Alpha rays are made of two neutrons and two protons. Their penetration range is very short in sediments, approximately 10 µm to 40 µm. Beta rays consist of electrons, and their penetration range goes up to 2 mm. Gamma rays belong to the electromagnetic spectrum. They can penetrate sediments up to 30 cm depth (DeWitt, 2015). Radiation from radioisotopes can originate within the mineral grains themselves (*internal dose rate)*, or from their surroundings (*external dose rate*). In the case of OSL dating of sand-sized quartz, the contribution from external alpha particles is often removed through etching, because of their low penetration range, and the internal dose is very small compared to the external dose (Vandenberghe *et al.*, 2008; Duller, 2015). Further details about the contribution of each source of radiation are found in e.g. Ankjaergaard & Murray (2007) and Vandenberghe *et al.* (2008).

The dose rate is most commonly obtained either by directly measuring radioactive emissions, or by analysing elemental concentrations of U, Th and K. A range of analytical methods is

available (see e.g. Hossain, 2003) and the choice of one over another depends on the type of sample that is measured and practical considerations. In this work, gamma ray spectrometry was employed to determine the specific activities of the radionuclides in the investigated sediments. From the latter, dose rates were calculated using conversion factors derived from published nuclear data (e.g. Adamiec & Aitken, 1998). Experimental details are explained in section *Methodology*.

A final consideration when determining the dose rate is the water content, because all measurements are made on dried samples in this work. Actually, water in the interstices between mineral grains absorbs a proportion of the radiation, leading to a decrease in the radiation absorbed by minerals. In the case of sand-sized quartz, it is usually assumed that a 1 % increase in water content leads to an approximate 1 % increase in the luminescence age (Duller, 2008, 2015). It is usually not straightforward to estimate the average degree of wetness experienced by a sample throughout its the burial period, and thus represents a major source of uncertainty (which is reflected in the uncertainty associated with the age result).

4. Methodology

4.1. Sample collection

As OSL measures the time elapsed since sediments were last exposed to light, all sampling and handling must avoid daylight exposure. The samples were collected following widely adopted protocols (Duller, 2008; Murray *et al.*, 2021), requiring careful preparation of the sampling sites.

The surface of the sedimentary sequence is first cleaned by scraping back the outermost layer. This step removes the light-exposed few millimetres to centimetres (or more) of sediment and simultaneously reveals a clean stratigraphic profile. In this way, areas potentially affected by (superficial) post-depositional disturbances, such as roots or bioturbation features, can be identified and avoided. The first few centimetres must be at least cleaned and, ideally, more than one metre of excavation would fully eliminate the influence of air exposure. In this way, the sampled material is representative of the long-term redox conditions and moisture content.

Before sampling, the exposed section should be photographed to document the stratigraphic context and exact sample locations. Sampling for OSL dating usually consists of taking at least two samples: one for OSL measurements (equivalent dose determination), and a second for radiochemical analysis (dose rate determination). We also collected a third undisturbed sample for determining the *in situ* moisture content, saturation level and packing density. Two main sampling methods can be employed for D_e determination.

The simpler and more commonly used method was preferred, which involves inserting opaque tubes directly into the exposed stratigraphic face, under daylight conditions. These tubes, typically 3-5 cm in diameter and made of opaque metal or plastic, are driven horizontally into the section. Ideally, the sampling location should be at least 15 cm away from any layer boundary to minimise gamma radiation gradient across the sample. To stabilise the sediment during insertion and prevent collapse or mixing of exposed and unexposed material, a paper or plastic plug is placed at the end of the tube. Once filled, either completely with sediment or packed to prevent movement, the tube is sealed and transported to the laboratory. There, the outermost 2-3 cm at both ends of the tube, potentially light-exposed, are removed and set aside for supplementary analyses, such as water content and/or radionuclide concentration for dose

rate determination, grain size, or mineralogy. The protected inner portion of the sample is retained for OSL analyses and equivalent dose determination.

The second approach is to sample in the dark, either at night or under an opaque covering (e.g. tarpaulin). It is applied, for instance, if the unit is too thin to be sampled with a tube or if the sediments are too consolidated or coarse for hammering in tubes.

For dose rate determination, sediment samples were collected from the same stratigraphic layer as the D_e samples, with a minimum of ~300–400 g retrieved per location. The additional sample for water content was obtained using a 100 cm³ Kopecky ring; the method of its evaluation is described below.

4.2. Sampling sites

Sixteen samples were collected during summer 2024. Nine samples are from the Rougerie stream, four are from the Schinderbach-B stream and three are from the Schinderbach-A stream. Their relative localisations are illustrated in Figure III.8 and Figure III.9, and Table III.1 summarises their coordinates in Lambert 72 projection (EPSG: 31370).

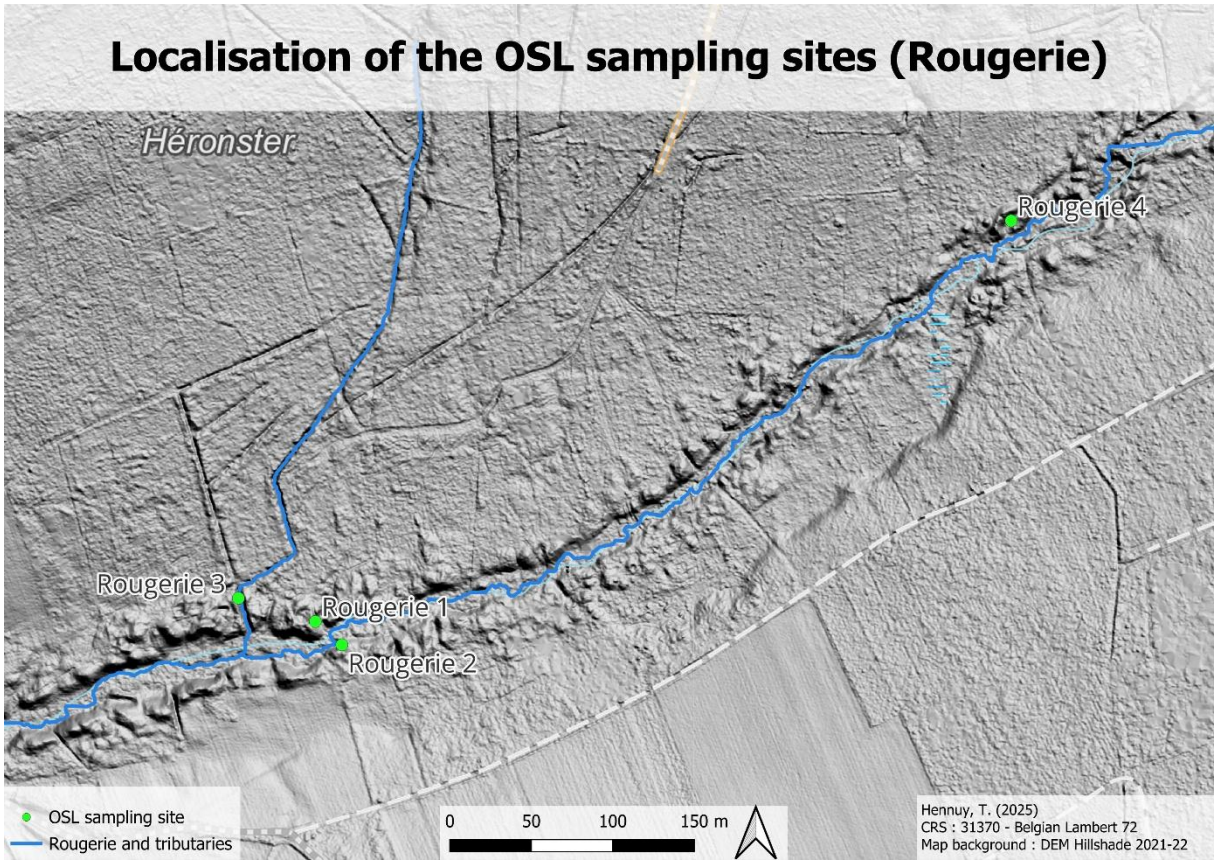

Figure III.8: Localisation of the OSL sampling sites along the Rougerie.

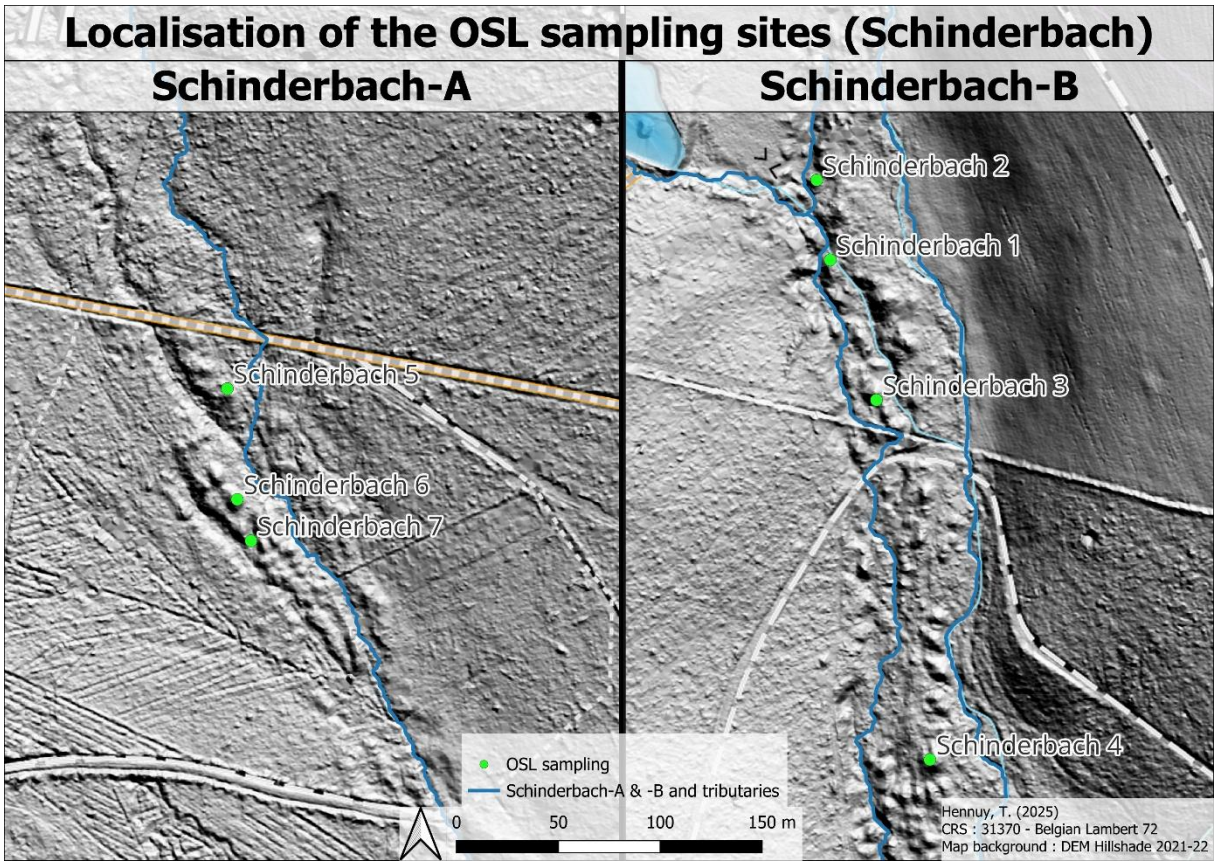

Figure III.9: Localisation of the OSL sampling sites along the Schinderbach.

	Lab code (GLL)	X	Y	Z
Rougerie 1	246301 & -02	262338.6	107157.4	471.7
Rougerie 2	246303	262354.9	107143.1	471.9
Rougerie 3	246304, -05 & -06	262294.1	107174.0	475.2
Rougerie 4	246307, -08 & -09	262765.6	107403.0	486.6
Schinderbach 1	246310	276780.1	120550.7	493.6
Schinderbach 2	246311	276773.4	120589.9	494.4
Schinderbach 3	246312	276802.7	120482.0	490.4
Schinderbach 4	246313	276829.0	120305.4	485.7
Schinderbach 5	246314	276367.9	119826.8	477.6
Schinderbach 6	246315	276372.8	119772.4	473.3
Schinderbach 7	246316	276379.5	119752.1	470.3

Table III.1: OSL sampling sites coordinates (Lambert 72 – EPSG: 31370).

Pictures of samples situation are found in Appendix 3, and described as follows:

- GLL 246301: Mound deposits. Fine gravel in a sandy matrix.
- GLL 246302: Sandy silt layer right below mound deposits.
- GLL 246303: Mound deposit.
- GLL 246304 and -05: Sandy vein above paleochannel gravel deposits.
- GLL 246306 : Ochre-coloured sandy vein above the pre-cited.
- GLL 246307, -08 and -09: Mound deposit.
- GLL 246310 : Mound deposit.
- GLL246311: Mound deposit.
- GLL246312: Mound deposit.

- GLL 246313: Mound deposit.
- GLL 426314: Mound deposit.
- GLL 246315: Mound deposit.
- GLL 246316: Sandy silt vein in a clay accumulation.

4.3. Sample preparation

In the laboratory, the *OSL* tube is opened in a dark room, a room protected from any light source (daylight or artificial light) potentially affecting the OSL signal. It is illuminated with red and orange lights. The outer 2-3 cm (depending of the sample) of each end of the tube, which was exposed to light during sampling, is first removed and the inner part is retained for further sample preparation. Throughout the process, the material should be maintained at or near room temperature to prevent any potential thermal fading of the OSL signal.

To remove carbonates, the sample is first treated with 10 % HCl during minimum 30 minutes, or until the gas emitted by the reaction stops completely. In the present work, the material was left in solution for at least one night. This is followed by the rinsing of the sediment with demineralised water. The sample is then treated with, first, 10 % and then 30 % H_2O_2. The process dissolves organic matter and can take up to a few days. The sediment is then once again thoroughly rinsed with demineralised water.

The remaining material, composed primarily of quartz, feldspar, and heavy mineral grains, is wet sieved using a 63 µm mesh to separate silts from sands. Grain-size separation is essential, as the dose rate is grain-size dependent. The selected size range depends on the abundance of grains within each fraction. A preliminary separation into the 63–250 µm range is commonly employed as a first division before potentially subdividing the sample in future dry sieving. Grains smaller than 63 µm are not retrieved, as sand-sized fraction offers some advantages, such as the possibility of physical and chemical purification, and the simplification of dose rate calculations.

Preceded by a short etch using 10 % HF, the next step is a heavy liquid density separation, using a density at 2.58 $g.cm^{-3}$, to separate fractions enriched in quartz (> 2.58 $g.cm^{-3}$) from K-feldspar-enriched fractions (< 2.58 $g.cm^{-3}$). As this step would take a long time naturally, due to the slight difference in density, the solution is put in a centrifuge for 30 minutes.

To retrieve only quartz grains, the heavy mineral grains resulting from the separation are placed in a concentrated 40 % HF solution. Because HF is particularly dangerous if used incorrectly (it can be lethal), this operation was proceeded by a specialist from the lab, and not by the author of this work. One hour is typically enough to remove remaining feldspar, as well as the outer ~10 µm alpha-irradiated rinds of the quartz grains, facilitating dose rate calculations.

After etching, the sample is dry-sieved on the original smallest mesh-width (63 µm) to remove partially dissolved feldspar grains and/or quartz grains that have become too small. As part of this exploratory work, quartz grains within the 90–212 µm and 212–250 µm size fractions were selected to assess the potential influence of grain size on signal resetting in the fluvial environment and during the subsequent panning.

The *bulk* material that was collected from the immediate surroundings of the OSL tubes for dose rate determination, is first completely dried at 110 °C, until constant weight. It is then powdered for 15 minutes in an agate ball mill. This operation is repeated multiple times, if

necessary, until a homogenised pulverised material is obtained. The powdered material is then cast in wax (~70 % sediment – 30 % wax) and stored for at least one month before being measured by gamma-ray spectrometry (De Corte *et al.*, 2006).

The sampling tube used to determine average water content is weighted in its "natural" state. It is then progressively filled with water to reach sediment saturation, where the sample is weighed again. Next, it is dried completely and the weight is measured. From the dry weight, the maximum water content is obtained by deducting from the saturation, and the water content at the time of sampling is calculated from the "natural" weight.

4.4. Sample measurement

As explained above, the inner portion of the OSL sampling tubes was prepared according to established protocols for the extraction of sand-sized quartz grains (Murray et al., 2021). Grains were fixed using silicone oil onto stainless steel discs (9.7 mm in diameter, 0.5 mm thick), in two configurations: large aliquots (inner 8 mm diameter of the discs) and small aliquots (inner 2 mm diameter).

Luminescence measurements were conducted using a Risø TL/OSL automated reader, equipped with blue (λ_{max} = 470 nm) and infrared (λ_{max} = 875 nm) LEDs, delivering approximately 35 mW/cm² and 120 mW/cm² at the sample position, respectively (Sørensen P., Risø DTU, pers. comm., 2023). The OSL signal was detected via a bialkali EMI 9235QA photomultiplier tube through a 7.5 mm Hoya U-340 filter. Irradiations were performed using an internal calibrated $^{90}Sr/^{90}Y$ beta source. Details on the measurement facilities can be found in Bøtter-Jensen *et al.* (2003, 2010).

Equivalent dose (D_e) values and luminescence properties were determined using the single-aliquot regenerative-dose (SAR) protocol (Murray & Wintle, 2000, 2003). Unless otherwise specified, a preheat at 180 °C for 10 seconds and a cut heat to 160 °C were applied. Optical stimulation was carried out at 125 °C for 38.5 seconds. The OSL signal was calculated using the initial 0.31 seconds of the decay curve, minus a background derived from the subsequent 0.77 seconds ("early background subtraction"; Cunningham & Wallinga, 2010). To minimize recuperation, each test dose (~4.9 Gy) measurement was followed by a 38.5-second blue-light stimulation at 280 °C (Murray & Wintle, 2003).

To assess potential feldspar contamination, the OSL infrared depletion ratio (Duller, 2003) was calculated for each aliquot. A ratio lower than 0.9 (considering uncertainties) was taken as indicative of feldspar presence.

Gamma spectrometry measurements were conducted using a high-purity germanium (HPGe) detector with an extended energy range. Specific activities were converted into dose rates using conversion factors from Adamiec & Aitken (1998). A beta attenuation factor of 0.90 (±5%) was applied to account for grain size and etching effects (Mejdahl, 1979), and water content correction followed the methodology described in Aitken (1985).

Sampling was conducted in summer 2024 under dry conditions. Consequently, the natural water content (W_n) measured in the laboratory is considered to be lower than the time-averaged water content over the burial period. A range of values of water content is adopted between the upper limit, i.e. the saturation water content (determined in laboratory), and the lower limit, i.e. complete dryness of the sample (rarely less than 5 % for sandy sediments) (Duller, 2008).The

latter is estimated from the saturation water content (W) and the fraction of time at saturation (F). As a first approximation, F is calculated as $F = W_n/W$. If this value exceeds 0.5, it is retained. If it is lower, the value is set to 0.5, based on the assumption that Ardenne soils are saturated for at least half the year, during the rainy and snowy seasons. Uncertainty is derived from the measured saturation content and an assumed minimum water content of 5% (typical for sandy sediments), and is reported as 2σ.

An internal dose rate of 0.013 ± 0.003 Gy/ka for quartz was assumed (Vandenberghe *et al.*, 2008). The contribution of cosmic rays was calculated using the formulae of Prescott & Hutton (1994), with a 15% relative uncertainty assigned to this component.

5. OSL results

5.1. Luminescence characteristics and procedural tests

Representative OSL decay curves are shown in Figure III.10 and illustrate the considerable variability in brightness (i.e. initial signal intensity) that can be observed between different aliquots (an order of magnitude or higher). Such differences likely reflect variations in grain-to-grain sensitivity. It is of interest that the variability can be detected at the multiple-grain level (small and large aliquots), and may indicate that only a limited fraction of all the grains on a disc contribute to the observed OSL-signal. Still, in all instances, the initial OSL intensity is clearly above background and decreases rapidly within the first seconds of stimulation, suggesting dominance of the fast component.

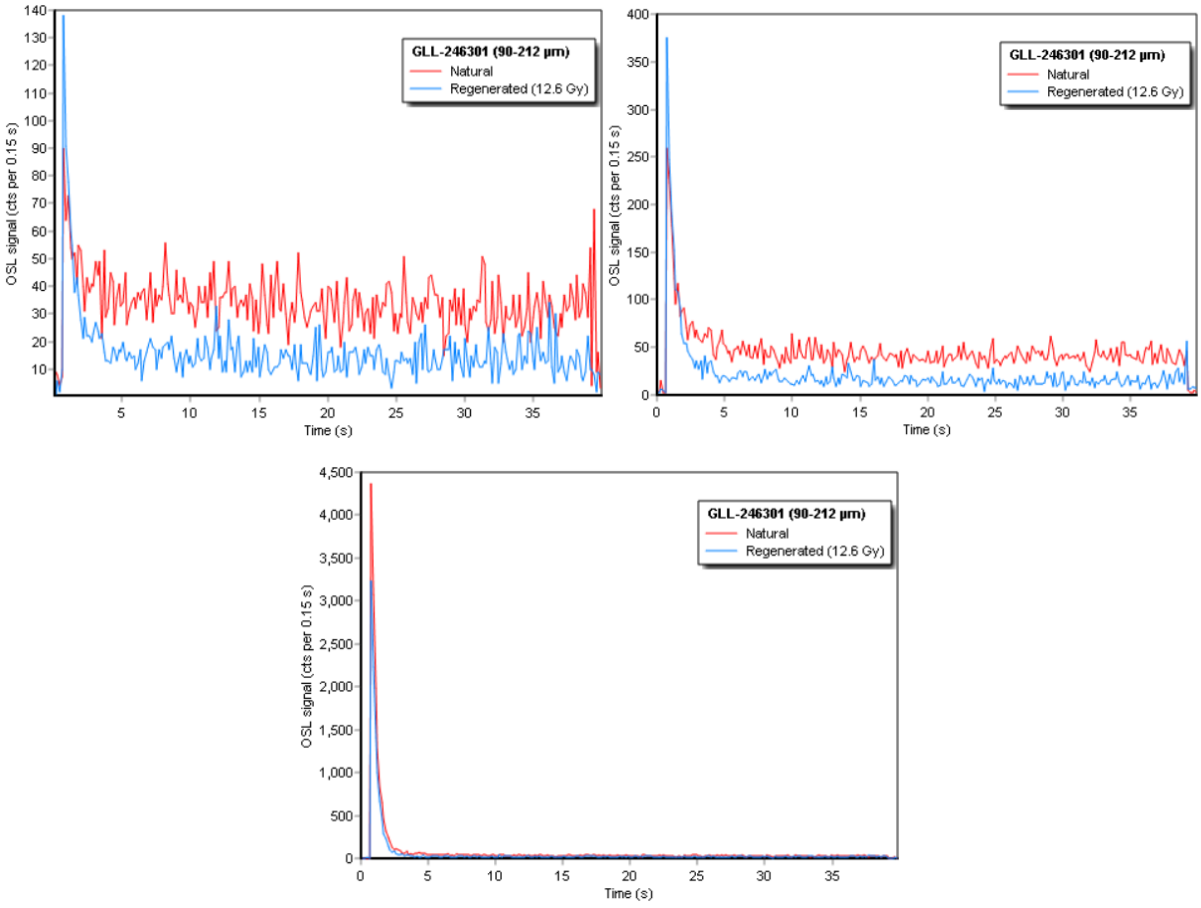

Figure III.10: Illustrative OSL decay curves for three small (2 mm) aliquots of 90-212 µm quartz grains from sample GLL-246301; The signal is clearly distinguishable from the background level and decays rapidly with stimulation time.

Signal composition can be qualitatively examined by normalising decay curves to the initial intensity and comparing them to that observed from calibration quartz on a given measurement device (Figure III.11). As expected, the calibration quartz shows a rapid decay that is characteristic for a signal that is dominated by the fast OSL component. The curves illustrate differences in signal intensity: some are bright, others are comparatively dim. However, all signals rapidly decay to a near-constant background. This behaviour points out that all signals are dominated by a fast component, with weaker curves reflecting lower overall intensity.

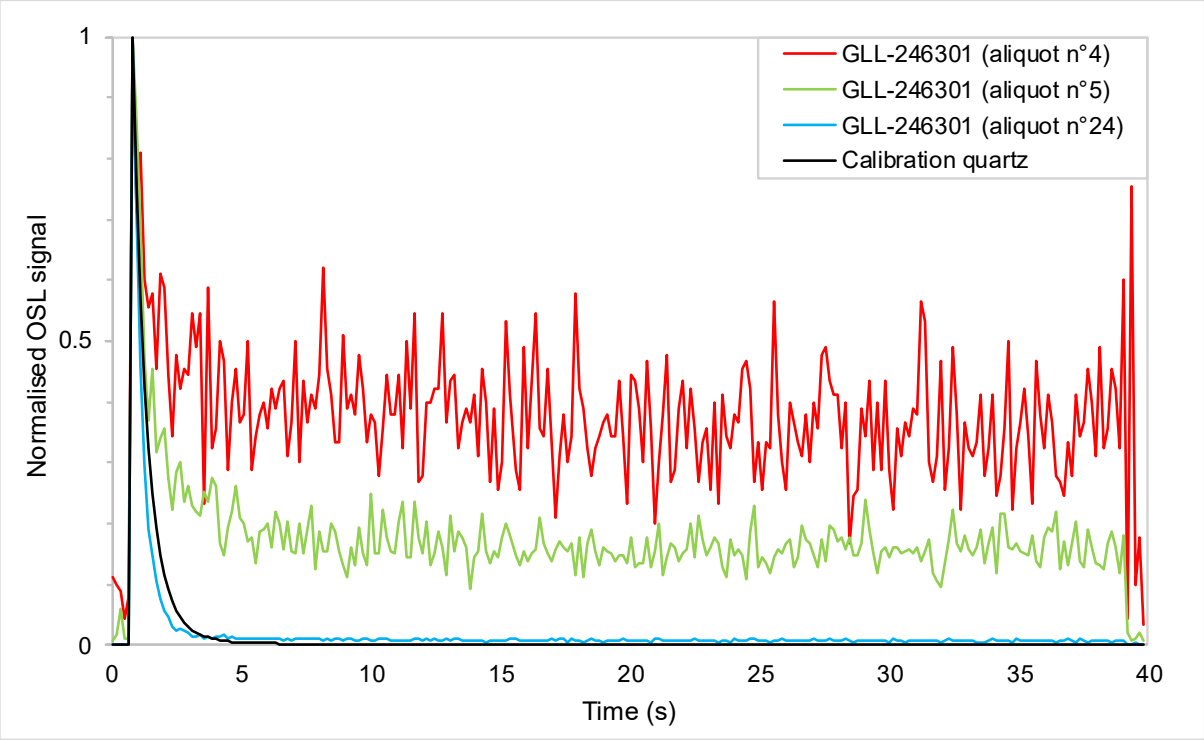

Figure III.11: Comparison of normalised representative OSL signals (GLL-246301) with that of calibration quartz.

Figure III.12 illustrates the dose-response curves of two aliquots from sample GLL-246301. The growth with dose can generally be represented well by a single saturating exponential or a combination of an exponential and linear function. Also here, significant intra-aliquot variability can be observed, with the dose-response curves for some aliquots apparently saturating at significantly higher doses than others. Figure III.12 already indicates that the equivalent dose in different aliquots of a single sample can vary considerably (~27.5 Gy difference between the aliquots in the given example).

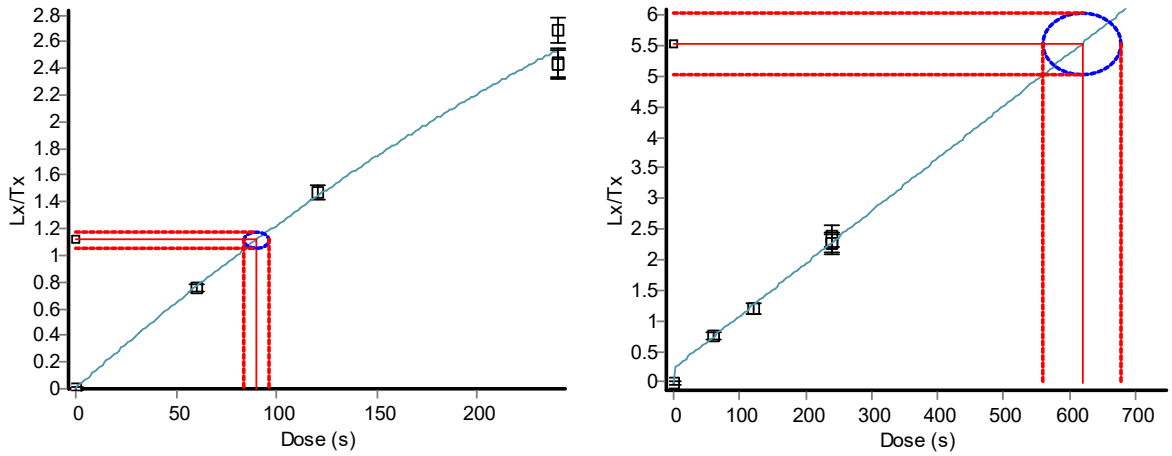

Figure III.12: Representative OSL dose-response curve for two small (2 mm) aliquots of 90-212 µm quartz grains from sample GLL-246301. The beta-source strength at the time of measurement was 0.052674 Gy/s.

To identify the optimum measurement parameters for the SAR laboratory measurement procedure, a series of dose recovery tests was carried out. In a first test, 3 small natural 2mm-aliquots of 4 samples (GLL-246301, -05, -12, and -16) were first exposed twice to the blue diodes for 250 s at room temperature, with a 10.000 s pause in between. They were then given a known laboratory dose chosen to approximate the expected natural dose, and measured using the SAR protocol using a preheat of 10 s at 220 °C and a cut heat to 160 °C. The results are shown in Figure III.13.

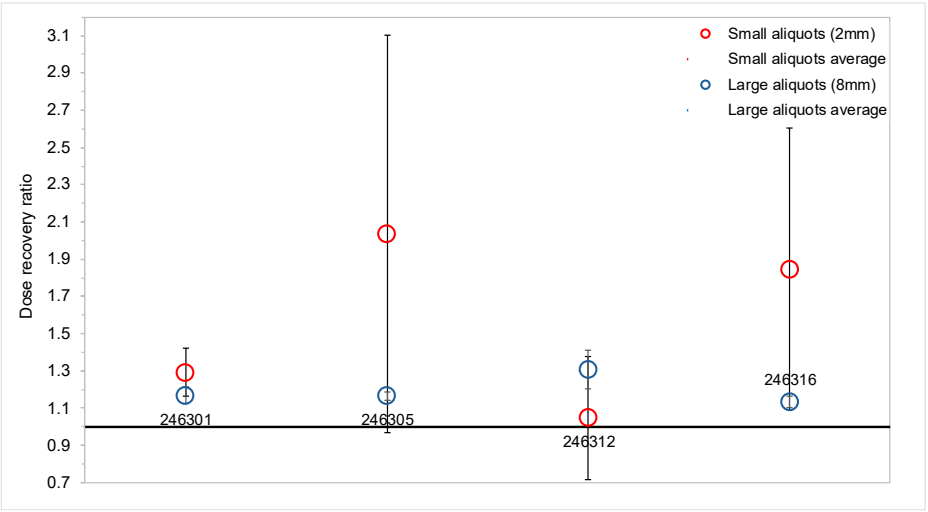

Figure III.13: Average dose recovery ratios (±1 std error) of small (2mm) and large (8mm) aliquots from sample GLL-246301, -05, -12 and -16. The solid horizontal black line (eye guide) marks the ideal value of unity.

The data show a considerable scatter but generally indicate that the measurement procedure overestimates the known dose. Assuming that the samples more or less behave in the same manner, leads to an overall average dose recovery ratio (± 1 standard error; n = 21) of 1.52 ± 0.24. On the other hand, the overall average recycling ratio of 1.06 ± 0.07 is consistent with unity, indicating that sensitivity changes occurring throughout the SAR protocol are adequately corrected for, and recuperation is negligible (3 ± 3 % of the sensitivity-corrected natural OSL signal).

This test was repeated using large, 8 mm diameter aliquots (Figure III.13) in order to improve precision. The overall average dose recovery ratio is 1.19 ± 0.03, which is indeed more precise and confirms that the laboratory measurement procedure significantly overestimates the given

dose. The corresponding overall average recycling ratio is 0.98 ± 0.02, while recuperation is consistent with 0%.

To further investigate this, we examined the dependence of measured dose on the preheat temperature using sample GLL-246316. This was done through a dose recovery test as outlined in the above but, this time, groups of three large aliquots were measured at each of seven preheat temperatures in the range of 160 °C – 280 °C. The results are shown in Figure III.14 (red dots).

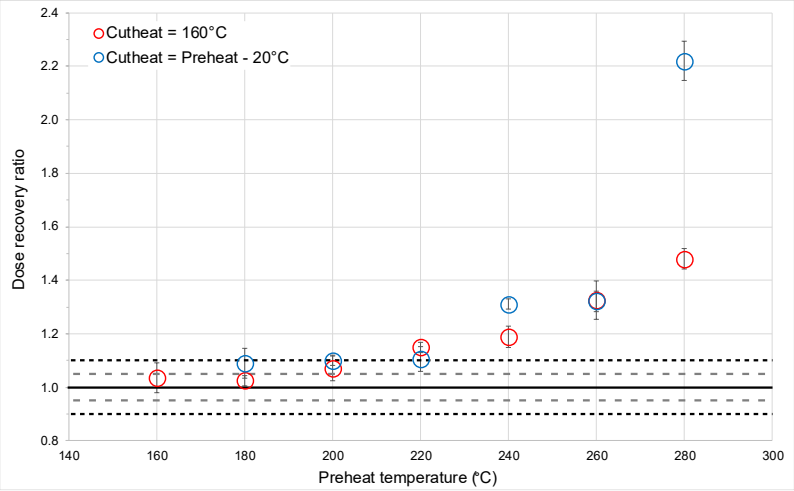

Figure III.14: Average dose recovery ratios (±1 std error) using different preheat and cutheat temperatures on large aliquots from sample GLL-246316. The solid horizontal black line (eye guide) marks the ideal value of unity. The dashed grey and black lines(eye guide) represent 5% and 10% deviation from unity, respectively.

There is a clear tendency for the given dose to be overestimated with increasing preheat temperature; this overestimation becomes significant for preheats higher than 200 °C onwards. At lower preheat temperatures, however, the dose recovery ratio remains close to unity. The recycling ratio shows the opposite trend although (data not shown), within uncertainties, it does not differ by more than 10 % from unity. Recuperation remains well below 1%, regardless of preheat temperature. The dose recovery test was then repeated but this time using a cut heat that tracked the preheat temperature by minus 20 °C (Figure III.14). Higher cut heat temperatures do not seem to improve our ability to accurately measure a known laboratory dose, it even exacerbates overestimation.

Based on these results, a preheat of 10 s at 180 °C and a cut heat to 160 °C was identified as the most appropriate temperature combination. To confirm this, the dose recovery test was repeated using 3 large aliquots of samples -01, -05, -12 and -16. This resulted in an overall dose recovery ratio of 1.05 ± 0.02 (n = 12), indicating a small but systematic overestimation of the known given dose. In view of other complexities (see further) we consider the performance of the chosen SAR protocol satisfactory. As already indicated in the above, using the overall average as an average descriptor implies that all samples behave more or less the same. This is not necessarily the case, and it can be noted that the individual average dose recovery ratios for each sample are, within 1 standard error, not consistent with unity. For instance, the given dose is slightly underestimated for sample GLL-246305, while it is overestimated and to a larger extent for sample GLL-246316.

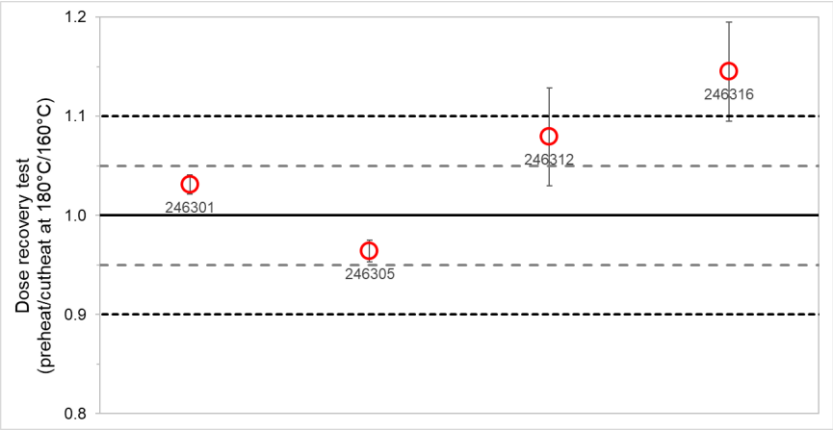

Figure III.15: Dose recovery ratios using 180°C preheat and 160°C cutheat on large aliquots from samples GLL-246301, -05, -12 and -16.

Deviations between average measured and given doses are on the order of 5-10%. The extent to which any apparent inaccuracy in the laboratory measurement procedure is translated to measuring doses equivalent to natural doses remains to be established, however (Guérin *et al*., 2015; Murray *et al*., 2021). Ultimately, the accuracy of OSL ages can only be evaluated through comparisons with independent age information.

5.2. Equivalent dose determination

Following from the above, we adopted of 10s at 180°C and a cut heat to 160°C for equivalent dose (D_e) determination. All analyses were made using small (2mm diameter) aliquots to better detect any incomplete resetting. Quartz grains in the 90-212 µm fraction were analysed for 7 samples (GLL-246301, -03, -04, -06, -09, -12, -15); for samples GLL-246312 and -15, the distribution of D_e in small aliquots of quartz from the 212-250 µm fraction was examined as well. The rationale for including the coarser fraction follows Vandenberghe *et al.* (2007), who investigated the degree of resetting of the quartz OSL signal in different grain size fractions extracted from recent alluvial deposits in the Ardenne region. They concluded that coarser (212-250 µm) quartz grains appear better reset than finer (e.g. 63-90 µm) ones. It should be noted that Vandenberghe *et al.* (2007) examined natural deposits, whereas the present work specifically investigates anthropogenic sediments.

For two selected samples, also dose recovery tests were conducted (see section 5.1) but this time to have an idea on the maximum precision that can be attained using small-aliquot analyses As in this test any spread owing to incomplete resetting or dose rate inhomogeneity is largely – if not completely – removed, it gives an any on the spread that can be observed in ideal conditions. The results are summarised in Figure III.16.

Sample GLL-246306 (90-212 µm) yields central dose (weighted average) recovery ratio of 1.002 ± 0.027, with a dispersion (RSD[6]) of 7.5 %. The ratio very close to unity indicates an excellent agreement with the given dose, associated with a very limited spread, highlighting the effectiveness of the procedure. Sample GLL-246315 (212-250 µm) exhibits a central value of 0.857 ± 0.048, with a dispersion of 18 %, reflecting an underestimation and a wider spread in the recovered doses.

[6] Relative Standard Deviation

These results show that precision is sample-dependent, even in ideal controlled conditions, but also that the performance of the protocol varies between samples as well, which was already indicated by the earlier finds (Figure III.15).

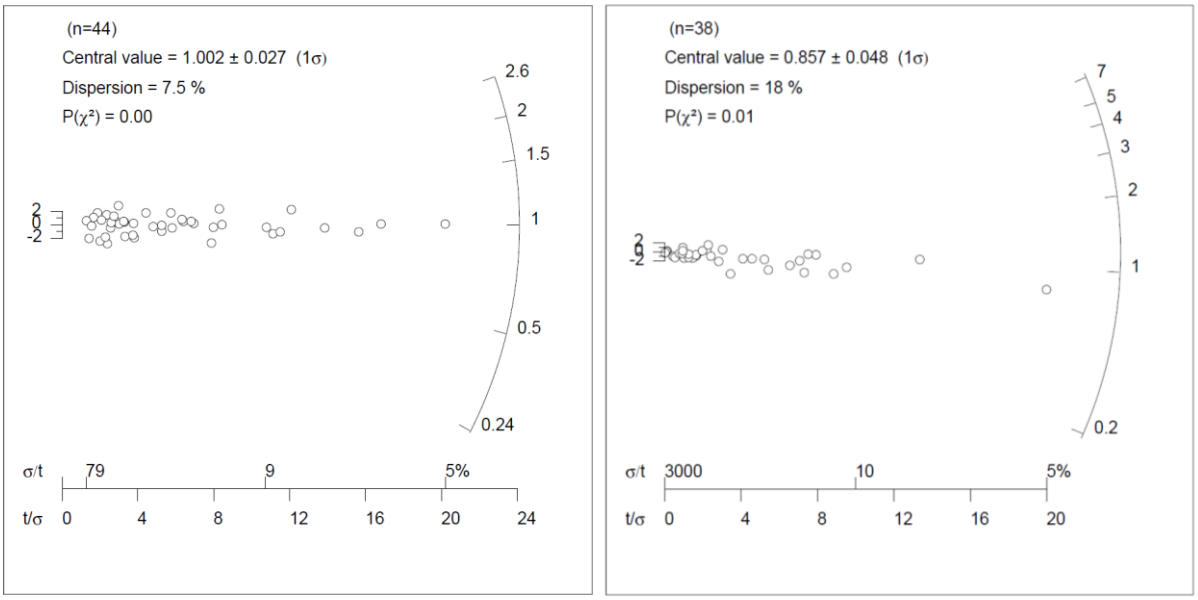

Figure III.16: Dose recovery tests for samples GLL-246306 (90-212 µm, left) and GLL-246315 (212-250 µm, right).

The equivalent dose distributions for the five samples (GLL-246301, -04, -06, -09 and -12), using 90-212 µm grain fraction, are displayed in Figure III.17. Histograms do not take into account the uncertainty by which each individual equivalent dose was determined. Therefore, a plot of uncertainty versus D_e is added on top of the graph. You should also clarify that the median of the uncertainties was used for binning the data (Lepper *et al.*, 2000).

In all samples, D_e values are spread over some dose range and give rise to apparently asymmetric distributions. Some samples, such as GLL-246306, show relatively tight clustering around the mean (RSD = 37%), whereas others, such as GLL-246301 and -12, extend towards higher equivalent doses. In most cases, these high D_e values are associated with larger individual uncertainty estimates. Relative standard deviation (RSD) varies from 37 % (GLL-246306) to 82 % (GLL-246312), highlighting significant differences within each sample, related to intrinsic spread and/or external spread (caused by e.g. incomplete resetting).

These results indicate that all samples consist of a mixture of grains for which the OSL clock has been reset to a different extent, and that at least for some portion of the grains, resetting was incomplete. On the other hand, the asymmetric nature of the D_e-distributions, with a peak towards lower values, can be interpreted as indicative of at least some exposure prior to final deposition and hence to a certain degree of resetting prior to burial. These values are more likely (a phrasing that acknowledges the effect of averaging intrinsic to multi-grain analyses) to reflect the event of interest (gold mining activity). The key challenge is extracting these most likely values from the observed distributions.

Within the timeframe available for this dissertation, equivalent dose values were calculated using an iterative approach, in which aliquots differing by more than 3σ from the unweighted mean are excluded until no further values can be rejected. This is a very first approach that is also in line with one of the main objectives of this study (assessing the potential of OSL-dating for establishing chronologies of gold exploitation in the study region). While we acknowledge

that sophisticated statistical models (minimum age models; MAM) have been developed for dealing with incompletely reset sediments (Galbraith & Roberts, 2012; Chamberlain *et al.*, 2018), they all require knowledge on the spread that can be expected for a well-reset sample with comparable luminescence characteristics. Such knowledge is lacking for the deposits under investigation here. A first way to address this would be to evaluate the relevance of aliquot-specific criteria, based on the recycling ratio, recuperation, test-dose error and/or precision, or even sensitivity variations throughout the SAR cycle. These parameters can help identify aliquots that yield reliable D_e estimates and exclude those affected by incomplete bleaching or measurement instability, thereby reducing overdispersion in the absence of well-defined reference data.

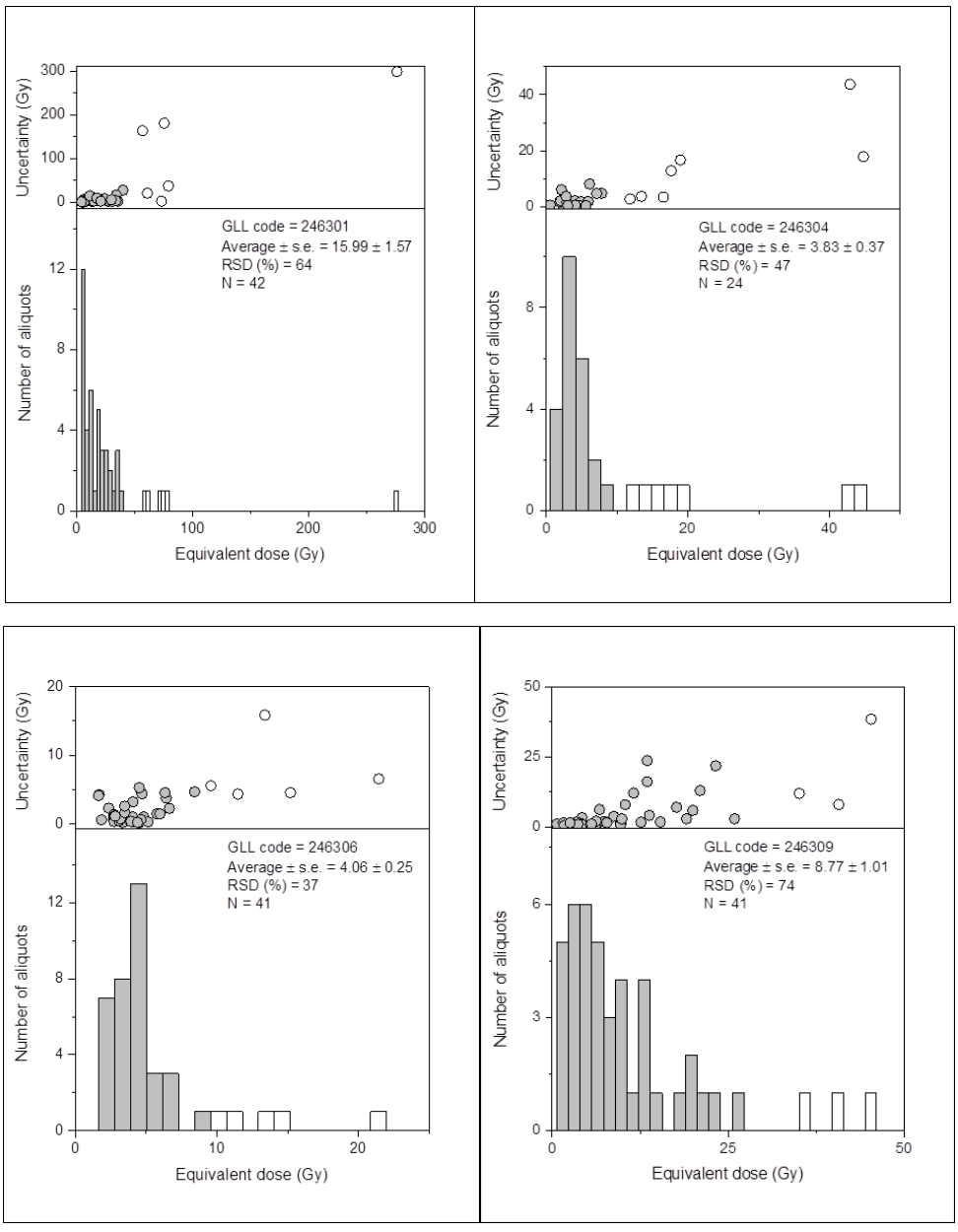

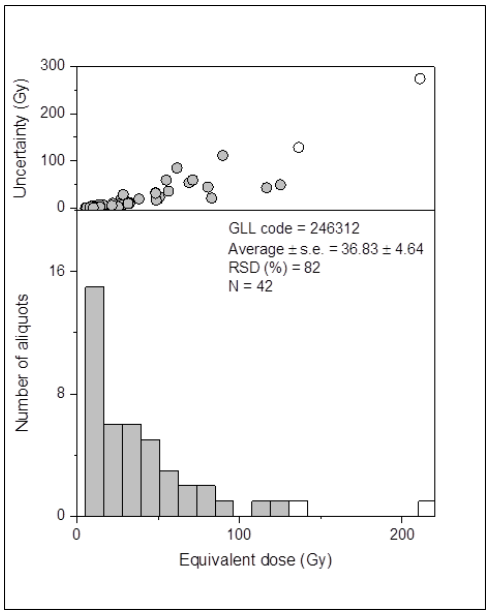

Figure III.17:D_e results obtained using small 2mm aliquots of 90-212 µm quartz grains from sample GLL-246301, -04, -06, -09 and -12. For each sample, 48 aliquots were measured; N is the number that could be accepted.

5.3. OSL ages

First of all, it is important to note that the OSL ages presented in this study are based on simple averages, which, as previously discussed, are inaccurate and systematically overestimate the actual age of gold mining. Uncertainties on the OSL ages were calculated as summarised in Aitken (1985), with systematic sources of uncertainty as in Vandenberghe (2004) and Vandenberghe *et al.* (2004).

Along the Rougerie, OSL ages range from 64 AD to 16,416 BC (Table III.2), covering a time span from the end of the Last Glacial Maximum (~18 ka) to the early 3rd century AD, when uncertainties are taken into account. Ages obtained for the Schinderbach are, on average, older than those from the Rougerie, ranging from 5936 BC to 11,416 BC, with substantial uncertainties exceeding 1,000 years. The smallest uncertainty was recorded for sample GLL-246306, collected from a sandy infill of a paleochannel running parallel to the Rougerie. The stratigraphic context of this sample is described in more detail in Chapter V1.3. Compared to most other samples, which were taken from gold-panning mounds, the grains in this sample were likely transported by the channel, increasing the probability that a greater proportion was exposed to daylight. Sample GLL-246304, also from this sandy accumulation but taken from a lower layer beneath sample -06, yielded a similarly young age, consistent with the probable periods of gold mining. However, based on the full dataset, no definitive conclusions can yet be drawn. Samples taken from mounds tend to show higher uncertainties, likely due to the limited transport distance of grains within the sluice boxes.

These results highlight both the impact of incomplete resetting of quartz grains and the potential of the OSL method to approach the estimated timeframes of gold mining, as illustrated by samples GLL-246304 and -06. As noted above, equivalent dose distributions often show a majority of aliquots with low D_e values, underlining the promise of the technique. Further research, particularly in refining site selection, sampling procedures, and post-measurement data treatment, would likely improve the precision and reliability of the results.

Sample site	Sample code	Grain size	K (%)	^{234}Th ($mg.kg^{-1}$)	^{226}Ra ($mg.kg^{-1}$)	^{210}Pb ($mg.kg^{-1}$)	Time-averaged water content	W_n	Cosmic dose rate ($Gy.ka^{-1}$)	Dose rate ($Gy.ka^{-1}$)	Equivalent dose (Gy)	Age (yr before 2024 AD)	Age (BC-AD)	Situation
Rougerie 1-34	GLL246301	90-212 µm	1.57 ± 0.01	3 ± 0.2	3.33 ± 0.07	1.8 ± 0.2	24.3 ± 0.2	24.3	0.197 ± 0.03	2.3 ± 0.04	15.99 ± 1.57	6950	4926 ±790 BC	Mound
Rougerie 2-2	GLL246303	90-212 µm	1.71 ± 0.01	3.6 ± 0.2	3.4 ± 0.03	2 ± 0.2	16.5 ± 1.4	13.6	0.231 ± 0.04	2.71 ± 0.03	49.98 ± 3.41	18440	16416 ±1660 BC	Mound
Rougerie 3-A42	GLL246304	90-212 µm	1.01 ± 0.01	1.4 ± 0.2	1.8 ± 0.04	0.7 ± 0.2	12.5 ± 0.8	11.8	0.196 ± 0.03	1.53 ± 0.03	3.83 ± 0.37	2510	486 ±290 BC	Paleochannel
Rougerie 3-1	GLL246306	90-212 µm	1.24 ± 0.01	2.4 ± 0.1	2.12 ± 0.07	1.6 ± 0.2	12.5 ± 0.8	11.8	0.202 ± 0.03	2.07 ± 0.04	4.06 ± 0.25	1960	64 ±170 AD	Paleochannel
Rougerie 4-A43	GLL246309	90-212 µm	1.63 ± 0.01	2.1 ± 0.2	2.03 ± 0.02	1.6 ± 0.1	10.1 ± 0.2	6.5	0.236 ± 0.04	2.56 ± 0.03	8.77 ± 1.01	3420	1396 ±440 BC	Mound
Schinderbach 3-A36	GLL246312	90-212 µm	1.76 ± 0.01	2.5 ± 0.2	2.66 ± 0.04	1.7 ± 0.2	14.8 ± 1.2	13.4	0.247 ± 0.04	2.74 ± 0.04	36.83 ± 4.64	13440	11416 ±1870 BC	Mound
Schinderbach 3-A36	GLL246312	212-250 µm	1.76 ± 0.01	2.5 ± 0.2	2.66 ± 0.04	1.7 ± 0.2	14.8 ± 1.2	13.4	0.247 ± 0.04	2.74 ± 0.04	26.03 ± 4.41	9500	7476 ±1700 BC	Mound
Schinderbach 6-A60	GLL246315	90-212 µm	1.3 ± 0.01	2 ± 0.1	2.37 ± 0.03	1.6 ± 0.1	9.8 ± 0.4	9	0.236 ± 0.04	2.49 ± 0.03	25.01 ± 2.6	10050	8026 ±1200 BC	Mound
Schinderbach 6-A60	GLL246315	212-250 µm	1.3 ± 0.01	2 ± 0.1	2.37 ± 0.03	1.6 ± 0.1	9.8 ± 0.4	9	0.236 ± 0.04	2.49 ± 0.03	19.80 ± 2.13	7960	5936 ±980 BC	Mound

Table III.2: Summary of dosimetry and luminescence dating result (2σ uncertainties).

[Tapez ici] [Tapez ici] [Tapez ici]

5.4. Comparison with radiocarbon dating

Regardless of the presumed quality of the OSL results, they must be compared against independent chronological controls, such as radiocarbon dating. In this study, two ^{14}C dates were obtained from the bases of gold-panning mounds: one from the Rougerie, in collaboration with AWaP (Draily *et al*., 2025), and one from the Schinderbach-A. The assumption here is that the dates correspond to the beginning of the mound accumulation. These provide a means of comparing the OSL ages and represent a significant advance in understanding Ardennes gold mining chronology.

The first date (Figure III.18) comes from a charcoal-rich layer[7] at the base of the mound where sample GLL-246303 was collected. The dated charcoal was identified as alder (*Alnus* sp.) and yielded an age of 1754 ± 25 BP (95.4% probability), corresponding to 230–380 cal. AD. This result confirms that gold mining occurred in the Belgian Ardennes during the Late Roman Empire. It is also in excellent agreement with the dates obtained from the Trou des Massotais mine (260–434 cal. AD and 249–440 cal. AD). This discovery offers new insights into human activity in a region long assumed to have been sparsely inhabited during that period. The details of this dating are provided in Draily *et al.* (2025).

The OSL sample corresponding to this ^{14}C-dated level, GLL-246303, was taken only a few centimetres above the charcoal layer (Figure III.8). It yielded the oldest age in the dataset (16,416 ± 1,660 BC), representing a striking difference with the radiocarbon result. This gap is most likely due to incomplete resetting of the luminescence signal. It is also possible that the mound represents an accumulation of sterile debris, with almost no gold, that had not undergone washing and was therefore only minimally exposed to daylight before burial.

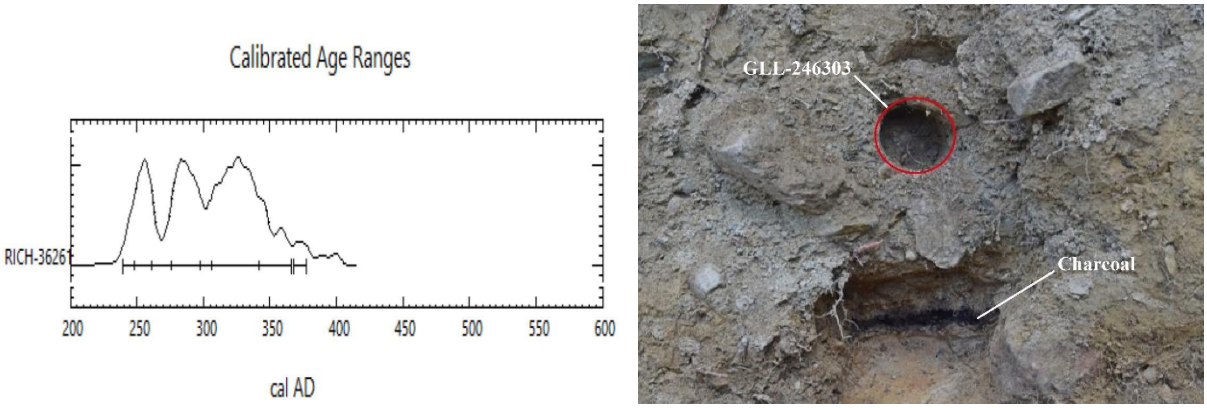

Figure III.18: Radiocarbon dating on a charcoal along the Rougerie (Draily et al., 2025).

The second radiocarbon date (Figure III.19) comes from core site SCHIN 6, taken from the top of one of the largest mounds along the Schinderbach-A. At 2 cm below the base of the mound, at a weighted depth of 148 cm, micro-charcoal fragments were recovered from a silty-clay matrix (Figure III.20). The sample yielded an age of 2100 ± 30 BP, corresponding to 196-41 cal. BC (93.9% probability), indicating that gold mining in this sector occurred either before or at the very beginning of the Roman period. When compared with the Rougerie date, this result highlights the complexity of establishing a definitive chronology for alluvial gold mining in the Ardennes. It suggests two possibilities: either gold mining at the Schinderbach

[7] See Chapter V1.3

pre-dated activity at the Rougerie, or there were multiple phases of exploitation, which seems more likely.

This divergence also underscores the value of OSL dating, which does not depend on finding organic remains or artefacts from the target period, which are only very rarely found in the mounds. Furthermore, OSL directly dates the burial age of the sediment itself (unless in case of incomplete resetting) and requires no assumptions about the relationship between the dated material and the deposit, like it is needed with radiocarbon dating.

The OSL sample corresponding to this radiocarbon date, GLL-246315, was not taken from the same mound but from an adjacent mound of similar size. The ages obtained were 8026 ± 1200 BC for the 90–212 µm fraction and 5936 ± 980 BC for the 212–250 µm fraction. In both sample GLL-246312 and -15, where two grain-size ranges were measured, the coarsest fraction yielded the youngest ages, suggesting better bleaching with the 212-250 µm grains.

As with the Rougerie, these results do not align with the radiocarbon date and would benefit from further post-measurement data processing. However, a very preliminary screening of the brightest aliquots (i.e., those yielding the most precise results) produced ages of ~5 ka and ~2.5 ka for sample GLL-246315, corresponding to the 90–212 µm and 212–250 µm fractions, respectively. Although this remains a superficial approach requiring further investigation, it nevertheless demonstrates the potential to approximate reliable radiocarbon ages.

Although the OSL ages do not align with the radiocarbon results, the ^{14}C dates are considered more reliable and represent a major advance in understanding the chronology. They provide a valuable framework for evaluating the robustness of the OSL ages and confirm the age overestimation suggested by the equivalent dose distributions, thereby helping to refine luminescence interpretations. Moreover, they represent a major advance in their own right, as no gold-panning mound in the Belgian Ardennes had been directly dated prior to this study.

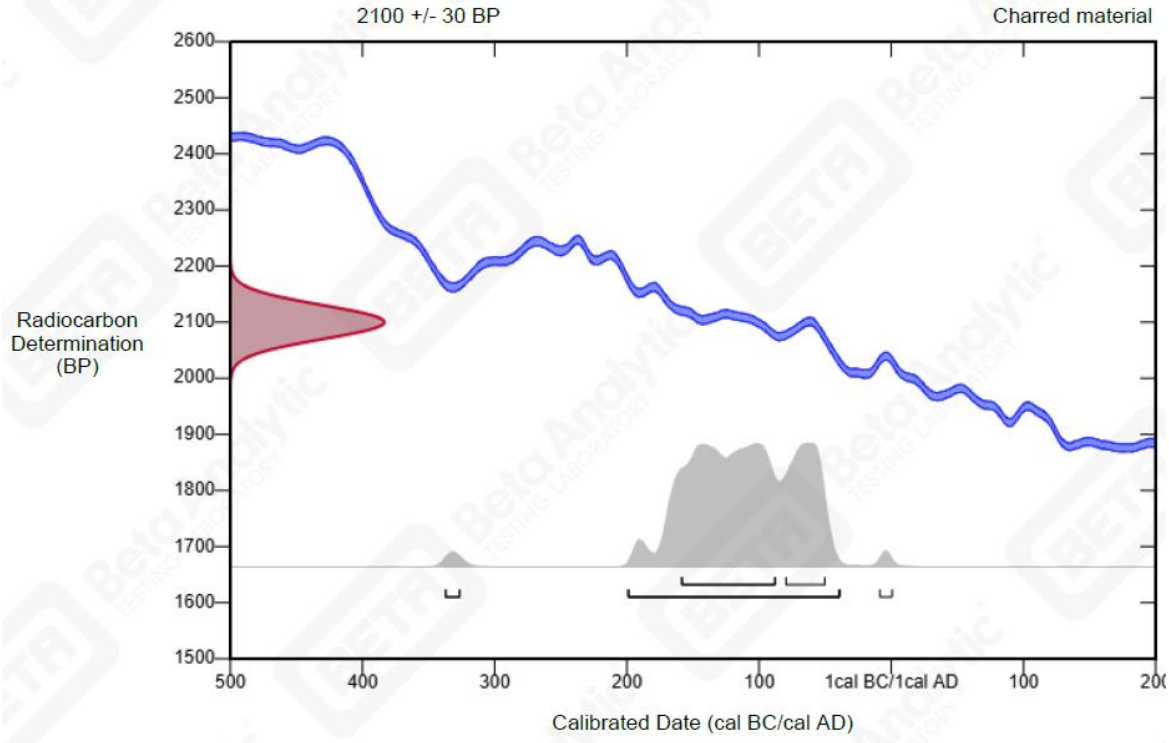

Figure III.19: Radiocarbon dating on a charcoal along the Schinderbach (SCHIN6/148). Calibrated with BetaCal 5.0: High Probability Density Range Method: IntCal20. Detailed age probabilities in Appendix 1.

Figure III.20: Location of the micro-charcoal layer and pictures of the charcoal dated..

Chapter IV : METHODOLOGY

Summary of chapter IV: This chapter describes the methods used to collect and process the data for evaluation of the impact of gold mining on streams.

Reliable result come from a structured and well thought out methodology. Various methods have been applied in the present work, they are presented in this section. Most of the data were acquired on the field and were later processed in laboratory and by using computer software, such as ArcGIS© or Adobe Illustrator©.

1. Profile and stratigraphic section determination

Before any field sampling, the first step is to determine specific sampling sites inside the study areas in order to obtain the most representative data. Following the same logic as for the selection of the study site, initial observations are made on LiDAR imagery (Hillshade, explained below). Then, field observations are required to validate, or not, the pre-selected sampling sites. The final decision depends on the representativeness, the accessibility and, especially the ability of the site to explain the sedimentary dynamics of the study area.

Two features are looked for, the localisation of a transverse profile and a stratigraphic section.

The first mentioned consists in determining a profile, often perpendicular to the valley axis in order to consider the lateral mobility of the river. A topographic survey is proceeded to retrieve the actual morphology. Then, core sampling is made at regular intervals and at morphological changes, such as along a river channel, at the bottom of a paleochannel, or on top of a mound. Thanks to mechanical core samples, the stratigraphic sequence is preserved and analysed in laboratory, where information like the granulometry is retrieved. Finally, a general representation of soil characteristics and of the particular levels is obtained by connecting similar sedimentary levels.

The second feature, stratigraphic sections, is sought to observe the effective soil structure and put in perspective the observations from the corings. In practical terms, the appropriate sites are an eroded riverbank, an abrupt slope, or a natural (or even anthropogenic) trench. The section is cleared of the sediments accumulated vertically in front of the real soil structure. A drawing of the stratigraphic units is afterward made and descriptions of these units are noted in a field notebook. The drawing must be an accurate representation of the section, survey nails (Figure IV.1) are therefore placed to then be measured using a total station. The nails are used as points of reference to improve the precision of the drawing, to determine the exact dimensions of the section, and to create a vertical reference frame. In the present study, two stratigraphic sections are described for the Rougerie study site, one precise and one schematic. However, no representative stratigraphic section was found along the Schinderbach-A, essentially because no trench and no mound eroded by the river was observed.

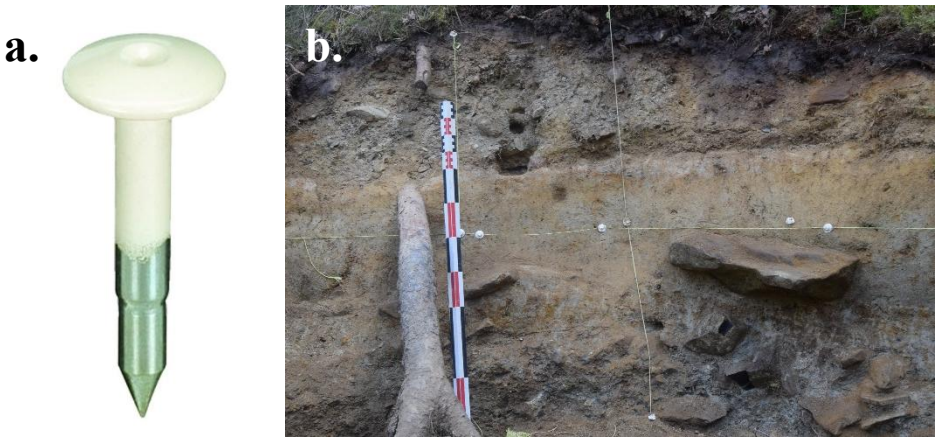

Figure IV.1: (a) Survey nail, and (b) nails on a stratigraphic section (Rougerie, ROUG-A, Chapter V1.3)..

2. Coring and laboratory analyses

2.1. Core sampling

As explained above, core sampling is required to obtain an overall representation of the transverse profile, and subsequently of the valley bottom structure. A decametre is stretched along the defined profile and core samples are taken at regular intervals and at changes in morphology. At the core sampling locations, stakes are driven into the ground, so that they can later be surveyed using a total station. Additionally, stakes are surveyed using a RTK GPS receiver to improve the precision and accuracy of measurement, but also to fix the reference frame of the total station. Therefore, exact locations of the core samples are recorded for eventual future studies.

In this work, a mechanical coring drill was used instead of a traditional auger. It consists of a 1-metre-long metal tube (Figure IV.2c) with a conical, truncated cone-shaped, head at its base. This shape facilitates penetration into the ground while allowing sediments to enter the tube. At the top of the tube, a threaded head is attached featuring a hole that allows the air to be released so that the tube can be driven into the ground. The threaded head is used to screw in either a striking head, for the first metre, or a 1-metre extension rod for subsequent depths. A jackhammer is then placed on the striking head to drive the corer into the ground, as illustrated on Figure IV.2a. A reference mark is engraved on both the metal tube and the extension rods at a 1-meter point, indicating the depth to stop at, when the marker reaches ground level.

To retrieve the sediments sampled, a 50 mm diameter PVC tube is inserted into the metal tube. This tube can be pulled out and replaced with a new empty one for the next metre of coring. The openings are sealed tightly with tape and the tube is set aside. Once the corer is filled, i.e. went down one metre, it is extracted using a motorised hydraulic extractor (Figure IV.2b), as the combined weight of the equipment filled by sediments can be quite heavy. This is especially true in wet deposits, where suction from the surrounding soil can make retrieval difficult. The extractor is operated by one person while another ensures that the core does not fall back into the hole. This process (driving the corer down one metre and then extracting it) is repeated until the jackhammer can no longer drive the corer any deeper. This blocking, called *refusal*, is typically due to very resistant material (e.g., large boulder, coarse layer, (weathered) bedrock). In most cases, the last coring will not reach one metre, it is therefore necessary to measure the remaining distance between the ground surface and the 1-metre mark to determine the penetration depth, also referred to as the *refusal depth*.

Between each core, all components of the corer must be thoroughly cleaned, both to prevent sample contamination and to remove any grease build-up. Grease is applied to prevent component overheating but can become dirty and lose effectiveness if not cleaned and re-applied.

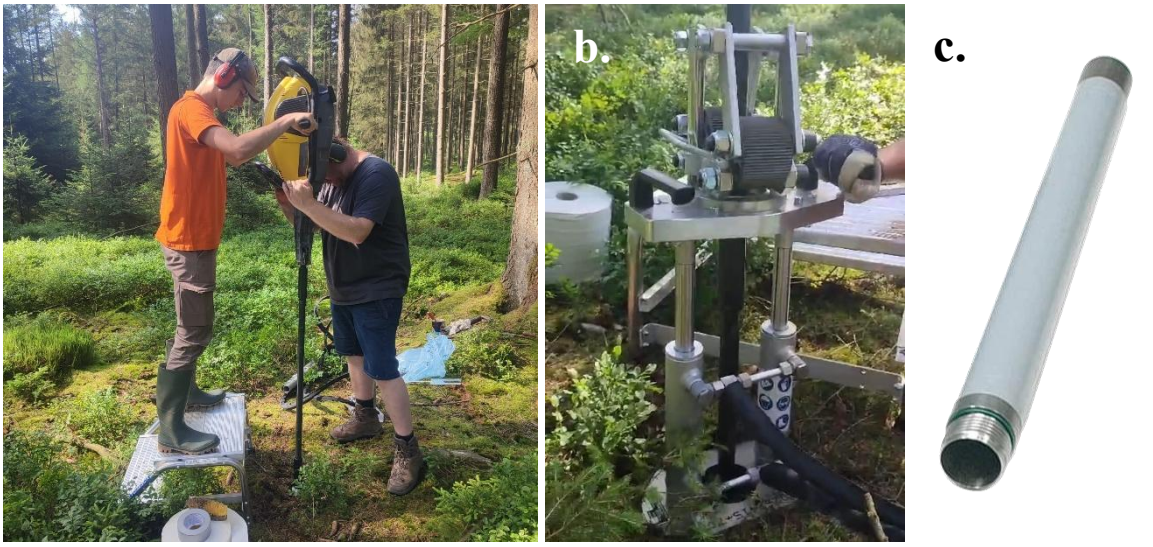

Figure IV.2: Core sampling equipment: (a) jackhammer driving the coring tube into the ground, (b) lifting unit controlled by the hydraulic extractor, (c) coring tube.

The use of a mechanical corer instead of a hand auger presents several advantages. The most significant benefit lies in the ability to collect samples in a closed PVC tube, which helps preserve the stratigraphic sequence with minimal contamination compared to an auger. The use of PVC tubes also facilitates the transport, as samples are hermetically sealed, reducing the risk of mixing or perturbation. Additionally, beyond the fact that driving the core into the ground is easier, the mechanical corer allows penetration through gravel layers by breaking pebbles up to 10 cm in size. This capacity enables the operator to reach significantly greater depths than with an auger.

To ensure proper sample identification in the laboratory, some information must be recorded at the time of sampling. Directly on the cleaned PVC tube, the following details must be written: the distance from the starting point of the profile (as indicated on the decametre), the core sampling site code, the sample depth range, and the sampling date. In addition, field notes should include qualitative observations, such as the ease or difficulty of driving the corer, any sudden impact (indicating a coarse layer), or the aspect of the sediments at the bottom of the core. In some cases, the core is not completely filled because sediments are too loose, causing them to shift aside rather than enter the tube, or because a stone blocked the corer head. In such cases, empty parts are filled with paper towels, and the PVC tube is sometimes cut down when the void is too large.

In total, 43 cores were collected (30 from the Schinderbach and 13 from the Rougerie), distributed across 17 coring sites, including 3 failed attempts due to early refusal likely caused by large boulders. Coordinates of the core sampling sites can be found in Appendix 2.

2.2. Core opening

Back in the laboratory, cores are stored in a freezer (-20 °C) to prevent the growth of fungi due to moisture in the samples. Cores to be opened are placed in a refrigerator (2 °C) one or two days before opening to defrost.

To be opened, the core tube is placed in a prop that holds it fixed (Figure IV.3a), with 25 mm high edges (half the diameter of the PVC tube). The edges of the tube are then cut using an angle grinder placed on the prop edge to obtain two equal halves. A wire is passed across the core and then slid along its entire length to separate the two halves without cutting gravels and pebbles (Figure IV.3b). Each core is therefore divided into two parts, ‘a’ and ‘b’: part ‘a’ is set aside in a freezer as a control sample for potential future analysis, while part ‘b’ is used for the present analysis.

Once opened, an initial description of the core is proceeded, including: a description of the different sedimentary levels based on their texture, grain size and colour, but also the limits and contacts between levels, any particular features (cola, root, peat, coarse pebble), and the colour of the levels according to the Munsell Soil Colour Charts. Because some cores were not completely filled with sediments, but still covered a depth of 1 m, the depth of the contacts are weighted to cover the entire depth of the core. In addition, except for the first cores (0-100 cm deep), a ~10 cm thick layer of contamination is found in every core. When extracting and reinserting the core sampling tube into the ground, a fraction of the sediments from the sides of the hole fall at the bottom and is after sampled. Contamination is distinguished by an odd texture and colour, and by the presence of humus or a mix of different layers (Figure IV.3c).

Detailed descriptions are found in Appendix 4. Stratigraphic logs (Chapter V) are based on these descriptions.

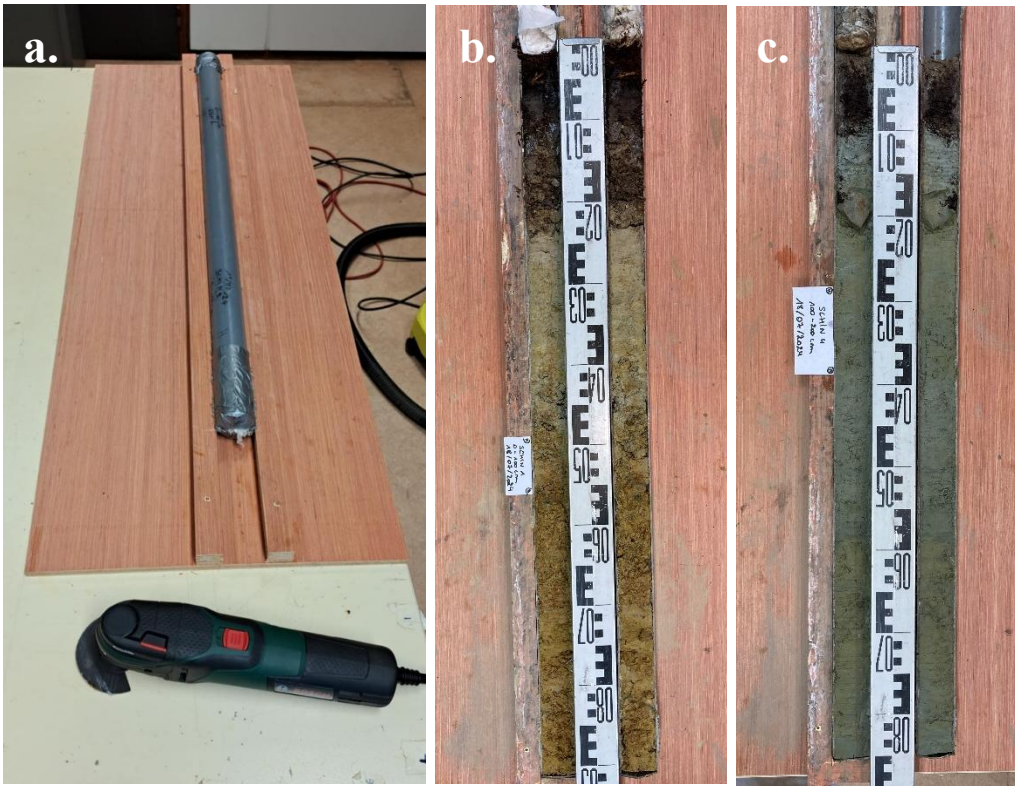

Figure IV.3: (a) Core opening equipment, (b) 0-100 cm deep core opened in two halves, (c) 10 cm thick contamination.

2.3. Granulometry

Granulometry is the analysis of the statistical distribution of grain size particles constituting a sample, commonly expressed as percentage of total weight. Grain size distribution is represented on a logarithmic scale. In concrete terms, the distribution is obtained by sampling each sedimentary layer, wet and dry sieving it, and weighing each grain size class after drying in an oven. Laser granulometry is applied to fraction finer than 212 µm.

The first step is therefore to sample a sedimentary layer. According to the previously mentioned description, sediments of each layer are put in different beakers. In the case of a thick layer (more than 30-40 cm), the latter is divided into subsections to maintain the accuracy of the results. To avoid contamination, sediments within 1 cm on both sides of the layer limits are not sampled.

The second step is the wet sieving. Before sieving, hot water is added to the beakers to break up the aggregates. Sediments are then sieved under running water using a 212 µm sieve, in order to separate the coarse fraction (> 212 µm) from the fine fraction (< 212 µm). A bucket is placed under the sieve to collect the fine fraction. It is then placed in a stable location to let suspended sediments settle. Coarse sediments, i.e. those that do not pass through the sieve, are collected in a beaker and then placed in an oven at 100 °C to be dried. From then on, the fine and coarse fractions undergo different treatments.

Coarse sediments, after being dried, are dry sieved. A sieve column is formed, where sieves of increasing size are stacked to isolate each grain size class. The mesh sizes used range from 212 µm to 26,500 µm, increasing in increments of 0.5 phi ($\sqrt{2}$) (Table IV.1). After sieving, each grain size class is weighed. In the case of pebbles larger than 26.5 mm, their b-axis is measured with a calliper and they are weighed individually. The b-axis corresponds to the maximum width perpendicular to the a-axis, i.e. the maximum length. In most cases, some of the sediments considered coarse are actually smaller than 212 µm. This weight of this fraction is therefore added to the total weight of the fine fraction (< 212 µm). Pictures of the coarse fraction of each sample are taken to evaluate their general characteristics (bluntness and rock type).

Size (PHI)	Size (µm)	Sieve mesh sizes (µm)
-4.75	26,909	26,500
-4.25	19,027	19,000
-3.75	13,454	13,200
-3.25	9514	9500
-2.75	6727	6700
-2.25	4757	4750
-1.75	3364	3350
-1.25	2378	2360
-0.75	1682	1700
-0.25	1189	1180
0.25	841	850
0.75	595	600
1.25	420	425
1.75	297	300
2.25	210	212

Table IV.1: Conversion of mesh sizes (phi - µm).

Fine sediments, on the other hand, are left to settle in a bucket. The water overlying is partially siphoned off until only a 2-3 cm layer remains above the settled sediments. There, they are resuspended and a portion is collected using a small container. This portion will be used for laser granulometry. The rest of the sediments are left to settle again and the water is then siphoned off again. Fine fraction is transferred to beakers to be dried in the oven at 100 °C. Once dry, it is weighed.

Laser granulometry (Figure IV.4: (a) Mastersizer 3000, (b) Laser granulometry principle (©Malvern Panalytical).) rely on Mie theory of light scattering to determine the grain size distribution. Based on the optical properties of both the sample and the dispersant, the device measures the angular variation in light intensity of a laser beam scattered by the sample particles. The size of the interfering particles thus determined is based on the fact that large particles scatter light at smaller angles than small particles. The method does not retrieve the effective size of the particles, but rather the diameter of a volume equivalent sphere. Fraunhofer approximation is applied to grain larger than 50 µm. The device used in the present work is a Mastersizer 3000, measuring grain size between 0.01 µm and 3500 µm (Malvern Panalytical, 2025). The samples are measured using the wet method and the dispersant used is water, with a 10 to 20 % obscuration rate. For each sample, three measurements are proceeded and the average of the two last is used because they are considered as the most reliable. Less than 2 g of sample is required for laser granulometry, thus the rest of the sample is brought back to the laboratory to be dried, weighed, and included in the fine fraction.

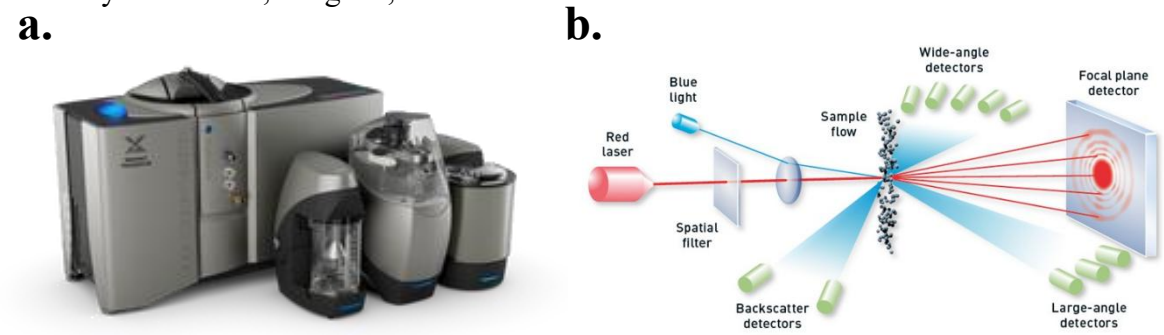

Figure IV.4: (a) Mastersizer 3000, (b) Laser granulometry principle (©Malvern Panalytical).

Finally, the results of the laser granulometry are converted into weight, knowing the percentage by volume of each class and the total weight of the fine fraction. The complete grain size distribution is obtained by gathering these data with those from dry sieving.

2.4. Gold panning

Once that all the analyses are completed, the samples from the same coring site are grouped according to the similarity of their grain size distribution, provided they come from contiguous depths. They are then panned to determine any richer level, or even detect unexploited gold-bearing levels. It is important to bear in mind that the absence of gold is not indicative, given the small amount of sediment sampled. Conversely, the presence of gold is indicative.

Gold panning is carried out using the methods explained in Chapter I3.2, using an American pan and a batea.

3. Topography

Topographic data were obtained with three complementary methods. Longitudinal profile and morphologies determination are based on LiDAR technology (DEM, available on the Walloon geoportal; SPW, 2025a). The transverse profiles and the reference points for the stratigraphic sections require more precise measurements, which are taken using a total station. Core sampling sites and control points are relocated in a coordinated reference system using RTK GPS measurements.

3.1. LiDAR – Light Detection And Ranging

LiDAR (Light Detection And Ranging) is a method used in remote sensing to measures distances. Its principle is similar to the radar (radio detection and ranging), with the difference that an infrared laser beam is used instead of radio waves. From an aircraft, a laser pulse is sent by a transmitter, which then captures the signal reflected by the ground surface (soil, vegetation, buildings, etc.) (Dong & Chen, 2017). Based on the speed of light c and the time t elapsed between the transmission and reception of the signal, the distance d between the aircraft and the ground surface is obtained using the formula : $d = \frac{c*t}{2}$.

The signal reflected back to the aircraft is used to create a 3D point cloud, with each point associated with local X, Y and Z coordinates (). These points are then georeferenced based on the precise position and orientation of the aircraft at the moment the signal is transmitted and received. To achieve this, the aircraft is equipped with a GPS system, which is corrected in real time using the WALCORS network of GNSS reference stations in Wallonia. The georeferenced 3D point cloud is finally interpolated to produce a continuous cover (SPW, 2024).

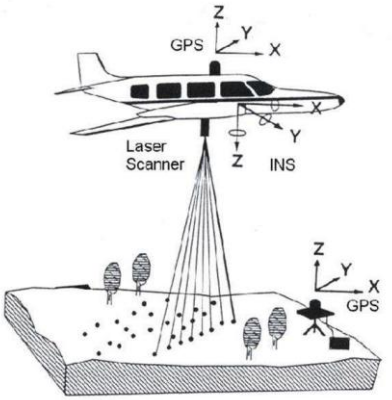

Figure IV.5: Principle of airborne LiDAR (SPW, 2024).

In case of a 'multi-layer' surface, with for instance vegetation cover and soil surface, multiple response signals are captured by the receiver from the same unique transmitted signal. After pre-treatment, this property is used to generate both a digital surface model (DSM) and a digital elevation model (DEM). The first is a representation of the earth surface, including all objects overlying (vegetation, buildings, etc.), whereas the second represents the bare ground surface without any object (Dong & Chen, 2017).

Up to now, two LiDAR coverage maps of the Wallon region are available on the geoportal (SPW, 2025a), one from 2013-2014 winter and the other from 2021-2022 winter, with a third in preparation. The most recent is the most accurate, with 7 pulse/m² in 2021-2022 against 1.5 pulse/m² in 2013-2014. The resulting DTM has a planimetric precision of 0.5 m and an

altimetric precision of 0.12 m on average. The coordinate reference system is the Belgian Lambert 08 (EPSG: 3812) (SPW, 2024).

3.2. Total station

Transverse profile topography requires high precision measurements, ensured by a total station (Leica TC600©). This device is an electronic surveying instrument that combines a theodolite for horizontal and vertical angles measurements and a distance measuring device. It is combined with a rod topped with a reflective prism that allows to observe the points of the profile.

The method used to retrieve the coordinates of the points is free stationing, also known as *resection*. The total station is set on an unknown point, where all the points to be measured are visible. The vertical and horizontal alignment of the station must be checked. This step is performed first using spherical spirit levels and then using precise electronic levels integrated into the station.

Once the device is correctly installed, a minimum of three points with known coordinates (using RTK GPS, for example) are recorded. These, also called *control points*, will serve as a basis for subsequently placing the measured points in a coordinate reference system. Then, points along the profile can be aimed at with the total station. Following the same principle as LiDAR, the station emits a laser signal towards the prism and measures the times elapsed between the emission and reception of the signal to retrieve the distance. It is then combined with horizontal and vertical angles to determine the local coordinates of the point. Based on the control points, an Helmert transformation is applied to calculate the coordinates in Lambert 08.

To determine the most representative profile, points are surveyed at regular intervals and around particular features, such as riverbanks, slope breaks or core sampling sites. During the survey, it is essential to record the height of the prism and clearly identify each particular feature using their measurement IDs. This ensures accurate calculations and facilitates the interpretation of the profile.

3.3. RTK GPS – Real Time Kinematic

Real Time Kinematic (RTK) is a technique applied in high precision positioning. It uses phase measurements of carrier waves emitted by GNSS[8] satellites, especially GPS. The technique relies on network of base stations, whose precise location are known, that transmit real-time corrections and allow for centimetre-level accuracy. Generally, the accuracy is degraded by 1 cm for every 10 km from the reference station. RTK receivers provide X, Y and Z coordinates in less than a minute. Two GNSS station networks are available in Wallonia, the French open source Centipede network, and WalCORS (Wallonia Continuously Operating Reference System). The closest base station to the study sites is in both cases the Saint-Vith station (VITH) (CentipedeRTK, 2025; SPW, 2025b).

4. Gold mining morphologies

To differentiate between different types of gold mining morphologies, a typology has been defined based on Belgian and French literature on the subject (Godfroid, 1980; Baudoux, 2018; Trément, 2023b, 2025). It is presented in Table V.1. In practical terms, morphologies are

[8] Global Navigation Satellite System

identified through two different visualisation methods: the hillshade view and the relative elevation map of the valley (Figure IV.6).

The hillshade view is a slope shading view of the 2021-2022 DTM. This view highlights the relief using a shading effect obtained by simulating a light source equivalent to the Sun, which illuminates each pixel differently. The parameters used for the light source are: 30° azimuth and 30° elevation.

The relative elevation map is a visualisation that allows to represent landscapes surrounding rivers. It is obtained by removing the longitudinal slope of the valley. To this end, the following steps are carried out in ArcGIS Pro:

1. Calculate the local minimum elevation using a 3 m x 3 m moving window: Using the *FocalMin* function of the *Focal Statistics* tool (Spatial Analyst), a raster layer is generated in which each pixel takes the value of the minimum elevation observed in the 3 m x 3 m window centred on that pixel.

2. Create points spaced 5 m apart along the river axis: The *Create Point Features Along a Line* tool (Create Features) is used to perform this operation by determining the desired distance between each point (here 5 m).

3. Extract the local minimum elevation values at these points: The minimum elevation values obtained in step 1 are assigned to the points obtained in step 2 using the *Extract values to points* tool (Spatial Analyst).

4. Filtering the extracted values of the longitudinal profile: Erratic points due to bridges, residual vegetation after DTM generation, etc. are identified and removed. To do this, the longitudinal profile is generated from the points obtained in step 3 using the *Create Graph* tool (Layer Attribute Table) and the erratic points are identified visually.

5. Interpolation of the filtered points using the IDW (Inverse Distance Weighting) method: The *IDW* tool (3D Analyst) requires the following inputs:

    - Processing extent: Same as the original LiDAR layer
    - Cell size: Same as the original LiDAR layer
    - Search Radius Distance: 100 m. This is the distance on either side of the watercourse axis where the analyses are performed. Too large a value would cause excessive altitude differences and 'mask' local variations in relative altitude.

6. Subtracting the original LiDAR using the interpolation obtained: This operation is performed using the *Raster Calculator* tool (Spatial Analyst) and the formula:

$$Original\ LiDAR\ layer\ -\ IDW\ layer\ (step\ 5)$$

7. Modifying the legend to highlight the morphologies: using the layer's symbology parameters

Figure IV.6 illustrates the interest of using both hillshade and relative elevation maps in the identification of the morphologies. The hillshade view provides a visual representation of topographic relief and surface variation, whereas the relative elevation view facilitates altitude comparisons and helps define the limits of the landforms.

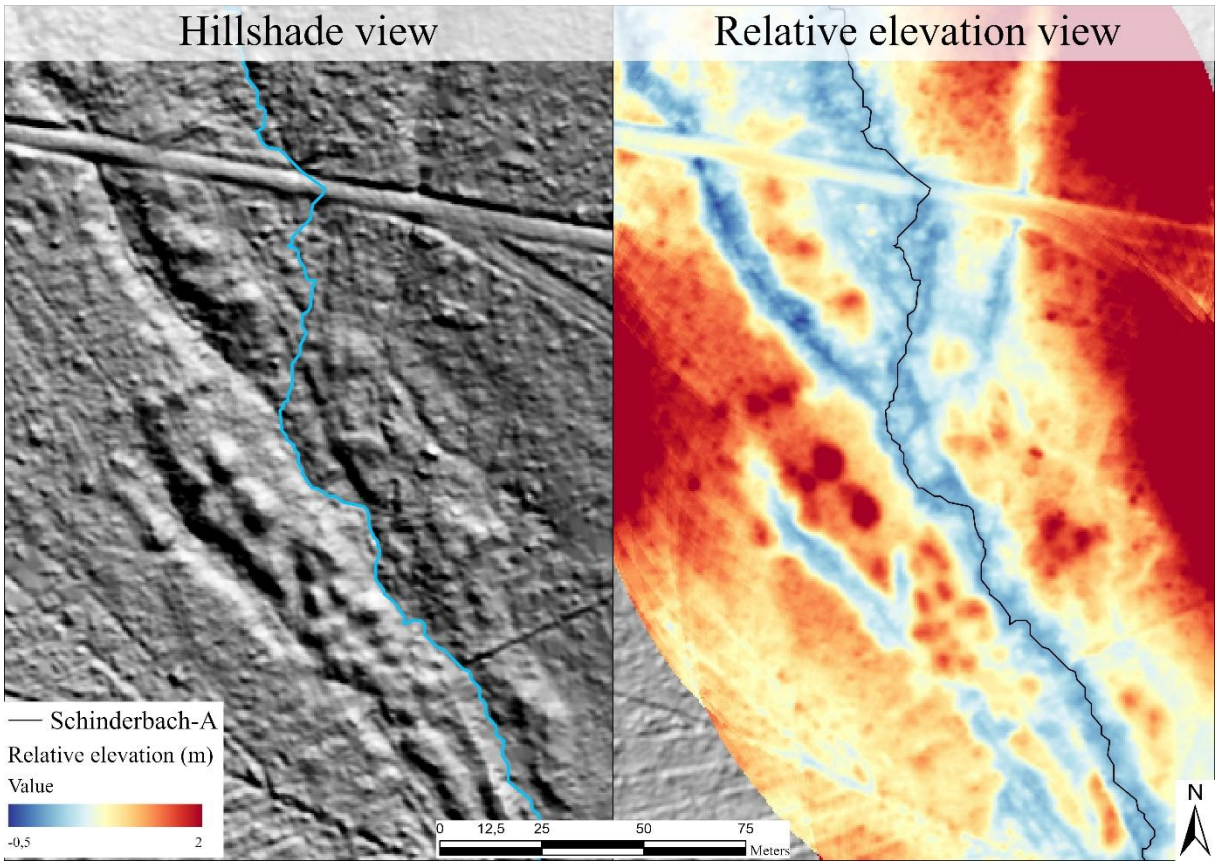

Figure IV.6: Comparison between hillshade and relative elevation views.

Chapter V:
IMPACTS OF GOLD MINING

Summary of chapter V: This chapter assesses the impacts of gold mining on valley bottoms. A typology of the gold mining remains is first presented. Then, both study sites (Rougerie and Schinderbach-A) are analysed through grain-size analyses, mapping of the morphologies, and stratigraphic sections studies.

1. Typology of gold mining remains

The typology of gold mining morphologies (Table V.1) is adapted from the classification proposed by Godfroid (1980), which originally included only three types of features: mounds, excavations, and channels. In the present study, these three main categories are expanded into subcategories to better reflect the full range of alluvial gold mining forms. Godfroid's subcategories for excavations (deep and shallow) are not retained here, as the 0.3 m depth threshold lacks sufficient relevance to reliably distinguish anthropogenic excavations from natural topographic variations. Two additional categories are introduced to address omissions in the original typology: mining fronts (Class D) and perturbed areas (Class E).

It should also be noted that the construction of any typological system inevitably requires the imposition of categorical boundaries, even though the features being analysed, such as gold mining forms, often exist along a morphological continuum without distinct breaks. Consequently, closely related forms may be placed into separate categories, not due to substantive differences, but as a result of the classification thresholds inherent to the typological approach.

Code	Morphology	Definition
A	**Mound**	
A1	Narrow mound	Mound rising less than 1 meter above the surrounding ground surface.
A2 & A3	Thick mound : isolated (A2) or coalescent (A3)	Mound rising more than 1 meter above the surrounding surface. It may appear as an isolated feature (A2) or merged with adjacent mounds (A3).
B	**Excavation**	
B1	Excavation *sensu stricto*	Shallow and small-scale excavation with limited spatial extent.
B2	Water tank	Deep excavation of moderate extent, often with rectangular edges.
B3	Open-cast gold mine	Large and deep excavation (*aurière* in French), covering a substantial surface area.
C	**Channel**	
C1	Paleochannel	Elongated depression aligned with the valley axis, representing a former river course.
C2	Drain	Straight, elongated depression oriented across the valley axis, often perpendicular to the current river channel

C3	Trench	Broad depression, several to tens of meters wide, located in the valley floor. The present-day stream flows within it, and it is bordered by mounds.
D	**Mining front**	Slope break located several tens of meters from the valley bottom, running parallel to the watercourse.
E	**Perturbed area**	Area where gold mining-related landforms are present but have been levelled or significantly altered.

Table V.1: Typology of gold mining morphologies

A. Mound

According to Godfroid (1980), mounds are tailings resulting from gold exploitation and extraction. They can be isolated from each other or coalescent and their dimensions are highly variable. They are classified by their elevation: *narrow mounds* (A1) rise less than one meter above the average surrounding ground level, making them difficult to distinguish in the field but clearly visible in LiDAR imagery. In contrast, *thick mounds* (A2 and A3) rise more than one meter and are considered *isolated* (A2) if their perimeter is clearly defined, or *coalescent* (A3) if they intersect with adjacent mounds.

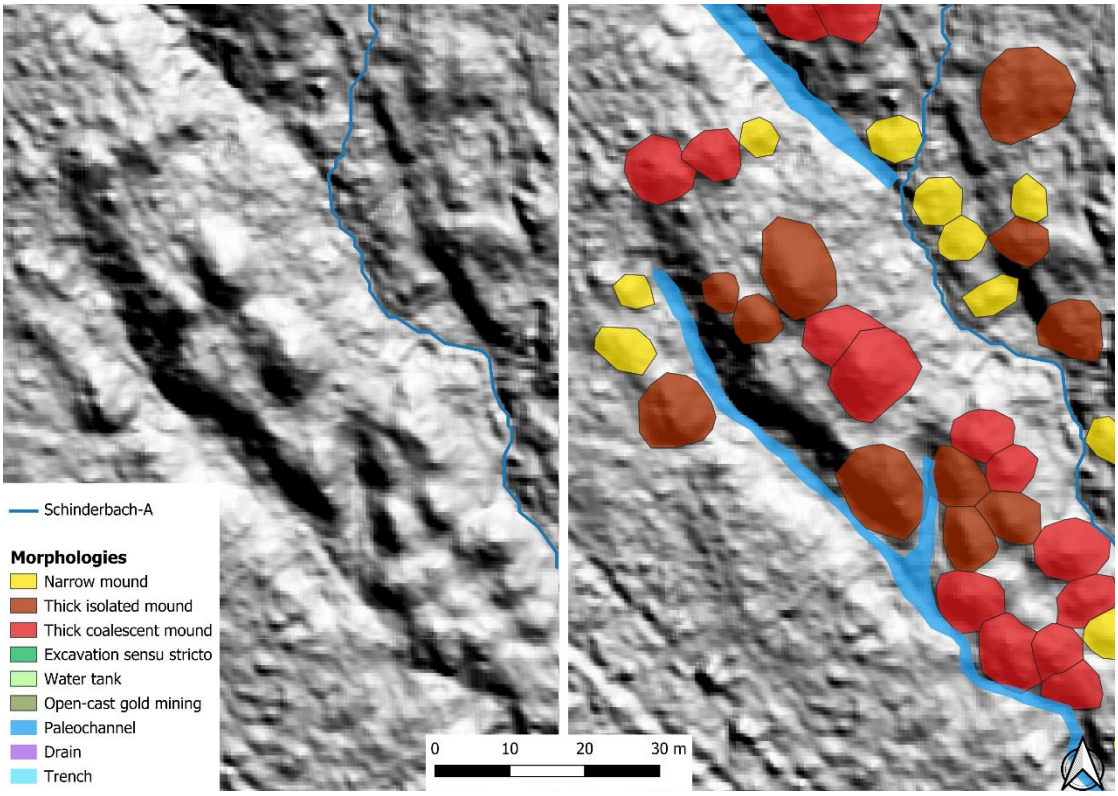

Figure V.1: Examples of mounds along the Schinderbach-A.

B. Excavation

Godfroid (1980) describes excavations as depressions with varied sizes and shapes. An *excavation sensu stricto* (B1) is a small, shallow depression often located on a mound, typically associated with gravel extraction. *Water tanks* (B2) are deeper excavations with moderate surface area, often rectangular. It was historically used to store water for washing operations or as a settling tank. These are typically found across watercourses or paleochannels. *Open-cast gold mines* (B3), referred to as *aurières* in French, are large-scale, deep excavations often

containing internal micro-topography similar to that of mounds and generally located farther from the river than other features.

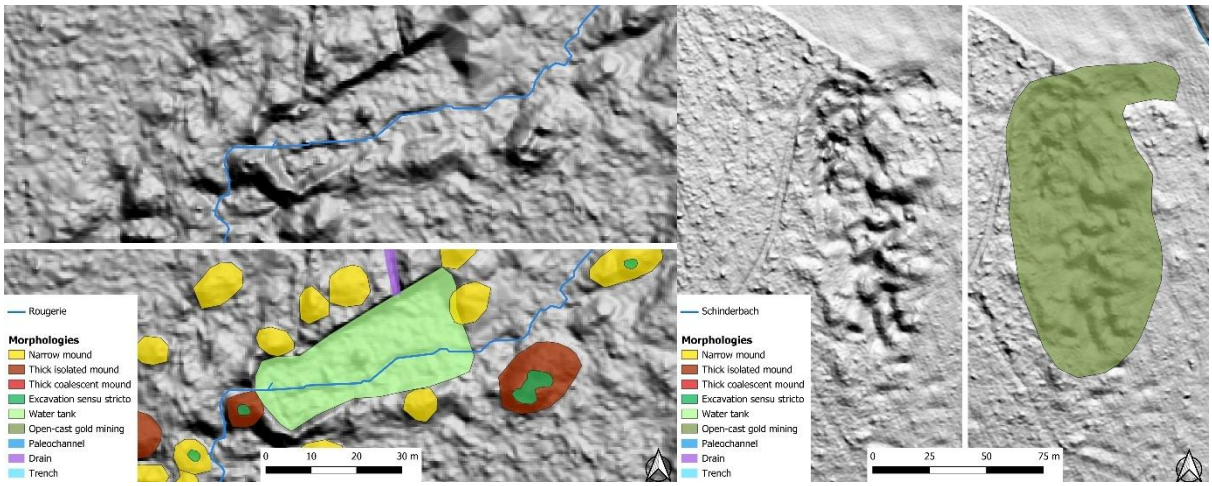

Figure V.2: Examples of B1 and B2 excavations along the Rougerie (left) and B3 along the Schinderbach (right).

C. Channel

Channels are elongated depressions with a length-to-width ratio greater than five (Godfroid, 1980). Depending on their orientation and location, three subtypes are identified:

- *Paleochannels* (C1) run parallel to the valley axis and represent ancient river course, either natural or anthropogenically modified.
- *Drains* (C2) are straight, narrow features cut perpendicular to the valley axis, often created to drain forested or agricultural land.
- *Trenches* (C3) are wide depressions, several to tens of meters wide, located centrally within the valley and currently containing the stream. They are typically bordered by mounds.

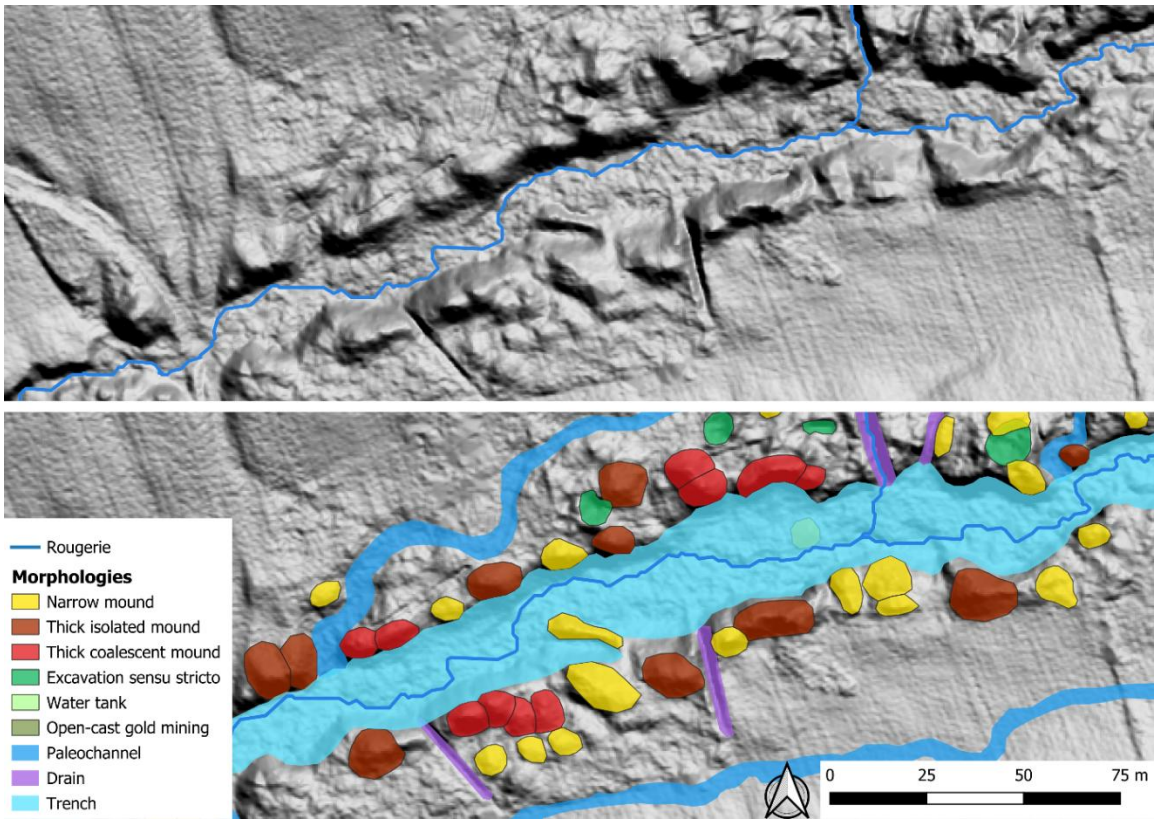

Figure V.3: Examples of channels along the Rougerie.

D. Mining front

Mining fronts (D) are slope breaks located several tens of meters away from the valley center, aligned parallel to the stream. They represent the upper limit of sediment extraction, probably not destined for gold panning but rather for river divertion.

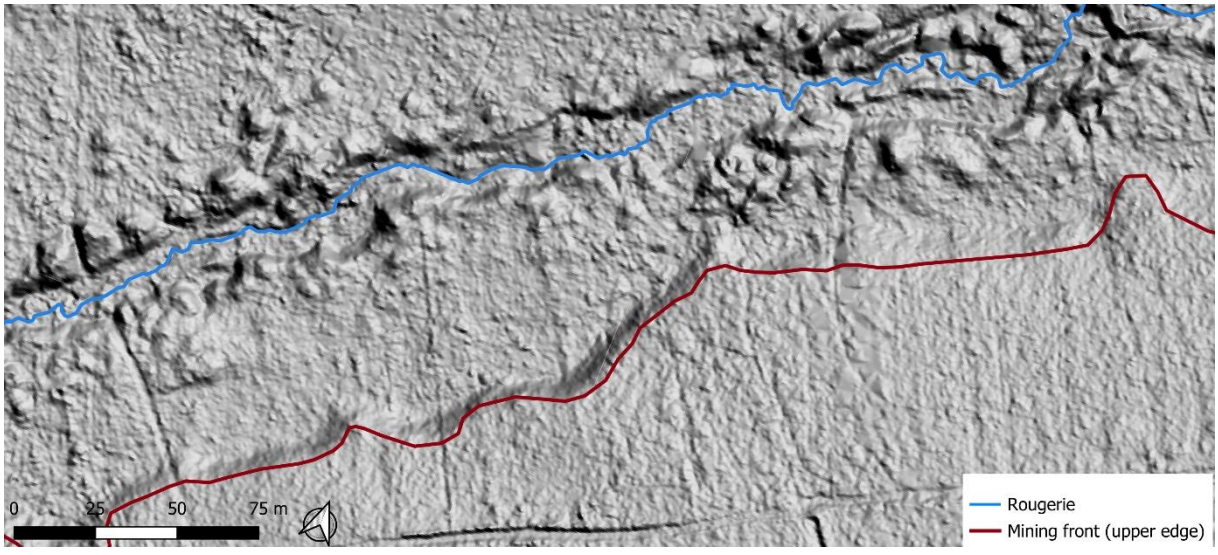

Figure V.4: Example of mining front along the Rougerie.

E. Perturbed area

Perturbed areas (E) are locations where mining-related morphologies have been flattened or modified due to agricultural or forestry activities. These forms are difficult to identify and to

delimit due to heavy disturbance. For example, remains of trenches, paleochannels, and mounds are perceived on Figure V.5 but they are heavily smoothed or altered.

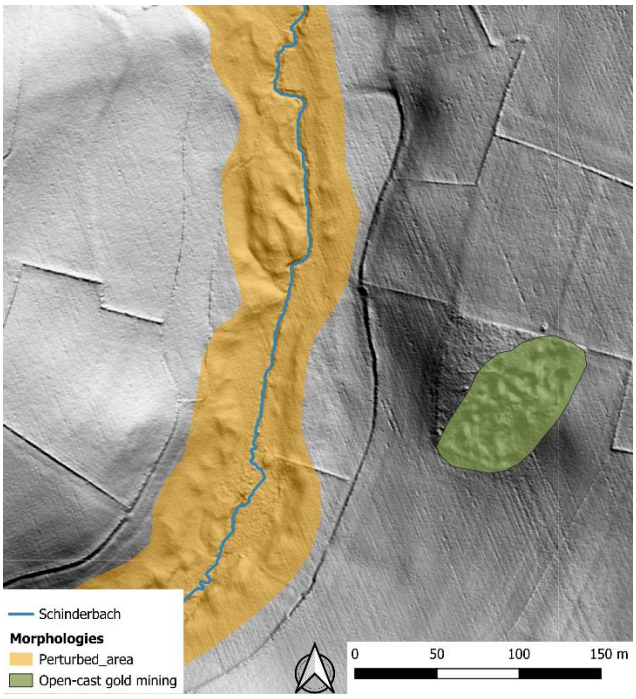

Figure V.5: Example of perturbed area along the Schinderbach.

2. Rougerie stream near Bèche (Vielsalm)

1.1. Topographic profiles and particle-size analysis

Coring operations conducted along a topographic profile using a total station (Figure V.6) allow for the correlation of sedimentary layers observed during laboratory core analyses (Figure V.7). From left to right across the valley, the profile includes core ROUG 5, the Rougerie stream, followed by cores ROUG 2, ROUG 1, ROUG 3, and ROUG 4. Each core was taken within the alluvial floodplain and is analysed individually in this order. The second topographic profile (ROUG-A to ROUG-B) follows approximately the same alignment as the profile RGR-2 from Baudoux (2018). It serves as a to correlate stratigraphic levels observed in the two sections with the sediment cores. Further details are provided in Baudoux (2018).

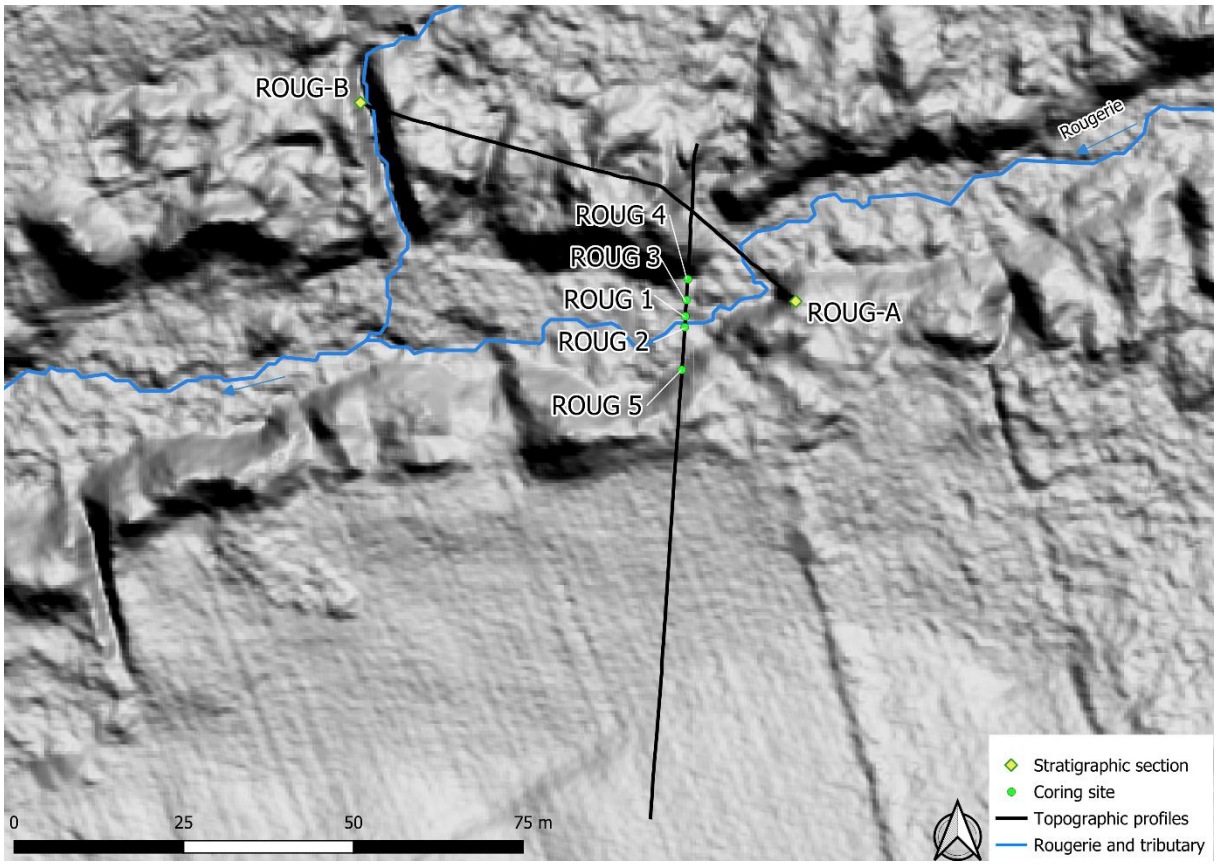

Figure V.6: Localisation of the topographic profiles and sampling sites of the Rougerie.

In general, the cores extracted from the right bank exhibit similar properties. They are composed of dark brown sediments with a silty-sandy matrix containing scattered gravel. Two specific stratigraphic levels are identified at comparable altitudes across several cores. The first, found at approximately 1 m depth in cores ROUG 1, 2, and 3, is characterized by centimetre-sized gravels within a matrix-poor layer. Beneath this layer lies a distinct layer of highly moist silty clay, with dispersed gravels and organic fragments. In core ROUG 3, this layer resembles peat.

The second distinctive level, found in all right-bank cores about 1.5 m deep, is another gravel layer with more smoothed gravels up to 2–3 cm in B-axis. It contains finer matrix than the upper gravel layer and varies in colour from dark olive (Munsell 5Y 4/3) to grayish olive (Munsell 5Y 5/3). It overlies a layer composed of sandy or clayey silt with occasional gravel.

The only left-bank core, ROUG 5, differs from the others (Figure V.7). It presents a relatively homogeneous profile of clayey silt containing sparse gravel throughout. The sediment is more compact and lighter in colour, ranging from grayish olive (Munsell 5Y 5/3) to bright brown (7.5YR 5/6) and bright yellowish brown (10YR 6/8). However, a distinct layer is visible throughout the entire profile, i.e. in every core including ROUG 5. It is located at approximately 2 meters deep and is characterized either by the presence of a large pebble obstructing the corer, or by a compact gravel layer. This horizon marks the transition to more compact sediments compared to the overlying deposits. These compact layers are composed of silty clay.

These compact deposits form the base of the stratigraphic sequence and likely represent the pre-exploitation surface. Extraction refusal often occurred here due to increased sediment resistance. The hydraulic extractor was required to retrieve the heavy cores, especially in these compact and saturated contexts. The depth of refusal, determined by the remaining distance

between the coring mark and the ground surface, was recorded for each core, indicating the maximum penetration depth achieved.

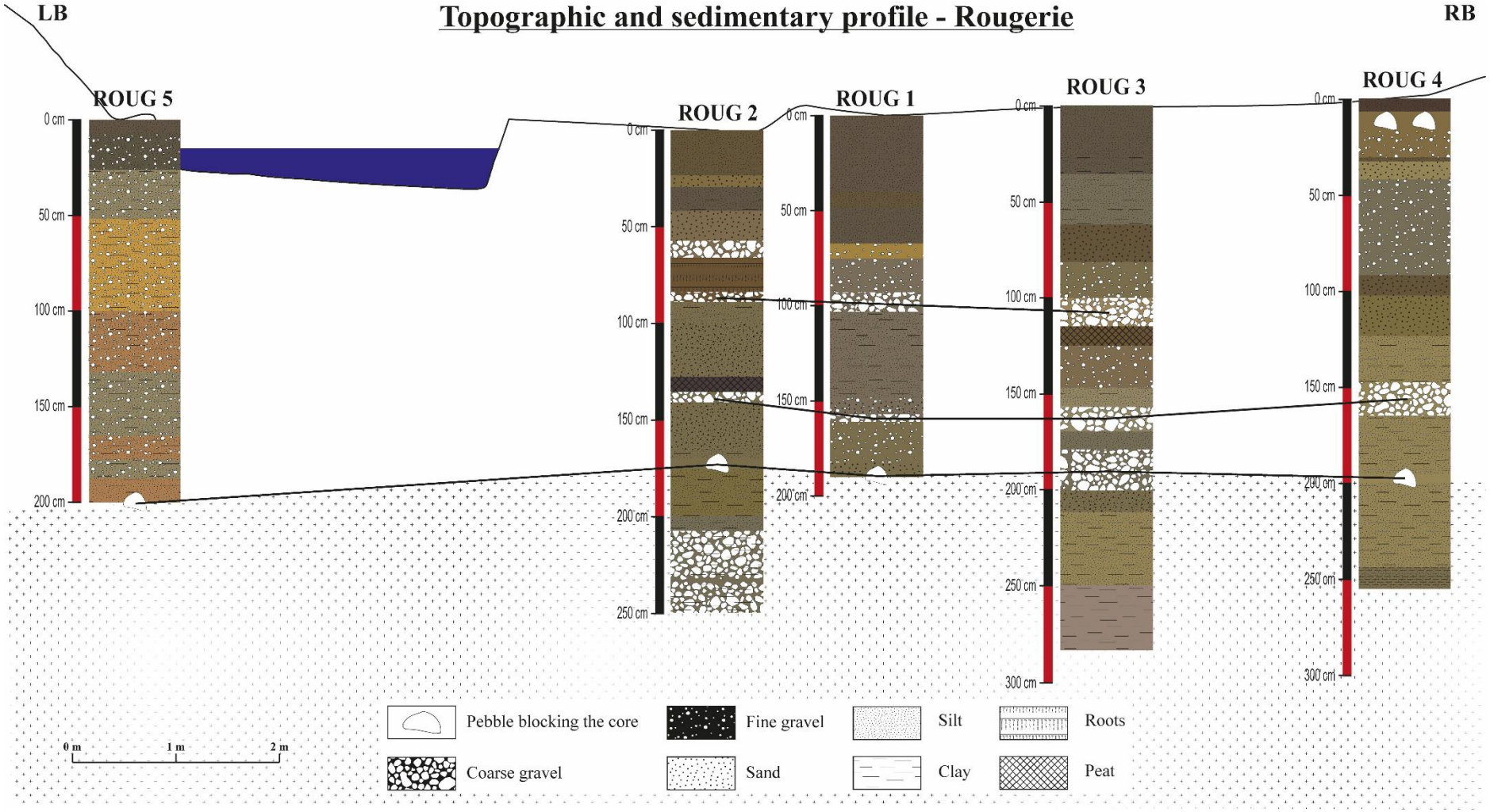

Figure V.7: Stratigraphic logs from sediment cores along the Rougerie topographic transect.

The stratigraphic logs and distinctive layers shown in Figure V.7 are primarily based on observations made during core opening. These are subsequently supported and refined through laboratory analyses, which provide detailed information on the composition of each core. Grain size distributions were obtained for each depth interval across all cores. These results were then processed to identify general trends and specific features.

To achieve this, the sediment texture was analyzed based on the relative proportions of four grain-size fractions following the Wentworth (1922) classification: gravel (2–64 mm), sand (63 µm–2 mm), silt (4–63 µm), and clay (<4 µm). In addition, a coarse-to-fine ratio was calculated using the formula: $\frac{\%_{Gravel}+\%_{Sand}}{\%_{Silt}+\%_{Clay}}$, based on the mass of each fraction.

The evolution of characteristic grain sizes with depth was analyzed using raw data. These data reveal local variations, such as the presence of pebbles that obstructed the coring process. A moving average with a window of three depth intervals was considered and tested. However, the degree of smoothing was too pronounced and tended to mask key stratigraphic features. As a result, these smoothed data are not included in the present study.

ROUG 5

Core ROUG 5, located on the left bank of the Rougerie stream, reached a depth of 2 m before refusal due to a reddish-brown quartzite fragment (Munsell 10R 4/4) obstructing the corer.

Overall, the homogeneity observed during core opening is confirmed by the granulometric data. The grain size distribution (Figure V.8) shows no abrupt changes, with samples generally composed of gravel, sand, and silt in roughly equal proportions, and a very low clay content. The coarse-to-fine ratio remains relatively stable across the sequence, ranging from 1 to 3 for most samples. Median grain size (D50) values range from 200 to 700 µm.

The uppermost layer consists of dark sandy humus devoid of gravel. It overlays a transitional layer of mixed organic material and gravels, which is poorly compacted and displays the highest coarse-to-fine ratio in the core (4.3). This marks a shift toward lighter-colored deposits. Between 26 cm and 178 cm, the sediments, ranging from olive to ochre and light brown, maintain a relatively consistent composition: 35 % gravel, 32.5 % sand, 31 % silt, and 1.5 % clay on average. The coarse-to-fine ratio here slightly exceeds 2, reflecting a higher proportion of gravel and sand relative to silt. An exception is observed in the deposit between 100 and 131 cm depth, where the gravel content is notably lower.

Between 178 and 188 cm, the gravel content increases to 61 %, reflected in a coarse-to-fine ratio exceeding 3 and is due to a coarse gravel (b-axis = 4 cm). The deepest layers show a modest rise in clay content (up to 3.9 %) and the highest silt fraction (44 %). No coarse gravel is observed in this zone, and the coarse-to-fine ratio drops to approximately 1, indicating a more balanced texture between fine and coarse fractions.

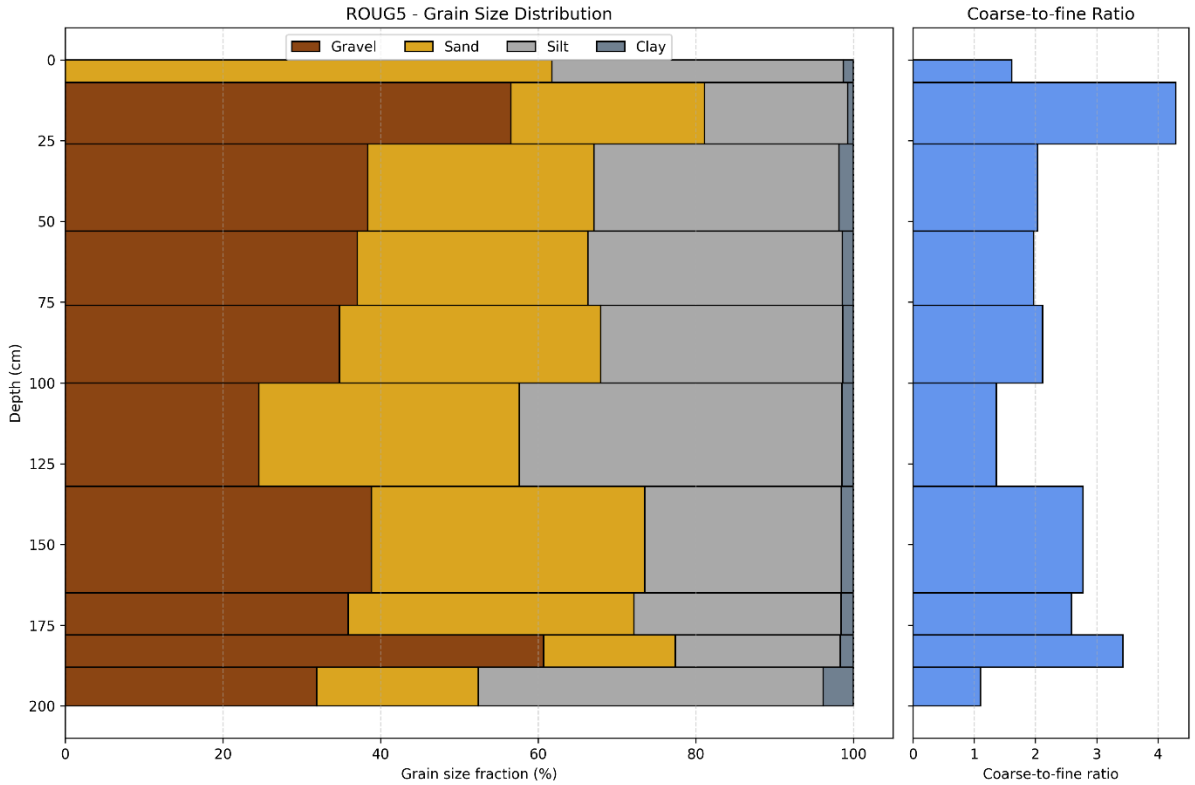

Figure V.8: Profile of the grain size distribution and coarse/fine ratio – ROUG 5.

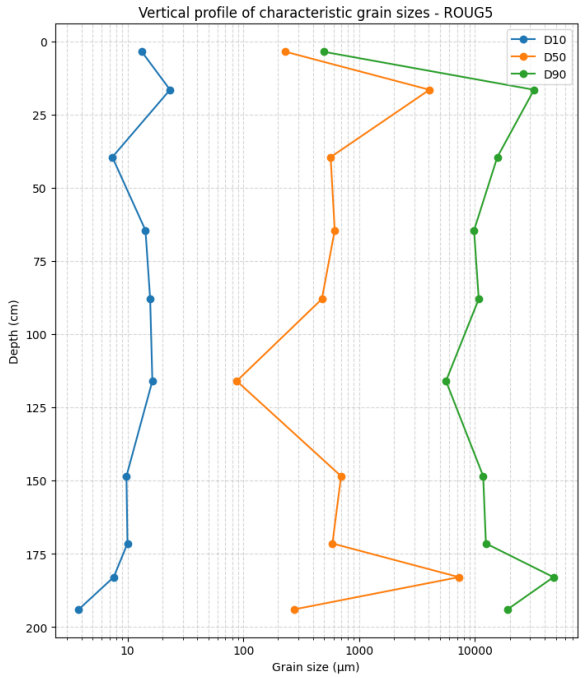

Figure V.9: Characteristic grain size – ROUG 5

ROUG 2

Located on the right bank of the Rougerie stream, Core ROUG 2 reached a depth of 2.5 m before refusal on a coarse gravel layer. The deposits in this core are darker than those in ROUG 5, showing a consistent dark grayish-brown colour throughout the profile. The sequence is notably heterogeneous, with alternating silty-sandy deposits, coarse gravel layers, and an

organic-rich peat-like horizon. This heterogeneity is reflected in both sediment texture and grain size metrics.

The upper 50 cm of the core is dominated by sand (>50 %), with silt also present in significant proportions (about 40 %). A 6 cm-thick sandy layer containing fine gravel (3-4 mm diameter) is embedded within this layer. Beneath, the next 40 cm becomes markedly coarser, with a coarse-to-fine ratio averaging 6. This layer contains centimetre-sized pebbles within a sandy matrix, visually similar in colour to the overlying layers. The D_{50} exceeds 1,000 µm, and D_{10} values fluctuate around 30 µm. A root was observed traversing this layer between 66 and 83 cm.

Below this coarse unit lies a finer deposit, between 89 and 136 cm, with a D_{50} comparable to the D_{10} of the overlying coarse layer. This section is silt-dominated but still contains substantial sand and minimal gravel. Between 128 and 136 cm, a peat-like organic-rich silty sand horizon is encountered, marking a transitional zone.

At 136-142 cm, a second, thinner gravel layer is present, again composed of centimetre-sized pebbles. Its median grain size is similar to the upper gravel layer (D_{50} = 1,360 µm). This is followed by silty-sandy layers with scattered gravel.

A significant obstruction at 170-174 cm was caused by a large gravel. Although partially masked by surrounding fine sediment (as seen in Figure V.10), the stone's impact is clearly highlighted in Figure V.11. The D_{50} at this level reaches 16,156 µm, equal to or greater than the D_{90} values of the rest of the profile, indicating extremely coarse material.

Below this, from 174 to 208 cm, the sediment becomes more compact. Although compositionally similar to the 142-170 cm section, the compactness being the key difference. The base of the sequence (208-250 cm) is characterized by large gravels embedded in a compact silty matrix with low sand content. The D_{50} for this unit is approximately 5,000 µm, and D_{90} reaches ~48,000 µm, reflecting the extreme coarseness of the gravels.

At the base of core ROUG 2, the abundance of coarse gravel obscures the fact that the surrounding matrix is silty. This interpretation is supported by the low D_{10} value, which is comparable to those recorded at the base of cores ROUG 3 and ROUG 4.

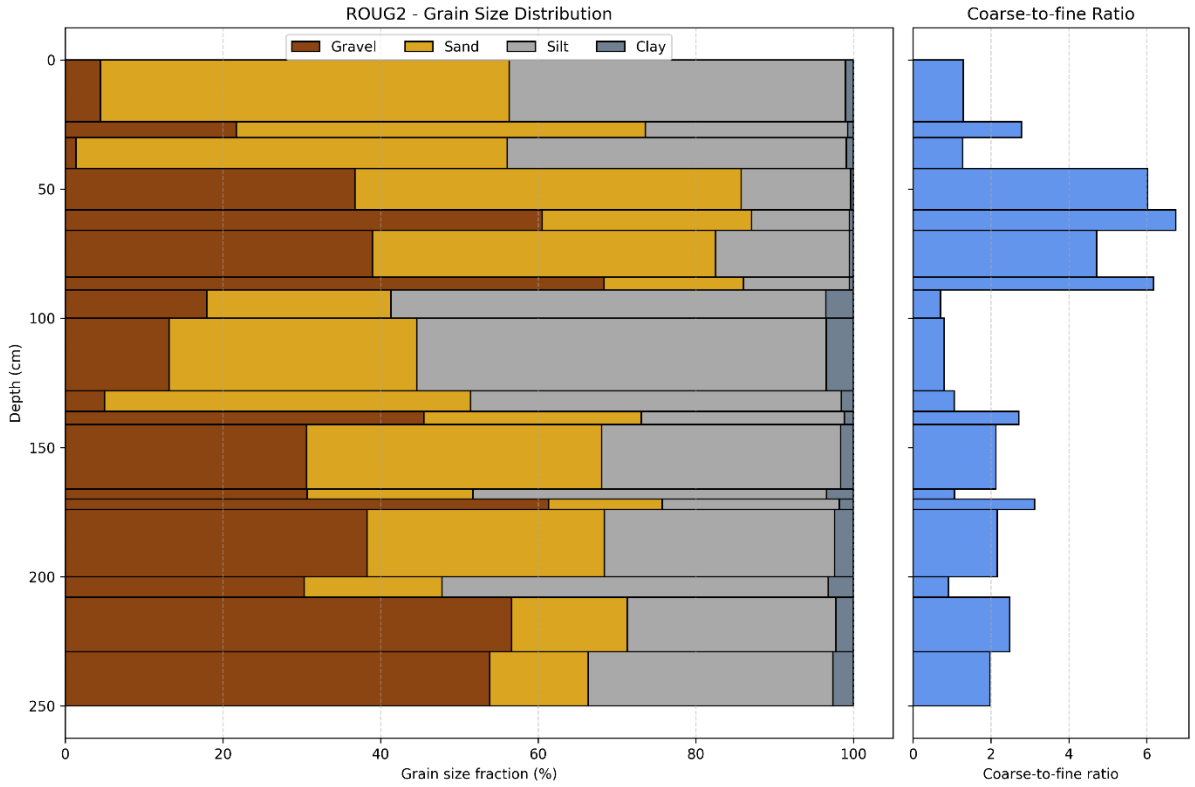

Figure V.10: Profile of the grain size distribution and coarse/fine ratio – ROUG 2.

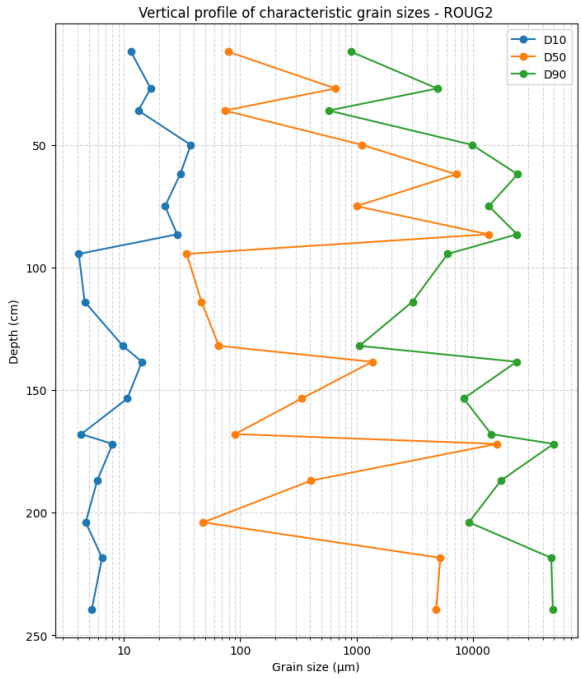

Figure V.11: Characteristic grain size – ROUG 2.

ROUG 1

Core ROUG 1 is the shallowest of the profile, reaching a depth of 188 cm. Coring was stopped due to refusal on a quartz fragment embedded within a fine silty matrix.

Overall, the sequence consists primarily of silty-sandy sediments intersected by two gravel-rich layers, each approximately 30 cm thick. The sediment colour is relatively consistent throughout

the core, presenting a grayish-olive hue. One exception is a lighter-coloured layer at 67-75 cm, which corresponds to a sandy gravel deposit with minimal silt.

The uppermost 67 cm comprises dark silty sand. Together, the sand and silt fractions account for approximately 93 % of the grain size distribution, with sand alone contributing about 60 %. This results in relatively low coarse-to-fine ratios compared to the gravel layers, averaging around 2.1. This is due to the sand content being roughly twice that of silt. In these upper layers, both D_{50} and D_{90} are the lowest of the core, with mean values of 145 µm and 1,230 µm, respectively.

Between 67 and 103 cm lies the first coarse layer. Gravel content increases dramatically from 6 % to 68 %, and the coarse-to-fine ratio rises sharply to 11.5. This is accompanied by a notable decrease in both sand (to 21%) and silt (to 8%), with almost no clay. Within this layer, grain size increases with depth, supporting field observations of finer gravel overlaying coarser pebbles. The D_{10} for this layer is comparable to the D_{50} of the overlying silty-sand layer.

Beneath this, the interval from 103 to 148 cm is composed of moist, fine-textured deposits dominated by silt and scattered pebbles. Gravel still comprises around 30 % of the sediment, while silt increases to 40 %, and clay reaches its peak at 2.5 %. This results in a lower D_{50} (245 µm) and a minimum D_{10} of just 6 µm.

The second coarse layer appears from 148 to 182 cm, with a coarse-to-fine ratio of 9.5. Unlike the upper coarse layer, this unit contains a higher sand content (43%) and slightly less gravel (47%). Consequently, its D_{50} is markedly lower (~2,000 µm compared to 15,800 µm for the upper gravel layer), while the D_{10} remains similar, indicating similar fine fractions.

The final layer, from 182 to 188 cm, is nearly devoid of gravel and consists mainly of coarse sand (75 %), with silt accounting for 21%. Characteristic grain sizes decrease accordingly, and the D_{90} is lower than in the preceding gravel-rich layer, confirming the near absence of gravel at the base of this core.

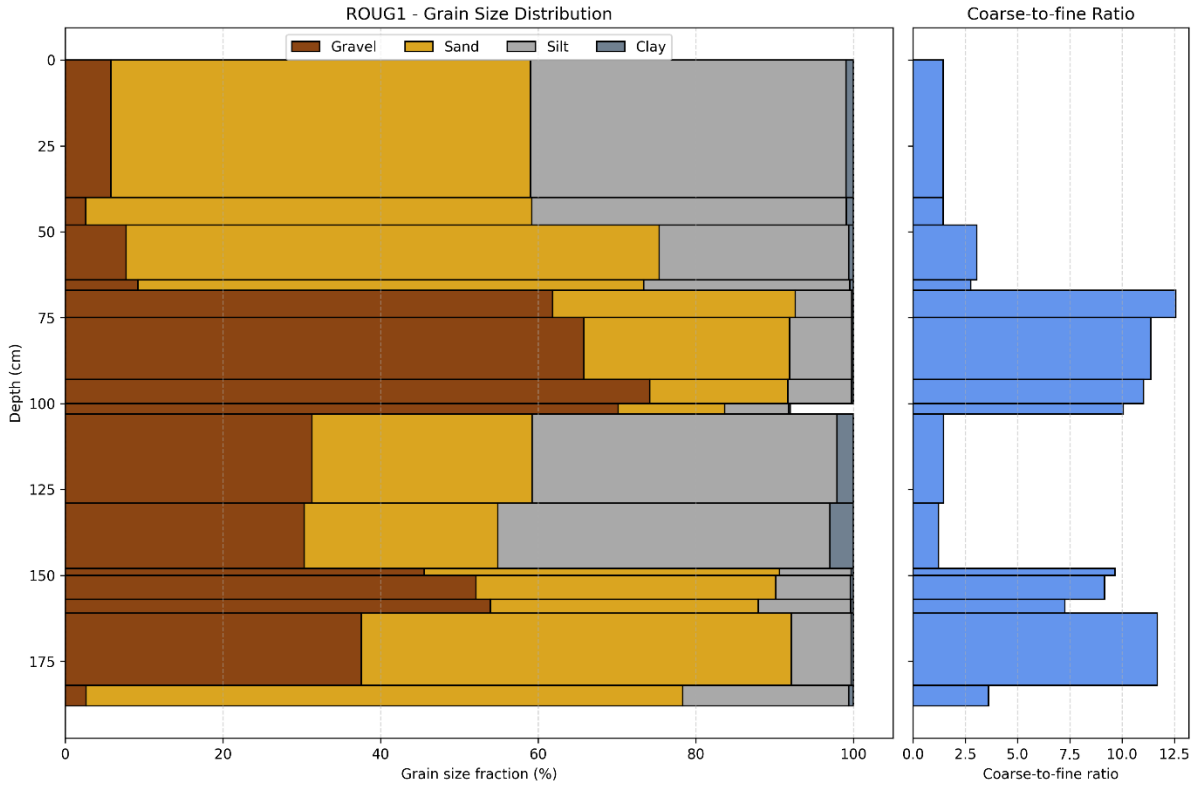

Figure V.12 Profile of the grain size distribution and coarse/fine ratio – ROUG 1.

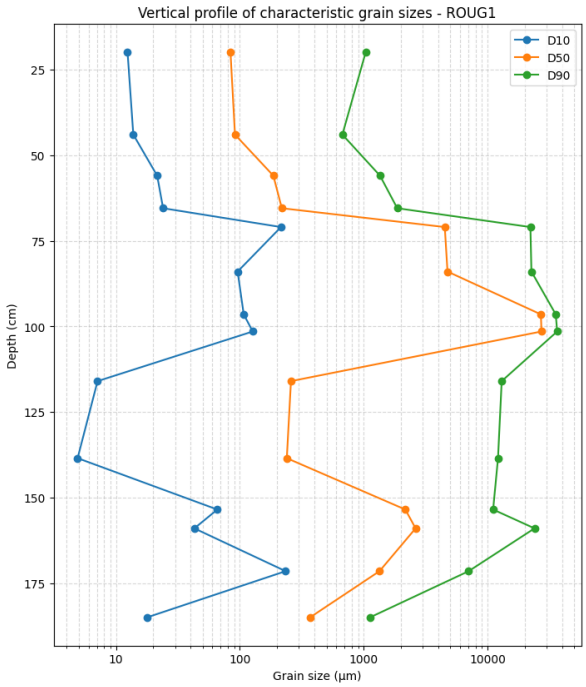

Figure V.13: Characteristic grain size – ROUG 1

ROUG 3

Core ROUG 3 is the deepest in the profile, reaching a total depth of 2.83 m. Refusal was not caused by a single large clast but rather by a dense accumulation of angular fragments embedded within a gray silty-clay matrix.

Compared to other cores, coarse layers in ROUG 3 are less sharply defined, though the granulometric distribution (Figure V.14) highlights three main gravel-rich units at 82-115 cm, 157-169 cm, and 179-211 cm depths. The intermediate sections between these levels consist mainly of silty-sandy deposits, with one organic-rich layer devoid of macro-remains observed between 115 and 125 cm.

From the surface down to 82 cm, the sediment is dominated by sand (49 %) and silt (41 %), yielding a coarse-to-fine ratio of approximately 1.5. The D_{50} is around 120 µm, indicating a fine texture.

The first coarse layer, between 82 and 115 cm, stands out with a coarse-to-fine ratio of 5.2. Gravel dominates (50 %), with sand accounting for about 33 % and silt dropping to 15 %. The median grain size increases to 2,000 µm, which is comparable to the D_{90} of the overlying finer layers (~2,700 µm).

Between 115 and 157 cm, gravel content decreases to 11 %, while sand and silt return to values similar to those in the uppermost portion of the core (~46 % and 42 %, respectively). Characteristic grain size also realign with these finer textures: D_{10} at 13 µm, D_{50} at 133 µm, and D_{90} at 2,230 µm.

The second coarse layer appears at 157-169 cm and is composed of large gravel within a fine silty-sandy matrix. While the D_{50} here is 820 µm, this value is influenced downward by the presence of abundant fines. However, the D_{90} is higher than in the first coarse layer, reaching 19,880 µm compared to an average of 14,700 µm previously. This layer is flanked by two thin (~10 cm) intermediate horizons that are compositionally similar, containing 10 % gravel, 31 % sand, and ~55 % silt. These layers show a D_{50} of just 47 µm, emphasizing their fine nature.

The third and most prominent coarse layer spans 179-211 cm. It closely resembles the first gravel unit but is even coarser, with 53 % gravel, 22 % sand, and 24 % silt. The D_{50} increases significantly to 5,200 µm, surpassing the D_{90} values of most of the intermediate levels.

The basal portion of the core, below 211 cm, consists of highly compacted silt (55 %) with elevated clay content (4.2 %). While scattered gravel remains present, these are angular and unweathered, including schists fragments. The D_{10} and D_{50} reach their lowest values in this section (3.3 µm and 36 µm, respectively), but the D_{90} remains elevated at 18,300 µm due to persistent coarse inclusions.

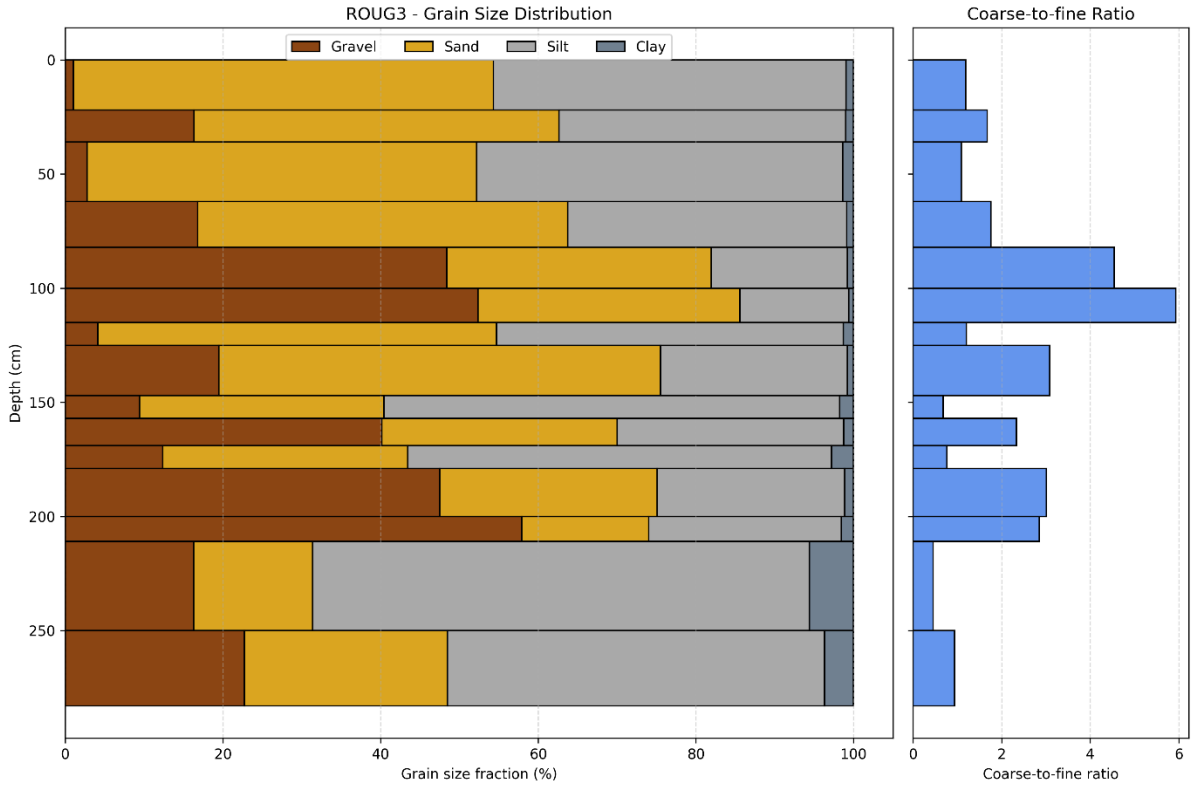

Figure V.14: Profile of the grain size distribution and coarse/fine ratio – ROUG 3.

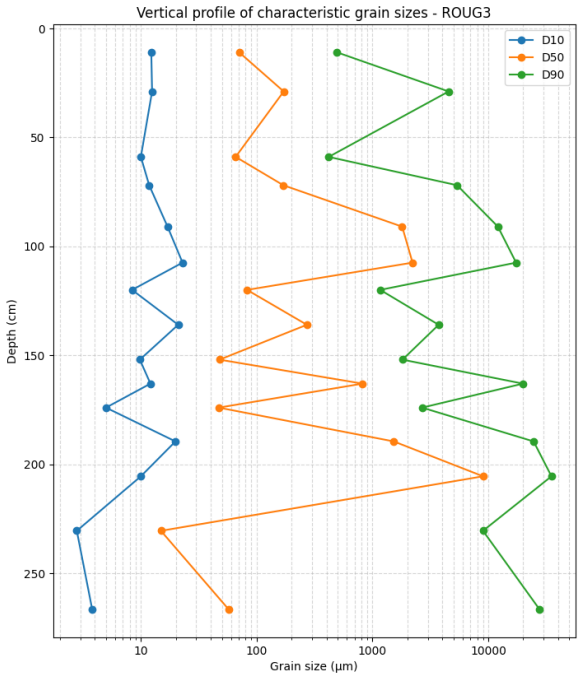

Figure V.15: Characteristic grain size – ROUG 3

ROUG 4

Core ROUG 4 is the sampling point located furthest from the current stream channel, positioned on the right bank just a few decimetres from the base of a mound. The core reached a depth of 2.55 meters before refusal. The cause of refusal was undetermined, but the final layer consisted of compact clayey silt with scattered gravels.

Unlike other cores, ROUG 4 does not present clearly defined gravel layers. The upper 124 cm is relatively coarse overall, with an average coarse-to-fine ratio exceeding 4. This interval includes two thin, fine-textured, organic-rich silty-sandy layers at 31-33 cm and 92-103 cm.

Below 124 cm, the sediment becomes finer, with increasing dominance of the silt fraction, except for two interruptions: a gravelly layer between 148 and 165 cm, and a large gravel that obstructed the corer at 195-200 cm. The rising silt content leads to a decline in the D_{10}, while D_{50} and D_{90} remain relatively stable.

Excluding the coarse gravel at 195-200 cm, the final 70 cm of the sequence is texturally homogeneous, consisting mainly of silt (average 50 %), with substantial sand (30 %) and increasing clay (3.5 %). The coarse-to-fine ratio drops to 0.7, confirming that fine fractions (silt and clay) dominate in this portion of the core. Despite the abundance of fine material, some coarse gravels remain, keeping D_{90} values consistent with the rest of the core (~13,700 µm compared to an average of ~14,800 µm). In contrast, D_{10} and D_{50} decrease significantly, reaching 4.7 µm and 50 µm, respectively, compared to average values of 13.7 µm and 995 µm in the upper portion of the core[9].

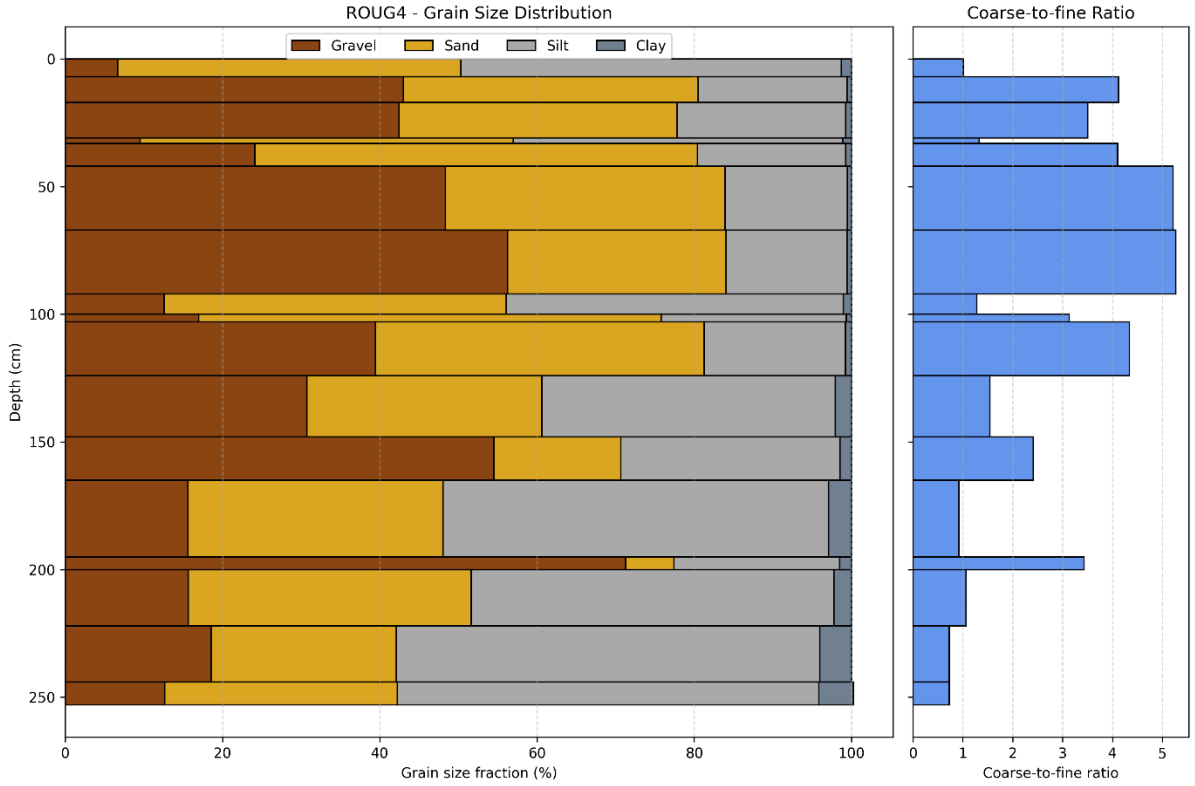

Figure V.16: Profile of the grain size distribution and coarse/fine ratio – ROUG 4.

[9] Valeurs calculées en excluant le galet à 195-200 cm.

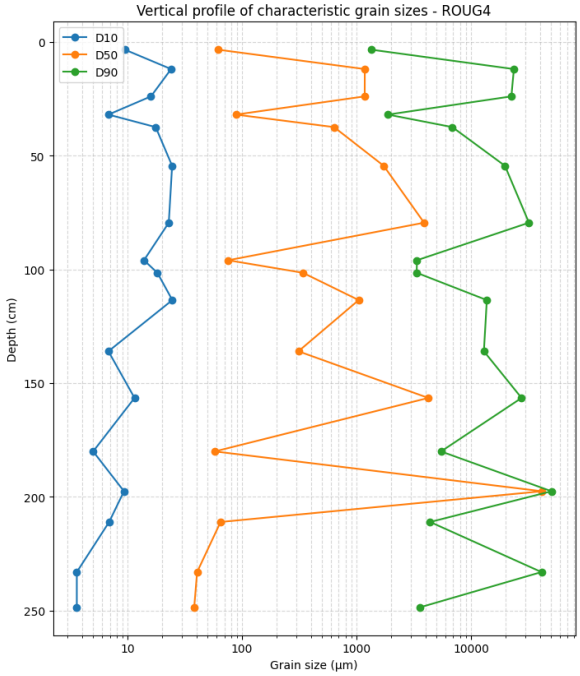

Figure V.17: Characteristic grain size – ROUG 4

1.2. Gold panning remains

Along both banks of the Rougerie stream, a total of 234 mounds associated with gold mining have been identified (Figure V.18). These features vary in size and collectively cover 17,015 m², resulting in an average mound surface of approximately 73 m². Three primary mound clusters, Rou-1, Rou-2, and Rou-3 (Figure V.18), were defined based on spatial continuity and density. The Rou-2 site is the largest, containing 189 mounds, while Rou-1 and Rou-3 host 24 and 15 mounds, respectively. An additional six isolated mounds were observed between or downstream of these clusters. The spatial distribution of these features reflects land use history. Today, the mounds are almost exclusively found beneath forest cover, which does not appear to be managed for timber production. In contrast, areas devoid of mounds are generally occupied by grasslands or have been modified by dense drainage networks, suggesting that historic agricultural activity likely erased former mining features in these zones.

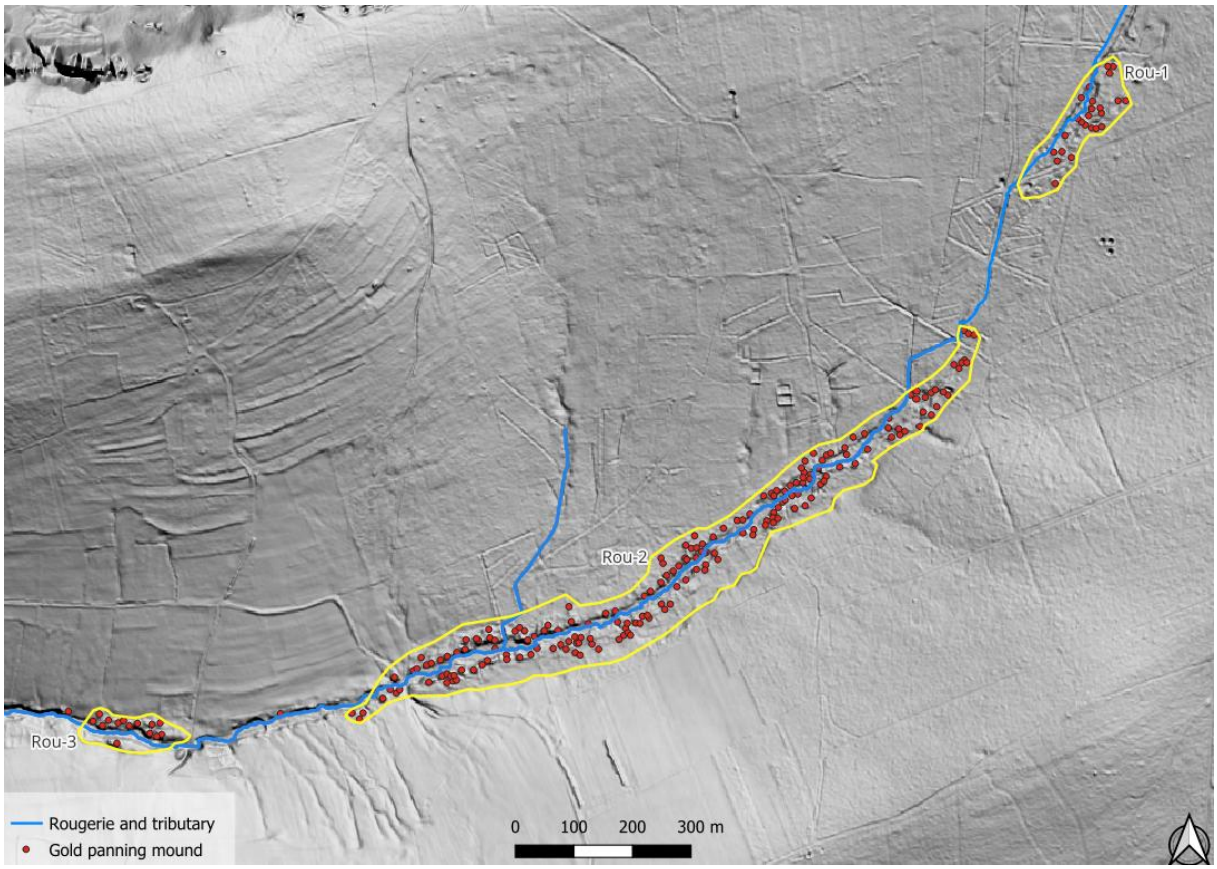

Figure V.18: Group of mounds along the Rougerie.

Out of the 234 total mounds recorded, 158 are classified as narrow mounds (A1), with an average surface area of 55.9 m². The remaining 96 mounds are categorized as thick mounds (A2 and A3), and together they cover a comparable total area. As such, their average size is significantly greater, approximately 109 m² per mound, almost double that of narrow mounds. When considered individually, isolated thick mounds (A2) tend to be larger (121.5 m² on average) than coalescent mounds (A3), which average 90.5 m².

In the Rou-2 and Rou-3 areas, the Rougerie stream currently flows within a trench (C3) that averages 10–15 meters in width, reaching up to 25 meters in certain segments. The trench is typically 1.5 to 2 meters deep compared to the surrounding unexploited zones, and up to 3 meters deep locally in the lower section of Rou-2. This feature corresponds to the alluvial sediments extracted during gold mining operations and spans a total area of 24,075 m². Mounds are typically located along the edges of the trench, often in close proximity to its boundaries.

Previous estimates by Baudoux (2018) stating that mounds reach 5 metres in height on average, and up to 10 metres from the trench bottom, appear to be overestimated. Field measurements and data from the 2021–2022 digital elevation model (DEM), as well as total station surveys, indicate that mound heights average only 1.6 meters relative to the unexploited terrain and 3.2 meters relative to the trench bottom.

In terms of excavations, 18 excavations sensu stricto (B1) were identified, with an average surface area of 44 m². Their smaller size is consistent with their frequent location within mounds. Additionally, three large water tanks (B2) were mapped along the Rougerie, averaging 516 m² in area. Based on their present boundaries, these tanks likely had an average storage capacity of 650 m³, roughly a quarter of an Olympic swimming pool (assuming 2 m depth). The

largest of these reservoirs, located in the upstream part of Rou-2 and depicted in Figure V.2, had an estimated capacity of 1,053 m³.

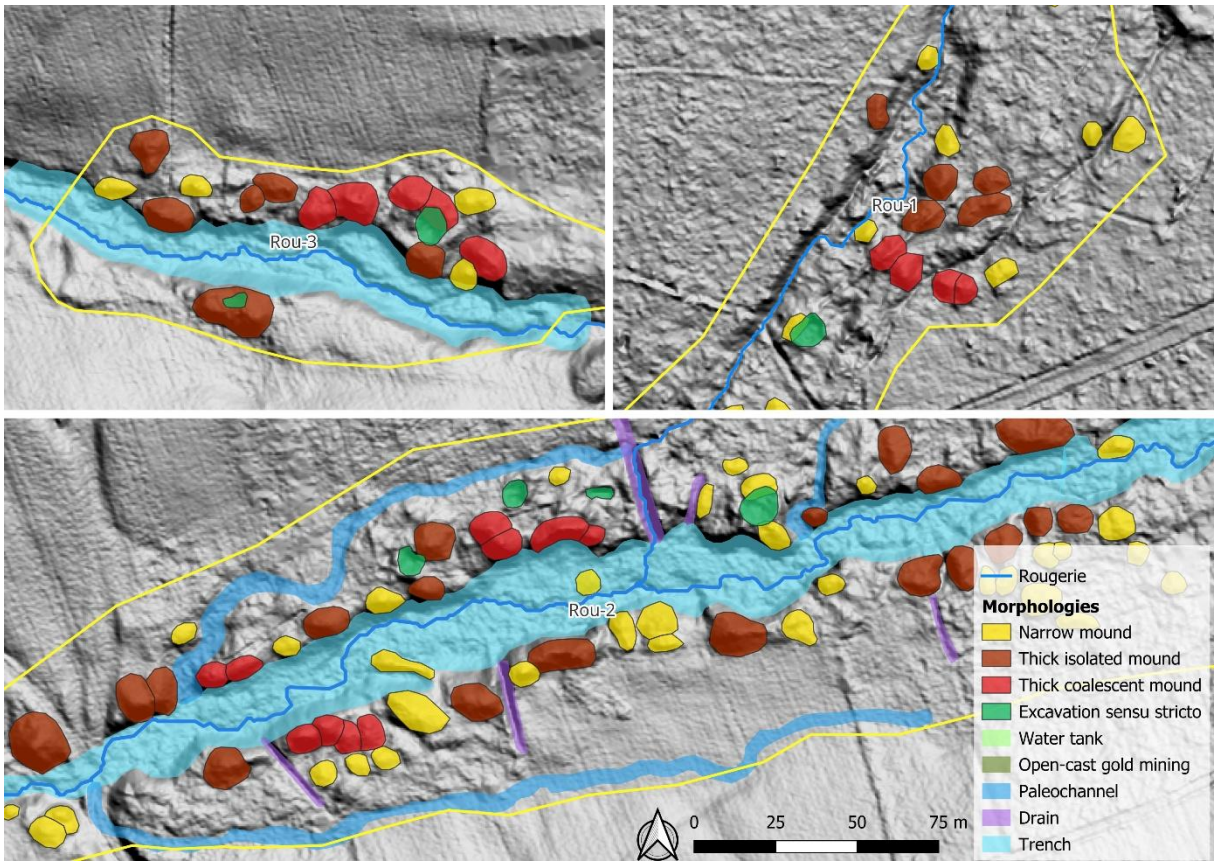

Figure V.19 : Morphologies of Rougerie sites. Same scale for the three sites.

A total of five paleochannels (C1) have been identified within the study area, all of which converge toward the Rougerie stream and are located within the Rou-2 sector. Their lengths vary from 55 m to 283 m, with a cumulative length of 732 m. These channels are currently dry, with the exception of one on the left bank in the downstream portion of Rou-2 (Figure V.43). It carries a diffuse water flow during the wetter months, i.e. late autumn through early spring.

A network of drains (C2), mostly dating from the 20th century, has been dug perpendicular to the valley axis, following the natural slope. Nine main drains flow directly into the Rougerie, while many smaller channels form a dense drainage network extending upslope and between the Rou-1 and Rou-2 sectors.

On the left side of the Rougerie, a slope break runs parallel to the current watercourse and can be traced throughout the entire Rou-2 sector. This linear feature corresponds to a mining front (D), the uppermost boundary of sediment removal during past gold mining operations. The front extends approximately 1.5 kilometres and lies at an average distance of 50 metres from the left edge of the trench.

1.3. Stratigraphic section

Rougerie section (ROUG-A, left bank)

This vertical section, located on the left bank of the Rougerie stream (Figure V.6), was originally formed through natural erosion and recently cleaned and deepened manually by

B. Van Eerdenbrugh. The dug hole reached 1.3 m below the stream level, exposing weathered bedrock. The total face is approximately 3.5 m high and varies in width from 0.5 to 2.5 m. The stratigraphy was recorded by unit (US[10]), and described with the help of C. Draily, as follows:

- **US 1**: Dark humus with rolled pebbles oriented toward the stream, overlaid by a thick mat of moss and bilberry vegetation.
- **US 2**: Gold-panning mound deposits. Patchy light gray to yellow sediments with scattered small rounded gravels and abundant roots. Contains pebbles ranging from 1 to ± 10 cm (b-axis). The dominant texture is coarse, with very little fine silt. Includes OSL sample GLL246303 (collected in July 2024). Charcoal sampled at the base of the unit, near contact with US 3.
- **US 3**: Slightly clay-rich gray silt with orange-yellow sptos. Manganese concretions are common, especially in the lower part, where smoothed quartzite blocks and rust stains are abundant. Sediment becomes more compact below the quartzite blocks.
- **Interface US2–US3**: Sharp and horizontal. A burrow descending from US2 into US3 disturbs the charcoal layer. A distinct 10 cm wide by 1 cm thick charcoal lens was sampled in July 2024 and extends deeper into the section.
- **US 4**: Very compact layer with a high concentration of rolled quartzitic gravel (1-10 cm b-axis). Orange spots are visible near weathered shale gravels. The matrix is minimal, and the sandstone gravels appear vertical.
- **US 5**: Gold-panning mound deposits. Dark brown, fine-grained silt with signs of bioturbation. Contains fine gravel in a silty matrix, distinguishing it from US2.
- **US 6**: Identified only on the right side of the section, beneath US5. Not preserved in the description.
- **US 7**: Light brown to orange compact clay with quartzitic gravel (1-10 cm), appearing cemented by clay. Represents the lowest level reached by roots.
- **US 8**: Coarse brown sand with scattered quartzitic gravels. Interspersed with orange manganese-rich lenses.
- **US 9**: Thick lens of gray coarse sand with disseminated pebbles (2-3 cm).
- **US 13**: Orange-ochre clay lens within US9, filled with flattened shale gravels cemented by compact clay and rich in manganese.
- **US 10**: Grayish gravel with a sandy matrix and quartz inclusions. Manganese concretions abundant at the top of the unit.
- **US 11**: Reddish clay with heterogeneous rounded gravels (up to 10 cm, mainly quartzite) and quartz fragments.
- **US 12**: Base of the section, composed of blue-gray weathered bedrock (phyllade) with embedded quartz and quartzite blocks. This layer is rich in gold, as confirmed by

[10] *Unité Stratigraphique* in French.

panning tests, particularly 50 cm below the section base, where a large nugget was recovered. Clast sizes increase toward the base (10-20 kg blocks).

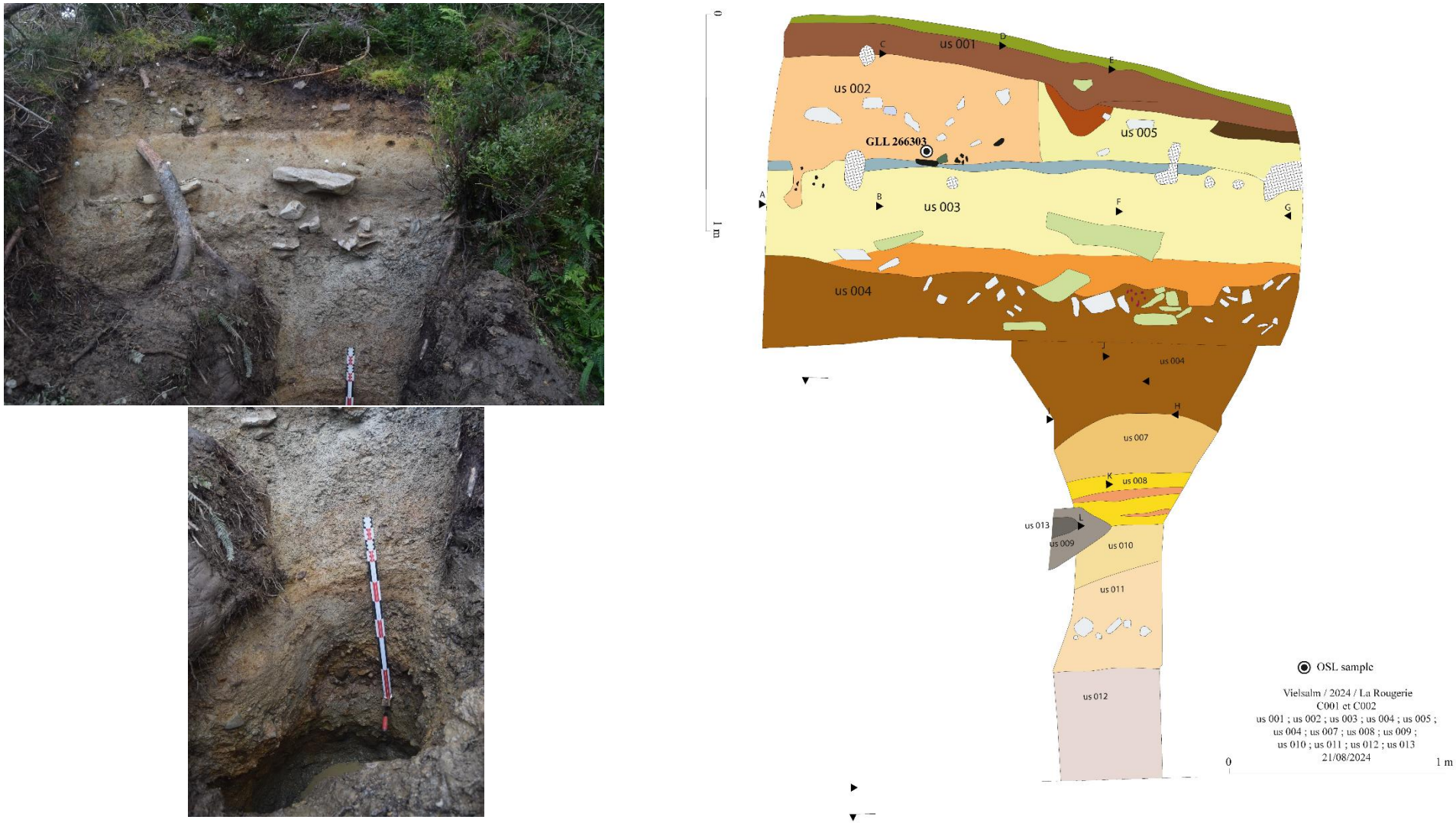

Figure V.20: Picture and drawing of ROUG-A stratigraphic section

Drain/Heronster section (ROUG-B, right bank)

This section is located on the right bank of the Rougerie (Figure V.6), along a modern drain where the Heronster stream is flowing. The section reaches a maximum height of 1.5 m and a width of 2.5 m. It was exposed through mechanical erosion caused by water flowing from the drain into the Rougerie. The stratigraphy was recorded in 13 stratigraphic units (US) and observed laterally across the section.

- **US 1**: Thin brownish-grey humus layer, less than 10 cm thick. Slightly thicker towards the left, downslope in the direction of the stream. The humus is less organic than usual, with a grass cover on top.
- **US 2**: Light grey to light brown layer with scattered, rounded small pebbles and fine roots. Pebbles range from 1 cm up to approximately 15 cm in b-axis length. The layer is dominated by gravel, with only minor amounts of fine silt. Very low cohesion.
- **US 3**: Brown in colour, containing scattered rounded small pebbles from 1 cm to approximately 10 cm (b-axis). A greater amount of fine silt is present compared to US2, though gravel remains the dominant component. Low cohesion.
- **US 4**: Light brown silt with scattered small, rounded gravels.
- **US 5**: Gray sand with occasional scattered gravels (2-3 cm in diameter). Two OSL samples were collected: GLL246304 and GLL246305.
- **US 6**: Sandy lens within US4 and US5, composed of coarse ochre to rusty-coloured sand. Contains small manganese concretions dispersed in thin veins throughout the sand, along with a few scattered gravels (2-3 cm). OSL sample GLL246306 was collected from the ochre sand.
- **US 7**: Pebble-rich layer with clasts ranging from 1 to approximately 10 cm in b-axis length, embedded in dark grey fine silt. The dominant fraction varies within the unit, some zones are gravel-rich, while others contain more silt. Forms a depression in the centre of the section.
- **US 8**: Compact brownish-grey clayey silt with scattered gravels (1 to ~10 cm, b-axis). A large quartzitic sandstone block is present on the left side.

The deposits visible at the bottom of the picture in Figure V.21 correspond to material removed during the cleaning of the profile and are not represented in the stratigraphic diagram.

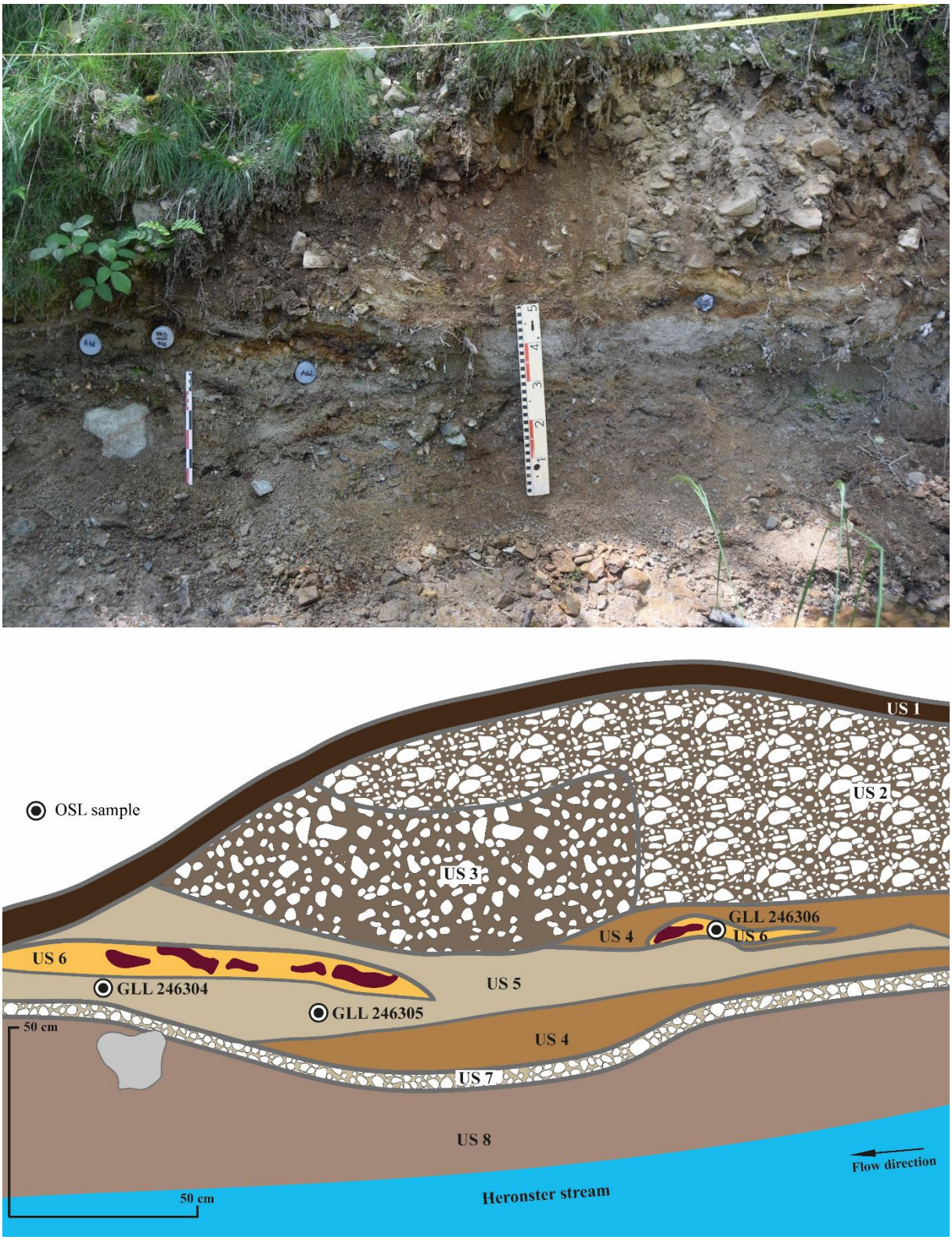

Figure V.21: Picture and drawing of ROUG-B stratigraphic section

2. Schinderbach

2.1. Topographic profile and particle-size analysis

As with the Rougerie, core samples were collected along a topographic profile established using a total station (Figure V.22). Core IDs (SCHIN 1 to SCHIN 9) are ordered from the left bank to

the right bank of the stream. Field observations indicated that SCHIN 1 and SCHIN 9 were likely located outside the mined zone, offering reference points for comparison with cores SCHIN 2 to SCHIN 8, situated within the exploited area.

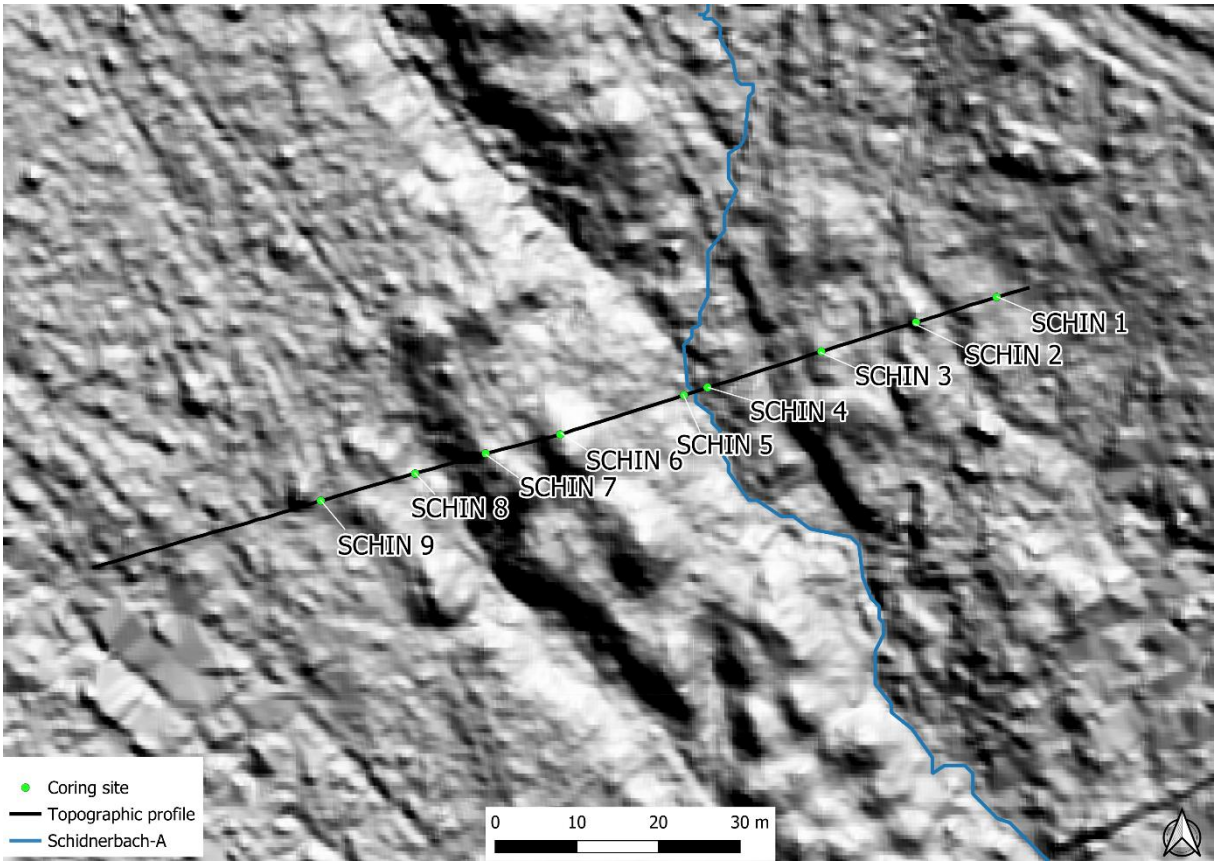

Figure V.22: Localisation of the topographic profile and sampling sites of the Schinderbach-A.

Unlike the Rougerie, where the cores lie at relatively uniform elevations, Schinderbach displays more significant vertical differences. For instance, the top of core SCHIN 6 lies nearly three metres higher than SCHIN 4, reflecting considerable local relief. Nonetheless, three characteristic sedimentary levels were consistently identified in several cores.

The first level corresponds to the base of the mound deposits, characterized by friable, ochre-coloured coarse sand (Munsell 10YR 6/8 – yellowish brown) with scattered centimetre-sized gravel. These deposits are weakly cohesive and are observed at the surface beneath the humus layer in cores SCHIN 3, 6, and 7, though at slightly varying elevations.

The second level appears in SCHIN 3, 6, 7, and 9, and consists of compact silty deposits with scattered pockets of sand and isolated centimetre-sized gravel. The silty matrix is gray (Munsell 7.5Y 5/2 – grayish olive), while the sandy inclusions are multicoloured, ranging from light beige (Munsell 10Y 5/2 – olive gray) to yellow-orange (Munsell 10YR 5/8 – yellowish brown). These distinctive units correlate well in elevation with the base of mound deposits described above.

The third level marks the top of the weathered bedrock, composed of gray clay (*gley*), nearly devoid of gravel or sand, except for occasional quartz fragments. This layer was found in SCHIN 2, 4, 6, 7, and 8, always at a similar elevation. As this elevation also corresponds to the refusal depth in other cores, this weathered substratum was extrapolated across the full transect.

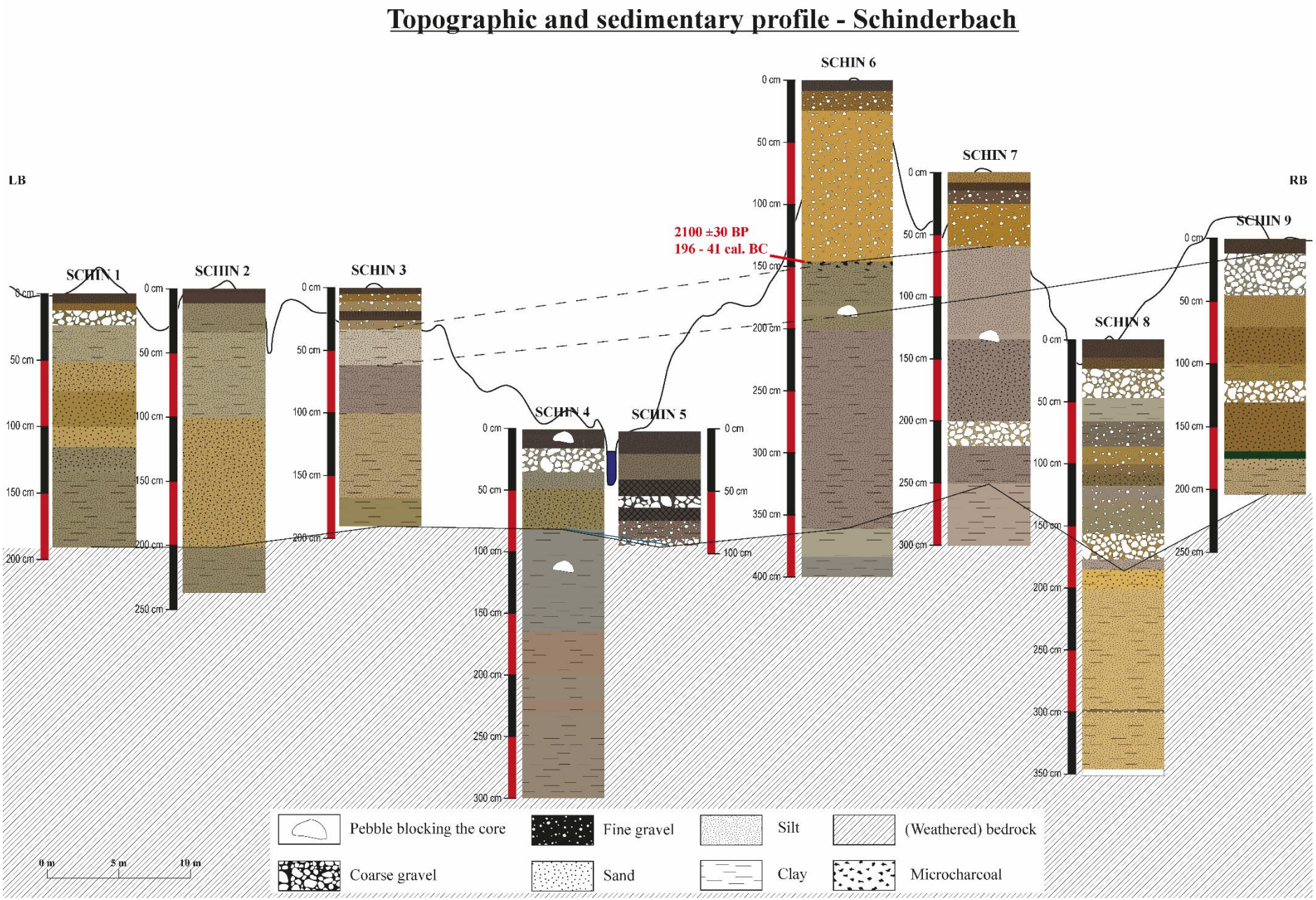

Figure V.23: Stratigraphic logs from sediment cores along the Schinderbach-A topographic transect

In general, sedimentary horizons at Schinderbach are more sharply defined than at the Rougerie. Colour variations are clearer, whereas Rougerie deposits tend to be uniformly dark brown with subtle contrast.

SCHIN 1

Core SCHIN 1 reached a total depth of 190 cm. Refusal was not due to coarse gravel but rather to a compact layer, as supported by granulometric evidence from the base of the sequence.

The stratigraphy is relatively homogeneous and silt-dominated, with a coarse-to-fine ratio consistently below 2. The upper 50 cm consists of silty sand, with 60 % silt and 25 % sand. The coarse-to-fine ratio is 0.6, indicating a fine matrix dominance. Sparse gravel is present.

From 52 to 100 cm, the gravel content increases, and the coarse-to-fine ratio rises to 1.4, though silt remains dominant (38 %) and sand remains stable (26 %). The gravel fraction increases from 11 % to 33 %, with D_{50} rising from 32 µm to 230 µm, and D_{90} from 5060 µm to 14,250 µm. However, D_{10} remains constant (~4 µm), underlining the consistent presence of fine particles.

Between 100 and 115 cm, gravel decreases while sand and silt increase, marking a transition to finer units. In the bottom section (115-190 cm), fine sediment clearly dominates again. The coarse-to-fine ratio drops to 0.4, meaning the fine fraction is more than double the coarse. Gravel content returns to the upper layer level (11.7 %), sand declines to 15.7 %, and silt rises to 67 %. This finer texture is reflected in low D_{10} and D_{50} values (2.7 µm and 11.4 µm, respectively), while D_{90} remains elevated at 11,500 µm, indicating the continued presence of scattered pebbles.

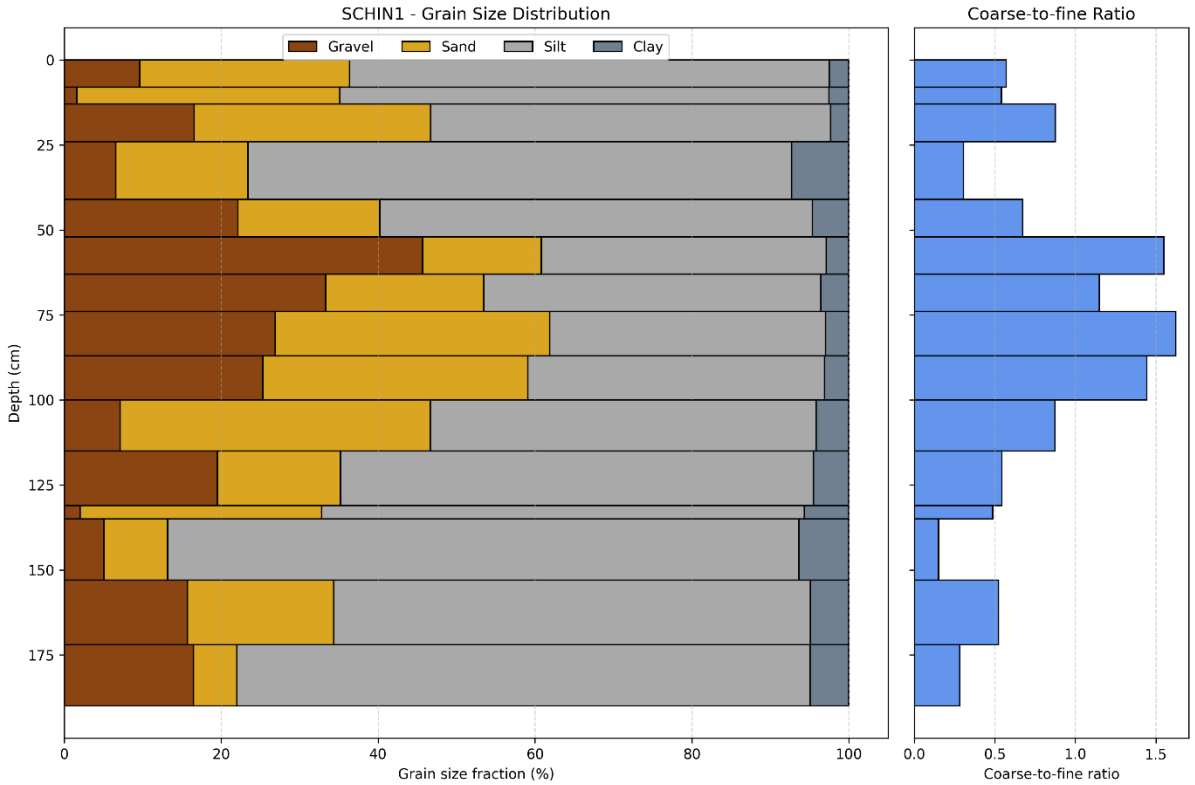

Figure V.24: Profile of the grain size distribution and coarse/fine ratio – SCHIN 1.

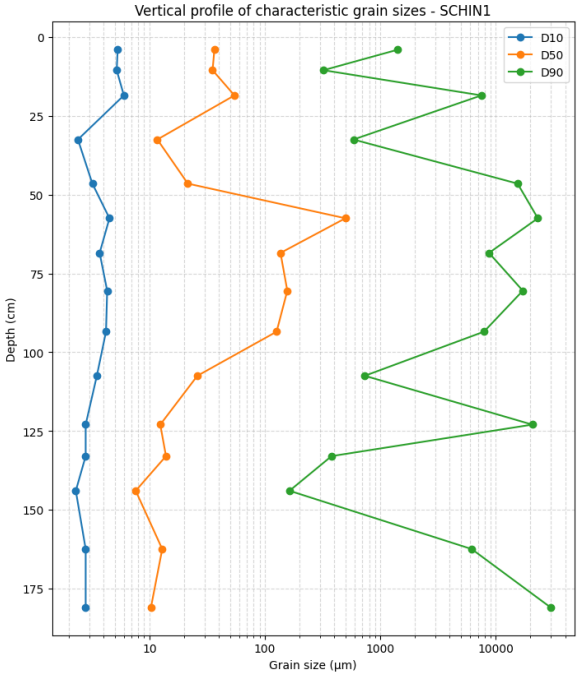

Figure V.25: Characteristic grain size – SCHIN 1.

SCHIN 2

Core SCHIN 2 was driven to a depth of 245 cm, with refusal caused by a large pebble blocking the corer. The sediment sequence is relatively uniform, showing no major shifts in grain size distribution. Overall, it is characterized by a dominance of fine material, with moderate variation in sand content. Gravel remains a minor component throughout.

The upper 110 cm consist of silty-sandy deposits, with approximately 55.7 % silt, 31% sand, and 9 % gravel. The coarse-to-fine ratio is low, around 0.7, indicating a strong predominance of fine-grained sediment. A few scattered gravels are present, increasing slightly with depth. This trend is reflected in particle size metrics: while D_{90} increases downwards, both D_{10} and D_{50} decrease. Average values for this upper section are: D_{90} = 3137 µm, D_{50} = 35 µm, and D_{10} = 3.8 µm.

Between 110 cm and 176 cm, the gravel and sand fractions increase to 16.5 % and 41.5 %, respectively, while the silt content decreases to 39 %. The coarse-to-fine ratio rises to 1.4, marking a coarser interval within the sequence. This is also reflected in a rise in D_{50}, which reaches 122.5 µm in this section.

In the lower portion of the core (176-245 cm), the sequence returns to a finer overall texture, while still containing larger individual gravels. Silt increases to 60 %, sand decreases to 14.3 %, and gravel reaches 21 %. The coarse-to-fine ratio drops back to 0.6, indicating renewed dominance of fine sediments. Grain size percentiles confirm this trend: D_{10} and D_{50} return to values comparable to the upper section (3.1 µm and 27.6 µm, respectively), while D_{90} increases significantly to 23,150 µm, indicating the presence of larger gravels in the fine matrix.

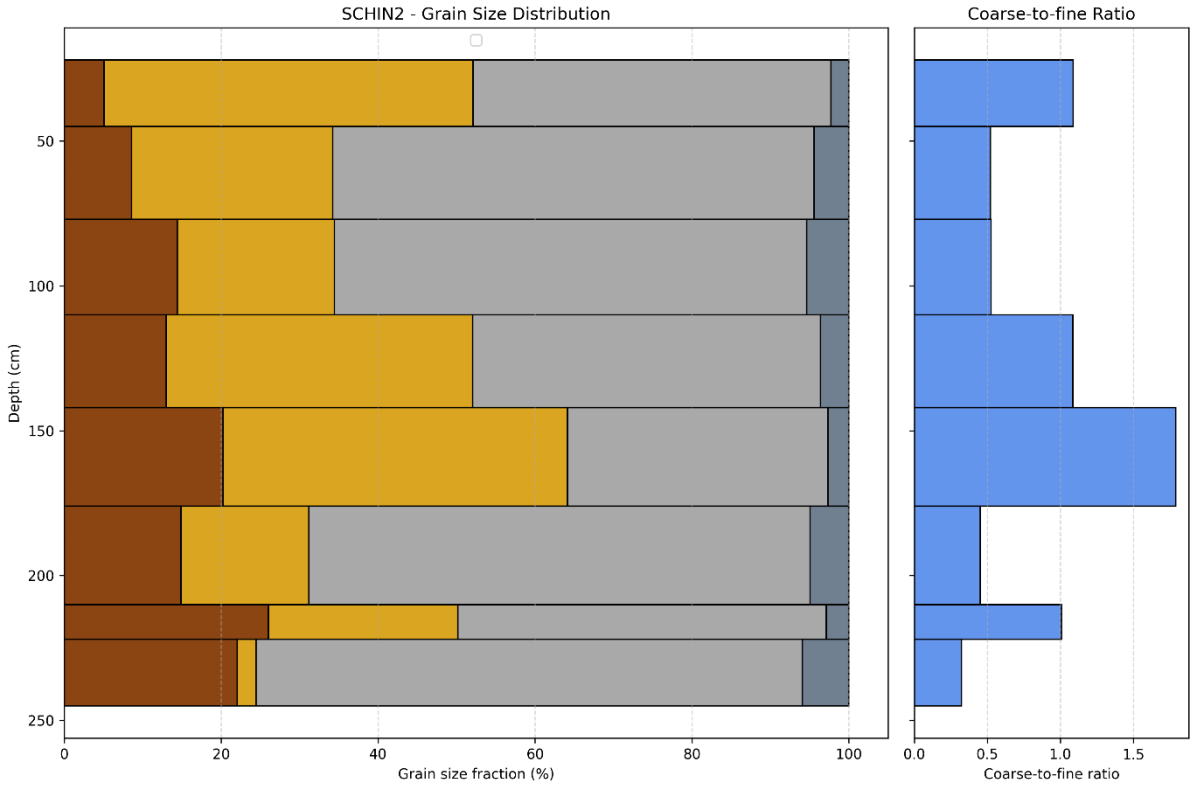

Figure V.26: Profile of the grain size distribution and coarse/fine ratio – SCHIN 2.

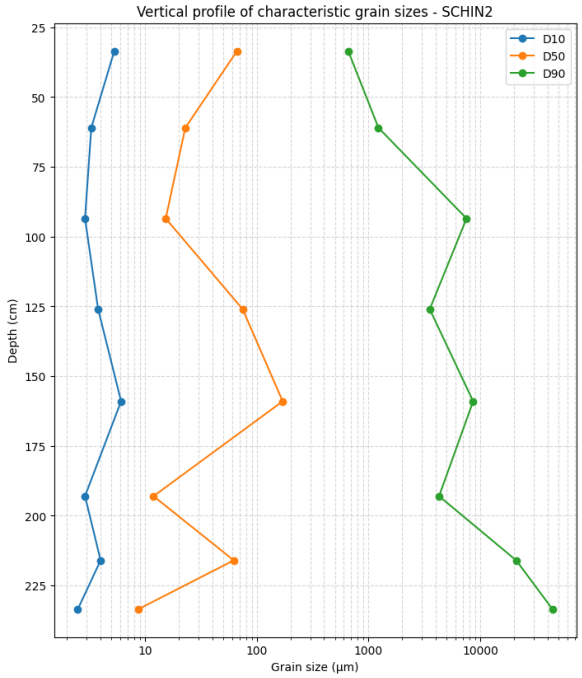

Figure V.27: Characteristic grain size – SCHIN 2.

SCHIN 3

Core SCHIN 3 reached a depth of 190 cm. Refusal is likely due to significant compaction of the basal sediments. The sedimentary sequence exhibits marked vertical heterogeneity, with a surface gravel layer overlying sandy-silty deposits.

The uppermost layer, extending from 0 to 33 cm, is dominated by coarse material. Numerous centimetre-scale clasts are visible to the naked eye, embedded in a loosely cohesive ochre-colored sandy matrix. The coarse-to-fine ratio is high, with an average value of 5.1. Gravel is the predominant fraction, accounting for 49 %, followed by sand at 33 %, and silt at 17 %. This dominance of coarse particles is further reflected in the characteristic grain sizes: D_{10} is 25 µm, D_{50} is 2500 µm, and D_{90} reaches 17,500 µm.

The intermediate layer, from 33 to 63 cm, is characterized as sandy-silty. The silt fraction is predominant at 43 %, while sand remains significant at 32 %. The gravel content decreases substantially to 22 %, a value that remains consistent in the underlying layers. At this depth, the coarse and fine fractions are nearly equivalent, with a coarse-to-fine ratio of 1.1. The reduction in gravel content and the relative increase in fine material are evident in the grain size distribution, with D_{10} at 4.7 µm and D_{50} at 5100 µm. However, the size of coarse particles remains similar to the surface layer, with D_{90} measured at 13,500 µm.

The lower section, from 63 to 190 cm, maintains a stable gravel proportion of 22 %, as previously noted. This interval is also marked by a progressive decrease in median grain size, corresponding to a reduction in sand content and a concurrent increase in silt content. The layer is composed of multicoloured silt interspersed with sandy pockets and scattered gravels. Quantitatively, from the top to the base of this section, sand content decreases from 53 % to 30 %, while silt increases from 20 % to 50 %. The coarse-to-fine ratio declines from 3.8 to 0.9, with characteristic grain sizes showing a similar trend: D_{10} decreases from 19 to 4.4 µm, and D_{50} from 240 to 56 µm. In contrast, the size of the coarse fraction increases, with D_{90} rising from 9000 to 18,600 µm.

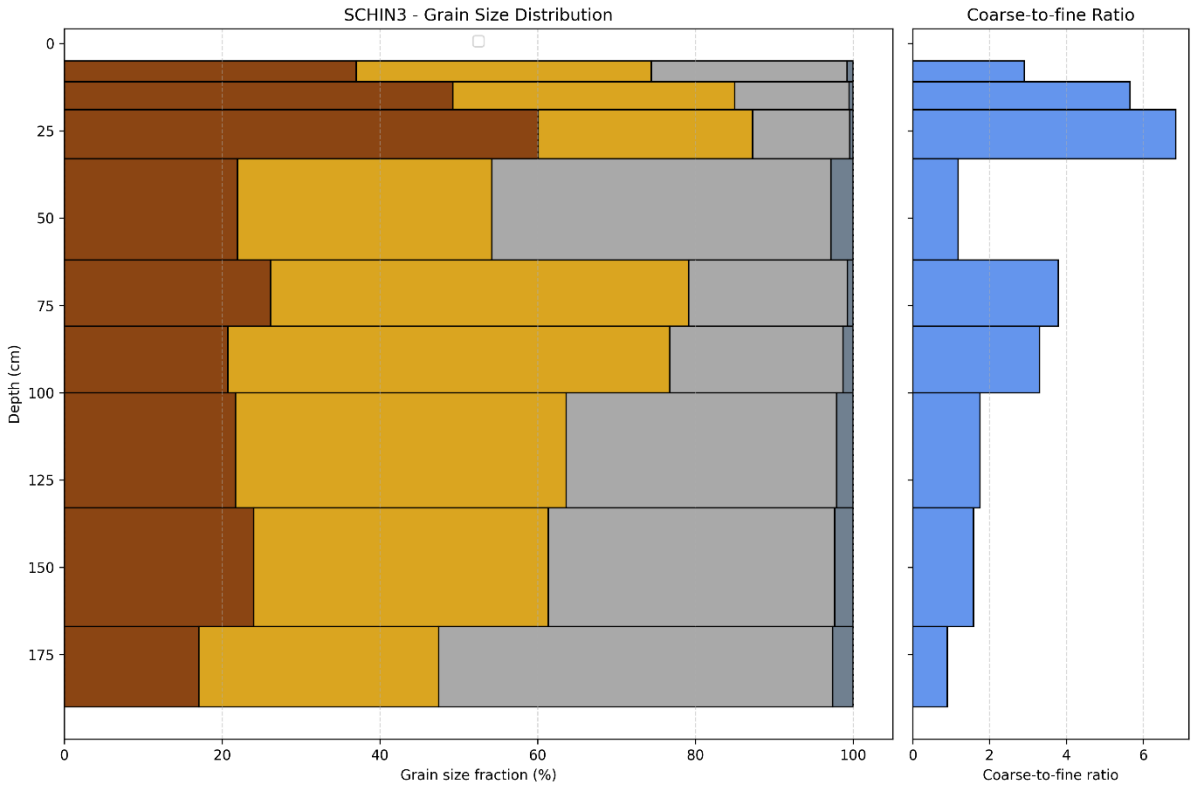

Figure V.28: Profile of the grain size distribution and coarse/fine ratio – SCHIN 3.

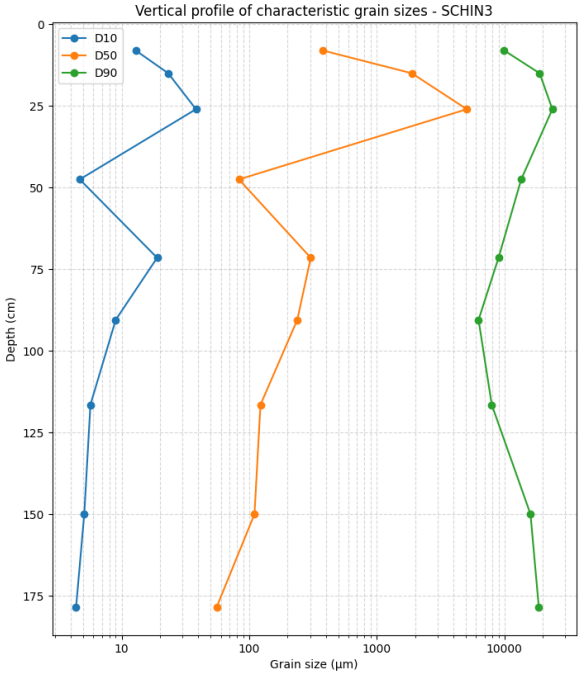

Figure V.29: Characteristic grain size – SCHIN 3.

SCHIN 4

The SCHIN 4 core reached a depth of 300 cm, making it the deepest core. Refusal is likely associated with the presence of a highly compacted, cohesive layer, probably corresponding to weathered bedrock. The stratigraphy displays a clear binary structure: an upper section enriched in coarse material (0-81 cm), and a lower section (114-300 cm) entirely devoid of gravel. These two units are separated by a transitional sandy-silty layer approximately 33 cm thick.

From 0 to 81 cm, sedimentation is strongly dominated by coarse material, with sand accounting for 49 % and gravel for 37 %, while silt comprises only 13 %. The coarse-to-fine ratio is particularly high, averaging 8.2. Grain size parameters are consistent with this trend, with D_{10} at 46 µm, D_{50} at 570 µm, and D_{90} at 14,500 µm. This unit contrasts with the surface layer of SCHIN 3, notably through its greenish-grey colour and the presence of larger, rounded gravels.

The intermediate layer, extending from 81 to 114 cm, shows a gradual transition toward finer material. Silt content increases significantly, averaging 50 %, while sand slightly decreases to 38 %, and gravel drops markedly to 8.75 %. The coarse-to-fine ratio declines to 0.9, indicating a near balance between coarse and fine fractions. This fining trend is mirrored in the grain size distribution, with D_{10} and D_{50} decreasing to 4.8 µm and 54 µm, respectively. Coarse particles remain present, however, as reflected in a D_{90} of 10,100 µm. The sediment matrix appears more compact, with fewer visible coarse gravels.

The lower portion of the core, from 114 to 300 cm, is characterized by an almost complete absence of gravel, with the gravel fraction dropping to just 0.18 %. Clay content becomes more pronounced, averaging 5.3 %. The deposit is fine-grained, homogeneous, and exhibits greater compaction than the overlying units. Within this section, two sub-units can be distinguished. From 114 to 222 cm, the sediments are nearly pure silt (90 %), with a very low coarse-to-fine ratio of 0.05. Between 222 and 245 cm, the texture shifts toward silty-sand, comprising 67 % silt and 28.5 % sand, with a coarse-to-fine ratio of 0.4. This evolution is further confirmed by grain size parameters: in the 114-222 cm sub-unit, D_{10} is 2.5 µm, D_{50} is 8 µm, and D_{90} is 39

µm; whereas in the 222-245 cm sub-unit, D_{10} increases to 3.5 µm, D_{50} to 25 µm, and D_{90} to 108 µm.

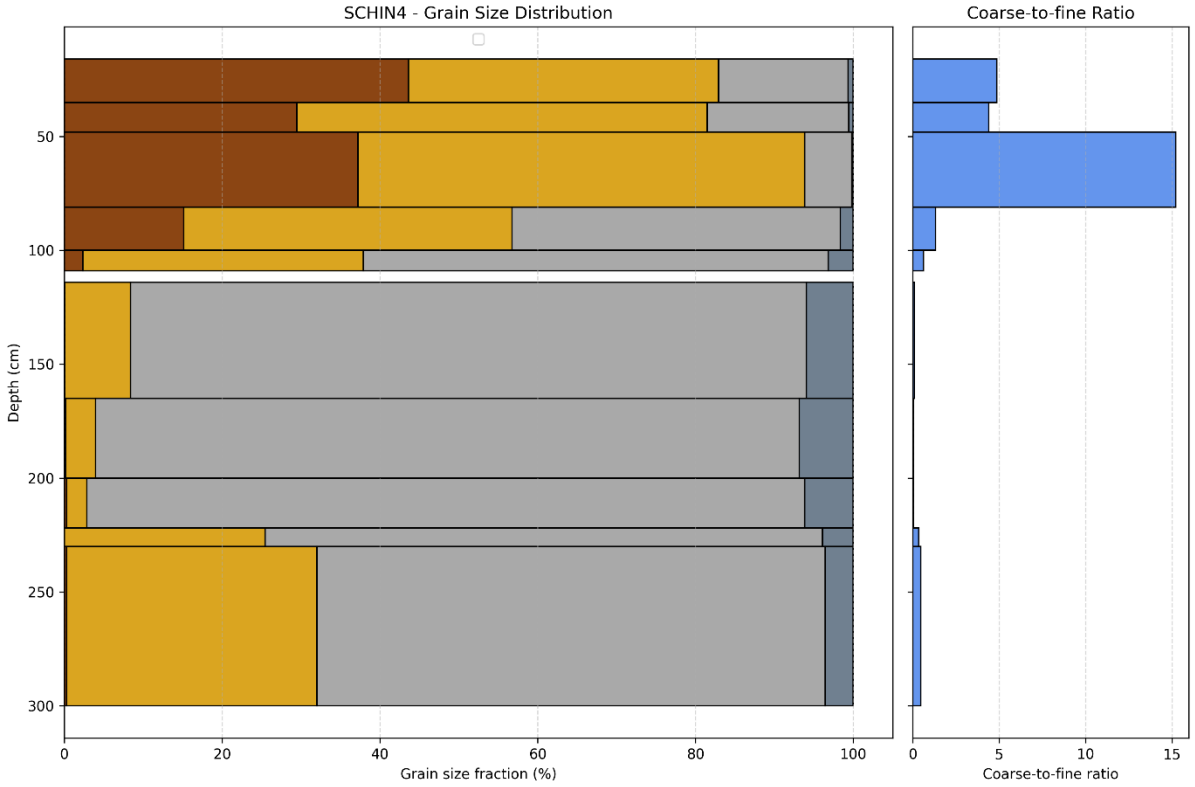

Figure V.30: Profile of the grain size distribution and coarse/fine ratio – SCHIN 4.

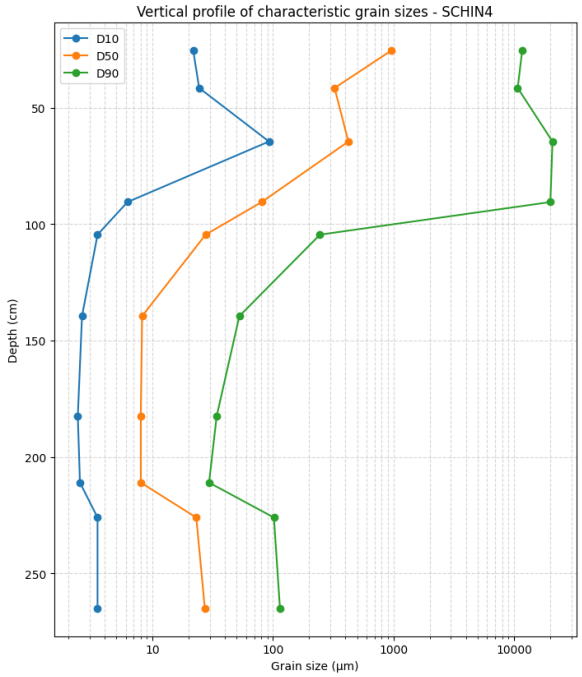

Figure V.31: Characteristic grain size – SCHIN 4.

SCHIN 5

The SCHIN 5 core reached a depth of 92 cm and reveals a sedimentary structure characterized by the alternation of organic-rich layers and fluvially derived gravel beds. Core refusal was caused by a large cobble obstructing the coring drill.

The intervals from 0 to 52 cm and from 61 to 72 cm display similar characteristics. These layers consist of dark brown to nearly black organic to peaty sandy-silty sediments. The grain-size distribution is composed of 59 % sand, 30 % silt, and 10.5 % gravel. The coarse-to-fine ratio is 2.3, and the grain size parameters reflect moderate values: D_{10} is 17.8 µm, D_{50} is 138 µm, and D_{90} reaches 2900 µm.

In contrast, the segments from 52 to 61 cm and from 72 to 92 cm are predominantly composed of coarse fluvial material, with gravel accounting for 63 % of the sediment, embedded within a silty matrix (19 %). The coarse-to-fine ratio rises to 4, indicating a pronounced dominance of coarse elements. The finer matrix is highlighted by a slightly lower D_{10} value (14.3 µm) compared to the overlying organic layers. Meanwhile, the gravel-rich nature of these levels is clearly evidenced by a D_{50} of 14,300 µm and a D_{90} of 28,850 µm.

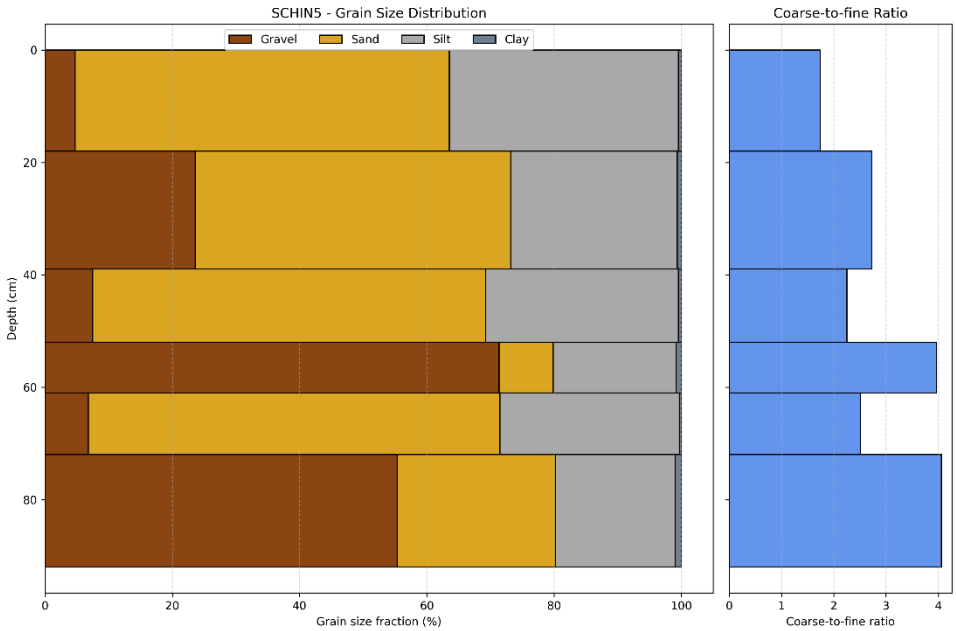

Figure V.32: Profile of the grain size distribution and coarse/fine ratio – SCHIN 5.

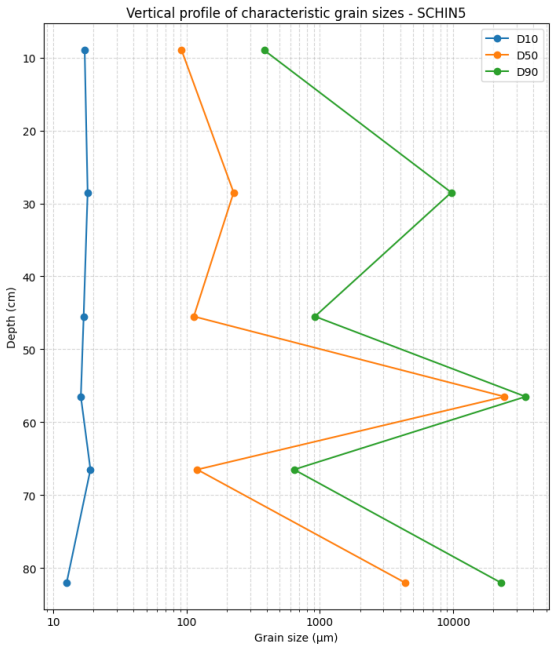

Figure V.33: Characteristic grain size – SCHIN 5.

SCHIN 6

The SCHIN 6 core reached a depth of 400 cm, making it the longest sedimentary sequence sampled. Core refusal appears to correspond to a dense, clay-rich layer, likely representing weathered bedrock. The sedimentary succession is characterized by well-defined stratification, with four distinct units observed beneath the humus layer (0-9 cm).

The first unit, extending from 9 to 146 cm, is markedly dominated by coarse material. This deposit closely resembles the ochre gravelly sand layer described in the upper part of SCHIN 3. Gravel accounts for 44 %, sand for 42 %, and silt for just 13 %. The coarse-to-fine ratio is particularly high, averaging 7, reflecting the predominance of coarse particles. The deposit is highly friable and weakly cohesive, composed of centimetre-scale gravel within a poorly consolidated sandy-silty matrix. Grain size parameters are relatively large, with D_{10} at 41.3 µm, D_{50} at 1460 µm, and D_{90} at 10,680 µm. The relatively moderate D_{90} value, compared to some other cores, indicates the absence of large cobbles and a dominance of finer gravel.

The second unit, from 146 to 300 cm, exhibits a decrease in gravel content. Notably, the interval between 189 and 300 cm corresponds to the mottled silt layer with scattered sand pockets and isolated gravels previously identified in SCHIN 3. In this unit, silt content increases to 49 %, while sand and gravel decrease to 32 % and 16.5 %, respectively. Consequently, the coarse-to-fine ratio drops to 1.1. Grain size metrics also reflect this fining trend: D_{10} is 5.2 µm, D_{50} is 73 µm, and D_{90} reaches 4900 µm.

The underlying unit, from 300 to 361 cm, is defined by the presence of four large cobbles embedded in a grey silty-sandy matrix. This coarse material increases the gravel fraction to 48 %, while sand and silt represent 28 % and 22.5 %, respectively. The coarse-to-fine ratio rises to 3.2, and D_{90} increases significantly to 31,800 µm. Meanwhile, the fine fraction remains present, with D_{10} at 11.4 µm and D_{50} at 723.5 µm.

The basal unit, from 361 to 400 cm, is composed almost entirely of fine material (97.8 %). Silt dominates the composition at 91.5 %, with clay contributing 6.3 %. No gravel is present, and

sand comprises only 2.2 % of the sediment. The coarse-to-fine ratio is extremely low, at just 0.02. Grain size parameters confirm this fine nature: D_{10} is 2.5 µm, D_{50} is 7.75 µm, and D_{90} is 30 µm.

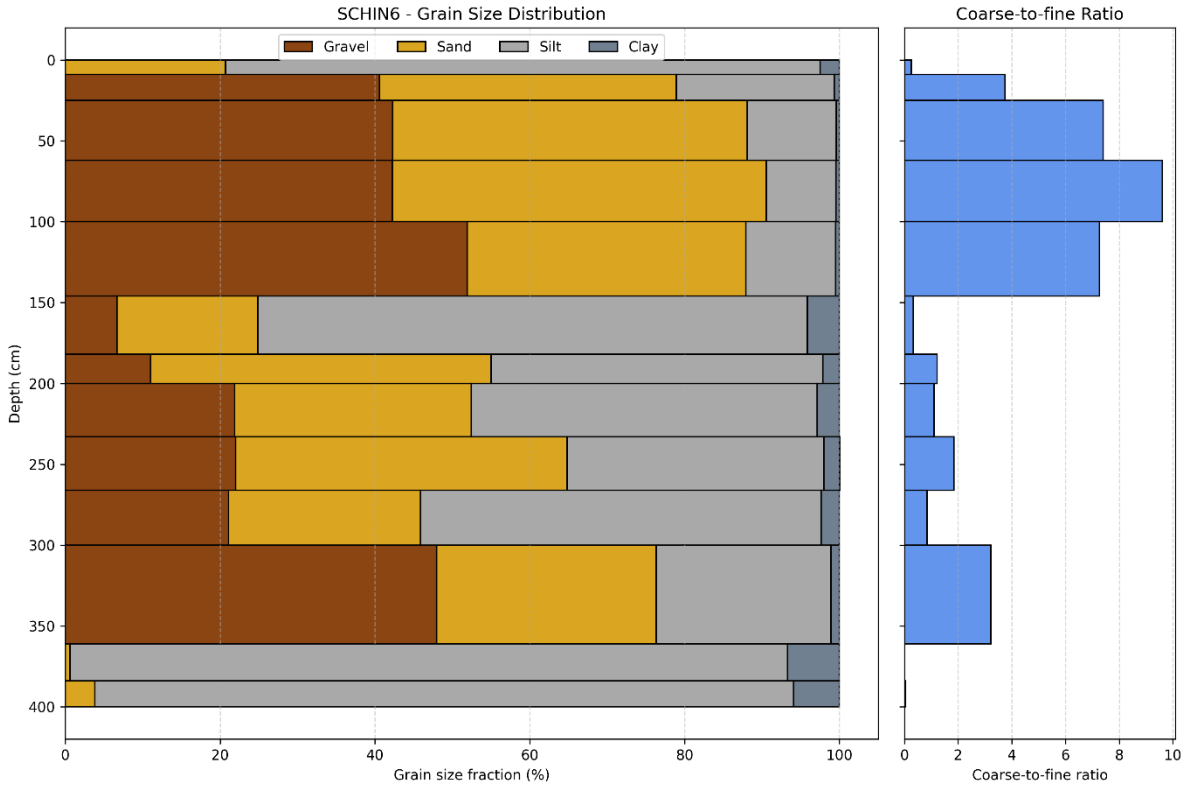

Figure V.34: Profile of the grain size distribution and coarse/fine ratio – SCHIN 6.

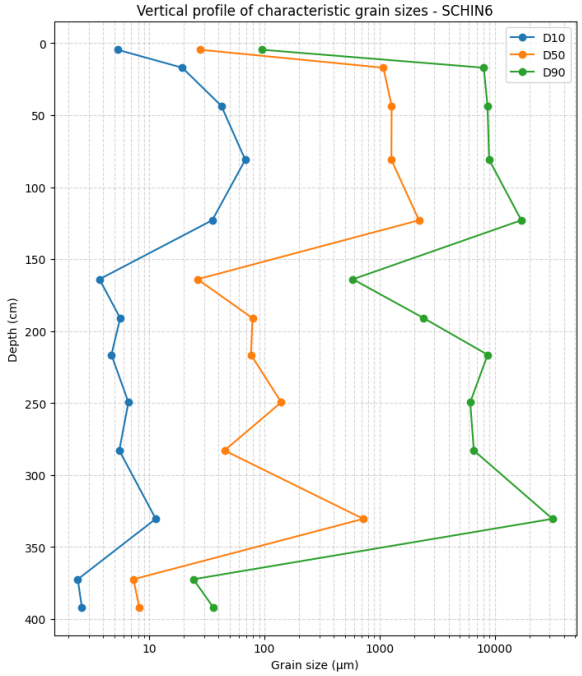

Figure V.35: Characteristic grain size – SCHIN 6.

SCHIN 7

The SCHIN 7 core reached a depth of 300 cm and exhibits a heterogeneous stratigraphy. Three principal units can be distinguished. The general grain size evolution resembles that observed in SCHIN 6, with a coarse surface layer overlying a sandy-silty unit characterized by a reduced gravel content, followed by a nearly gravel-free basal layer. However, the SCHIN 7 sediments are generally coarser than those of SCHIN 6.

The uppermost unit, between 9 and 60 cm, is distinctly dominated by coarse material. Gravel constitutes 53.7 %, sand 30 %, and silt only 16 %. The coarse-to-fine ratio is high, averaging 5.3, reflecting the limited fine matrix within the sedimentary fabric. This deposit is very friable and weakly cohesive, containing numerous centimetre-sized gravels. Grain size parameters are high, with D_{10} at 35.7 µm, D_{50} at 13,500 µm, and D_{90} reaching 30,675 µm.

The intermediate unit, from 60 to 250 cm, shows a relative decrease in coarse fractions accompanied by an increase in silt content to 32 %, a slight increase in sand to 36 %, and a reduction of gravel to 29 %. The coarse-to-fine ratio decreases to 2.2. This unit is characterized by multicoloured sandy pockets and gravel inclusions within a grey silty matrix, comparable to layers identified in SCHIN 3 and SCHIN 6. The presence of substantial gravel is reflected in a D_{90} of 19,997 µm, while D_{10} and D_{50} decrease to 8 µm and 345 µm, respectively.

Finally, the lowermost unit, from 250 to 300 cm, is dominated by sand (54.6 %) and silt (40.6 %), with gravel contributing a mere 2.6 %. The coarse-to-fine ratio of 1.3 indicates a predominance of fine matrix. This unit is more homogeneous and compact than those above, with very few visible coarse elements. Grain sizes correspond accordingly: D_{10} is 4.7 µm, D_{50} is 83 µm, and D_{90} is 235 µm.

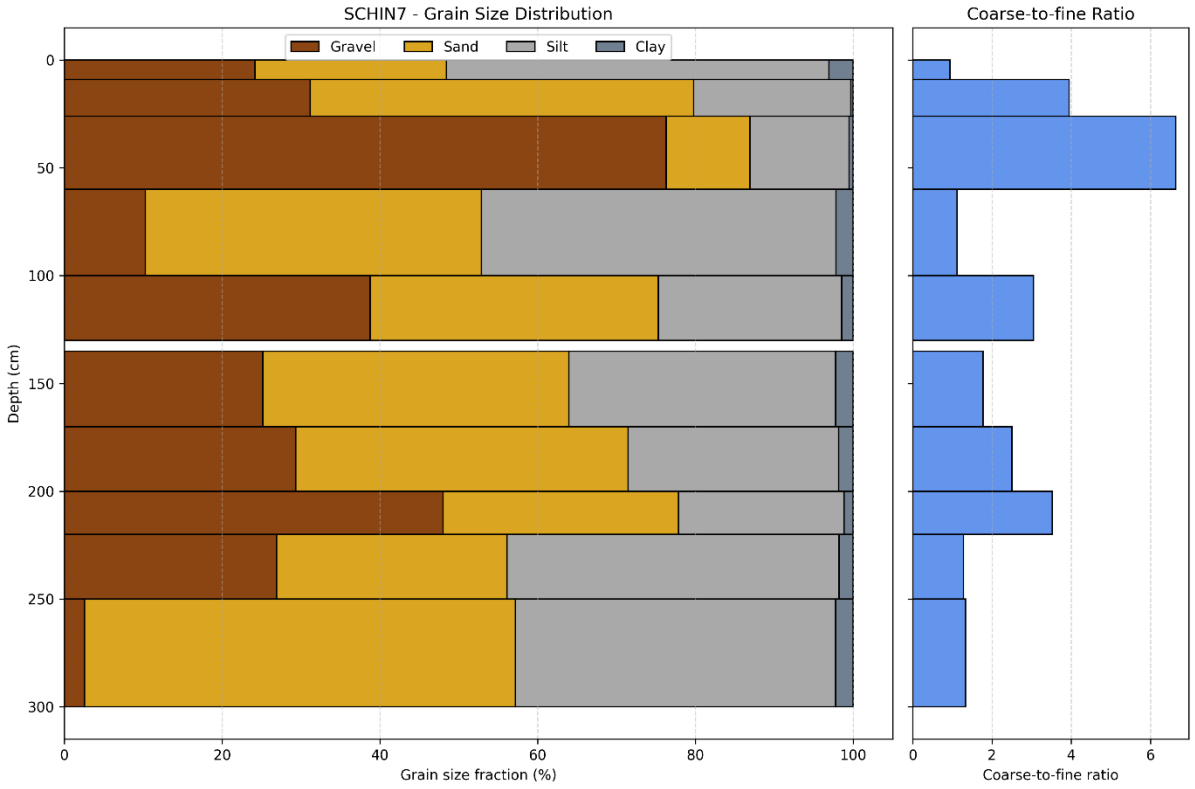

Figure V.36: Profile of the grain size distribution and coarse/fine ratio – SCHIN 7.

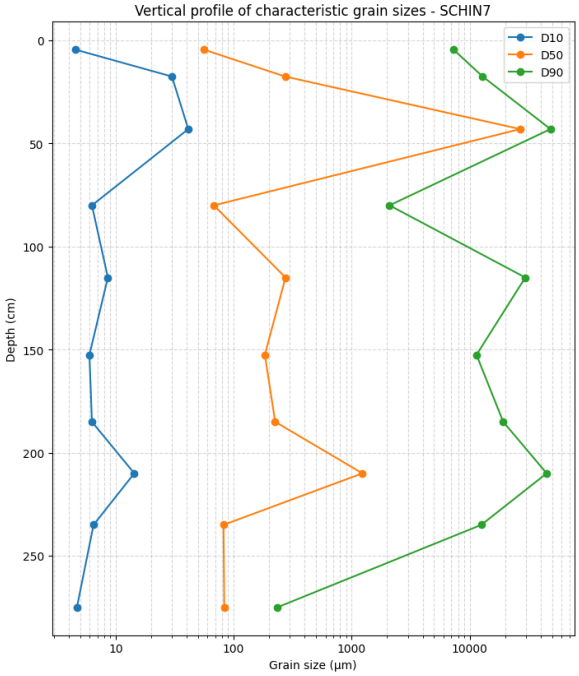

Figure V.37: Characteristic grain size – SCHIN 7.

SCHIN 8

The SCHIN 8 core reached a depth of 351 cm. However, the last five centimetres are partially empty. The hypothesis is that the refusal corresponds to a large stone that was partially drilled but not recovered. The sedimentary sequence is highly heterogeneous, exhibiting pronounced variations in grain size and colour. Consequently, stratification is less distinct than in previous cores, though two main units can be distinguished below the humus layer (0–23 cm), separated by a transitional, predominantly sandy layer.

The upper unit, from 23 to 185 cm, is characterized by fluctuating proportions of gravel, sand, and silt, which are overall relatively evenly distributed. On average, sand constitutes 37 %, gravel 31 %, and silt 30 %. The coarse-to-fine ratio reaches 2.7, indicating a dominance of coarse fractions. Grain size parameters reflect this heterogeneity, with a relatively low D_{10} of 11.5 µm contrasting with elevated D_{50} and D_{90} values of 535 µm and 13,480 µm, respectively.

The transitional unit, between 185 and 200 cm, marks the shift from the coarse upper unit to the fine silty lower unit. Sand becomes clearly dominant at 66.7 %, silt remains stable at 27 %, and gravel decreases sharply to 4.8 %. The coarse-to-fine ratio is 2.5, driven by the sandy dominance. This deposit is more compact than the overlying layers. Grain sizes decrease accordingly, particularly the D_{90}: D_{10} is 6.5 µm, D_{50} is 143 µm, and D_{90} is 392 µm.

The basal unit, from 200 to 346 cm, is dominated by fine material. Silt content rises markedly to 83.5 %, sand decreases to 4 %, and gravel remains steady at 4.8 %. Clay increases to 7.6 %. The coarse-to-fine ratio drops sharply to 0.1, reflecting the dominance of fine fractions. This unit is considerably more homogeneous and compact than the layers above. Grain size metrics corroborate these observations, with D_{10} at 2.2 µm, D_{50} at 7.1 µm, and D_{90} at 161 µm. Very few coarse elements are visible, except for the layer between 298 and 300 cm, which appears to be contamination and is therefore excluded from the results of the lower unit (200-346 cm).

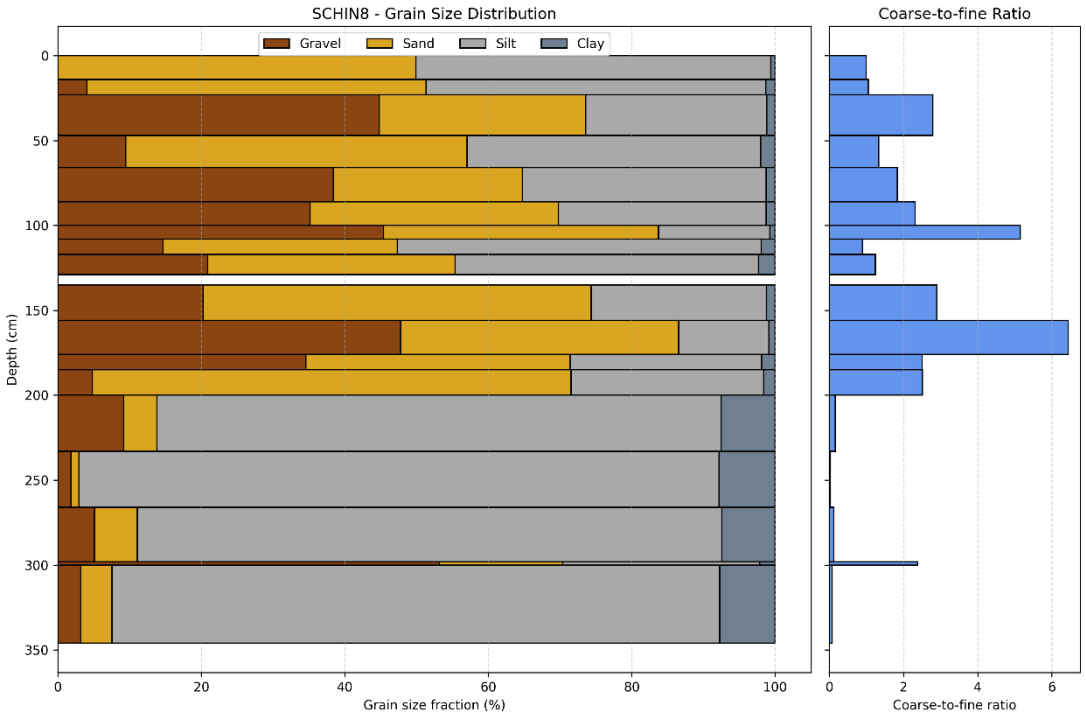

Figure V.38: Profile of the grain size distribution and coarse/fine ratio – SCHIN 8.

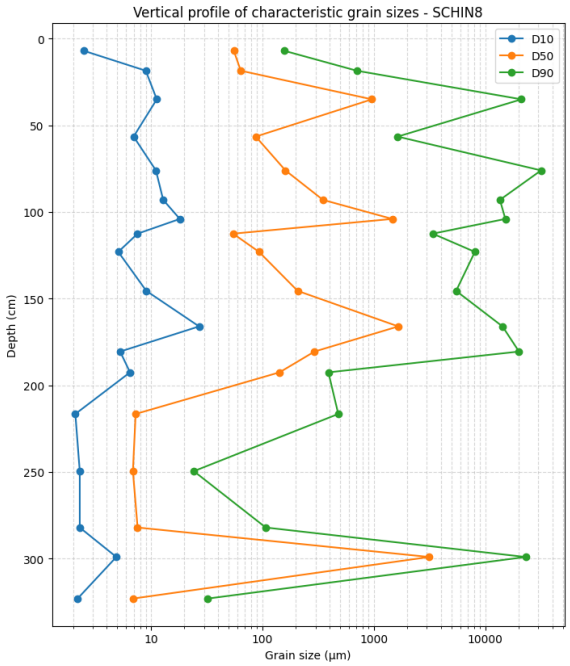

Figure V.39: Characteristic grain size – SCHIN 8.

SCHIN 9

According to field observations, the SCHIN 9 core is located outside the exploited zone. It reaches a depth of 200 cm and is distinguished from other cores by a notably homogeneous sedimentary sequence and pronounced compaction, particularly within the lower intervals. The overall structure remains relatively consistent, with a fairly balanced distribution among gravel, sand, and silt fractions.

The upper unit, from 0 to 170 cm, consists of approximately equal proportions of gravel, sand, and silt, representing 36 %, 30 %, and 32 %, respectively. The coarse-to-fine ratio remains stable throughout this interval, averaging 2.1. Extreme grain size parameters are also relatively constant, with a D_{10} of 8 µm and a D_{90} of 17,300 µm. In contrast, the median grain size (D_{50}) increases with depth, rising from 211 µm (0-114 cm) to 1,480 µm (114-170 cm). This trend indicates a coarsening of the sediment despite the stable granulometric classes.

The intermediate unit, between 170 and 175 cm, is distinct due to a dominance of silt (54.5 %) and reduced proportions of gravel (17 %) and sand (25 %). This shift is reflected in the coarse-to-fine ratio, which decreases to 0.7. Grain size values decrease accordingly, with a D_{10} of 3.5 µm and a D_{50} of 22 µm. Gravel fractions remain present, maintaining a D_{90} of 3900 µm.

The basal unit, from 175 to 200 cm, closely resembles the upper part of the core. Gravel, sand, and silt fractions are balanced at 34 %, 36 %, and 29 %, respectively. The coarse-to-fine ratio slightly increases to 2.3 compared to the core's surface. Grain size parameters are marginally lower, with a D_{10} of 7.1 µm, D_{50} of 543 µm, and D_{90} of 11,850 µm.

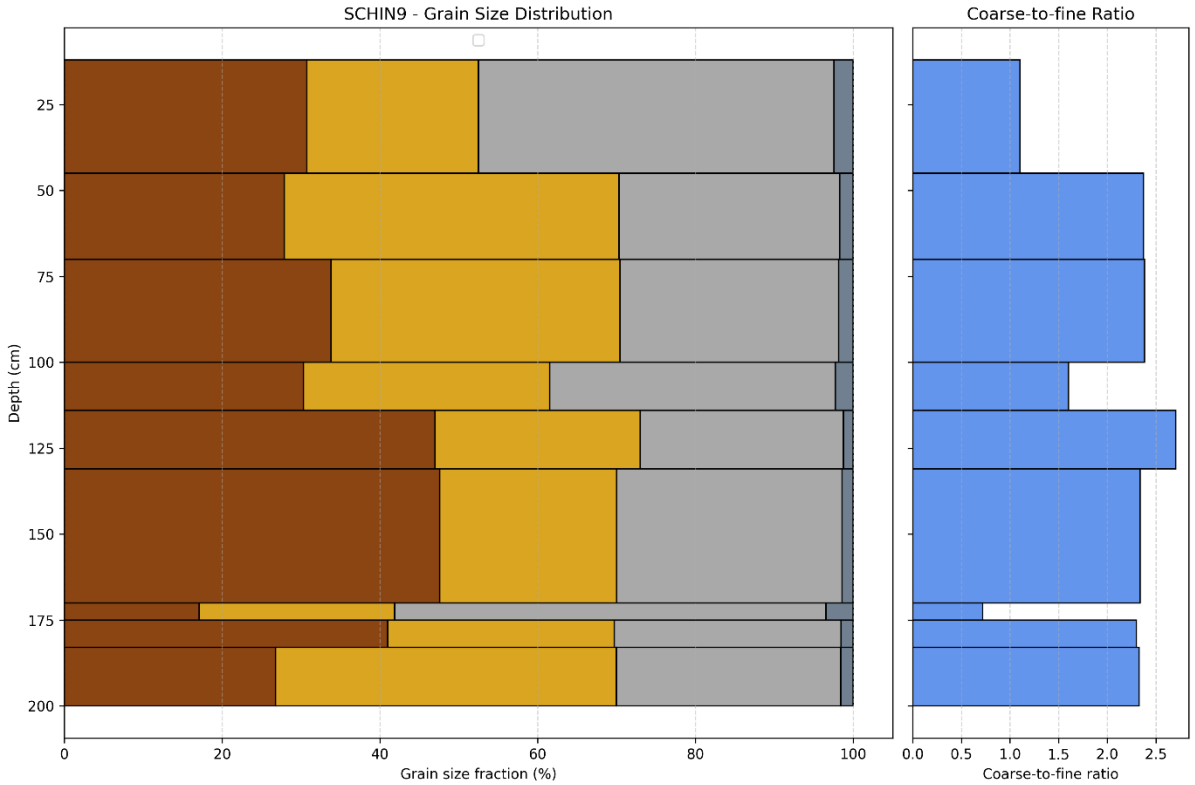

Figure V.40: Profile of the grain size distribution and coarse/fine ratio – SCHIN 9.

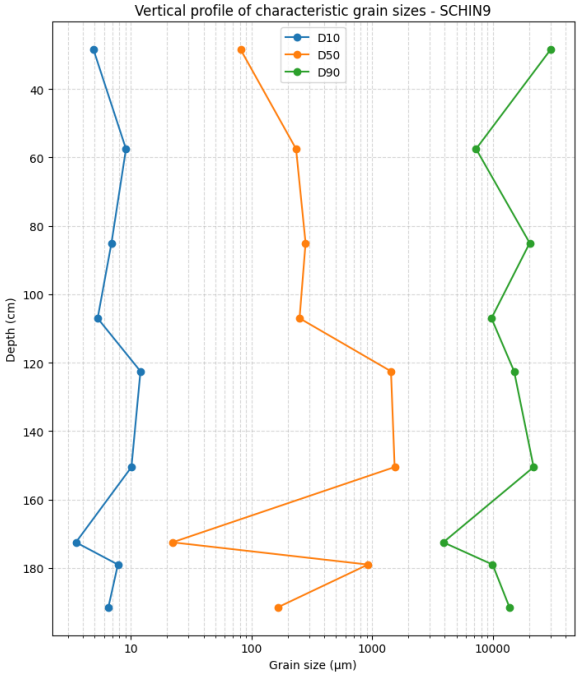

Figure V.41: Characteristic grain size – SCHIN 9.

2.2. Gold panning remains

Regarding gold mining remains, the Schinderbach-A stream is boarded by 171 mounds of varying sizes (Figure V.18). These mounds collectively cover an area of 8,280 m², resulting in an average mound size of approximately 48.5 m². In contrast to the Rougerie site, the mounds are distributed continuously along the entire watercourse. The entire stream is currently covered by forest, and the majority of the area falls within a state-managed reserve.

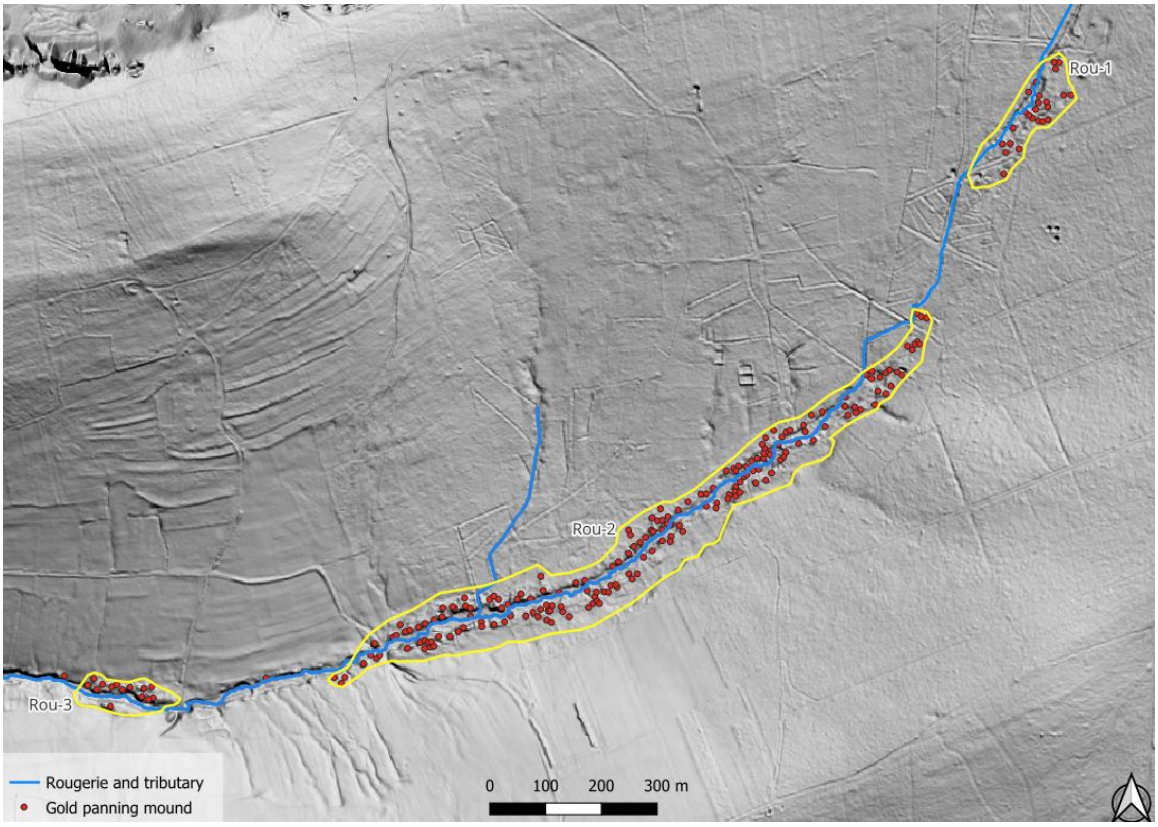

Figure V.42: Group of mounds along the Rougerie.

More specifically, among the 171 mounds present at Schinderbach-A, 92 are classified as narrow mounds (A1), each occupying an average surface area of 35 m² and exhibiting a mean height of 1.1 m. The remaining 79 mounds are categorized as thick mounds, which collectively cover a surface area exceeding that of the narrow mounds, with an average mound size of 64 m² each. No significant size differences were observed between isolated and coalescent mounds. The largest mound within the study area is a coalescent thick mound, measuring 151.7 m². At the confluence, the landscape is predominantly characterized by narrow mounds (Figure V.43), with an average height of 0.8 m and a mean surface area of 39 m². Notably, the largest mound in the study site is situated immediately upstream of this zone. Midway along the longitudinal profile of the stream, a sector is mainly occupied by thick mounds, which exhibit an average height of 1.3 m and a mean surface area of 51.4 m². These thick mounds are predominantly located between the current stream channel and one of the longest paleo-channels.

Six paleochannels (C1) are visible within the study area, all of which flow into the Schinderbach-A and extend along the stream for several tens to hundreds of meters. Three of these are located in the downstream sector of the stream, coinciding spatially with the narrow mounds, and are relatively small, measuring 63 m, 68 m, and 39 m long respectively. Upstream, the other three paleochannels are considerably longer, paralleling the current channel over a combined length of 575 m. The longest paleochannel measures 315 m, while the other two extend 110 m and 151 m. Portions of these paleochannels lie below the present-day level of the Schinderbach-A. Although no active flow is currently observed within these features, they remain notably moist, often exhibiting marsh-like conditions.

Regarding excavations, six excavations sensu stricto have been identified, each covering an average area of 27 m², with a maximum extent of 39 m². It is expected that the spatial footprint of these excavations is smaller than that of the mounds, as the excavations are situated within the mounds themselves.

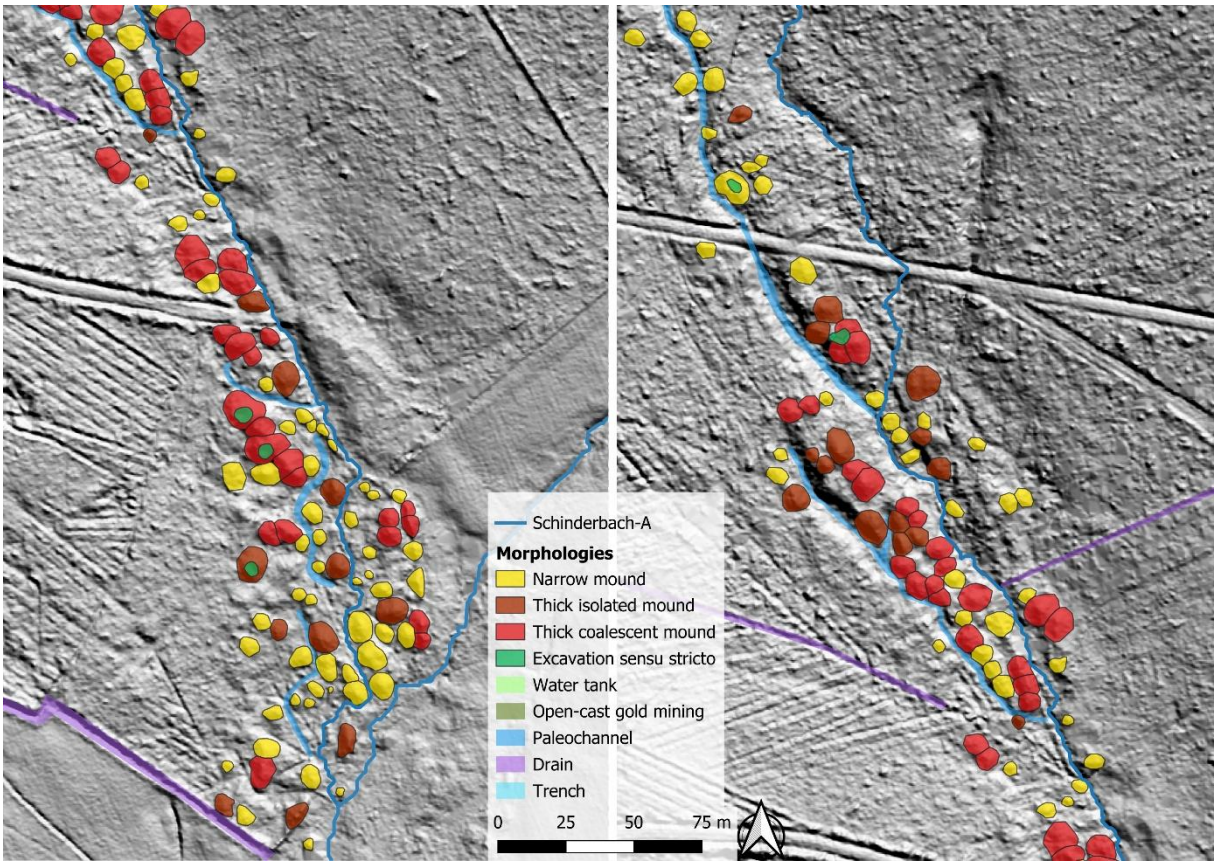

Figure V.43 : Morphologies of the Schinderbach-A.

Several drains (C2) were dug in the 20th century, oriented downslope and perpendicular to the main valley axis. Three principal drains have been identified. The longest extends over 488 m and, actually does not discharge into the Schinderbach-A but in the Schinderbach. However, it is considered in the present analysis because, according to official IGN maps, the Schinderbach-A is depicted as flowing into this drain. In the field, the stream follows the course mapped in this work. The two other main drains measure 101 m and 146 m, respectively, while numerous smaller drains form a dense network along the right-bank slope.

The morphologies along the 'actual' Schinderbach are located predominantly within a perturbed area (E), although certain gold-mining-related landforms remain detectable. A former extraction front is still visible in places, with a cumulative length of approximately 880 m. Among the most noteworthy features along the Schinderbach are three open-cast gold mines, or *aurières*. The first and most extensive one is located in the upstream sector, on the right bank slope, approximately 4 to 5 m above the current stream level. It spans an area of 7,600 m² and is characterized by pronounced topography (Figure V.44a). A second open-cast mining feature, with similar morphological characteristics, including strong relief and substantial surface area, covers 4,650 m² (Figure V.44b). The third and smallest *aurière* has a less pronounced topography and an area of 1,940 m² (Figure V.44c). The two downstream open-cast mines (Figure V.44b & c) are located on the left bank of the Schinderbach, yet they lie significantly higher than the upstream *aurière*, each situated approximately 20 m above the current river channel.

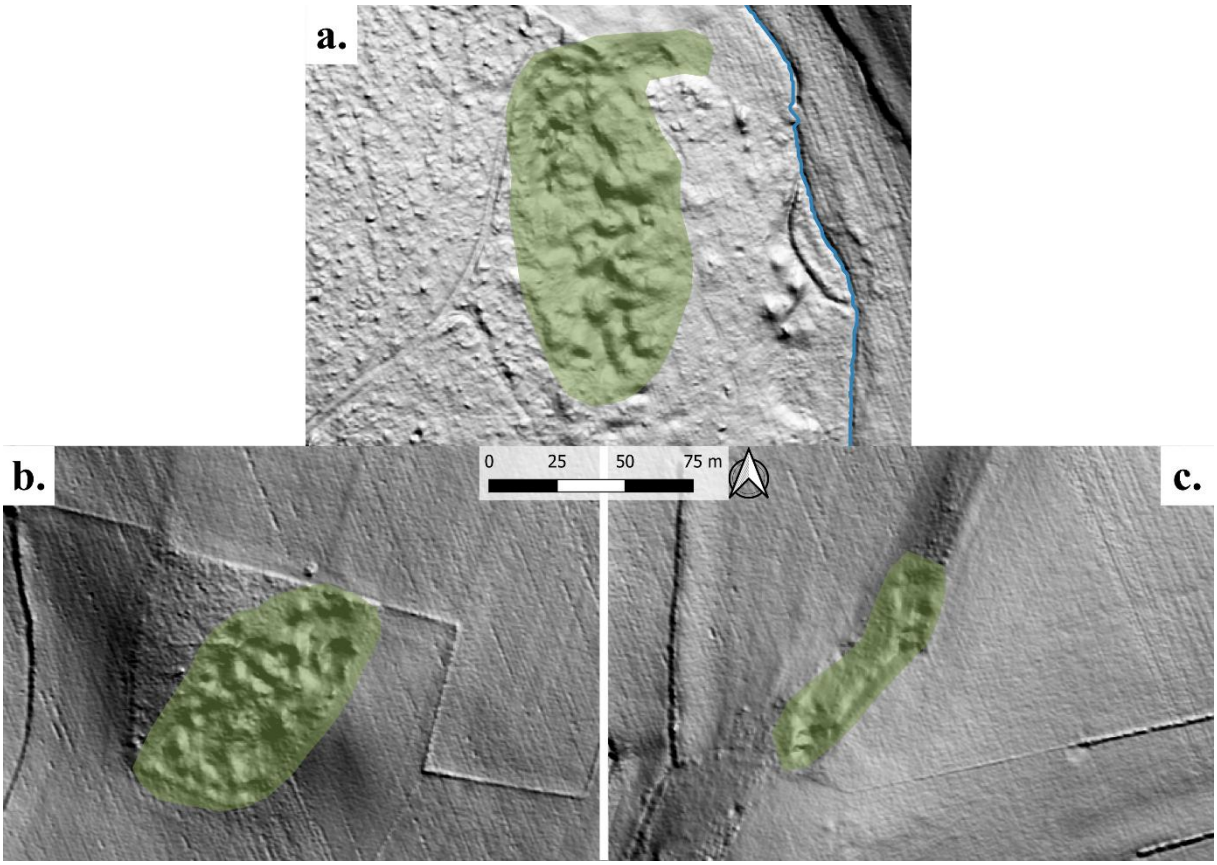

Figure V.44: Open-cast gold mines along the Schinderbach.

Chapter VI:
DISCUSSION

Summary of chapter VI: This chapter builds on the results presented in Chapter V by providing their interpretation. It refines the conceptual model of valley-bottom evolution for the Rougerie and introduces a new model for the Schinderbach-A.

The stated objectives of this study were, first, to date gold-panning mounds and to assess the potential of the OSL method for this purpose. This aspect was addressed in Chapter III. The second objective was to reconstruct past gold-exploitation methods. Several complementary approaches were employed to achieve this goal. Sediment cores were collected along transects perpendicular to the valley axis, providing cross-sectional views of the sedimentary deposits and sequences from the altered bedrock to the surface. The stratigraphic levels identified in the cores were then correlated using topographic surveys, which provided accurate elevation data for each coring site. In addition, two stratigraphic sections were examined, one of which exposed *in situ* deposits along the river channel. These sections were also georeferenced within the same altimetric framework using topographic measurements.

A second way to investigate historical exploitation techniques involved cartographic analysis. LiDAR data were processed in QGIS and ArcGIS Pro to generate a relative elevation map of the terrain on either side of the river. This map was then compared with the hillshade view of the Digital Terrain Model (DTM) to identify and delineate landforms and morphologies present at the study sites.

To classify the observed morphologies, a dedicated typology was developed, drawing on published work from Belgium (Godfroid, 1980; Baudoux, 2018) and France (Trément, 2023b, 2025). On the Stavelot Massif, Godfroid (1980) initiated an early classification of gold-mining features, which is revisited in Chapter I3.1. His framework is of particular interest as it distinguishes three main types of structures: mounds, excavations, and paleochannels. However, it remains general and does not account for the full spectrum of shapes and dimensions within each category. The typology proposed in the present study seeks to capture these variations (Table V.1), building on and refining the three types defined by Godfroid (1980).

Mounds are subdivided according to height into *narrow* or *thick* classes, with a maximum height of 1 m serving as the threshold between the two. Thick mounds, which vary in shape, are further divided into *isolated mounds*, whose boundaries are clearly defined, and *coalescent mounds*, whose perimeters merge partially with adjacent mounds. Narrow mounds are not subdivided in this way, as their boundaries are inherently more difficult to discern in both field observations and mapping due to their small size. Other classification criteria were considered. However, height emerged as the most representative parameter for distinguishing mound types, both in the field and in cartographic analysis.

Excavations are subdivided here into three categories. Godfroid (1980) distinguished only two, based on a depth threshold of 0.3 m: deeper excavations were interpreted as related to gold extraction, whereas shallower ones were associated with gravel exploitation. However, a 0.3 m depth threshold appears too small and insufficiently representative to reliably separate

anthropogenic excavations from natural surface depressions. Moreover, an excavation located at the centre of four coalescent mounds shows no evidence of gold extraction but rather appears to be a remnant of gravel extraction. At 1 m deep, this example further calls into question the relevance of Godfroid's proposed threshold.

In the present study, excavations are instead classified as *excavations sensu stricto*, *water tanks*, and *open-cast gold mines*. Excavations *sensu stricto* correspond to Godfroid's generic category of "excavation" and are not differentiated here by origin, although most appear to be linked to gravel extraction. Water tanks are deeper (1–2 m) and more extensive features. Historically, they served multiple purposes: as reservoirs to maintain sufficient water flow in sluice systems during summer months, or as settling basins for clarifying water prior to gold washing. In the latter case, suspended fine particles would settle in the still water before it was reused for panning. Finally, *open-cast gold mines,* or *aurières* in French, are large and deep open-pit excavations, often exceeding two meters in depth. These are well-documented in France, notably in the Limousin (Trément, 2023). Similar features are reported near the hamlet of Goldgrube, close to Recht (Detaille & Van Eerdenbrugh, 2014), though their auriferous origin has been questioned, partly because no gold has been recovered from associated trenches or tailings. Nevertheless, the authors emphasize that only archaeological excavation could resolve these uncertainties. In this study, such morphologies are included given their proximity to auriferous streams and their close resemblance to exploited alluvial zones.

Godfroid (1980) identified channels as the third major morphological category, defining them as elongated excavations with a length-to-width ratio of at least five. This criterion is retained here, and the "channel" category is subdivided into *paleochannels*, *drains*, and *trenches*. The first two are distinguished primarily by their shape, sinuous versus straight, and by their orientation, parallel or transverse to the valley axis. Many drains have been excavated recently as part of forestry operations, highlighting the importance of distinguishing them from paleochannels, which often have older (natural or anthropogenic) origins. Trenches differ from both in their larger scale and are the product of alluvial removal during gold-mining activities. Such forms are also common in other historical gold-mining regions worldwide that experienced gold rushes (Lapierre et al., 1983; Nelson & Church, 2012; Davies et al., 2019).

Two additional categories have been incorporated into the typology: *mining fronts* and *perturbed areas*. Mining fronts are slope breaks, often located several tens of meters from the active channel, marking the upper limit of sediment removal. Their considerable distance from the valley floor is difficult to explain, as auriferous concentrations at such elevations would be extremely low or absent, making gold washing improbable. A partial explanation may lie in the presence of nearby paleochannels: sediment removal from the slope could have been intended to lower its elevation,. This would enable the excavation of a diversion channel to drain the valley center, where gold was concentrated, thus avoiding work in muddy, waterlogged conditions typical of Belgium's cold climate. This hypothesis remains tentative, relying primarily on spatial association, and would benefit from further investigation through coring, tomography, or high-precision surveying (e.g., total station or drone-based).

Perturbed areas reflect the condition of many auriferous sites today. Anthropogenic pressures such as agriculture and forestry have flattened or destroyed numerous mounds, particularly in

recent decades. In these areas, only topographic remnants persist, their original dimensions and boundaries are no longer clearly identifiable.

1. Rougerie

Coring across the Rougerie alluvial plain revealed a marked contrast between the left and right banks. On the left bank, core ROUG 5 displays a high degree of homogeneity throughout its depth, with no abrupt textural transitions. The deposits are compact, and the gravel, sand, and silt fractions are relatively balanced, although gravel is slightly dominant. This uniformity is reflected in other indicators: the coarse-to-fine ratio remains close to 2, and the median grain size (D_{50}) is consistently around 500 µm. The two coarser intervals observed are attributable to the presence of large pebbles or cobbles, which artificially elevate the D_{50} values.

On the right bank, the cores share similar characteristics, namely pronounced heterogeneity within the upper two meters, where coarse layers alternate with organic-rich horizons and silty-sandy deposits. Compared to ROUG 5, these sediments are wetter, less compact, and noticeably darker (dark grayish brown). They also show no correspondence to any stratigraphic units recorded in section ROUG-A (Figure V.20). This suggests that, for the right-bank cores, the upper two meters represent deposits from post-mining infilling. By contrast, the deposits in ROUG 5 appear unexploited, consistent with observations from section ROUG-A (discussed below).

Beneath these surficial layers, the deposits become more compact and are dominated by a silt-rich matrix. Sparse gravels, occasionally coarse, are still present but differ from those above: they are angular rather than rounded. This shift in texture and gravel shape suggests a transition to unexploited substrate, potentially weathered bedrock. The elevation of these unexploited levels corresponds closely to that of weathered bedrock unit US 12 identified at the base of section ROUG-A. This unit consists of bluish-gray weathered bedrock containing blocks of quartz and quartzite. Such correspondence supports the hypothesis that the top of the weathered bedrock lies approximately two meters below the present alluvial plain surface.

Within the wet, unconsolidated deposits, several coarse layers are interbedded. The deepest marks the contact between *in situ* deposits and post-mining sediments, at a depth of roughly two meters. This layer is the only one present in all cores, including ROUG 5, indicating that it predates gold-mining activity. It is characterized either by a large pebble obstructing the corer or by a compact gravel layer. Its elevation matches that of stratigraphic unit US 11 in ROUG-A. The similarity extends to composition: both consist of clay containing rounded gravels and quartz fragments, although the fine matrix in the core is reddish rather than the bluish hue observed in ROUG-A. In both cases, US 11 or its equivalent overlies weathered bedrock.

A second coarse layer, found at approximately 1.5 m depth in the right-bank cores, is composed of well-rounded gravels 2–3 cm in diameter, embedded in a fine, sand-dominated matrix. This is the least pronounced of the three coarse units.

The third and shallowest coarse layer occurs at about 1 m depth in cores ROUG 1, 2, and 3. It consists of rounded gravels coarser than those in the intermediate layer and is poor in fine matrix. It is overlain by finer, centimetric gravels indicative of a fluvial gravel-bed deposit. ROUG 1 provides a clear example (Figure VI.1), showing centimetric gravels over a layer of coarse, rounded gravels. This unit lies below the present streambed of the Rougerie, which is situated roughly 40 cm beneath the surface, for comparison.

Figure VI.1: Fluvial gravel in ROUG 1 (0-100 cm). Distances from ground surface. Unweighted raw values.

The coarse layers identified in the Rougerie cores may reflect phases of channel stability, during which a dynamic equilibrium existed between erosion and deposition. Under such conditions, the river would have migrated laterally, depositing well-sorted coarse sediments along its course. An alternative hypothesis is that they resulted from an exceptional flood event, which eroded nearby mounds and reworked gravelly and sandy sediments into the floodplain. This second scenario appears more likely for the layer at 1.5 m depth, which is less pronounced in the sequence and characterized by centimetric rounded gravels embedded in a significant sandy matrix, closely resembling the composition of the mining mounds. By contrast, the layer at approximately 1 m depth appears more consistent with the first scenario, representing a period of stability and lateral channel migration. This unit is coarser, better sorted, and more clearly expressed across the cores than the intermediate layer.

The overall stratigraphic sequence in right-bank cores ROUG 1 to 4 closely matches observations by Hanssen *et al.* (1986) from the Ladebach, a stream located midway between the Rougerie and the Schinderbach. At that site, they described infill sequences consisting of "cycles of unconsolidated alluvium, more or less silty, separated by a very thin basal gravel layer." This description aligns well with the Rougerie cores and supports the present interpretation: these deposits likely represent the natural backfilling of trenches excavated during ancient alluvial gold mining.

As noted above, section ROUG-A provides a clear record of naturally deposited valley bottom sediments. Here, the mound deposits (US 2 and US 5) overlie compact *in situ* silts. At the top of US 4, abundant coarse gravels, sometimes including large quartzite blocks at the base of US 3, are embedded in a silty matrix. Some stones are vertically oriented, a feature characteristic of periglacial deposits subjected to processes such as frost heaving and/or solifluction. Consequently, these sediments, along with those below, are interpreted as pre-Holocene in age, most likely dating to the Weichselian glaciation or earlier, and were not disturbed during ancient mining.

Field evidence indicates that ancient miners excavated to depths approximately two meters below the present alluvial surface. When the average depth of the exploitation trench (1.5–2 m) is added, this suggests that 3.5–4 m of alluvium were removed during mining at this location. Coring within the trench, either upstream or downstream, would help determine whether this interpretation applies to the entire excavated area. If confirmed, the total volume extracted for

the trench site alone would approach 90,000 m³ of sediment. This estimate remains tentative, as it is based on a single cross-sectional profile and requires corroboration from additional cores. The uncertainty is further underscored by core ROUG 5, which contains *in situ* deposits despite being located on the inner margin of the trench.

Following mining, the site appears to have undergone a phase of aggradation, as also proposed by Baudoux (2018). Observations reveal an accumulation of approximately 2 m of post-mining sediments, within which two coarse gravel layers occur. These may represent periods of channel stability, during which the stream migrated laterally and deposited coarser material.

The spatial distribution of mounds along the Rougerie is strongly influenced by land use. Mounds occur almost exclusively beneath forest cover not managed for timber production, while they are entirely absent from pasturelands between sites Rou-2 and Rou-3, as well as from heavily drained areas between Rou-1 and Rou-2 and upstream of Rou-1 (Figure V.18). As noted by multiple authors (Gillet, 1970; Detaille & Van Eerdenbrugh, 2014; Baudoux, 2018), many mounds have been destroyed in recent decades by agriculture and forestry. No other gold-mining-related morphologies are found in areas without mounds, further supporting the interpretation that they were removed by more recent land-use practices. This suggests that in the past, mounds and other mining features likely extended at least from Rou-1 to Rou-2, and possibly further upstream and/or downstream.

Within site Rou-2, the arrangement of paleochannels is noteworthy (Figure V.19). The most upstream feature, located on the right bank, may represent a former course of the Heronster stream, as proposed by Baudoux (2018). Our interpretation supports this hypothesis, given the presence of a sinuous depression resembling a watercourse, visible in both the hillshade imagery and the relative elevation model.

A second paleochannel is present on the right bank, downstream from the Heronster-Rougerie confluence. At first glance, this appears to be the former course of the tributary before it was intercepted and redirected perpendicularly by a drainage channel during the 20th century. However, the *Atlas des voiries vicinales* of 1841 (available via the Walloon geoportal; SPW, 2025a) shows that at that time, the Heronster flowed into the upstream paleochannel. This implies that the downstream paleochannel predates the upstream one. The absence of mounds within the channel, and their presence along its margins, suggests that the two features are contemporary. The channel may have been used during ancient times to divert either the Heronster or the Rougerie stream in order to facilitate exploitation of the valley bottom.

1.1. Evolution of the valley

Following the investigation of this site, the conceptual model for the formation of gold-mining-related landforms proposed by Baudoux (2018) can be further refined. The refinements presented here are based on the sediment core analyses and morphological observations detailed in this study and are illustrated in Figure VI.2.

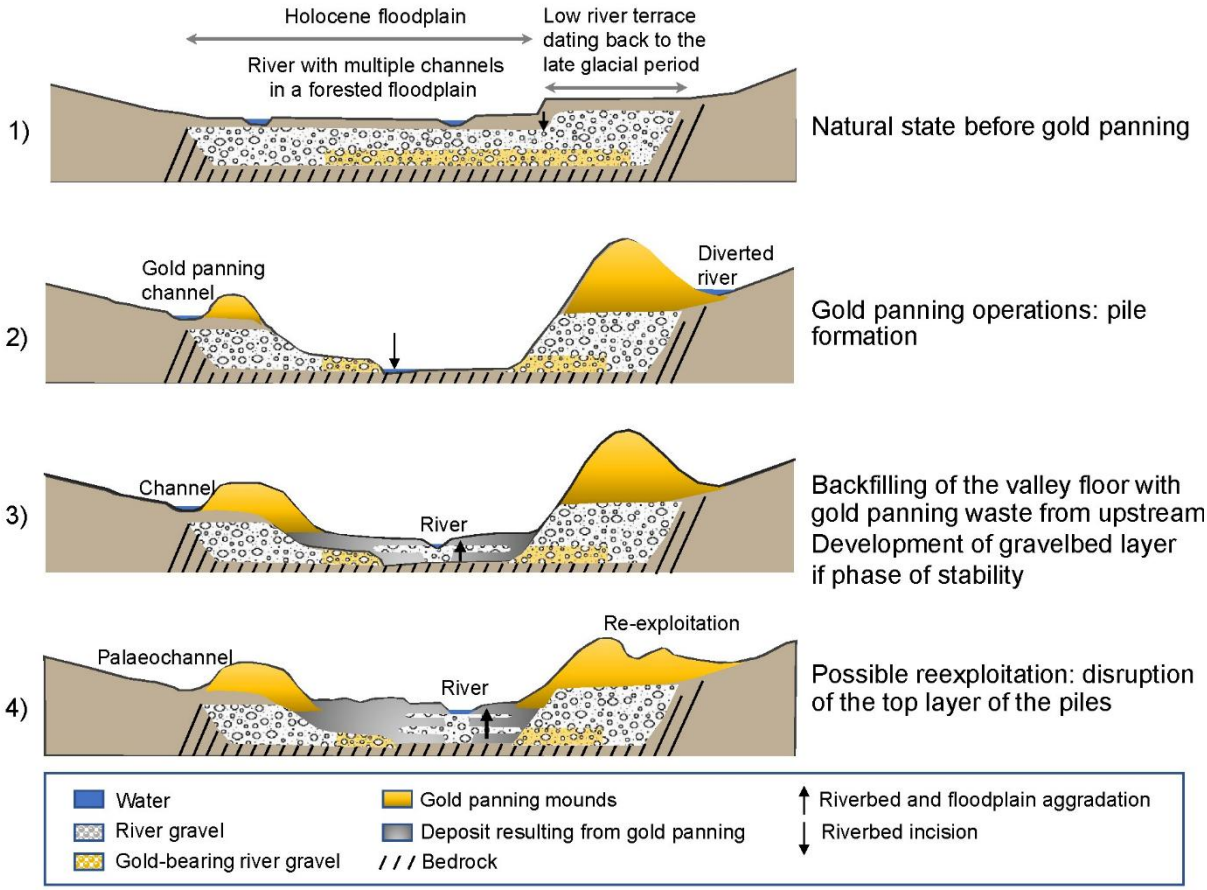

Figure VI.2: Conceptual model of the formation of the gold-mining morphologies (modified from Baudoux, 2018).

The evolution of the valley can be reconstructed as follows (Baudoux, 2018):

1) **Pre-mining state:** The valley exists in its natural, undisturbed condition, with a gravel layer overlying the weathered bedrock. The base of this gravel deposit is enriched in gold. The river flows within the valley floor, occupying its Holocene alluvial plain and potentially dividing into several channels. A low terrace level, dating from the last glaciation, is present alongside the alluvial plain

2) **Gold-mining phase**: Alluvial gold extraction results in an incision of approximately 3.5 to 4 metres, reaching either the top of the weathered bedrock or sedimentary horizons with low gold content. The extracted alluvium is washed and panned: fine particles are transported downstream in suspension, while the coarser residual material is piled into mounds along both sides of the river. The channel is partially or entirely diverted into artificial channels to control flow and partially drain the valley bottom, facilitating mining operations.

3) **Abandonment and initial aggradation**: Abandonment of the site, following the upstream shift of gold-mining activity, leads to increased sediment supply and aggradation of the valley floor. Bank collapses and exceptional floods erodes the mounds, depositing coarse sediments across the alluvial plain.

4) **Post-mining natural evolution** – In the following centuries, aggradation continues under natural processes. The channel floor stabilises approximately two metres above its lowest mining-incision level but remains lower than its pre-mining elevation. A new gravel layer forms during a period of lateral channel migration and relative stability. Some mounds are reworked for gravel extraction, while others are partially eroded. More recently, the construction of drainage channels has likely contributed to fine sediment input.

2. Schinderbach-A

On the Schinderbach-A, the geomorphological and hydrological context differs markedly from that of the Rougerie. The stream length (0.99 km) and catchment area (0.74 km²) are both considerably smaller than those of the Rougerie (5.4 km and 6.65 km², respectively). These differences likely influenced the mining techniques employed, particularly given the steeper gradient and lower discharge. This question is explored here through sediment core analysis and morphological mapping. Nine sediment cores were extracted along a transect across the valley.

Based on field observations, the first and last cores are located outside the exploited area and serves as reference points for grain-size analysis. The granulometric results confirm this assumption: SCHIN 1 and SCHIN 9 display a high degree of compaction and relative homogeneity throughout their depth profiles, with no abrupt granulometric changes. SCHIN 1 is dominated by silt, with gradual variations in gravel content, whereas SCHIN 9 shows a more balanced proportion of gravel, sand, and silt. These contrasts highlight cross-valley differences that must be accounted for when interpreting results from the mined section.

SCHIN 2 was initially hypothesised to be within the mined area, based on topography. However, granulometric results suggest otherwise: the profile is homogeneous, silt-dominated, and devoid of marked textural breaks. Characteristic grain sizes and coarse-to-fine ratios are consistent with undisturbed deposits.

SCHIN 3 is the first core clearly located within the mined zone. The upper 33 cm are composed of gravelly-sandy sediment with almost no clay fraction, typical of mound material. As discussed earlier, the fine fraction was removed during gold-washing, leaving coarse, poorly cohesive residues. Below this layer, the sequence transitions to compact, homogeneous deposits with higher silt and clay content and reduced gravel, resembling the unexploited sediments of SCHIN 2. This suggests that the mound rests directly upon undisturbed valley-fill.

SCHIN 4, positioned along the present channel on the left bank, contains in its upper metre a gravel- and sand-dominated layer interpreted as natural post-mining infill. Gravel content decreases with depth until a large pebble at 109–114 cm. Beneath this lies a highly homogeneous, grey (*gley*) silt with increasing fine sand toward the base, interpreted as weathered bedrock.

SCHIN 5, on the opposite bank, also lacks a clay fraction and is dominated by sand. However, it differs in that it contains two gravel-bed layers overlain by peat accumulations not found in SCHIN 4. The upper gravel bed coincides with the present channel thalweg, suggesting hydraulic connectivity.

SCHIN 6 and SCHIN 7 share similar stratigraphic structures. Both are topped by mound deposits (146 cm thick in SCHIN 6, 60 cm in SCHIN 7) overlying compact, multicoloured silty-sands with scattered fine gravels and sandy veins. These lower units appear undisturbed and likely represent the pre-mining soil surface. Between mound material and the underlying multicoloured deposits lies a uniform grey silty-sand layer with minimal gravel. This intermediate layer may have been disturbed by repeated trampling during mining prior to mound construction. Charcoal recovered from this horizon in SCHIN 6 is therefore likely contemporaneous with gold-mining activity. The basal sediments in SCHIN 6 closely match those of SCHIN 4 (grey (gley) silt) and occur at identical elevations, confirming the interpretation as weathered bedrock.

SCHIN 8, located within a palaeochannel depression, contains 185 cm of heterogeneous fill composed of alternating gravel beds, coarse sands, and sandy silts. Boundaries between layers are sharp, with colours ranging from rust to grey to yellowish. This infill likely represents a mixture of sources: slumping from adjacent mounds and colluvial input from nearby slopes, given the channel's position at the edge of the mined zone. Beneath this infill, light yellow silty deposits are interpreted as weathered bedrock. It lies at the approximate same elevation as both SCHIN 4 and SCHIN 6 weathered bedrock, and is texturally similar, even if it contains sparse fine gravel.

The repeated recovery of weathered bedrock in several cores, combined with the relatively uniform refusal depths in others, allows correlation of these horizons across the transect (Figure V.22).

A useful comparison is provided by Nelson & Church (2012), who described four textural facies of placer-mining tailings: loess, fluvial sand, fluvial gravel, and mass wasting deposits. Based on granulometric composition, they distinguish five particle size classes: silt and clay (SC), sand and granules (SG), gravel (G), cobbles (C), and boulders (B). Although class boundaries were not explicitly stated, visual inspection of their grain-size plots suggests close correspondence to those used in the present study. Among the Schinderbach tailings, SCHIN 3 and SCHIN 7 most closely resemble the "mass wasting" facies, interpreted as resulting from both debris-flow and colluvial processes. SCHIN 6 does not match any of the specific facies but approximates the "average tailings" texture. Even if their study was conducted on deposits from a mountainous river in California (Fraser River) mined during the 19th-century American gold rush, tailing compositions show similarities. This suggests that mining methods have changed little from antiquity to not so long ago.

	Nelson & Church (2012)[11]					SCHIN 3	SCHIN 6	SCHIN 7
	Loess	Fluvial sand	Fluvial gravel	Mass wasting	Average tailings			
Gravel	7	0	50 ± 16	49.4 ± 10	37.2 ± 10	48.8	44.3	43.9
Sand and granules	88	52	43.8 ± 9	34.5 ± 7	47.7 ± 5	33.4	42.1	27.8
Silt and clay	5	48	6.3 ± 3	16.1 ± 7	15.1 ± 5	17.8	13.6	28.3

Table VI.1: Summary table comparing the results of Church & Nelson (2012) with those obtained from cores SCHIN 3, SCHIN 6, and SCHIN 7. Values are expressed as percent by weight.

[11] The boulders and cobbles fractions are excluded from the analysis. Percentages for the SC, SG, and G fractions were subsequently normalised to sum to 100%.

Furthermore, the stratigraphic configuration closely resembles that described for gold-mining tailings deposited during the American gold rush in California (James, 1991). James observed that “tailings occur in horizontally bedded deposits with abrupt contacts between distinct strata. The older alluvium is also stratified, but contacts are gradational.” He further noted that tailings samples contained less clay than samples from the underlying natural soil, and that “the bottom of the tailings at this site fines upward, but the upper is relatively sandy.” This latter observation is also evident in cores SCHIN 3, 6, and 7, although in these cases the gravel fraction remains relatively abundant.

Regarding the morphologies of the Schinderbach-A, mounds are distributed continuously along the stream, with none of the spatial discontinuities observed along the Rougerie. This pattern is largely explained by the continuous forest cover over the stream corridor. The forest here is less intensively drained than along the Rougerie, with only a single drainage network on the right bank.

In terms of mound characteristics, the Schinderbach-A can be divided into three sectors (downstream, central, upstream), differentiated primarily by mound size. The downstream sector, covering the 200 m immediately before the confluence, is dominated by narrow mounds. Here, the stream gradient decreases, the alluvial plain widens, and merges with that of the main Schinderbach. The channel divides into several small distributaries. The central sector, roughly 300 m long, is characterised by thick mounds, both isolated and coalescent. The stream is confined within a deep active gully, with a second, dry gully running parallel to it. The upstream sector, extending to the source, is again marked by narrow mounds, aligned along a paleochannel of the Schinderbach-A that fragments into several shallow gullies.

From these observations, mound characteristics appear to be closely related to flow concentration and alluvial thickness. Where flow is dispersed among shallow channels (as in the upstream and downstream sectors), mound size is smaller, reflecting a lesser accumulation of alluvium. Conversely, the larger mounds in the central sector are associated with one or two deep, concentrated channels, where alluvial accumulation was greater. This hypothesis should be tested by additional coring in the upstream and downstream sectors, to be compared with the cores collected from the central sector in the present study.

Of the six paleochannels identified, three are located in the downstream sector. As noted, this part of the stream is divided into several channels, suggesting these features are abandoned distributaries. The paleochannels upstream of this zone are notably longer and run parallel to the modern channel. Their configuration strongly suggests they represent a former course of the Schinderbach-A. Core analysis supports this interpretation: in one paleochannel, the weathered bedrock lies slightly deeper than in surrounding areas, and is overlain by a layer of rounded gravels, consistent with the deposits of a former riverbed.

Along the main Schinderbach, three *aurières* (open-cast gold mines) were identified and surveyed in the field. They display a chaotic micro-topography reminiscent of mound fields and are extensive in area. They occur between 5 m and 20 m above the present alluvial plain. No clear explanation has yet been found for their location. Comparable topographic settings occur elsewhere along the river, but these sites are not positioned at lithological boundaries, nor near mapped faults. Further detailed investigation of these features would be of interest.

1.2. Evolution of the valley

As with the Rougerie, the analyses conducted at this site allow the reconstruction of the main stages in the formation of the mining-related deposits and landforms. The sequence of events, summarised in Figure VI.3, is based on evidence from sediment cores and the geomorphological analysis of the gold-mining features.

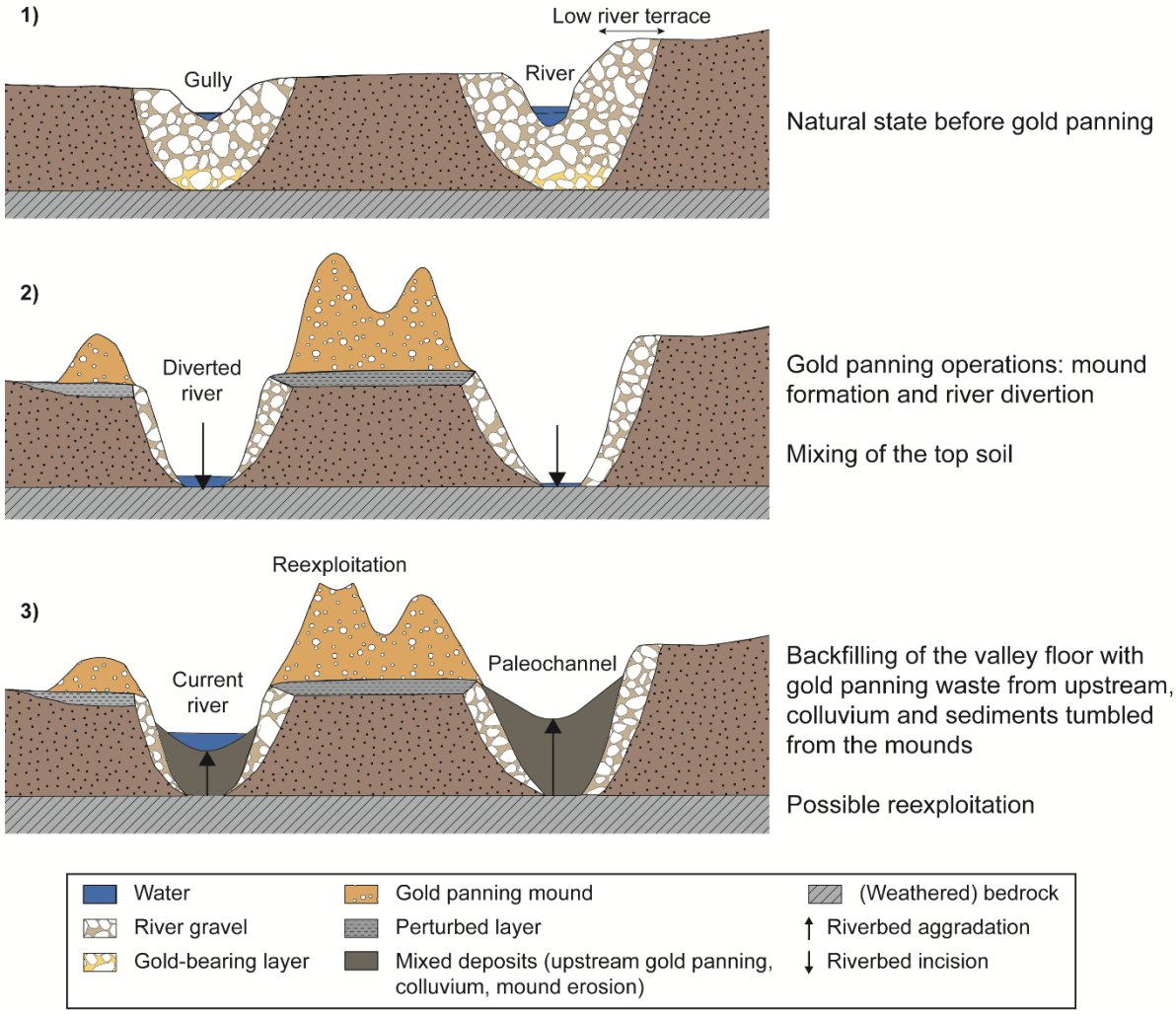

Figure VI.3: Conceptual model of the formation of the gold-mining morphologies.

The valley's geomorphological development likely proceeded as follows:

1) **Pre-mining natural state**: The valley remains in its natural condition, having undergone no major anthropogenic disturbance. The stream flows through a series of small ravines on the valley floor. Gold is concentrated at the base of the gravel layer, in direct contact with the weathered bedrock. A low-terrace level may be present along the main channel. The ravines are separated by colluvial accumulations.

2) **Gold-mining phase**: Mining operations begin, with the main channel probably diverted into an adjacent ravine to lower the water level and facilitate extraction. Auriferous gravels is removed down to the weathered bedrock or to layers of reduced gold content

in both channels. During excavation, sediment removal, and washing, frequent movement of workers around the diverted stream disturbs the uppermost layer of the *in situ* soil adjacent to the working area. Mounds are formed directly on top of the undisturbed deposits surrounding the washing zone, but most prominently on the bank located between the two auriferous gravel bodies.

3) **Post-mining infilling and reworking**: As mining activities shift upstream, the site is abandoned. Depressions are progressively infilled with sediments from multiple sources. Upstream mining releases fine material that accumulates mainly within the active channel, and to a lesser extent in the abandoned channel during flood events. Collapses of adjacent mounds and hillslope-derived inputs also contributes to the infilling. The river's flow removes some of this sediment, maintaining a lower bed level than in the abandoned channel, where sediment removal occurs only during exceptional floods. As observed along the Rougerie, some mounds were later re-exploited for gravel.

3. Général

Based on observations from both study sites, mining activities along the Rougerie appear to have been of greater scale than those at the Schinderbach-A.

Both sites display similar morphological features commonly found along mined streams: mounds, paleochannels, drains, and excavations. However, the Rougerie also exhibits three water reservoirs, a large-scale trench, and a mining front extending for several kilometres, features absent along the Schinderbach-A. These differences are likely explained, at least partially, by the size of the rivers.

The Rougerie is 5.4 km in length, compared with only 0.99 km for the Schinderbach-A, and presents a well-developed floodplain. Gold was therefore probably concentrated across a greater width than at the Schinderbach-A, necessitating larger-scale extraction and the formation of a substantial trench. This process generated larger mounds and required a steady supply of water, prompting the construction of reservoirs for both storage and sediment-settling purposes. This interpretation is supported by the observation that, further upstream, forms indicative of such extensive works (e.g., trench and reservoirs) disappear. Closer to the source, the floodplain narrows, and gold was likely distributed across a smaller area and at shallower depths (a point requiring further verification). Here, less sediment would have needed to be removed, resulting in smaller mounds and eliminating the need for a trench or reservoirs.

At the Schinderbach-A, the alluvial cover is thinner, and the floodplain markedly narrower. Large trenches were unnecessary, especially given that the stream flows within natural gullies along part of its course. It is likely that miners deepened these ravines directly to reach the weathered bedrock, depositing waste material to form mounds on the *in situ* substrate. The main channel was probably diverted into adjacent ravines, and washing operations did not require the construction of reservoirs. Given the short length of the watercourse, it is also plausible that any reservoirs would have had to be situated far upstream, where discharge are insufficient to fill them efficiently.

While river size appears to have been a decisive factor in shaping the mining strategy, a further possibility is that the two sites were exploited at different times. This hypothesis is supported by the radiocarbon dates, which indicate a later phase of activity at the Rougerie (230–380 cal. AD, Roman period) compared with the Schinderbach-A (196–41 cal. BC, Late Iron Age or early Gallo-Roman). The methods employed at the Schinderbach-A may therefore have been more rudimentary and less elaborate than those observed at the Rougerie. This theory still needs to be confirmed or denied by complementary dates.

Chapter VII :
CONCLUSION

This study builds upon more than a century of research on gold exploitation in the Ardennes, contributing significant new insights into both extraction techniques and their chronology. Two primary objectives were established:

1. To test the applicability of Optically Stimulated Luminescence (OSL) dating on gold-panning mounds, assessing both the potential of the method and its limitations.

2. To understand the methods of gold exploitation, through an inventory of mining-related morphologies, the study of exploited valley-bottom deposits, and the reconstruction of their formation.

The two study sites, the Rougerie stream and the Schinderbach-A, proved particularly well-suited for these objectives, thanks to the excellent preservation of gold-mining remains and the limited modern disturbance of their catchment areas. The marked contrast between the two rivers, one entrenched in its alluvial plain and the other flowing through individual gullies, highlighted the decisive role of geomorphological setting in determining extraction strategies.

The application of OSL dating to gold-mining tailings, unprecedented in this context, demonstrated promising potential. Based on the hypothesis that sediment grains were sufficiently exposed to daylight during washing to reset their luminescence signal, nine OSL ages were obtained after a series of test to optimise measurement procedure. The results revealed limitations, primarily linked to incomplete resetting, leading to an overestimation of ages. However, analysis of equivalent dose distributions indicated that a significant number of aliquots displayed low signals compatible with effective bleaching. This suggests that targeted post-measurement statistical treatments could, in future research, yield more accurate ages.

Chronological objectives were nevertheless achieved through two radiocarbon dates obtained from charcoal at the base of two mounds: 230–380 cal. AD for the Rougerie (Roman period) and 196–41 cal. BC for the Schinderbach-A (Celtic or Gallo-Roman period). These constitute the first reliable absolute dates for gold-panning mounds in the Stavelot Massif, providing a new chronological benchmark for the history of settlement and resource exploitation in the Ardennes.

Dating was only one goal of the present work. Understanding how the valleys were exploited required combining landforms mapping, stratigraphic observations, and sediment analyses. A typology of mining-related morphologies was developed to facilitate comparison between sites and to interpret spatial patterns linked to exploitation methods.

Combined with core samples and stratigraphic sections, this approach allowed the clear distinction between *in situ* deposits and post-exploitation infill, the estimation of initial valley-bottom incision, and the reconstruction of subsequent aggradation phases. Lateral channel shifts and mound erosion during stable phases added further complexity to valley evolution.

These results led to a refinement of the conceptual model previously proposed by Baudoux (2018) for the Rougerie, and the development of a new model for the Schinderbach-A. In both cases, mining involved marked incision down to the altered bedrock, followed by partial infilling linked to the downstream transport of fine sediments from upstream workings and the erosion of mounds. Periods of channel stability produced well-sorted gravel deposits associated with lateral channel migration. Despite modern reworking of gravels, the ancient mining features, such as mounds, trenches, and paleochannels, remain clearly visible in the landscape.

By combining OSL dating, radiocarbon chronology, morphological typology, and sedimentology, this study provides a complete, interdisciplinary, reconstruction of ancient gold exploitation in the Ardennes. It refines existing conceptual models, updating that of Baudoux (2018) for the Rougerie and establishing a new one for the Schinderbach-A, and offers the first securely dated framework for these gold-panning mounds in the Stavelot Massif.

Yet important questions remain and other avenues could be investigated, such as: targeted coring in peat-filled depressions to identify and date activity phases, magnetic susceptibility analyses to characterise sediment sources, improved OSL applications using post-measurement statistical filtering to isolate well-bleached grains.

Such approaches, applied across a larger sample of auriferous valleys, would make it possible to develop the technical and chronological history of gold mining in the Ardennes, and to situate these activities more firmly within the broader context of European mining history.

BIBLIOGRAPHY

Adamiec, G. & Aitken, M.J. (1998). Dose-rate conversion factors: update. *Ancient TL*, 16(2), 37-50. https://doi.org/10.26034/la.atl.1998.292

Agostinetti, P.P., Bergonzi, G., Cattin, M., Del Soldato, M., Gambari, F.M. & Tizzoni, M. (1995). Gold in the Alps: A view from the south. *In* Morteani, G. & Northover, J.P. (eds). *Prehistoric gold in Europe: Mines, metallurgy and manufacture.* Dordrecht: Springer, Applied Sciences, 280, 199-218. https://doi.org/10.1007/978-94-015-1292-3_14

Aitken, M.J. (1985). *Thermoluminescence dating.* London : Academic Press, 359 p. ISBN: 0120463814

Aitken, M.J. (1998). *An introduction to optical dating: The dating of Quaternary sediments by the use of photon-stimulated luminescence.* Oxford: Oxford University press, 267 p. ISBN: 0198540922

Aitken, M.J., Tite, M.S. & Reid, J. (1964). Thermoluminescent dating of ancient ceramics. *Nature*, 202, 1032-1033. https://doi.org/10.1038/2021032b0

Aitken, M.J., Zimmerman, D.W. & Flemming, S.J. (1968). Thermoluminescent dating of ancient pottery. *Nature*, 219, 442-445. https://doi.org/10.1038/219442a0

Ancel, B., Cauuet, B. & Cowburn, I. (2000). *The Dolaucothi gold mines, Carmarthenshire (Wales, U.K.).* Archaeological appraisal: Intermediate report, 85 p. https://www.researchgate.net/publication/284026447_The_Dolaucothy_Gold_Mines_Carmarthenshire_Wales_UK, accessed on April 30, 2025.

Ankjaergaard, C. & Murray, A.S. (2007). Total beta and gamma dose rates in trapped charge dating based on beta counting. *Radiation measurements*, 42(3), 352-359. https://doi.org/10.1016/j.radmeas.2006.12.007

Auclair, M., Lamothe, M. & Huot, S. (2003). Measurement of anomalous fading for feldspars IRSL using SAR. *Radiation measurements*, 37(4-5), 487-492. https://doi.org/10.1016/S1350-4487(03)00018-0

Bastin, J. (1911). Anciennes mines d'or dans l'Ardenne septentrionale. *Annales du XXIIe congrès de la fédération des archéologues et historiens de Belgique*, 2, 639-655.

Bateman, M.D. (ed.) (2019). *Handbook of luminescence dating*. Dunbeath: Whittles publishing, 416 p. https://doi.org/10.2138/gselements.16.2.146

Baudoux, A. (2018). *Impacts de l'orpaillage sur les rivières ardennaises.* Master thesis in Geography, University of Liege, 134 p. http://hdl.handle.net/2268.2/5562, accessed on May 6, 2025.

Beckers, A. (2010). *Facteurs de propagation des knickpoints dans un réseau hydrographique. Modélisation dans le bassin de l'Ourthe.* Master thesis in Geography, University of Liege, 170 p. https://orbi.uliege.be/bitstream/2268/98422/1/memoire_abeckers.pdf, accessed on August 9, 2025.

Blaber, M.G., Ford, M.J. & Cortie, M.B. (2009). The physics and optical properties of gold. *In* Corti, C. & Holliday, R., *Gold: science and applications*. Boca Raton (USA) : Taylor & Francis group, CRC press, 13-30. http://dx.doi.org/10.1201/9781420065268-c2

Boericke, W.F. (1936). *Prospecting and operating small gold placers.* Second edition. New York: John Wiley & Sons, 144 p.

Bøtter-Jensen, L. (1997). Luminescence techniques : instrumentation and methods. *Radiation measurements*, 27(5-6), 749-768. https://doi.org/10.1016/S1350-4487(97)00206-0

Bøtter-Jensen, L., Andersen, C.E., Duller, G.A.T. & Murray, A.S. (2003). Developments in radiation, stimulation and observation facilities in luminescence measurements. *Radiation measurements*, 37(4-5), 535-541. https://doi.org/10.1016/S1350-4487(03)00020-9

Bøtter-Jensen, L., Thomsen, K.J. & Jain, M. (2010). Review of optically stimulated luminescence (OSL) instrumental developments for retrospective dosimetry. *Radiation measurements*, 45(3-6), 253-257. https://doi.org/10.1016/j.radmeas.2009.11.030

Bouezmarni, M. & Debbaut, V. (2013). *Carte hydrogéologique de Wallonie : Bovigny – Beho 56/5-6 (notice epxlicative).* Namur: Service Public de Wallonie, DGARNE-DGO3, 81 p. https://environnement.wallonie.be/files/eDocs%20Environnement/Milieux/Eau/Hydrogeologie/cartosig/Notices/5656.pdf, accessed on May 24, 2025.

Bruni, Y. & Hatert, F. (2017). Étude minéralogique de l'or et de ses minéraux accompagnateurs sur le pourtour du massif cambro-ordovicien de Serpont, Belgique. *Bulletin de la société royale des sciences de Liège*, 86, 113-168. https://hdl.handle.net/2268/211424

Burnham, B. & Burnham, H. (2004). *Dolaucothi-Pumsaint: Survey and excavations at a roman gold-mining complex 1987-1999.* Oxford: Oxbow books, 339 p. ISBN: 1842171127

Buylaert, J.-P., Jain, M., Murray, A.S., Thomsen, K.J., Thiel, C. & Sohbati, R. (2012). A robust feldspar luminescence dating method for Middle and Late Pleistocene sediments. *Boreas*, 41(3), 435-451. https://doi.org/10.1111/j.1502-3885.2012.00248.x

Buylaert, J.-P., Újvári, G., Murray, A.S., Smedley, R.K. & Kook, M. (2018). On the relationship between K concentration, grain size and dose in feldspar. *Radiation measurements*, 120, 181-187. https://doi.org/10.1016/j.radmeas.2018.06.003

Cauuet, B. (1991). L'exploitation de l'or en Limousin, des Gaulois aux Gallos-Romains. *Annales du Midi*, 103(194), 149-181. https://doi.org/10.3406/anami.1991.2292

Cauuet, B. (2004). *L'or des Celtes du Limousin.* Limoges: Culture & patrimoine en Limousin, 123 p. https://www.archeomine.org/bcauuet/cauuet-or-celtes.pdf, accessed on April 29, 2025.

Cauuet, B. (2005). Les mines d'or antiques d'Europe hors péninsule Ibérique. État des connaissances et travaux récents. *Pallas*, 67, 241-291. https://www.jstor.org/stable/43605698

Cauuet, B. & Tãmas, C.G. (2017). Une source de l'or pyrénéen et son exploitation dans l'Antiquité. *Treballs d'arqueologia*, 21, 205-222. https://doi.org/10.5565/rev/tda.63

CentipedeRTK. (2025). *CentipedeRTK : Le Real Time Kinematic collaborative, ouvert et open source.* Réseau Centipede RTK. https://docs.centipede.fr/, accessed on July 6, 2025.

Cesar, E., Ruthy, I. & Dassargues, A. (2017). *Carte hydrogéologique de Wallonie : Bütgenbach – Büllingen – Losheimergraben 50/7-8, 50A/5 (notice explicative).* Namur: Service Public de Wallonie, DGARNE-DGO3, 114 p. https://environnement.wallonie.be/files/eDocs%20Environnement/Milieux/Eau/Hydrogeologie/cartosig/Notices/5078.pdf, accessed on July 3rd, 2025.

Chamberlain, E.L., Wallinga, J. & Shen, Z. (2018). Luminescence age modelling of variably-bleached sediment: Model selection and input. *Radiation measurement*, 120, 221-227. https://doi.org/10.1016/j.radmeas.2018.06.007

Chauris, L. (1989). Les exploitations minières dans le massif armoricain. Déclin ou progrès. *Norois*, 141, 5-32. https://doi.org/10.3406/noroi.1989.4414

Cordier, S. (2010). Optically stimulated luminescence dating: procedures and applications to geomorphological research in France. *Géomorphologie : relief, processus, environnement*, 16(1), 21-40. https://doi.org/10.4000/geomorphologie.7785

Cresswell, A.J., Carter, J. & Sanderson, D.C.W. (2018). Dose rate conversion parameters : Assessment of nuclear data. *Radiation measurements*, 120, 195-201. https://doi.org/10.1016/j.radmeas.2018.02.007

Cuningham, A.C. & Wallinga, J. (2010). Selection of integration time intervals for quartz OSL decay curves. *Quaternary geochronology*, 5(6), 657-666. https://doi.org/10.1016/j.quageo.2010.08.004

Dalmont, M.A. (2013). *L'exploitation de l'or dans les Pays de la Loire et en IIIe et Vilaine aux périodes protohistoriques et gallo-romaines.* Unpublished Master thesis, Nantes, University of Nantes, 278 p.

Davies, P., Lawrence, S., Turnbull, J., Rutherfurd, I., Grove, J., Silvester, E. & Macklin, M. (2019). Mining modification of river systems: A case study from the Australian gold rush. *Geoarcheology*, 35, 384-399. https://doi.org/10.1002/gea.21775

De Corte, F., Vandenberghe, D., De Wispelaere, A., Buylaert, J.-P. & Van den Haute, P. (2006). Radon loss from encapsulated sediments in Ge gamma-ray spectrometry for the annual radiation dose determination in luminescence dating. *Czechoslovak journal of Physics*, 56(4), D183-D194. https://doi.org/10.1007/s10582-006-0504-9

Dejonghe, L. (2000). L'or des Ardennes. *Athéna*, 164, 69-71. https://www.researchgate.net/publication/283482683_L'or_des_Ardennes, accessed on May 6, 2025.

Deprez, S., De Dapper, M., Almeida, N., Carvalho, J., De Paepe, P., Cunha, P., Van Damme, D., Vandenberghe, D. & Vermeulen, F. (2018). Roman gold exploitation in the Tagus river valley – the Conhal of Arneiro (northeast Alentejo, Portugal): a geoarchaeological case study. *In* Tristant, Y. & Ghilardi, M. (eds). *Landscape archaeology: Egypt and the Mediterranean World.* Cairo: Institut français d'archéologie orientale, 205-221.

De Rauw, H. (1912). L'or en Ardenne (1ère note). *Annales de la société géologique de Belgique*, 40, 104-114.

De Rauw, H. (1920). Les alluvions aurifères de la Haute Belgique. *Annales de la société géologique de Belgique*, 43, 270-278.

Destatte, P. (2013). *Histoire succincte de la Wallonie.* Namur: Institut Destrée, 157 p. https://ediwall.wallonie.be/histoire-succincte-de-la-wallonie-2013-numerique-103675, accessed on April 10, 2025.

Detaille, J. (2012). De l'or en Ardenne : "I see wonderful things". *Association des géologues amateurs de Belgique*, 45(2), 1-15.

Detaille, J. & Van Eerdenbrugh, B. (2014). *Les miettes des miettes… Chercheurs d'or en Belgique.* Self-publishing, 127 p. https://www.agab.be/orpaillage/livre%20complet.pdf, accessed on May 6, 2025.

Dewalque, G. (1896). Découverte de l'or en Ardenne. *Annales de la société géologique de Belgique*, 23, 43-44.

Dewalque, G. (1897). L'exploitation de l'or en Ardenne. *Annales de la société géologique de Belgique*, 24, 63-64.

DeWitt, R. (2015). Radiation and Radioactivity. *In* Rink, W.J. & Thompson, J.W. (eds) *Encyclopedia of scientific dating methods.* Dordrecht: Springer, 390-404. https://doi.org/10.1007/978-94-007-6304-3_81

Domergue, C. (1990). *Les mines de la péninsule Ibérique dans l'Antiquité romaine.* Rome: Collection de l'école française de Rome, 625 p. https://www.persee.fr/doc/efr_0000-0000_1990_ths_127_1, accessed on April 29, 2025.

Domergue, C. & Hérail, G. (1999). Conditions de gisements et exploitation antique à Las Médulas (León, Espagne). *L'Or dans l'Antiquité. Aquitania supplement*, 9, 93-116. https://horizon.documentation.ird.fr/exl-doc/pleins_textes/pleins_textes_7/b_fdi_51-52/010019968.pdf, accessed on April 29, 2025.

Dong, P. & Chen, Q. (2017). *LiDAR remote sensing and applications.* 1st edition. Boca Raton: CRC press, 220 p. https://doi.org/10.4324/9781351233354

Duller, G.A.T. (1991). Equivalent dose determination using single aliquots. *Nuclear tracks and radiation measurements*, 18(4), 371-378. https://doi.org/10.1016/1359-0189(91)90002-Y

Duller, G.A.T. (2003). Distinguish quartz and feldspar in single grain luminescence measurements. *Radiation measurements*, 37(2), 161-165. https://doi.org/10.1016/S1350-4487(02)00170-1

Duller, G.A.T. (2008). *Luminescence dating: Guidelines on using luminescence dating in archaeology.* Swindon: English heritage, 43 p. https://www.researchgate.net/publication/297669518_Luminescence_Dating_Guidelines_on_using_luminescence_dating_in_archaeology, accessed on March 16, 2025.

Duller, G.A.T. (2015). Luminescence dating. *In* Rink, W.J. & Thompson, J.W. (eds) *Encyclopedia of scientific dating methods.* Dordrecht: Springer, 390-404. https://doi.org/10.1007/978-94-007-6304-3_125

Dumont, J.-M. (1976). Haldes d'orpaillage et réserves naturelles en Ardenne. *Glain et Salm, Haute-Ardenne*, 4, 64-71.

Dumont, J.-M. (1979). Première datation d'un tertre d'orpaillage en Ardenne. *Glain et Salm, Haute-Ardenne*, 10, 87-88.

Dumont, J.-M. (1980). Orpaillage celtique à l'époque de la Tène au Plateau des Tailles. *Glain et Salm, Haute-Ardenne*, 13, 42-45.

Draily, C. (2022). État des connaissances, perspectives de recherches et révision des datations des tertres d'orpaillage dits « celtes » de l'Ardenne belge. *Archéo-Situla*, 40, 121-134. https://www.researchgate.net/publication/382918580_Etat_des_connaissances_perspectives_de_recherches_et_revision_des_datations_des_tertres_d'orpaillage_dits_celtes_de_l'Ardenne_belge, accessed on May 6, 2025.

Draily, C., Marion, J.-M., Van Eerdenbrugh, B. & Hannut, F. (2022). La pelle du *Trou des Massotais/Âs Massotais* (Plateau des Tailles, Vielsalm, Belgique). Un témoignage exceptionnel de l'activité minière en Ardenne à la fin de l'époque romaine. *Archéo-Situla*, 40, 135-154. https://www.researchgate.net/publication/382918477_La_pelle_du_Trou_des_Massotais_As_Massotais_Plateau_des_Tailles_Vielsalm_Belgique_Un_temoignage_exceptionnel_de_l'activite_miniere_en_Ardenne_a_la_fin_de_l'epoque_romaine, accessed on May 6, 2025.

Ferguson, R.I., Church, M., Rennie, C.D. & Venditti, J.G. (2015). Reconstructing a sediment pulse: Modeling the effect of placer mining on Fraser river, Canada. *Journal of geophysical research: Earth surface*, 120, 1436-1454. https://doi.org/10.1002/2015JF003491

Fernández-Lozano, J. & Sanz-Ablanedo, E. (2021). Unravelling the morphological constraints on roman gold mining hydraulic infrastructure in NW Spain. A UAV-derived photogrammetric and multispectral approach. *Remote sensing*, 13(2), 291. https://doi.org/10.3390/rs13020291

Fernández-Lozano, J., Gutiérrez-Alonso, G., Fernández-Morán, M.Á.(2015). Using airborne LiDAR sensing technology and aerial orthoimages to unravel roman water supply systems and gold works in NW Spain (Eria valley, León). *Journal of archaeological science*, 53, 356-373. https://doi.org/10.1016/j.jas.2014.11.003

Fernández-Lozano, J., Palao-Vicente, J.J., Blanco-Sánchez, J.A., Gutiérrez-Alonso, G., Remondo, J., Bonachea, J., Morellón, M. & González-Díez, A. (2019). Gold-bearing Plio-Quaternary deposits: Insights from the airborne LiDAR technology into the landscape evolution during the early Roman mining works in north-west Spain. *Journal of archaeological science: Reports*, 24, 843-855. https://doi.org/10.1016/j.jasrep.2019.03.001

Galbraith, R.F. & Roberts, R.G. (2012). Statistical aspects of equivalent dose and error calculation and display in OSL dating: An overview and some recommendations. *Quaternary geochronology*, 11, 1-27. https://doi.org/10.1016/j.quageo.2012.04.020

Ghezzi y Alvarez, A. (2022). Ruina montium : l'oro di Roma nelle miniere di Las Médulas. *Firenze architettura*, 26(1), 162-173. https://doi.org/10.36253/FiA-13944

Gillet, J.-C. (1970). Les gisements aurifères de Belgique. *Bulletin de la société royale Belge d'études géologiques et archéologiques*, 21, 121-163.

Godfrey-Smith, D.I., Huntley, D.J. & Chen, W.-H. (1988). Optical dating studies of quartz and feldspar sediments extracts. *Quaternary science reviews*, 7(3-4), 373-380. https://doi.org/10.1016/0277-3791(88)90032-7

Godfroid, J. (1980). *Étude géomorphologique des vestiges d'orpaillage dans le bassin de la haute Amblève.* Unpublished master thesis in Geography, Liege, University of Liege, 141 p.

Graf, W.L. (1979). Mining and channel response. *Annals of the association of American geographers*, 69(2), 262-275. https://www.jstor.org/stable/2563070

Grailet, L. (1998). *De l'or en Ardenne.* Tongres : Self-publishing, 112 p.

Grierson, P. (1999). *Byzantine coinage*. Second edition. Washington, D.C.: Dumbarton Oaks research library and collection, 68 p. http://www.serbianmedievalcoins.com/resources/Byzantine%20Coinage%20Philip%20Grierson.pdf, accessed on July 1st, 2025.

Guérin, G., Combès, B., Lahaye, C., Thomsen, K.J., Tribolo, C., Urbanova, P., Guibert, P., Mercier, N. & Valladas, H. (2015) Testing the accuracy of a Bayesian central-dose model for single-grain OSL, using known-age samples. *Radiation measurements*, 81(1), 62-70. https://doi.org/10.1016/j.radmeas.2015.04.002

Hanssen, E. & Viaene, W. (1979). Données minéralogiques sur les paillettes d'or de la bordure S. et S.E. du massif de Stavelot. *Bulletin de la société belge de géologie*, 88(3), 225-235. https://biblio.naturalsciences.be/rbins-publications/bulletin-de-la-societe-belge-de-geologie/088%20-%201979/bsbg_88_1979_p225-235.pdf, accessed on May 10, 2025.

Hanssen, E., Viaene, W. & Gullentops, F. (1986). Stratigraphie et minéralogie des alluvions aurifères de la bordure SE du massif de Stavelot, Ardennes belges. *Aardkundige medelingen*, 3, 95-106.

Harding, J. & Boothroyd, I. (2004). Impacts of mining. *In* Harding, J., Mosley, P., Pearson, C. & Sorell, B. (eds). *Freshwaters of New Zealand*. Christchurch: New Zealand hydrological and limnological societies, 36.1-36.10. https://www.researchgate.net/publication/239537966_Chapter_36_Impacts_of_mining, accessed on June 30, 2025.

Hilmes, M.M. & Wohl, E.E. (1995). Changes in channel morphology associated with placer mining. *Physical geography*, 16(3), 223-242. https://doi.org/10.1080/02723646.1995.10642551

Hossain, S.M. (2003). *A critical comparison and evaluation of methods for the annual radiation dose determination in the luminescence dating of sediments.* Phd thesis in Science, Ghent, Ghent University, 192 p. https://doi.org/1854/265

Huntley, D.J. & Lamothe, M. (2001). Ubiquity of anomalous fading in K-feldspars and the measurement and correction for it in optical dating. *Canadian journal of earth sciences*, 38(7), 1093-1106. https://doi.org/10.1139/e01-013

Huntley, D.J., Godfrey-Smith, D.I. & Thewalt, M.L.W. (1985). Optical dating of sediments. *Nature*, 313, 105-107. https://doi.org/10.1038/313105a0

Hütt, G., Jaek, I. & Tchonka, J. (1988). Optical dating: K-feldspars optical response stimulation spectra. *Quaternary science reviews*, 7(3-4), 381-385. https://doi.org/10.1016/0277-3791(88)90033-9

James, L.A. (1991). Incision and morphologic evolution of an alluvial channel recovering from hydraulic mining sediment. *Geological society of America bulletin*, 103(6), 723-736. https://doi.org/10.1130/0016-7606(1991)103%3C0723:IAMEOA%3E2.3.CO;2

Lamothe, M. & Auclair, M. (1999). A solution to anomalous fading and age shortfalls in optical dating of feldspar minerals. *Earth and planetary science letters*, 171, 319-323. https://doi.org/10.1016/S0012-821X(99)00180-6

Lapierre, J.D., Bjerklie, D.M., Simmons, R.C., Van Nieuwenhuyse, E., Wagener, S.M. & Reynolds, J.B. (1983). Effects of gold placer mining on interior Alsakan stream ecosystems. *In* Aldrich, J.W. *Managing water resources for Alaska's development: Proceedings*. Fairbanks: American water resources association, 251-284. http://hdl.handle.net/11122/1818, accessed on June 30, 2025.

Le Carlier, C. (2023). Mines et métallurgies à l'âge du Fer sur le massif armoricain. *In* Meunier, E., Fabre, J.-M., Hiriart, E., Mauné, S. & Tãmas, C.G. *Mines et métallurgies anciennes. Mélanges en l'honneur de Béatrice Cauuet*. Pessac: Dan@, 119-126. https://una-editions.fr/mines-et-metallurgies-sur-le-massif-armoricain/, accessed on April 30, 2025.

Lefevre, P. & Hatert, F. (2003). Or natif, arsenopyrite et minéraux secondaires dans les quartzites devilliens de Hourt, massif de Stavelot, Belgique. *Geologica Belgica*, 6(3-4), 193-200. https://hdl.handle.net/2268/29176

Lepper, K., Larsen, N.A. & McKeever, S.W.S. (2000). Equivalent dose distribution analysis of Holocen eolian and fluvial quartz sands from Central Oklahoma. *Radiation measurements*, 32(5-6), 603-608. https://doi.org/10.1016/S1350-4487(00)00093-7

Mahan, S.A., Rittenour, T.M., Nelson, M.S., Ataee, N., Brown, N., DeWitt, R., Durcan, J., Evans, M., Feathers, J., Frouin, M., Guérin, G., Haydari, M., Huot, S., Jain, M., Keen-Zebert, A., Li, B., López, G.I., Neudorf, C., Porat, N., Rodrigues, K., Sawakuchi, A.O., Spencer, J.Q.G. & Thomsen, K.J. (2023). Guide for interpreting and reporting luminescence dating results. *The geological society of America*, 135(5-6), 1480-1502. https://doi.org/10.1130/B36404.1

Malvern Panalytical. (2025). *Laser diffraction (LD).* Malvern Panalytical Ltd. https://www.malvernpanalytical.com/en/products/technology/light-scattering/laser-diffraction, accessed on July 5, 2025.

Mejdahl, V. (1979). Thermoluminescence dating: beta-dose attenuation in quartz grains. *Archaeometry*, 21(1), 61-72. https://doi.org/10.1111/j.1475-4754.1979.tb00241.x

Moayed, N.K. (2023). *Testing the potential of OSL dating for application to heated anthropogenic sediments (hearth and charcoal kiln remains).* Phd thesis in Geology, Ghent, Ghent University, 174 p. http://hdl.handle.net/1854/LU-01H4FYKPNBG95NEDNDX9YD54PQ

Moayed, N.K., Vandenberghe, D., Deforce, K., Kaptijn, E., Biernacka, P., De Clercq, W. & De Grave, J. (2023). OSL dating as an alternative tool fora ge determination of relic charcoal kilns. *Archaeometry*, 65(5), 939-954. https://doi.org/10.1111/arcm.12860

Murray, A.S. & Wintle, A.G. (2000). Luminescence dating of quartz using an improved single-aliquot regenerative-dose protocol. *Radiation measurements*, 32(1), 57-73. https://doi.org/10.1016/S1350-4487(99)00253-X

Murray, A.S. & Olley, J.M. (2002). Precision and accuracy in the optically stimulated luminescence dating of sedimentary quartz. *Geochronometria*, 21, 1-16. https://www.researchgate.net/publication/252350804_Precision_and_accuracy_in_the_optically_stimulated_luminescence_dating_of_sedimentary_quartz_A_status_review, accessed on May 27, 2025.

Murray, A.S. & Wintle, A.G. (2003). The single aliquot regenerative dose protocol: potential for improvements in reliability. *Radiation measurements*, 37(4-5), 377-381. https://doi.org/10.1016/S1350-4487(03)00053-2

Murray, A.S., Arnold, L.J., Buylaert, J.-P., Guérin, G., Qin, J., Singhvi, A.K., Smedley, R. & Thomsen, K.J. (2021). Optically stimulated luminescence dating using quartz. *Nature reviews methods Primers*, 72(1), 31 p. https://doi.org/10.1038/s43586-021-00068-5

Nelson, A.D. & Church, M. (2012). Placer mining along the Fraser river, British Columbia: The geomorphic impact. *Geological society of America*, 124(7-8), 1212-1228. https://doi.org/10.1130/B30575.1

Pentz, S.B. & Kostaschuk, R.A. (1999). Effect of placer mining on suspended sediment in reaches of sensitive fish habitat. *Environmental geology*, 37(1-2), 78-89. https://doi.org/10.1007/s002540050363

Petit, F., Gob, F., Houbrechts, G. & Assani, A.A. (2005a). Critical specific stream power in gravel-bed rivers. *Geomorphology*, 69(1-4), 92-101. https://doi.org/10.1016/j.geomorph.2004.12.004

Petit, F., Hallot, E., Houbrechts, G. & Mols, J. (2005b). Évaluation des puissances spécifiques de rivières de moyenne et de haute Belgique. *Bulletin de la société géographique de Liège*, 46, 37-50. https://popups.uliege.be/0770-7576/index.php?id=1904, accessed on May 23, 2025.

Petit, F., Hallot, E., Houbrechts, G., Levecq, Y., Mols, J., Peeters, A. & Van Campenhout, J. (2008). La typologie et les caractéristiques hydromorphologiques des cours d'eau wallons. *In La gestion physique des cours d'eau : Bilan d'une décennie d'ingénierie écologique*, October, 2007, Namur, Belgium. https://hdl.handle.net/2268/40148, accessed on May 23, 2025.

Prescott, J.R. & Hutton, J.T. (1994). Cosmic ray contributions to dose rates for luminescence and ESR dating: large depths and long-term time variations. *Radiation measurements*, 23(2-3), 497-500. https://doi.org/10.1016/1350-4487(94)90086-8

Preusser, F., Degering, D., Fuchs, M., Hilgers, A., Kadereit, A., Klasen, N., Krbetschek, M., Richter, D. & Spencer, J.Q.G. (2008). Luminescence dating: basics, methods and applications. *Quaternary science journal*, 57(1-2), 95-149. https://doi.org/10.3285/eg.57.1-2.5

Rhodes, E.J. (2011). Optically stimulated luminescence of sediments over the past 200,000 years. *The annual review of earth and planetary sciences*, 39, 461-488. https://doi.org/10.1146/annurev-earth-040610-133425

Seiler, S. (2015). Das Leben auf dem Lande in einer Randregion: Die römische Villa van Montenau. *In* Lejeune, C. & Engels, D. (eds), *Grenzerfahrungen*. *Eine Geschichte der deutschsprachigen Gemeinschaft Belgiens.* Eupen: 95-107.

Silva-Sánchez, N. & Armada, X.-L. (2023). Environmental impact of roman mining and metallurgy and its correlation with the archaeological evidence: A European perspective. *Environmental archaeology*, 1-25. https://doi.org/10.1080/14614103.2023.2181295

SPW. (2024). *Utilisation des produits LiDAR : Focus sur les produits issus de la campagne d'acquisition aéroportée LiDAR 2021-2022.* Namur: Service Public de Wallonie (SPW), 35 p. https://geoportail.wallonie.be/files/PDF/LiDAR24/Tuto_LiDAR%202.pdf, accessed on July 6, 2025.

SPW. (2025a). *Géoportail de la Wallonie : WalOnMap – Toute la Wallonie à la carte.* Service Public de Wallonie (SPW). https://geoportail.wallonie.be/walonmap, accessed on May 26, 2025.

SPW. (2025b). *Portail Walcors : Réseau permanent de stations GNSS de référence.* Service Public de Wallonie (SPW). https://gnss.wallonie.be/walcors.html, accessed on July 6, 2025.

Stoneham, D. (1991). Authenticity testing. *In* Göksu, H.Y., Oberhofer, M. & Regulla, D. (eds), *Scientific dating methods.* Dordrecht: Kluwer academic publishers, 174-194. ISBN: 0792314611

Trément, F. (2016). Le programme MINEDOR. À la recherche de l'or des Arvernes. *Revue d'Auvergne*, 130(618), 127-148. https://shs.hal.science/halshs-01834725v2, accessed on April 29, 2025.

Trément, F. (2023a). À la recherche de l'or des Arvernes. *Dossiers d'archéologie*, 399, 28-35. https://hal.science/hal-04291446v1, accessed on April 29, 2025.

Trément, F. (2023b). L'or des Arvernes retrouvé grâce au LiDAR. *Dossiers d'archéologie*, 406, 25-27. https://hal.science/hal-04291432v1, accessed on April 29, 2025.

Trément, F. (2025). *Apports du LiDAR HD MINEDOR-CRAIG à la caractérisation des activités minières anciennes en Haute-Combraille (Puy-de-Dôme). Exploration archéologique de deux vastes zones de tertres d'orpaillage dans la forêt domaniale de l'Eclache (Tortebesse, Prondines). Bilan de la campagne de fouilles de l'été 2024. In* Journée d'étude MINEDOR, June 18-19, 2025, Clermont-Ferrand, France. https://hal.science/hal-05122260v1, accessed on July 7, 2025.UNESCO. (2025). *World Heritage List: Las Médulas.* UNESCO - World Heritage Convention. https://whc.unesco.org/en/list/803/, accessed on April 29, 2025.

Van Ruymbeke, M. (2021). Le silence est d'or. *In* Cremer, S., Fraiture, P., Maggi, C., Strivay, D., Van Ruymbeke, M., Van Wersch, L. & Weitz, A. (eds), *Cerner le passé. Mélanges en l'honneur de Patrick Hoffsummer*. Liège: Atelier des presses, 241-271. http://hdl.handle.net/10993/51713, accessed on May 6, 2025.

Vandenberghe, D. (2004). *Investigation of the optically stimulated luminescence dating method for application to young geological sediments*. Unpublished PhD thesis in Analytical Chemistry, Ghent, Ghent University, 298 p.

Vandenberghe, D., Derese, C. & Houbrechts, G. (2007). Residual doses in recent alluvial sediments from the Ardenne (S Belgium). *Geochronometria*, 28, 1-8. https://doi.org/10.2478/v10003-007-0024-z

Vandenberghe, D., De Corte, F., Buylaert, J.-P., Kučera, J. & Van den haute, P. (2008). On the internal radioactivity in quartz. *Radiation measurements*, 43(2-6), 771-775. https://doi.org/10.1016/j.radmeas.2008.01.016

Vandenven, G. (1990). Explications de la carte géologique du synclinorium de l'Eifel (région de Gouvy-Sankt-Vith-Elsenborn). *Annales de la société géologique de Belgique*, 113(2), 103-113. https://popups.uliege.be:443/0037-9395/index.php?id=1350, accessed on May 20, 2025.

Vaudagna, A. (2012). *Bessa: Miniera d'oro romana.* Biella: DocBi centro studi biellesi, 46 p. https://www.calameo.com/books/000880928e189543f2d77, accessed on April 30, 2025.

Veiga, M.M., Metcalf, S.M., Baker, R.F., Klein, B., Davis, G., Bamber, A., Siegel, S. & Singo, P. (2006). *Manual for training artisanal and small-scale gold miners.* Vienna: United Nations Industrial Development Organization, 146 p. https://www.sdsg.org/s/Manual-for-Training-ASM-Gold-Miners-Removal-of-Barriers-to-Introduction-of-Cleaner-Artisanal-Gold-Mi.pdf, accessed on May 12, 2025.

Walker, M.J.C. (2005). *Quaternary dating methods.* Chichester: John Wiley & Sons, 286 p. https://doi.org/10.1002/jqs.1053

Wavreille, B. (1987). *Contribution à l'étude géomorphologique du massif de Serpont : Les vestiges d'orpaillage dans le bassin de la Lomme supérieure.* Master thesis in Geography, Liege, University of Liege, 121 p. https://explore.lib.uliege.be/permalink/32ULG_INST/oao96e/alma9923066435202321, accessed on July 8, 2025.

Wentworth, C.K. (1922). A scale of grade and class terms for clastic sediments. *The journal of geology*, 30(5), 377-392. https://www.jstor.org/stable/30063207

Wintle, A.G. (2008). Fifty years of luminescence dating. *Archaeometry*, 50(2), 276-312. https://doi.org/10.1111/j.1475-4754.2008.00392.x

Wintle, A.G. (2014). Luminescence dating methods. *Treatise on geochemistry (second edition)*, 14, 17-35. https://doi.org/10.1016/B978-0-08-095975-7.01203-1

Wintle, A.G. & Murray, A.S. (1998). Towards the development of a preheat procedure for OSL dating of quartz. *Radiation measurements*, 29(1), 81-94. https://doi.org/10.1016/S1350-4487(97)00228-X

Wintle, A.G. & Murray, A.S. (2006). A review of quartz optically stimulated luminescence characteristics and their relevance in single-aliquot regeneration dating protocols. *Radiation measurements*, 41(4), 369-391. https://doi.org/10.1016/j.radmeas.2005.11.001

Wintle, A.G. & Adamiec, G. (2017). Optically stimulated luminescence signals from quartz: a review. *Radiation measurements*, 98, 10-33. https://doi.org/10.1016/j.radmeas.2017.02.003

Zimmerman, D.W. (1967). Thermoluminescence from fine grains from ancient pottery. *Archaeometry*¸10(1), 26-28. https://doi.org/10.1111/j.1475-4754.1967.tb00610.x

X. APPENDIXES

See supplementary file “Appendix”.